2018

Acquisition and analysis of steady-state and time-resolved fluorescence data for applications in materials science, bioanalytical chemistry, and super-resolution microscopy

Kalyan Santra
Iowa State University

Acquisition and analysis of steady-state and time-resolved fluorescence data for applications in materials science, bioanalytical chemistry, and super-resolution microscopy

by

Kalyan Santra

A dissertation submitted to the graduate faculty

in partial fulfillment of the requirements for the degree of

DOCTOR OF PHILOSOPHY

Major: Physical Chemistry

Program of Study Committee:
Jacob W. Petrich, Major Professor
Xueyu Song
Emily A. Smith
Theresa L. Windus
Mark S. Hargrove

The student author, whose presentation of the scholarship herein was approved by the program of study committee, is solely responsible for the content of this dissertation. The Graduate College will ensure this dissertation is globally accessible and will not permit alterations after a degree is conferred.

Iowa State University

Ames, Iowa

2018

Dedicated to my parents

TABLE OF CONTENTS

ACKNOWLEDGEMENTS

The journey as a Ph.D. student has been a challenging yet worthwhile learning experience. I wouldn't be able to complete my dissertation without the support and contribution of a number of people through their direct and indirect involvements. It's my pleasure to take this opportunity to express my humble gratitude and appreciation to them, irrespective of whether they are mentioned here or not.

First and foremost, I would like to express my sincere gratitude to my research advisor, Prof. Jacob W. Petrich, for his invaluable guidance and support throughout my research. His knowledge and expertise in optical spectroscopy have given me the opportunity to learn many key concepts pertinent to this field and prepared me for the future challenges. This dissertation would not have been possible without his valuable support, and I am very thankful to him for his patience to critically evaluate this.

Besides my advisor, I would like to express my humble gratitude to other members of my Program of Study (POS) committee: Prof. Xueyu Song, Prof. Emily A. Smith, Prof. Theresa L. Windus and Prof. Mark S. Hargrove, for their helpful comments and suggestions throughout the course of the degree. Apart from having Prof. Song and Prof. Smith in my committee, I had an opportunity to work with them on a number of collaborative projects. The special one is the "nanodomain imaging" project, where I learned various theoretical and experimental aspect of single photon counting and super-resolution imaging techniques. A significant amount of research presented in this dissertation is the result of their collaboration. I would like to thank them sincerely. I am thankful to Prof. Windus and Prof. Hargrove for their suggestions, encouragement and precious time during POS meetings.

I would like to express my gratitude to a number of other collaborators at Iowa State University. A special thanks to Prof. Jared Anderson and Prof. George Kraus for their successful collaboration in "magnetic ionic liquids (MIL)" and "PFPDFHBI fluorescence" projects respectively. Thanks to their enthusiasm and support these two projects are now on the verge of being submitted to the journals. I would like to thank Prof. Marit Nilsen-Hamilton, Prof. Namrata Vaswani, Prof. Matthew Panthani, Prof. Sumit Chaudhary, Prof. Brett VanVeller and Prof. Mark Rasmussen for their valuable collaborations in several wonderful projects.

I am thankful to the members of our group, past and present, for their help and collaboration. I had an opportunity to work with few brilliant undergraduate students. Besides that, I would also like to thank members of Prof. Smith's group and Prof. Anderson's group for their collaboration. It was a wonderful experience to work with all these people. I would like to acknowledge all the help from the staffs of Department of Chemistry at Iowa State University and Ames Laboratory.

I am grateful to my M.Sc. advisor, Prof. Anindya Datta (IIT Bombay) for his encouragement, thoughtful guidance and for giving me an opportunity to gain experience in spectroscopy. My sincere thanks to Prof. Puspendu K. Das (IISc, Bangalore) for introducing me to nonlinear spectroscopy. I consider myself very fortunate to have many great teachers throughout my academic life. I am indebted to them for their teachings, encouragement, and inspiration.

I am so thankful to my friends in Ames who provided me a very homely atmosphere here. I deeply appreciate their help and encouragement and admire their enthusiasm. My staying in Ames was truly an enriching experience and enjoyable for their wonderful company.

Finally, I would like to express my heartfelt gratitude to my parents. Words are certainly not enough to acknowledge their contribution in every aspect of my life. The journey to Ph.D. wouldn't

have been possible without their endless encouragement and thereby I dedicate this dissertation to my parents. I am so thankful to my younger brother and elder sisters for their relentless support and encouragement. I would not miss this opportunity to thank my close relatives and friends for their help and support.

This work was supported by the U.S. Department of Energy (DOE), Office of Basic Energy Sciences, Division of Chemical Sciences, Geosciences, and at the Ames Laboratory under contract number DE-AC02-07CH11358. Ames Laboratory is operated for the DOE by Iowa State University. The document number assigned to this dissertation is IS-T 3241.

ABSTRACT

Steady-state and time-resolved fluorescence techniques enjoy widespread applicability in domains ranging from biology to materials science owing to their extraordinary sensitivity and dynamic range.

Among the most useful of these techniques is time-correlated, single-photon counting, which forms the basis of another: fluorescence lifetime imaging using stimulated emission depletion microscopy (FLIM-STED), which is used to obtain structural information on a subdiffraction-limited level (*i.e.*, 40 nm or less). The high spatial resolution afforded by this technique is, however, accompanied by a reduction in the number of photons collected. Thus, its utility can only be exploited when meaningful information can be retrieved from sparse data sets. This retrieval requires the use of proper modeling and efficient analysis techniques. In this dissertation, several such techniques and their significance in super-resolution imaging are discussed in the context of extracting excited state fluorescence lifetime of one or more fluorophores. Probability-based, maximum-likelihood (ML) methods are compared with residual minimization (RM) methods in order to determine the limiting number of photons that are required to provide a meaningful analysis of the data. The ML methods are more robust and show considerable improvement over RM methods. The ML methods are further improved by implementing a Bayesian framework, where a nonuniform prior distribution of the parameters is included in the form of a Gaussian, an exponential, or a Dirichlet distribution.

Two examples of the applications of the steady-state and time-resolved techniques are provided: the characterization of the properties of magnetic ionic liquids (MILs) and those of poly (3-hexylthiophene) (P3HT). MILs facilitate the solvent extraction of bioanalytes, *e.g.* DNA extraction from an aqueous solvent, with the help of an external magnetic field. The presence of

paramagnetic ions, however, introduces several mechanisms of nonradiative quenching for the fluorescence of the label. Several MILs are screened to find a suitable candidate for DNA extraction using fluorescence spectroscopy. P3HT is used as the active donor layer of organic photovoltaics owing to their high photon-conversion efficiency. The structural details of the polymer aggregates of a thin film of P3HT exposed to electric filed are studied using steady-state and time-resolved anisotropy. Preferential orientations of the polymer backbone are observed if the thin film is exposed to an electric field during preparation.

CHAPTER 1. GENERAL INTRODUCTION

1.1 Overview

The interaction of light with matter has a broad range of applications in the physical, chemical, and biological sciences. The classical description of light is that it is composed of oscillating electric and magnetic fields that carry energy and interact with the medium through which they travel, often changing their own characteristics.[1-7] The quantum theory of light, on the other hand, describes it as being composed of discrete packets of energy knows as photons.[3,7,8] When those photons interact with the atoms or molecules of the medium, they are scattered, absorbed, or emitted as new photons.[9-13] Optical spectroscopy is the field of study that exploits this quantum nature of light to "visualize" the various properties of materials. Steady-state and time-resolved fluorescence spectroscopy are among a few of the very sensitive and powerful techniques that have been used for last few decades to study materials that are important in physics, chemistry, and biology.[12-15] With the development of sophisticated laser technology and techniques, it has become possible to probe photophysical processes such as the relaxation of excited states, energy transfer, electron transfer, solvation dynamics, rotational orientation, diffusion, and many others that occur over times scales from femtosecond to microsecond and longer.[15] Time-resolved techniques such as time-correlated, single-photon counting (TCSPC), fluorescence upconversion, and pump-probe spectroscopy are extremely sensitive and reliable tools to quantify these processes.[7,14-18]

More recently, microscopy techniques based upon fluorescence or Raman spectroscopy have become widespread owing to their ability to map physical and chemical information in the spatial dimensions of the samples. The importance of super resolution microscopies was

acknowledged by a 2014 Noble Prize in chemistry. Some of the most popular and important super resolution techniques are stimulated emission depletion microscopy (STED),[19-21] stochastic optical reconstruction microscopy (STORM),[22] and photoactivated localization microscopy (PALM).[23,24] Super resolution imaging can also be performed using coherent anti-Stokes Raman (CARS) microscopy,[25,26] Development of super resolution techniques depends on progress in two areas. In one hand, there is the need for continued development and modification of instrumentation and the synthesis of suitable chemicals probe molecules, specifically, brighter and more stable fluorophores are undergoing. On the other hand, there is the need to develop efficient methods of analysis for the information-rich data sets that these experiments generate.[27-50] Analyses of the data obtained from super resolution microscopy techniques often pose unique challenges owing to factors ranging from low signal intensity, photodegradation of the sample, fitting models and data analysis, *etc*. The development of improved methods of data analysis can improve experimental design and reduce data acquisition time.

The dissertation will discuss: (1) efficient data analysis techniques that can improve the design of super resolution experiments and extract more information from them in **Chapters 3-5**; (2) various spectroscopic techniques in **Chapter 2**; and (3) their application for characterization of materials relevant to the bioanalytics, bioimaging, and solar energy in **Chapters 6-7**.

1.2 The Importance of Developing Improved Methods of Analyzing Time-Resolved Data: The Importance of Super Resolution Microscopy Techniques

1.2.1 Time-resolved stimulated emission depletion (STED) microscopy and the problems associated with fitting the data

Fluorescence-based techniques are the most commonly used for probe biological structure.[51,52] Despite continued development of optical systems and microscopes, their resolving power has a fundamental limit.[19,20,53-61] Owing to the wave nature of light, the signal from a point source undergoes diffraction and produces a three-dimensional intensity distribution with a finite width in the image plane. This intensity profile is known as point spread function (PSF). The width (full-width half-maximum, FWHM) of the PSF is given by the Abbe diffraction limit, which can be approximated by $0.61\lambda/NA$ in the lateral dimension, where λ is the wavelength of the light and NA is the numerical aperture of the focusing objective. In the axial direction, the diffraction limit is about twice that of the lateral direction.[62] For visible light, *i.e*., the wavelength range of 400-700 nm, the diffraction limits are about 200-350 nm in the lateral direction and about 400-700 nm in the axial direction. Two objects closer than the diffracting limit of the optical system cannot be resolved. In recent years, however, several super resolution techniques have been developed that overcome the diffraction limit. Stimulated emission depletion microscopy (STED) is one such technique.[19,20,62-67] Improved spatial resolution in STED is achieved by employing a collinear depletion pulse superimposed spatially and temporally upon an excitation pulse. (**Figure 1.1**). The depletion pulse has a donut-shape profile with zero-intensity at the center and is designed to remove fluorescent photons from the periphery of a sample by stimulated emission. Thus, the sample only provides photons from the subdiffraction limited center, resulting in a narrower PSF. The width of the PSF in the STED depends on the intensity of the depletion pulse.[63] STED is

amply described in the literature.[21] Theoretically, the spatial resolution comparable to the molecular dimensions can be achieved by employing very intense depletion pulse. A spatial resolution of less than 10 nanometers has been achieved in diamond to image the nitrogen-vacancy centers.[67] The photostability, however, of the fluorophores often limit the applicability of STED. should be taken into account to apply such intense light.

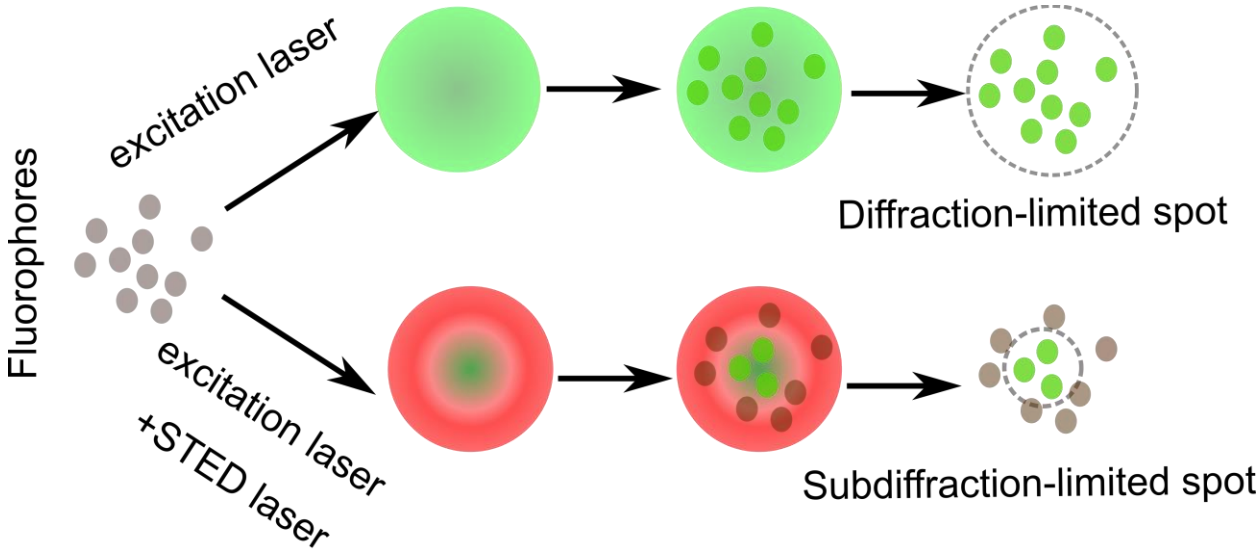

Figure 1.1. Diffraction-limited spot results from the excitation of fluorophores by the excitation laser. In STED-based modification, a colinear "donut-shaped" STED laser is superimposed with the excitation laser. Subdiffraction-limited spot results from the stimulated deexcitation of fluorophores at the periphery of the diffraction-limited spot.

Time-correlated, single-photon counting (TCSPC) is the core principle behind the fluorescence lifetime imaging microscopy using STED (FLIM-STED).[63-66] Owing to its ease of use, high sensitivity, and large temporal dynamic range TCSPC is also fundamental to a number of other important techniques such as Förster resonance energy transfer (FRET),[68-71] fluorescence correlation spectroscopy (FCS)[72-74], time-resolved fluorescence anisotropy.[75-77] A TCSPC instrument records the time difference between the arrival times of an excitation pulse and a pulse resulting from a photon detected from fluorescence emission. These time-tagged data are typically

collected for many cycles of a periodic excitation source to construct a histogram of the photon distribution and subsequently, the data can be analyzed to extract the mean excited state lifetime of the fluorophores. For fluorescence lifetime imaging using STED (FILM-STED), the sample is raster-scanned in the spatial dimension; and each pixel represents one histogram in the temporal dimension (**Figure 1.2**). The excited-state lifetimes of the fluorophores are sensitive to the local environment; and, therefore, FLIM-STED can, in principle, be used to probe spatial heterogeneity at sub-100 nanometer level.

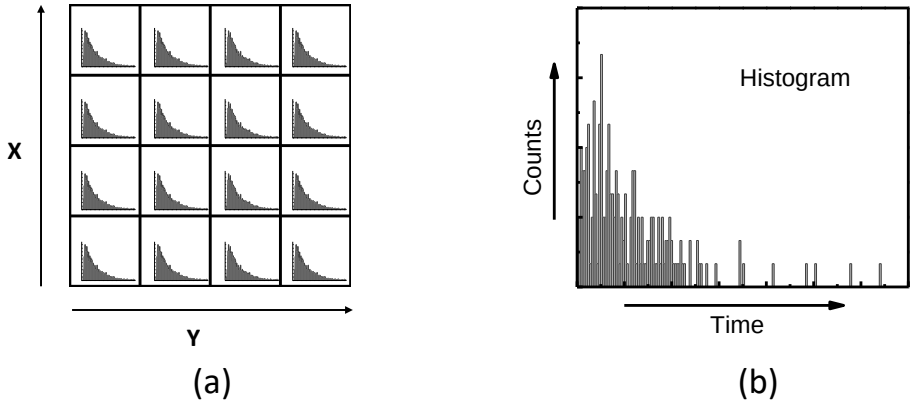

Figure 1.2. (a) Schematic diagram, showing a raster-scanned FILM-STED (b) A representative histogram corresponding to one pixel.

1.2.2 Analysis of time-resolved data

The spontaneous emission of photons from the excited state of a collection of molecules does not occur at the same time, but is given by a Poisson distribution,[78] just as for the emission of radiation from decaying nuclei.[79,80] The decay of the excited state of a single species commonly follows first-order kinetics (**Figure 1.3**). The fluorescence signal from a heterogeneous sample is usually given by the sum of decaying exponential functions.

$$F(t) = F(t_0)\sum_n a_n \exp(-\frac{t-t_0}{\tau_n}) \qquad (1.1)$$

where $F(t)$ is the fluorescence intensity at time t and is proportional to the number of photons collected. $F(t_0)$ is the fluorescence intensity at an arbitrary time t_0 after the excitation.

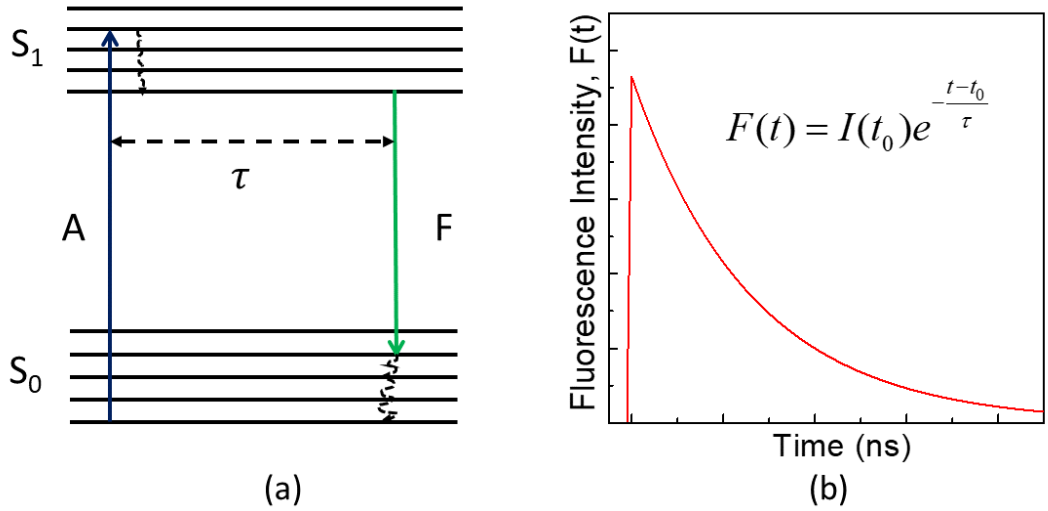

Figure 1.3. (a) Depiction of the excited state fluorescence lifetime in Jablonski diagram. A – absorption, F – fluorescence emission, τ – fluorescence lifetime, S_0 and S_1 are the ground and excited electronic states (singlet) respectively (b) An exponential decay function, the most popular model for the fluorescence lifetime of a single fluorophore.

The subscript n denotes the n-th species in the heterogeneous sample, τ_n and a_n are the mean excited state lifetime and the fractional composition respectively for the n-th species, where $\sum_n a_n = 1$. The excitation laser pulse is not a delta function, and each of the components of the detection system (for example, photo-detector, monochromator, and electronics) may further broaden and distort it, thus producing the instrument response function (IRF). The measured fluorescence decay, $D(t)$, is thus the convolution of the IRF with the undistorted excited-state fluorescence decay profile given in equation (1.1):

$$D(t) = \int_0^t F(t')I(t-t')dt' \qquad (1.2)$$

where $I(t)$ is the experimentally measured IRF.[14] The true form of the undistorted decay, $F(t)$, can not be easily obtained since the inverse problem is mathematically ill-formulated[81-83] (*i.e.*, many solutions may adequately describe the observed decay).

Most frequently, the analysis of TCSPC data to extract the mean lifetime(s) is performed using a nonlinear, least-squares technique, which is referred to as Residual Minimization (RM).[84,85] RM minimizes the weighted squares of the residuals[86-88] of the experimental data and the optimized fitting function. In RM-based analyses, a histogram of very high quality is required in order to extract the mean excited state lifetime with high accuracy; and such a histogram is only obtained with a large number of total photon counts.[84,85,89] The acquisition of such a high-quality histogram, however, is usually not possible for FLIM-STED. First, in this experiment, the improved spatial resolution is obtained by reducing the number of fluorophores with the STED depletion pulse. The effective focal volume from which the signal is obtained is, therefore, greatly reduced. Second, the improved spatial resolution is also gained by higher laser powers, which introduces photobleaching and irreversible photodamage. In order to minimize these, it is necessary to reduce the data collection time per pixel, which in turn also reduces the number of collected photons. Third, the mere fact of acquiring a super-resolution image usually implies the need for reducing the data collection time per pixel. A 10-fold improvement in the resolution requires a 100-fold increase in the number of pixel for a 2D sample and 1000-fold increase for a 3D sample and, thus, a proportional increase in the overall data acquisition time. Fourth, often because of the specific requirement of the experiment, one is limited to a fluorescent probe with a low quantum yield. Thus, FLIM-STED data may often be comprised of small numbers of photons counts yielding poor quality-histograms for lifetime analysis (**Figure 1.4**). Unless there is a certain

number of total counts, RM yields a poor estimate of the mean lifetime. The total number of photon counts can be increased by spatial binning of the adjacent pixels. This, however, compromises the spatial resolution, defeating the purpose of the super resolution imaging experiment in the first place. Binning time channel has also been demonstrated[89] to increase the total number of counts. But temporal binning also has some drawbacks. For example, it compromises the temporal resolution by lowering the dynamic range. There are numerous other analysis techniques such as Laguerre expansion,[90-93] Laplace transform,[14,94] global analysis,[95-97] maximum entropy method,[98-101] smoothed exponential series method,[102-104] basis pursuit denoising,[105,106] and compressive sensing.[83,107-109] that are applied to photon counting data. Each has several advantages and disadvantages. This dissertation, however, focuses on several probability-based methods that perform extremely well for data sets comprised of sparse photon counts.[84-86] A brief discussion of the key concepts is presented here. More details of the methodologies are provided in **Chapters 3-5**.

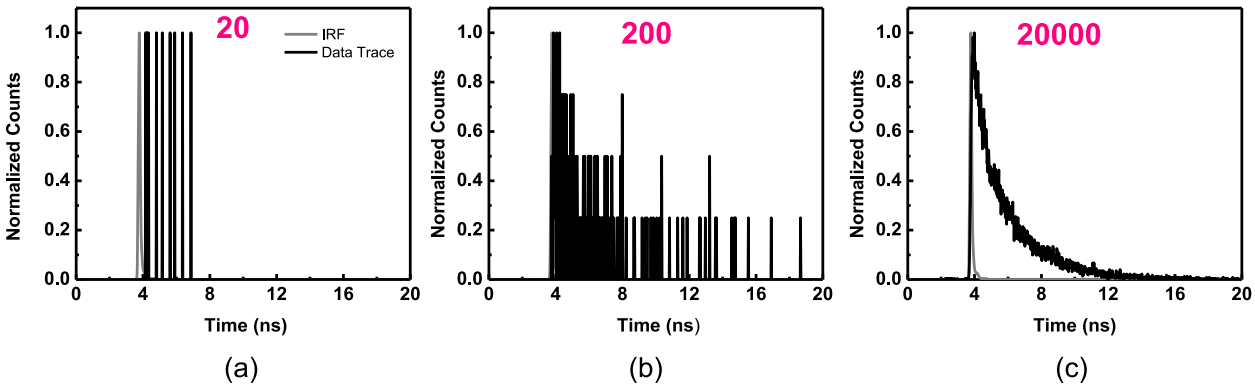

Figure 1.4. Examples of time-correlated single-photon counting data. The quality of the data directly related to the number of total photon counts (labeled in each panel).

1.2.3 Maximum likelihood (ML) method

Maximum likelihood (ML) is one of the most robust parameter-estimation methods in statistics. Its objective is to maximize the parametric likelihood function given by observed data.

Mathematically, the likelihood function is the joint probability distribution function of the observation under the assumed model. If X represents a random variable that follows the distribution, $f(X;\boldsymbol{\theta})$, where $\boldsymbol{\theta}$ denotes all the parameters, then the likelihood function is given by:

$$\mathcal{L}(\boldsymbol{\theta};\boldsymbol{x}) = \prod_{n=1}^{N} f(x_n;\boldsymbol{\theta}) \tag{1.3}$$

where, x_n is the n-th realization of the random variable X and $\boldsymbol{x}$ is the vector that represents the N number of observations without binning. It is often convenient to work with the log-likelihood:

$$\ell(\boldsymbol{\theta};\boldsymbol{x}) = \ln \mathcal{L}(\boldsymbol{\theta};\boldsymbol{x}) = \sum_{n=1}^{N} \ln f(x_n;\boldsymbol{\theta}) \tag{1.4}$$

The maximization of the log-likelihood occurs at the same point in the parameter space as the maximization of the likelihood itself. The optimized parameter is given by:

$$\widehat{\boldsymbol{\theta}} = \max_{\theta} \ell(\boldsymbol{\theta};\boldsymbol{x}) \tag{1.5}$$

For convoluted observed data, for example as in equation (1.2), a closed-form solution cannot be determined and therefore a numerical global optimization can be employed. The use of ML to analyze photon-counting data was popularized by Baker and Cousins[86] in the form of likelihood chi-square optimization and subsequently used by others[32,110-112]. The likelihood chi-square is given by the likelihood ratio of the parametric model and the true model (often approximated by the observed data[86]). Many comparisons of ML with RM appear in the literature, but they are typically limited to simulated data. Also, these comparisons typically do not consider important aspects of the experiment: *e.g.*, the instrument response function (IRF); bin size; shift parameter (which accounts for the wavelength difference between the instrument response function and the fluorescence signal); and, most importantly, the total number of photon counts.

1.2.4 Poisson distribution

The spontaneous emission of a photon from the excited state is fundamentally a random process, which is believed to follow the Poisson statistics.[78,113] The Poisson distribution describes the probability (P) of the occurrence of a certain number of events (N) for a given average number of events (λ) in that time interval. While the average number of events need not be an integer, the number of observed events (N) must be an integer; and the events are independent of each other. These criteria are fulfilled in TCSPC experiments since a single photon is detected from each periodic and identical excitation pulse. If the average number of counts (λ) is found from a model function, the Poisson probability is given by:

$$P(N;\lambda) = \frac{\lambda^N e^{-\lambda}}{N!} \tag{1.6}$$

The Poisson probability can be defined for all channels to obtain the distribution of the rate parameter (λ), and therefore the fluorescence lifetime can be obtained from the model function of the rate parameter.[84]

1.2.5 Binomial distribution

In a TCSPC experiment, the photon counts are registered in one of the bins in the temporal channel. The probability distribution of the number of success that a photon is registered in a particular channel can be described by the binomial distribution.[113] For N identical and independently distributed observations with success, θ_t, if the number of observed successes is k in the time channel t, then the probability distribution of that observation is given by:

$$P(k;N,\theta_t) = \binom{N}{k} \theta_t^k (1-\theta_t)^{N-k} \tag{1.7}$$

where the first factor on the right is the binomial coefficient. The probability distribution can be maximized for all channels to obtain the distribution of θ_t and thereafter to estimate the related parameters (*e.g.*, fluorescence lifetime) that model θ_t.[84]

1.2.6 Bayesian formulation

Although ML is a very robust estimation technique, it assumes a uniform probability distribution of the parameters. Thus, any prior knowledge of the distribution of the parameters is not utilized. Implementation of a suitable *nonuniform* distribution should, therefore, improve the estimation. Let $\boldsymbol{\beta}$ and $\boldsymbol{E}$ represent the parameter space and the evidence (*i.e.*, experimental observations), respectively. The *posterior* distribution of the parameters that defines the model for the experimental observation, $P(\boldsymbol{\beta}|\boldsymbol{E})$, is given by the Bayes' theorem[114-116]:

$$P(\boldsymbol{\beta}|\boldsymbol{E}) = \frac{P(\boldsymbol{\beta})P(\boldsymbol{E}|\boldsymbol{\beta})}{P(\boldsymbol{E})} \tag{1.8}$$

where $P(\boldsymbol{E}|\boldsymbol{\beta})$ is the likelihood of evidence given the set of parameters $\boldsymbol{\beta}$; and $P(\boldsymbol{\beta})$ is the *prior* distribution of the parameters, which can be obtained from the prior knowledge of the parameters. The normalization factor, $P(\boldsymbol{E})$, in the denominator is known as the marginal likelihood and it can be obtained by integrating the posterior probability all other the parameters space. Therefore, the posterior distribution contains both the prior knowledge about the parameters as well as the likelihood of the evidence for given values of those parameters. The posterior acts as the prior distribution for a new set of evidence and thus as new evidence are collected, the prior becomes more refined and gives better estimates of the parameters that describe the distribution. The initial choice of the prior distribution is the most important part of the Bayesian framework. In **Chapter 5**, Bayesian analyses using *Gaussian*, *exponential*, and the *Dirichlet* priors are been presented.

1.3 Ionic Liquids and Magnetic Ionic Liquids

Ionic liquids (ILs) are a class of compounds usually composed of a large organic cation and inorganic or organic anions (**Figure 1.5**). Sometimes they are referred to as being molten salts at room-temperature, or temperatures "close" to room temperature. The current working definition of ILs (which is somewhat arbitrary) is that of a liquid made of ions that is fluid at temperatures below 100 °C. ILs are usually viscous fluids with low vapor pressure and very high thermal stability. They have a range of catalytic properties. ILs are gaining much interest in industry and academics because of their being (usually) environmentally friendly solvents. They have a wide range of applications in organic synthesis,[117-121] liquid-liquid extractions[122,123] electrochemical studies,[124] and in matrix-assisted laser-desorption/ionization mass spectrometry (MALDI) owing to their ultralow volatility.[125]

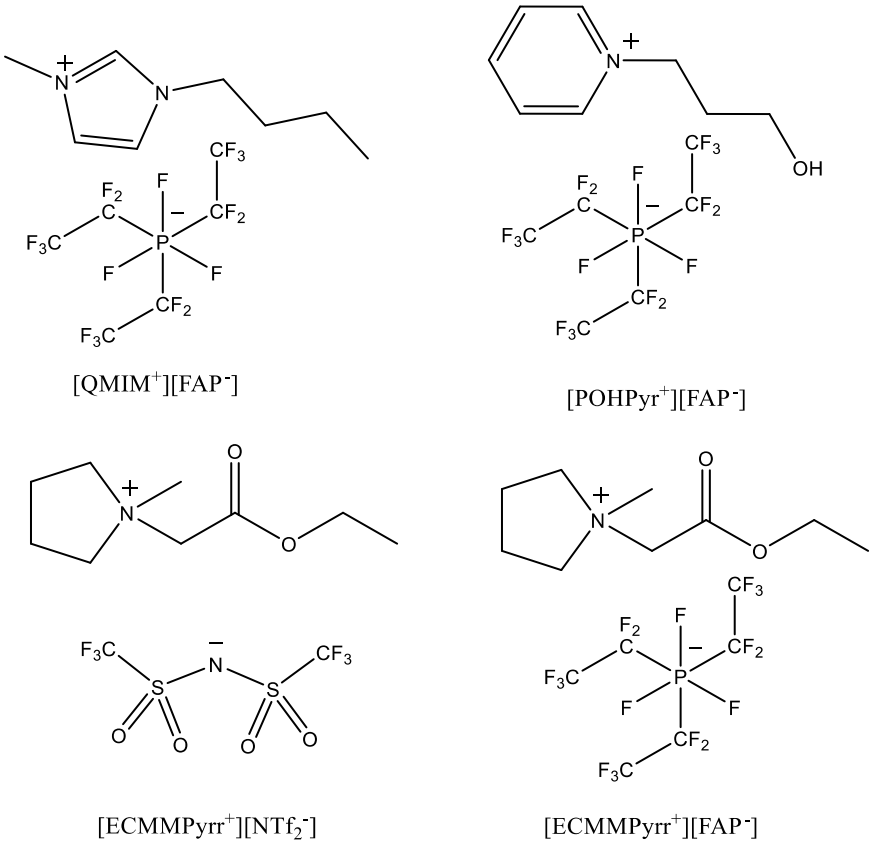

Figure 1.5. Examples of ionic liquids (ILs)

Magnetic ionic liquids (MILs) are a subclass of ILs that is gaining interest because of their potential for use in the analytical application.[126,127,128] The cation or the anion of a conventional IL is modified with a paramagnetic ion(**Figure 1.6**).[129-131] MILs have similar physicochemical properties as those of "traditional" ILs, with the added advantage that they exhibit a strong response in the presence of a magnetic field. The paramagnetic properties of an MIL was first reported in 1-butyl-3-methylimidazolium tetrachloroferrate(III) ([$BMIM^+$][$FeCl_4^-$]).[131] Various MILs were synthesized in order to optimize their physicochemical properties as well as their magnetic susceptibility[127,132-134]. Using combinations of a multi-cationic platform and a paramagnetic anion with large magnetic susceptibility, an effective magnetic moment of 11.56 Bohr magnetons has been achieved.[135] MILs are usually hydrophobic due to the instability of the paramagnetic ion in an aqueous medium,[135] and the viscosities are often high.[127] Recently, a series of MILs has been designed based on a metal complex of the hexafluoroacetylacetonate anion, which contributes to reducing the viscosity.[136]

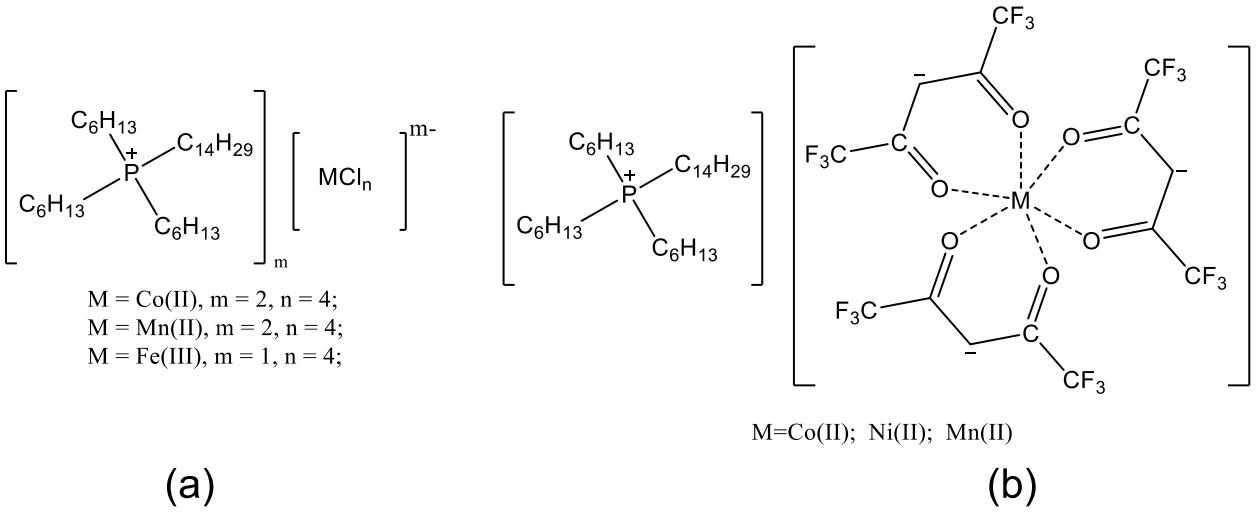

Figure 1.6. Examples of magnetic ionic liquids (MILs). (a) Structure of MILs with metal chlorides (b) Structure of MILs with metal hexafluoroacetylacetonate.

One potential application of MILs is the extraction of DNA or a similar biomolecule from the aqueous solution. MIL-based DNA extraction has been demonstrated recently.[137] It has been shown that the magnet-based extractions are fast and that the extraction efficiency can reach up to 57%, much higher than that of traditional liquid-liquid extraction. Although analysis of the extracted analyte can be done using quantitative PCR, a fluorescence-based assay using steady-state and time-resolved techniques will be more suitable because of the sensitivity afforded by fluorescence detection. Since, however, paramagnetic ions of heavy metals are present, a number of mechanisms (*e.g.*, intersystem crossing, excited-state electron transfer, Förster resonance energy transfer) can reduce the fluorescence. In **Chapter 6**, a quantitative analysis of the fluorescence behavior of the fluorescent probe, cyanine5 carboxylic acid (Cy5), isolated and bound to DNA, in the presence of MILs is discussed.

1.4 Poly (3-hexylthiophene) (P3HT)

Since their discovery, bulk-heterojunction (BHJ) organic photovoltaic (OPV) solar cells have shown great promise as a source of renewable energy.[138,139] Organic photovoltaic materials (OPV) are a low-cost alternative[140-142] and have higher efficiency (>10%) compared to conventional inorganic solar cell materials.[143-146] Many OPV materials are based on organic polymers with π-conjugation and have semiconductor properties because of delocalization arising from conjugation along the polymer backbone.[147] The most studied bulk-heterojunction system is the mixture of poly(3-hexylthiophene) and phenyl-C61-butyric acid methyl ester (P3HT:PCBM), where P3HT acts as the electron donor and PCBM acts as the electron acceptor (**Figure 1.7**).[138-146] P3HT:PCBM bulk heterojunctions are commonly deposited from solution onto a transparent

conducting oxide (*e.g.*, indium tin oxide, ITO) coated with a water-soluble, hole-conducting layer (*e.g.*, PEDOT:PSS).[144] The typical power-conversion efficiency is 3-6%.[139,148-150]

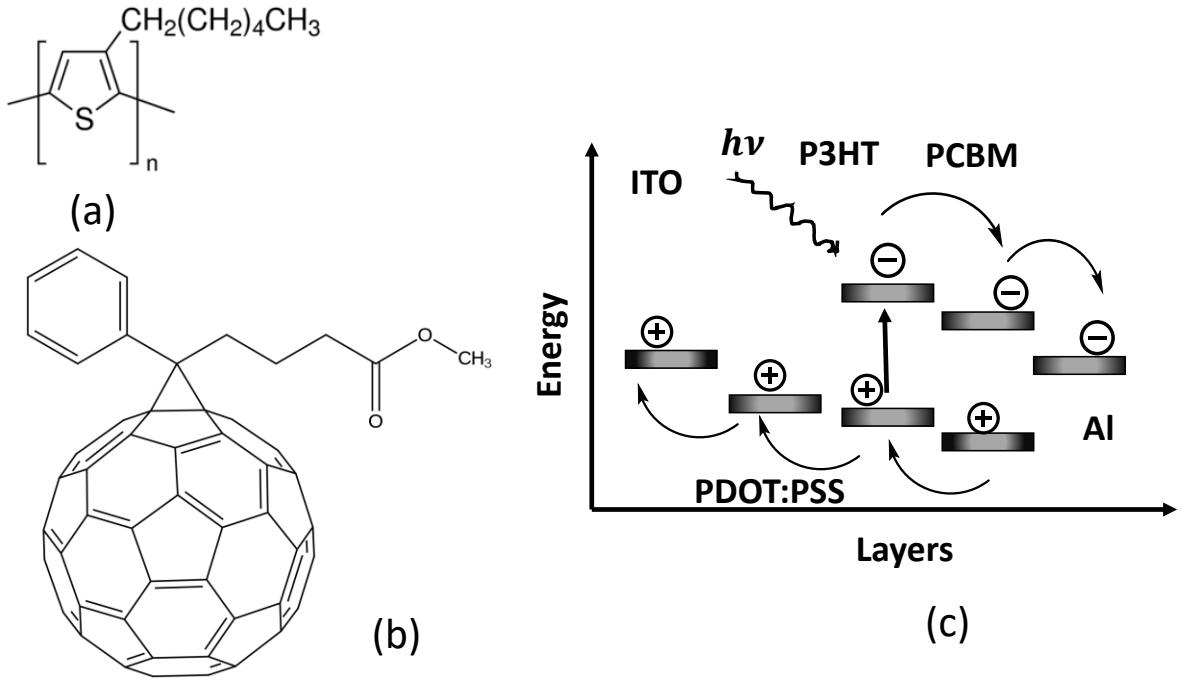

Figure 1.7. Structures of (a) poly(3-hexylthiophene) (P3HT) (b) phenyl-C61-butyric acid methyl ester (PCBM). (c) Schematic representation of the organic photovoltaics where P3HT and PCBM are used as the active layer.

There have been several studies on this system aiming to improve the power conversion efficiency that explored the morphological characteristics (size, shape, texture), interlayer diffusion dynamics, phase separation, molecular weight, heterogeneity, effect of temperature, effect of impurities, *etc.*[138-146,151-160 161] The most important factor that affects the efficiency of a photovoltaic is the overlap between the absorption spectrum of the polymer and spectrum of solar radiation. P3HT is an excellent absorber and has very wide-band of absorption in the UV-visible region. The band gap can be tuned by changing the composition of the P3HT:PCBM composite. The alignment of the polymer can also have an effect of on the band gap. It has been observed that a "Head-Tail" alignment of P3HT has a narrower band gap than a "Head-Head" alignment.[162]

Generation of photocarriers and their transfer to the heterojunction plays an important role in the overall efficiency and the proper function of the photovoltaics. Several studies have been performed to characterize the charge-transfer process between conducting polymers and the PCBM acceptor.[163-166] The excited-state lifetime of the polymer is greater than the time-scale of the charge transfer. This indicates that the charge-transfer efficiency can become very close to 100%.[167] Owing to its small exciton-diffusion length (3-8.9 nm) and relatively large charge-transfer radius (4.8-9 nm), the generated exciton can delocalize very rapidly and diffuse through the polymer domain.[168,169]

Another important factor that contributes to the high efficiency is the optimization of the regioregularity or the degree of crystallinity. In general, the higher the crystallinity the higher will be the charge-carrier mobility.[157-160] Lowering regioregularity, however, will lead to superior thermal stability.[156] The molecular weight of P3HT also plays a crucial role. It has been shown that polymers of P3HT with higher molecular weight show periodic lamellar structure,[151] and in such cases higher hole mobility has been observed in pure P3HT.[170,171] Photophysical studies suggest that the regioregular P3HT forms weakly interacting H-aggregates where polarization dipoles are perpendicular to the polymer backbone.[172-174] On the other hand, when the molecular weight is higher, a J-aggregate is preferred, where the polarization dipoles are parallel to the polymer backbone.[175-178] These two types of aggregates can be identified by the relative intensity of their vibronic transitions. The direction of the deposited layers, their thickness, and their composition also greatly affect the efficiency.[161,179,180] While thicker layers of P3HT:PCBM will allow greater absorption of light, the thinner layers enhance the charge transport.[181,182] The typical weight ratio of P3HT:PCBM lies between 1:0.8-1:1, which prevents phase separation of the two components.[182,183] The efficiency of this photovoltaics is also affected by the thermal annealing

of the P3HT:PCBM layers before or after the electrode deposition.[184] Steady-state and time-resolved fluorescence anisotropy of P3HT polymer exposed to electric fields are been discussed in **Chapter 7**.

1.5 Dissertation Outline

This dissertation is organized into seven chapters. A brief introduction to the topics and material systems discussed are presented in **Chapter 1**, which provides necessary background about the super-resolution imaging, time-correlated single-photon counting, and theoretical aspects of data analysis as well as background information about the ionic liquids, magnetic ionic liquids, and poly (3-hexylthiophene) films. **Chapter 2** describes basic principles of steady-state and time-resolved fluorescence techniques that are used throughout this dissertation. **Chapter 3** presents the maximum likelihood techniques used to extract the excited-state fluorescence lifetime of a fluorophore from sparse photon counting data. The application has been further extended to accommodate the mixture of fluorophores with various compositions in **Chapter 4**. It also provides an insight into the distribution of fluorescence lifetime by incorporating a bin-by-bin analysis. **Chapter 5** discusses a Bayesian formulation to improve the estimation of fluorescence lifetimes using Gaussian, exponential, and Dirichlet prior distributions. Criteria for selecting magnetic ionic liquids in DNA extraction are considered in **Chapter 6**. This chapter also discusses various fluorescence quenching mechanisms relevant to the study and use of fluorescence techniques for quantitative analysis of them**. Chapter 7** describes the characterization of poly (3-hexylthiophene) films, exposed to the electric fields, using steady-state and time-resolved polarization spectroscopy.

1.6 References

1. Meschede, D. *Optics, Light and Lasers: The Practical Approach to Modern Aspects of Photonics and Laser Physics* John Wiley & Sons: 2017.

2. Boyd, R. W. *Nonlinear Optics* Academic press: 2003.

3. Saleh, B. E.; Teich, M. C.; Saleh, B. E. *Fundamentals of Photonics* Wiley New York: 1991.

4. Csele, M. *Fundamentals of Light Sources and Lasers* John Wiley & Sons: 2011.

5. Papadopoulos, M. G.; Sadlej, A. J.; Leszczynski, J. *Non-Linear Optical Properties of Matter* Springer: 2006.

6. Verbiest, T.; Clays, K.; Rodriguez, V. *Second-Order Nonlinear Optical Characterization Techniques: An Introduction* CRC press: 2009.

7. Valkunas, L.; Abramavicius, D.; Mancal, T. *Molecular Excitation Dynamics and Relaxation: Quantum Theory and Spectroscopy* John Wiley & Sons: 2013.

8. Loudon, R. *The Quantum Theory of Light* Oxford University Press Oxford: 2000.

9. Valeur, B.; Berberan-Santos, M. N. *Molecular Fluorescence: Principles and Applications* John Wiley & Sons: 2012.

10. Harris, D. C.; Bertolucci, M. D. *Symmetry and Spectroscopy: An Introduction to Vibrational and Electronic Spectroscopy* Courier Corporation: 1978.

11. Levine, I. N. *Molecular Spectroscopy* Wiley: 1975.

12. Lakowicz, J. R. *Principles of Fluorescence Spectroscopy*, 3rd ed.; Springer: 2011.

13. Birks, J. B. *Photophysics of Aromatic Molecules* Wiley-Interscience: London, New York, 1970.

14. O'Connor, D. V.; Ware, W. R. Exciplex Photophysics. III. Kinetics of Fluorescence Quenching Of. Alpha.-Cyanonaphthalene by Dimethylcyclopentene-1, 2 in Hexane. *J. Am. Chem. Soc.* **1976**, *98* (16), 4706-4711.

15. Fleming, G. R. *Chemical Application of Ultrafast Spectroscopy* Oxford University Press: New York, 1986.

16. Becker, W. *Advanced Time-Correlated Single Photon Counting Techniques* Springer Science & Business Media: 2005.

17. Becker, W. *Advanced Time-Correlated Single Photon Counting Applications* Springer: 2016.

18. Peter, K.; Wahl, M.; Erdmann, R. *Advanced Photon Counting: Applications, Methods, Instrumentation* Springer: 2015.

19. Hell, S. W.; Wichmann, J. Breaking the Diffraction Resolution Limit by Stimulated Emission: Stimulated-Emission-Depletion Fluorescence Microscopy. *Opt. Lett.* **1994**, *19* (11), 780-782.

20. Klar, T. A.; Hell, S. W. Subdiffraction Resolution in Far-Field Fluorescence Microscopy. *Opt. Lett.* **1999**, *24* (14), 954-956.

21. Lesoine, M. D.; Bose, S.; Petrich, J. W.; Smith, E. A. Supercontinuum Stimulated Emission Depletion Fluorescence Lifetime Imaging. *J. Phys. Chem. B*. **2012**, *116* (27), 7821-7826.

22. Rust, M. J.; Bates, M.; Zhuang, X. Sub-Diffraction-Limit Imaging by Stochastic Optical Reconstruction Microscopy (STORM). *Nat. Methods*. **2006**, *3* (10), 793.

23. Hess, S. T.; Girirajan, T. P.; Mason, M. D. Ultra-High Resolution Imaging by Fluorescence Photoactivation Localization Microscopy. *Biophys. J.* **2006**, *91* (11), 4258-4272.

24. Betzig, E.; Patterson, G. H.; Sougrat, R.; Lindwasser, O. W.; Olenych, S.; Bonifacino, J. S.; Davidson, M. W.; Lippincott-Schwartz, J.; Hess, H. F. Imaging Intracellular Fluorescent Proteins at Nanometer Resolution. *Science*. **2006**, *313* (5793), 1642-1645.

25. Cheng, J.-x.; Volkmer, A.; Book, L. D.; Xie, X. S. An Epi-Detected Coherent Anti-Stokes Raman Scattering (E-CARS) Microscope with High Spectral Resolution and High Sensitivity. *J. Phys. Chem. B.* **2001**, *105* (7), 1277-1280.

26. Evans, C. L.; Xie, X. S. Coherent Anti-Stokes Raman Scattering Microscopy: Chemical Imaging for Biology and Medicine. *Annu. Rev. Anal. Chem.* **2008**, *1* 883-909.

27. Badieirostami, M.; Lew, M. D.; Thompson, M. A.; Moerner, W. Three-Dimensional Localization Precision of the Double-Helix Point Spread Function Versus Astigmatism and Biplane. *Appl. Phys. Lett.* **2010**, *97* (16), 161103.

28. Tang, J.; Akerboom, J.; Vaziri, A.; Looger, L. L.; Shank, C. V. Near-Isotropic 3D Optical Nanoscopy with Photon-Limited Chromophores. *Proceedings of the National Academy of Sciences*. **2010**, *107* (22), 10068-10073.

29. Enderlein, J. Theoretical Study of Detection of a Dipole Emitter through an Objective with High Numerical Aperture. *Opt. Lett.* **2000**, *25* (9), 634-636.

30. Ma, H.; Long, F.; Zeng, S.; Huang, Z.-L. Fast and Precise Algorithm Based on Maximum Radial Symmetry for Single Molecule Localization. *Opt. Lett.* **2012**, *37* (13), 2481-2483.

31. Deschout, H.; Neyts, K.; Braeckmans, K. The Influence of Movement on the Localization Precision of Sub-Resolution Particles in Fluorescence Microscopy. *Journal of biophotonics*. **2012**, *5* (1), 97-109.

32. Laurence, T. A.; Chromy, B. A. Efficient Maximum Likelihood Estimator Fitting of Histograms. *Nat. Methods*. **2010**, *7* (5), 338-339.

33. Mortensen, K. I.; Churchman, L. S.; Spudich, J. A.; Flyvbjerg, H. Optimized Localization Analysis for Single-Molecule Tracking and Super-Resolution Microscopy. *Nat. Methods*. **2010**, *7* (5), 377.

34. Kirshner, H.; Aguet, F.; Sage, D.; Unser, M. 3-D PSF Fitting for Fluorescence Microscopy: Implementation and Localization Application. *J. Microsc.* **2013**, *249* (1), 13-25.

35. Wolter, S.; Löschberger, A.; Holm, T.; Aufmkolk, S.; Dabauvalle, M.-C.; Van De Linde, S.; Sauer, M. rapidSTORM: Accurate, Fast Open-Source Software for Localization Microscopy. *Nat. Methods*. **2012**, *9* (11), 1040.

36. Huang, B.; Wang, W.; Bates, M.; Zhuang, X. Three-Dimensional Super-Resolution Imaging by Stochastic Optical Reconstruction Microscopy. *Science*. **2008**, *319* (5864), 810-813.

37. Quan, T.; Zhu, H.; Liu, X.; Liu, Y.; Ding, J.; Zeng, S.; Huang, Z.-L. High-Density Localization of Active Molecules Using Structured Sparse Model and Bayesian Information Criterion. *Optics express*. **2011**, *19* (18), 16963-16974.

38. Ram, S.; Ward, E. S.; Ober, R. J. Beyond Rayleigh's Criterion: A Resolution Measure with Application to Single-Molecule Microscopy. *Proc. Natl. Acad. Sci. U. S. A.* **2006**, *103* (12), 4457-4462.

39. Mukamel, E. A.; Babcock, H.; Zhuang, X. Statistical Deconvolution for Superresolution Fluorescence Microscopy. *Biophys. J.* **2012**, *102* (10), 2391-2400.

40. Zhu, L.; Zhang, W.; Elnatan, D.; Huang, B. Faster STORM Using Compressed Sensing. *Nat. Methods*. **2012**, *9* (7), 721.

41. Cox, S.; Rosten, E.; Monypenny, J.; Jovanovic-Talisman, T.; Burnette, D. T.; Lippincott-Schwartz, J.; Jones, G. E.; Heintzmann, R. Bayesian Localization Microscopy Reveals Nanoscale Podosome Dynamics. *Nat. Methods*. **2012**, *9* (2), 195.

42. Papoulis, A.; Pillai, S. U. *Probability, Random Variables, and Stochastic Processes* Tata McGraw-Hill Education: 2002.

43. Ober, R. J.; Ram, S.; Ward, E. S. Localization Accuracy in Single-Molecule Microscopy. *Biophys. J.* **2004**, *86* (2), 1185-1200.

44. Parthasarathy, R. Rapid, Accurate Particle Tracking by Calculation of Radial Symmetry Centers. *Nat. Methods*. **2012**, *9* (7), 724.

45. Abraham, A. V.; Ram, S.; Chao, J.; Ward, E.; Ober, R. J. Quantitative Study of Single Molecule Location Estimation Techniques. *Optics express*. **2009**, *17* (26), 23352-23373.

46. Deschout, H.; Zanacchi, F. C.; Mlodzianoski, M.; Diaspro, A.; Bewersdorf, J.; Hess, S. T.; Braeckmans, K. Precisely and Accurately Localizing Single Emitters in Fluorescence Microscopy. *Nat. Methods*. **2014**, *11* (3), 253.

47. Thompson, R. E.; Larson, D. R.; Webb, W. W. Precise Nanometer Localization Analysis for Individual Fluorescent Probes. *Biophys. J.* **2002**, *82* (5), 2775-2783.

48. Small, A.; Stahlheber, S. Fluorophore Localization Algorithms for Super-Resolution Microscopy. *Nat. Methods*. **2014**, *11* (3), 267.

49. Small, A. R. Theoretical Limits on Errors and Acquisition Rates in Localizing Switchable Fluorophores. *Biophys. J.* **2009**, *96* (2), L16-L18.

50. Ovesný, M.; Křížek, P.; Borkovec, J.; Švindrych, Z.; Hagen, G. M. ThunderSTORM: A Comprehensive Imagej Plug-in for Palm and STORM Data Analysis and Super-Resolution Imaging. *Bioinformatics*. **2014**, *30* (16), 2389-2390.

51. Giepmans, B. N.; Adams, S. R.; Ellisman, M. H.; Tsien, R. Y. The Fluorescent Toolbox for Assessing Protein Location and Function. *Science*. **2006**, *312* (5771), 217-224.

52. Lichtman, J. W.; Conchello, J.-A. Fluorescence Microscopy. *Nat. Methods*. **2005**, *2* (12), 910.

53. Willig, K. I.; Kellner, R. R.; Medda, R.; Hein, B.; Jakobs, S.; Hell, S. W. Nanoscale Resolution in GFP-Based Microscopy. *Nat. Methods*. **2006**, *3* (9), 721.

54. Schermelleh, L.; Heintzmann, R.; Leonhardt, H. A Guide to Super-Resolution Fluorescence Microscopy. *The Journal of cell biology*. **2010**, *190* (2), 165-175.

55. Harke, B.; Keller, J.; Ullal, C. K.; Westphal, V.; Schönle, A.; Hell, S. W. Resolution Scaling in STED Microscopy. *Optics express*. **2008**, *16* (6), 4154-4162.

56. Westphal, V.; Hell, S. W. Nanoscale Resolution in the Focal Plane of an Optical Microscope. *Phys. Rev. Lett.* **2005**, *94* (14), 143903.

57. Suhling, K.; French, P. M.; Phillips, D. Time-Resolved Fluorescence Microscopy. *Photochem. Photobiol. Sci.* **2005**, *4* (1), 13-22.

58. Hickey, P. C.; Swift, S. R.; Roca, M. G.; Read, N. D. Live-Cell Imaging of Filamentous Fungi Using Vital Fluorescent Dyes and Confocal Microscopy. *Methods in microbiology*. **2004**, *34* 63-87.

59. Fujita, K.; Kobayashi, M.; Kawano, S.; Yamanaka, M.; Kawata, S. High-Resolution Confocal Microscopy by Saturated Excitation of Fluorescence. *Phys. Rev. Lett.* **2007**, *99* (22), 228105.

60. Cox, G.; Sheppard, C. J. Practical Limits of Resolution in Confocal and Non-Linear Microscopy. *Microsc. Res. Techniq.* **2004**, *63* (1), 18-22.

61. Hell, S.; Stelzer, E. H. Fundamental Improvement of Resolution with a 4Pi-Confocal Fluorescence Microscope Using Two-Photon Excitation. *Opt. Commun.* **1992**, *93* (5-6), 277-282.

62. Huang, B.; Bates, M.; Zhuang, X. Super-Resolution Fluorescence Microscopy. *Annu. Rev. Biochem.* **2009**, *78* 993-1016.

63. Vicidomini, G.; Moneron, G.; Han, K. Y.; Westphal, V.; Ta, H.; Reuss, M.; Engelhardt, J.; Eggeling, C.; Hell, S. W. Sharper Low-Power STED Nanoscopy by Time Gating. *Nat. Methods*. **2011**, *8* (7), 571.

64. Auksorius, E.; Boruah, B. R.; Dunsby, C.; Lanigan, P. M.; Kennedy, G.; Neil, M. A.; French, P. M. Stimulated Emission Depletion Microscopy with a Supercontinuum Source and Fluorescence Lifetime Imaging. *Opt. Lett.* **2008**, *33* (2), 113-115.

65. Vicidomini, G.; Schönle, A.; Ta, H.; Han, K. Y.; Moneron, G.; Eggeling, C.; Hell, S. W. STED Nanoscopy with Time-Gated Detection: Theoretical and Experimental Aspects. *PLoS One*. **2013**, *8* (1), e54421.

66. Wildanger, D.; Rittweger, E.; Kastrup, L.; Hell, S. W. STED Microscopy with a Supercontinuum Laser Source. *Optics express*. **2008**, *16* (13), 9614-9621.

67. Arroyo-Camejo, S.; Adam, M.-P.; Besbes, M.; Hugonin, J.-P.; Jacques, V.; Greffet, J.-J.; Roch, J.-F.; Hell, S. W.; Treussart, F. Stimulated Emission Depletion Microscopy Resolves Individual Nitrogen Vacancy Centers in Diamond Nanocrystals. *ACS Nano*. **2013**, *7* (12), 10912-10919.

68. Van Der Meer, B. W.; Coker, G.; Chen, S.-Y. S. *Resonance Energy Transfer:Theory and Data* VCH New York: 1994.

69. Förster, T. *Intermolecular Energy Transfer and Fluorescence* National Research Council of Canada: 1955.

70. Scholes, G. D. Long-Range Resonance Energy Transfer in Molecular Systems. *Annu. Rev. Phys. Chem.* **2003**, *54* (1), 57-87.

71. Lee, M.; Tang, J.; Hochstrasser, R. M. Fluorescence Lifetime Distribution of Single Molecules Undergoing Förster Energy Transfer. *Chem. Phys. Lett.* **2001**, *344* (5), 501-508.

72. Thompson, N. L. *Fluorescence Correlation Spectroscopy* Springer: 2002.

73. Magde, D.; Elson, E. L.; Webb, W. W. Fluorescence Correlation Spectroscopy. II. An Experimental Realization. *Biopolymers*. **1974**, *13* (1), 29-61.

74. Elson, E. L.; Magde, D. Fluorescence Correlation Spectroscopy. I. Conceptual Basis and Theory. *Biopolymers*. **1974**, *13* (1), 1-27.

75. Das, K.; Dertz, E.; Paterson, J.; Zhang, W.; Kraus, G.; Petrich, J. Hypericin, Hypocrellin, and Model Compounds: Steady-State and Time-Resolved Fluorescence Anisotropies. *J. Phys. Chem. B.* **1998**, *102* (8), 1479-1484.

76. Vogel, S. S.; Thaler, C.; Blank, P. S.; Koushik, S. V. Time Resolved Fluorescence Anisotropy. *FLIM microscopy in Biology and Medicine*. **2009**, *1* 245-288.

77. Cross, A. J.; Fleming, G. R. Analysis of Time-Resolved Fluorescence Anisotropy Decays. *Biophys. J.* **1984**, *46* (1), 45-56.

78. Bevington, P.; Robinson, D. K. *Data Reduction and Error Analysis for the Physical Sciences*, 3rd ed.; McGraw-Hill: New York, 2002.

79. Pauling, L. *General Chemistry* Courier Corporation: 1988.

80. Berry, R. S.; Rice, S. A.; Ross, J. *Physical Chemistry* Oxford University Press: 2000.

81. Landl, G.; Langthaler, T.; Englt, H. W.; Kauffmann, H. F. Distribution of Event Times in Time-Resolved Fluorescence: The Exponential Series Approach—Algorithm, Regularization, Analysis. *J. Comput. Phys.* **1991**, *95* (1), 1-28.

82. Giurleo, J. T.; Talaga, D. S. Global Fitting without a Global Model: Regularization Based on the Continuity of the Evolution of Parameter Distributions. *J. Chem. Phys.* **2008**, *128* (11), 114114.

83. Groma, G. I.; Heiner, Z.; Makai, A.; Sarlós, F. Estimation of Kinetic Parameters from Time-Resolved Fluorescence Data: A Compressed Sensing Approach. *Rsc Advances*. **2012**, *2* (30), 11481-11490.

84. Santra, K.; Smith, E. A.; Petrich, J. W.; Song, X. Photon Counting Data Analysis: Application of the Maximum Likelihood and Related Methods for the Determination of Lifetimes in Mixtures of Rose Bengal and Rhodamine B. *J. Phys. Chem. A.* **2016**, *121* (1), 122-132.

85. Santra, K.; Zhan, J.; Song, X.; Smith, E. A.; Vaswani, N.; Petrich, J. W. What Is the Best Method to Fit Time-Resolved Data? A Comparison of the Residual Minimization and the Maximum Likelihood Techniques as Applied to Experimental Time-Correlated, Single-Photon Counting Data. *J. Phys. Chem. B.* **2016**, *120* (9), 2484-2490.

86. Baker, S.; Cousins, R. D. Clarification of the Use of Chi-Square and Likelihood Functions in Fits to Histograms. *Nucl. Instr. Meth. Phys. Res.* **1984**, *221* (2), 437-442.

87. Neyman, J.; Pearson, E. S. On the Use and Interpretation of Certain Test Criteria for Purposes of Statistical Inference: Part II. *Biometrika.* **1928**, *20A* (3/4), 263-294.

88. Neyman, J.; Pearson, E. S. On the Use and Interpretation of Certain Test Criteria for Purposes of Statistical Inference: Part I. *Biometrika.* **1928**, *20A* (1/2), 175-240.

89. Syed, A.; Lesoine, M. D.; Bhattacharjee, U.; Petrich, J. W.; Smith, E. A. The Number of Accumulated Photons and the Quality of Stimulated Emission Depletion Lifetime Images. *Photochem. Photobiol.* **2014**, *90* (4), 767-772.

90. Jo, J. A.; Fang, Q.; Marcu, L. Ultrafast Method for the Analysis of Fluorescence Lifetime Imaging Microscopy Data Based on the Laguerre Expansion Technique. *IEEE J. Sel. Top. Quantum Electron.* **2005**, *11* (4), 835-845.

91. Liu, J.; Sun, Y.; Qi, J.; Marcu, L. A Novel Method for Fast and Robust Estimation of Fluorescence Decay Dynamics Using Constrained Least-Squares Deconvolution with Laguerre Expansion. *Physics in Medicine & Biology*. **2012**, *57* (4), 843.

92. Pande, P.; Jo, J. A. Automated Analysis of Fluorescence Lifetime Imaging Microscopy (FLIM) Data Based on the Laguerre Deconvolution Method. *IEEE Transactions on Biomedical Engineering*. **2011**, *58* (1), 172-181.

93. Jo, J.; Fang, Q.; Papaioannou, T.; Marcu, L. Novel Ultra-Fast Deconvolution Method for Fluorescence Lifetime Imaging Microscopy Based on the Laguerre Expansion Technique. *Engineering in Medicine and Biology Society, 2004. IEMBS'04. 26th Annual International Conference of the IEEE* IEEE: 2004, 1271-1274.

94. Gafni, A.; Modlin, R. L.; Brand, L. Analysis of Fluorescence Decay Curves by Means of the Laplace Transformation. *Biophys. J.* **1975**, *15* (3), 263-280.

95. van Stokkum, I. H.; Larsen, D. S.; van Grondelle, R. Global and Target Analysis of Time-Resolved Spectra. *Biochimica et Biophysica Acta (BBA)-Bioenergetics*. **2004**, *1657* (2-3), 82-104.

96. Beechem, J. M.; Brand, L. Global Analysis of Fluorescence Decay: Applications to Some Unusual Experimental and Theoretical Studies. *Photochem. Photobiol.* **1986**, *44* (3), 323-329.

97. Knutson, J. R.; Beechem, J. M.; Brand, L. Simultaneous Analysis of Multiple Fluorescence Decay Curves: A Global Approach. *Chem. Phys. Lett.* **1983**, *102* (6), 501-507.

98. Siemiarczuk, A.; Ware, W. R. Temperature Dependence of Fluorescence Lifetime Distributions in 1, 3-Di (1-Pyrenyl) Propane with the Maximum Entropy Method. *J. Phys. Chem.* **1989**, *93* (22), 7609-7618.

99. Henry, E.; Deprez, E.; Brochon, J.-C. Maximum Entropy Analysis of Data Simulations and Practical Aspects of Time-Resolved Fluorescence Measurements in the Study of Molecular Interactions. *J. Mol. Struct.* **2014**, *1077* 77-86.

100. Brochon, J.-C. *[13] Maximum Entropy Method of Data Analysis in Time-Resolved Spectroscopy* Elsevier: 1994.

101. Swaminathan, R.; Periasamy, N. Analysis of Fluorescence Decay by the Maximum Entropy Method: Influence of Noise and Analysis Parameters on the Width of the Distribution of Lifetimes. *Proceedings of the Indian Academy of Sciences-Chemical Sciences* Springer: 1996, 39.

102. Phillips, D. L. A Technique for the Numerical Solution of Certain Integral Equations of the First Kind. *Journal of the ACM (JACM)*. **1962**, *9* (1), 84-97.

103. James, D. R.; Ware, W. R. Recovery of Underlying Distributions of Lifetimes from Fluorescence Decay Data. *Chem. Phys. Lett.* **1986**, *126* (1), 7-11.

104. Ware, W. R.; Doemeny, L. J.; Nemzek, T. L. Deconvolution of Fluorescence and Phosphorescence Decay Curves. Least-Squares Method. *J. Phys. Chem.* **1973**, *77* (17), 2038-2048.

105. Chen, S.; Donoho, D.; Saunders, M. Atomic Decomposition by Basis Pursuit. *SIA M Journal on Scientific Computing*. **1998**, *20* (33-61),

106. Gill, P. R.; Wang, A.; Molnar, A. The in-Crowd Algorithm for Fast Basis Pursuit Denoising. *IEEE Transactions on Signal Processing*. **2011**, *59* (10), 4595-4605.

107. Candès, E. J.; Wakin, M. B. An Introduction to Compressive Sampling. *IEEE signal processing magazine*. **2008**, *25* (2), 21-30.

108. Candes, E. J.; Romberg, J. K.; Tao, T. Stable Signal Recovery from Incomplete and Inaccurate Measurements. *Communications on pure and applied mathematics*. **2006**, *59* (8), 1207-1223.

109. Candès, E. J. Compressive Sampling. *Proceedings of the international congress of mathematicians* Madrid, Spain: 2006, 1433-1452.

110. Maus, M.; Cotlet, M.; Hofkens, J.; Gensch, T.; De Schryver, F. C.; Schaffer, J.; Seidel, C. An Experimental Comparison of the Maximum Likelihood Estimation and Nonlinear Least-Squares Fluorescence Lifetime Analysis of Single Molecules. *Anal. Chem.* **2001**, *73* (9), 2078-2086.

111. Nishimura, G.; Tamura, M. Artefacts in the Analysis of Temporal Response Functions Measured by Photon Counting. *Phys. Med. Biol.* **2005**, *50* (6), 1327.

112. Turton, D. A.; Reid, G. D.; Beddard, G. S. Accurate Analysis of Fluorescence Decays from Single Molecules in Photon Counting Experiments. *Anal. Chem.* **2003**, *75* (16), 4182-4187.

113. Feller, W. *An Introduction to Probability Theory and Its Applications: Volume I*, 3rd ed.; John Wiley & Sons, Inc. London-New York-Sydney-Toronto: 1968.

114. Koch, K.-R. *Bayes' Theorem* Springer: 1990.

115. Bishop, C. M. *Pattern Recognition and Machine Learning* Springer: 2006.

116. Lindley, D. V. *Making Decisions*, 2nd ed.; Wiley: 1991.

117. Mann, B. E.; Guzman, M. H. Dissolution of [RhCl (PPh3)3] in the Ionic Liquid, 1-Ethyl-3-Methyl Imidazolium Chloroaluminate (III), and Its Reaction with H2. The Stabilization of Rh (I) Species in an Ionic Liquid. *Inorg. Chim. Acta*. **2002**, *330* (1), 143-148.

118. Dyson, P. J.; Ellis, D. J.; Welton, T.; Parker, D. G. Arene Hydrogenation in a Room-Temperature Ionic Liquid Using a Ruthenium Cluster Catalyst. *Chem. Commun. (Cambridge, U. K.)*. **1999**, (1), 25-26.

119. Carmichael, A. J.; Earle, M. J.; Holbrey, J. D.; McCormac, P. B.; Seddon, K. R. The Heck Reaction in Ionic Liquids: A Multiphasic Catalyst System. *Org. Lett.* **1999**, *1* (7), 997-1000.

120. Wilkes, J. S.; Zaworotko, M. J. Air and Water Stable 1-Ethyl-3-Methylimidazolium Based Ionic Liquids. *J. Chem. Soc., Chem. Commun.* **1992**, (13), 965-967.

121. Welton, T. Room-Temperature Ionic Liquids. Solvents for Synthesis and Catalysis. *Chem. Rev.* **1999**, *99* (8), 2071-2084.

122. Dai, S.; Ju, Y.; Barnes, C. Solvent Extraction of Strontium Nitrate by a Crown Ether Using Room-Temperature Ionic Liquids. *Journal of the Chemical Society, Dalton Transactions*. **1999**, (8), 1201-1202.

123. Huddleston, J.; Willauer, H.; Swatloski, R.; Visser, A.; Rogers, R. Room Temperature Ionic Liquids as Novel Media for 'Clean' Liquid–Liquid Extraction *Chem. Commun. (Cambridge, U. K.)*. **1998**, *16* 1765-1766.

124. Enders Dickinson, V.; Williams, M. E.; Hendrickson, S. M.; Masui, H.; Murray, R. W. Hybrid Redox Polyether Melts Based on Polyether-Tailed Counterions. *J. Am. Chem. Soc.* **1999**, *121* (4), 613-616.

125. Armstrong, D. W.; Zhang, L.-K.; He, L.; Gross, M. L. Ionic Liquids as Matrixes for Matrix-Assisted Laser Desorption/Ionization Mass Spectrometry. *Anal. Chem.* **2001**, *73* (15), 3679-3686.

126. Hayashi, S.; Hamaguchi, H. O. Discovery of a Magnetic Ionic Liquid Bmim FeCl4. *Chem. Lett.* **2004**, *33* (12), 1590-1591.

127. Del Sesto, R. E.; McCleskey, T. M.; Burrell, A. K.; Baker, G. A.; Thompson, J. D.; Scott, B. L.; Wilkes, J. S.; Williams, P. Structure and Magnetic Behavior of Transition Metal Based Ionic Liquids. *Chem. Commun. (Cambridge, U. K.)*. **2008**, (4), 447-449.

128. Nacham, O.; Clark, K. D.; Yu, H.; Anderson, J. L. Synthetic Strategies for Tailoring the Physicochemical and Magnetic Properties of Hydrophobic Magnetic Ionic Liquids. *Chem. Mater.* **2015**, *27* (3), 923-931.

129. Inagaki, T.; Mochida, T. Metallocenium Ionic Liquids. *Chem. Lett.* **2010**, *39* (6), 572-573.

130. Yoshida, Y.; Saito, G. Design of Functional Ionic Liquids Using Magneto-and Luminescent-Active Anions. *Phys. Chem. Chem. Phys.* **2010**, *12* (8), 1675-1684.

131. Hayashi, S.; Hamaguchi, H.-o. Discovery of a Magnetic Ionic Liquid [Bmim] FeCl4. *Chem. Lett.* **2004**, *33* (12), 1590-1591.

132. Mallick, B.; Balke, B.; Felser, C.; Mudring, A. V. Dysprosium Room-Temperature Ionic Liquids with Strong Luminescence and Response to Magnetic Fields. *Angew. Chem. Int. Ed.* **2008**, *47* (40), 7635-7638.

133. Nockemann, P.; Thijs, B.; Postelmans, N.; Van Hecke, K.; Van Meervelt, L.; Binnemans, K. Anionic Rare-Earth Thiocyanate Complexes as Building Blocks for Low-Melting Metal-Containing Ionic Liquids. *J. Am. Chem. Soc.* **2006**, *128* (42), 13658-13659.

134. Peppel, T.; Köckerling, M.; Geppert-Rybczyńska, M.; Ralys, R. V.; Lehmann, J. K.; Verevkin, S. P.; Heintz, A. Low-Viscosity Paramagnetic Ionic Liquids with Doubly Charged [Co (NCS)4]2− Ions. *Angew. Chem. Int. Ed.* **2010**, *49* (39), 7116-7119.

135. Clark, K. D.; Nacham, O.; Purslow, J. A.; Pierson, S. A.; Anderson, J. L. Magnetic Ionic Liquids in Analytical Chemistry: A Review. *Anal. Chim. Acta*. **2016**, *934* 9-21.

136. Pierson, S. A.; Nacham, O.; Clark, K. D.; Nan, H.; Mudryk, Y.; Anderson, J. L. Synthesis and Characterization of Low Viscosity Hexafluoroacetylacetonate-Based Hydrophobic Magnetic Ionic Liquids. *New J. Chem.* **2017**,

137. Clark, K. D.; Nacham, O.; Yu, H.; Li, T.; Yamsek, M. M.; Ronning, D. R.; Anderson, J. L. Extraction of DNA by Magnetic Ionic Liquids: Tunable Solvents for Rapid and Selective DNA Analysis. *Anal. Chem.* **2015**, *87* (3), 1552-1559.

138. Yu, G.; Gao, J.; Hummelen, J. C.; Wudl, F.; Heeger, A. J. Polymer Photovoltaic Cells: Enhanced Efficiencies Via a Network of Internal Donor-Acceptor Heterojunctions. *Science*. **1995**, *270* (5243), 1789-1791.

139. Dang, M. T.; Hirsch, L.; Wantz, G. P3HT: PCBM, Best Seller in Polymer Photovoltaic Research. *Adv. Mater. (Weinheim, Ger.)*. **2011**, *23* (31), 3597-3602.

140. Hauch, J. A.; Schilinsky, P.; Choulis, S. A.; Childers, R.; Biele, M.; Brabec, C. J. Flexible Organic P3HT: PCBM Bulk-Heterojunction Modules with More Than 1 Year Outdoor Lifetime. *Sol. Energy Mater. Sol. Cells*. **2008**, *92* (7), 727-731.

141. Waldauf, C.; Scharber, M. C.; Schilinsky, P.; Hauch, J. A.; Brabec, C. J. Physics of Organic Bulk Heterojunction Devices for Photovoltaic Applications. *J. Appl. Phys.* **2006**, *99* (10), 104503.

142. Brabec, C. J. Organic Photovoltaics: Technology and Market. *Sol. Energy Mater. Sol. Cells*. **2004**, *83* (2-3), 273-292.

143. Katz, E.; Faiman, D.; Tuladhar, S.; Kroon, J.; Wienk, M.; Fromherz, T.; Padinger, F.; Brabec, C.; Sariciftci, N. Temperature Dependence for the Photovoltaic Device Parameters of Polymer-Fullerene Solar Cells under Operating Conditions. *J. Appl. Phys.* **2001**, *90* (10), 5343-5350.

144. Treat, N. D.; Brady, M. A.; Smith, G.; Toney, M. F.; Kramer, E. J.; Hawker, C. J.; Chabinyc, M. L. Interdiffusion of PCBM and P3HT Reveals Miscibility in a Photovoltaically Active Blend. *Adv. Energy Mater.* **2011**, *1* (1), 82-89.

145. Barnes, M. D.; Baghar, M. Optical Probes of Chain Packing Structure and Exciton Dynamics in Polythiophene Films, Composites, and Nanostructures. *Journal of Polymer Science Part B: Polymer Physics*. **2012**, *50* (15), 1121-1129.

146. Vanlaeke, P.; Swinnen, A.; Haeldermans, I.; Vanhoyland, G.; Aernouts, T.; Cheyns, D.; Deibel, C.; D'Haen, J.; Heremans, P.; Poortmans, J. P3HT/PCBM Bulk Heterojunction Solar Cells: Relation between Morphology and Electro-Optical Characteristics. *Sol. Energy Mater. Sol. Cells*. **2006**, *90* (14), 2150-2158.

147. Pope, M.; Swenberg, C. E. *Electronic Processes in Organic Crystals and Polymers* Oxford University Press on Demand: 1999.

148. Padinger, F.; Rittberger, R. S.; Sariciftci, N. S. Effects of Postproduction Treatment on Plastic Solar Cells. *Adv. Funct. Mater.* **2003**, *13* (1), 85-88.

149. Reyes-Reyes, M.; Kim, K.; Dewald, J.; López-Sandoval, R.; Avadhanula, A.; Curran, S.; Carroll, D. L. Meso-Structure Formation for Enhanced Organic Photovoltaic Cells. *Org. Lett.* **2005**, *7* (26), 5749-5752.

150. Ma, W.; Yang, C.; Gong, X.; Lee, K.; Heeger, A. J. Thermally Stable, Efficient Polymer Solar Cells with Nanoscale Control of the Interpenetrating Network Morphology. *Adv. Funct. Mater.* **2005**, *15* (10), 1617-1622.

151. Brinkmann, M.; Rannou, P. Effect of Molecular Weight on the Structure and Morphology of Oriented Thin Films of Regioregular Poly (3-Hexylthiophene) Grown by Directional Epitaxial Solidification. *Adv. Funct. Mater.* **2007**, *17* (1), 101-108.

152. Zen, A.; Saphiannikova, M.; Neher, D.; Grenzer, J.; Grigorian, S.; Pietsch, U.; Asawapirom, U.; Janietz, S.; Scherf, U.; Lieberwirth, I. Effect of Molecular Weight on the Structure and Crystallinity of Poly (3-Hexylthiophene). *Macromolecules.* **2006**, *39* (6), 2162-2171.

153. Trznadel, M.; Pron, A.; Zagorska, M.; Chrzaszcz, R.; Pielichowski, J. Effect of Molecular Weight on Spectroscopic and Spectroelectrochemical Properties of Regioregular Poly (3-Hexylthiophene). *Macromolecules.* **1998**, *31* (15), 5051-5058.

154. Zen, A.; Pflaum, J.; Hirschmann, S.; Zhuang, W.; Jaiser, F.; Asawapirom, U.; Rabe, J. P.; Scherf, U.; Neher, D. Effect of Molecular Weight and Annealing of Poly (3-Hexylthiophene) S on the Performance of Organic Field-Effect Transistors. *Adv. Funct. Mater.* **2004**, *14* (8), 757-764.

155. Brinkmann, M.; Rannou, P. Molecular Weight Dependence of Chain Packing and Semicrystalline Structure in Oriented Films of Regioregular Poly (3-Hexylthiophene) Revealed by High-Resolution Transmission Electron Microscopy. *Macromolecules.* **2009**, *42* (4), 1125-1130.

156. Woo, C. H.; Thompson, B. C.; Kim, B. J.; Toney, M. F.; Fréchet, J. M. The Influence of Poly (3-Hexylthiophene) Regioregularity on Fullerene-Composite Solar Cell Performance. *J. Am. Chem. Soc.* **2008**, *130* (48), 16324-16329.

157. Mauer, R.; Kastler, M.; Laquai, F. The Impact of Polymer Regioregularity on Charge Transport and Efficiency of P3HT: PCBM Photovoltaic Devices. *Adv. Funct. Mater.* **2010**, *20* (13), 2085-2092.

158. Urien, M.; Bailly, L.; Vignau, L.; Cloutet, E.; De Cuendias, A.; Wantz, G.; Cramail, H.; Hirsch, L.; Parneix, J. P. Effect of the Regioregularity of Poly (3-Hexylthiophene) on the Performances of Organic Photovoltaic Devices. *Polym. Int.* **2008**, *57* (5), 764-769.

159. Kim, Y.; Cook, S.; Tuladhar, S. M.; Choulis, S. A.; Nelson, J.; Durrant, J. R.; Bradley, D. D.; Giles, M.; McCulloch, I.; Ha, C.-S. A Strong Regioregularity Effect in Self-Organizing

Conjugated Polymer Films and High-Efficiency Polythiophene: Fullerene Solar Cells. *Nat. Mater.* **2006**, *5* (3), 197.

160. Urien, M.; Wantz, G.; Cloutet, E.; Hirsch, L.; Tardy, P.; Vignau, L.; Cramail, H.; Parneix, J.-P. Field-Effect Transistors Based on Poly (3-Hexylthiophene): Effect of Impurities. *Organic Electronics*. **2007**, *8* (6), 727-734.

161. Liu, C.-Y.; Holman, Z. C.; Kortshagen, U. R. Hybrid Solar Cells from P3HT and Silicon Nanocrystals. *Nano Lett.* **2008**, *9* (1), 449-452.

162. Cook, S.; Katoh, R.; Furube, A. Ultrafast Studies of Charge Generation in PCBM: P3HT Blend Films Following Excitation of the Fullerene PCBM. *J. Phys. Chem. C*. **2009**, *113* (6), 2547-2552.

163. Kraabel, B.; McBranch, D.; Sariciftci, N. S.; Moses, D.; Heeger, A. J. Subpicosecond Photoinduced Electron Transfer in Semiconducting Polymer-C60 Composites. *Molecular Crystals and Liquid Crystals Science and Technology. Section A. Molecular Crystals and Liquid Crystals*. **1994**, *256* (1), 733-738.

164. Kraabel, B.; Hummelen, J. C.; Vacar, D.; Moses, D.; Sariciftci, N.; Heeger, A.; Wudl, F. Subpicosecond Photoinduced Electron Transfer from Conjugated Polymers to Functionalized Fullerenes. *J. Chem. Phys.* **1996**, *104* (11), 4267-4273.

165. Zenz, C.; Lanzani, G.; Cerullo, G.; Graupner, W.; Leising, G.; DeSilvestri, S. Dissociation of Hot Excitons in Ladder-Type Polymer Light-Emitting Diodes. *Chem. Phys. Lett.* **2001**, *341* (1-2), 63-69.

166. Zenz, C.; Cerullo, G.; Lanzani, G.; Graupner, W.; Meghdadi, F.; Leising, G.; De Silvestri, S. Ultrafast Photogeneration Mechanisms of Triplet States in Para-Hexaphenyl. *Physical Review B*. **1999**, *59* (22), 14336.

167. Heeger, A. J. Nobel Lecture: Semiconducting and Metallic Polymers: The Fourth Generation of Polymeric Materials. *Reviews of Modern Physics*. **2001**, *73* (3), 681-700.

168. Wang, H.; Wang, H.-Y.; Gao, B.-R.; Wang, L.; Yang, Z.-Y.; Du, X.-B.; Chen, Q.-D.; Song, J.-F.; Sun, H.-B. Exciton Diffusion and Charge Transfer Dynamics in Nano Phase-Separated P3HT/PCBM Blend Films. *Nanoscale*. **2011**, *3* (5), 2280-2285.

169. Goh, C.; Scully, S. R.; McGehee, M. D. Effects of Molecular Interface Modification in Hybrid Organic-Inorganic Photovoltaic Cells. *J. Appl. Phys.* **2007**, *101* (11), 114503.

170. Verilhac, J.-M.; LeBlevennec, G.; Djurado, D.; Rieutord, F.; Chouiki, M.; Travers, J.-P.; Pron, A. Effect of Macromolecular Parameters and Processing Conditions on Supramolecular Organisation, Morphology and Electrical Transport Properties in Thin Layers of Regioregular Poly (3-Hexylthiophene). *Synth. Met.* **2006**, *156* (11-13), 815-823.

171. Goh, C.; Kline, R. J.; McGehee, M. D.; Kadnikova, E. N.; Fréchet, J. M. Molecular-Weight-Dependent Mobilities in Regioregular Poly (3-Hexyl-Thiophene) Diodes. *Appl. Phys. Lett.* **2005**, *86* (12), 122110.

172. Clark, J.; Silva, C.; Friend, R. H.; Spano, F. C. Role of Intermolecular Coupling in the Photophysics of Disordered Organic Semiconductors: Aggregate Emission in Regioregular Polythiophene. *Phys. Rev. Lett.* **2007**, *98* (20), 206406.

173. Spano, F. C. Absorption in Regio-Regular Poly (3-Hexyl) Thiophene Thin Films: Fermi Resonances, Interband Coupling and Disorder. *Chem. Phys.* **2006**, *325* (1), 22-35.

174. Spano, F. C. Modeling Disorder in Polymer Aggregates: The Optical Spectroscopy of Regioregular Poly (3-Hexylthiophene) Thin Films. *J. Chem. Phys.* **2005**, *122* (23), 234701.

175. Baghgar, M.; Labastide, J. A.; Bokel, F.; Hayward, R. C.; Barnes, M. D. Effect of Polymer Chain Folding on the Transition from H-to J-Aggregate Behavior in P3HT Nanofibers. *J. Phys. Chem. C*. **2014**, *118* (4), 2229-2235.

176. Baghgar, M.; Labastide, J.; Bokel, F.; Dujovne, I.; McKenna, A.; Barnes, A. M.; Pentzer, E.; Emrick, T.; Hayward, R.; Barnes, M. D. Probing Inter-and Intrachain Exciton Coupling in Isolated Poly (3-Hexylthiophene) Nanofibers: Effect of Solvation and Regioregularity. *The journal of physical chemistry letters*. **2012**, *3* (12), 1674-1679.

177. Baghgar, M.; Pentzer, E.; Wise, A. J.; Labastide, J. A.; Emrick, T.; Barnes, M. D. Cross-Linked Functionalized Poly (3-Hexylthiophene) Nanofibers with Tunable Excitonic Coupling. *ACS Nano*. **2013**, *7* (10), 8917-8923.

178. Martin, T. P.; Wise, A. J.; Busby, E.; Gao, J.; Roehling, J. D.; Ford, M. J.; Larsen, D. S.; Moulé, A. J.; Grey, J. K. Packing Dependent Electronic Coupling in Single Poly (3-Hexylthiophene) H-and J-Aggregate Nanofibers. *J. Phys. Chem. B*. **2012**, *117* (16), 4478-4487.

179. Stubhan, T.; Oh, H.; Pinna, L.; Krantz, J.; Litzov, I.; Brabec, C. J. Inverted Organic Solar Cells Using a Solution Processed Aluminum-Doped Zinc Oxide Buffer Layer. *Organic Electronics*. **2011**, *12* (9), 1539-1543.

180. Krebs, F. C.; Gevorgyan, S. A.; Alstrup, J. A Roll-to-Roll Process to Flexible Polymer Solar Cells: Model Studies, Manufacture and Operational Stability Studies. *J. Mater. Chem.* **2009**, *19* (30), 5442-5451.

181. Nam, Y. M.; Huh, J.; Jo, W. H. Optimization of Thickness and Morphology of Active Layer for High Performance of Bulk-Heterojunction Organic Solar Cells. *Sol. Energy Mater. Sol. Cells*. **2010**, *94* (6), 1118-1124.

182. Müller, C.; Ferenczi, T. A.; Campoy-Quiles, M.; Frost, J. M.; Bradley, D. D.; Smith, P.; Stingelin-Stutzmann, N.; Nelson, J. Binary Organic Photovoltaic Blends: A Simple Rationale for Optimum Compositions. *Adv. Mater. (Weinheim, Ger.)*. **2008**, *20* (18), 3510-3515.

183. Zhao, J.; Swinnen, A.; Van Assche, G.; Manca, J.; Vanderzande, D.; Mele, B. V. Phase Diagram of P3HT/PCBM Blends and Its Implication for the Stability of Morphology. *J. Phys. Chem. B.* **2009**, *113* (6), 1587-1591.

184. Kim, H.; So, W.-W.; Moon, S.-J. The Importance of Post-Annealing Process in the Device Performance of Poly (3-Hexylthiophene): Methanofullerene Polymer Solar Cell. *Sol. Energy Mater. Sol. Cells*. **2007**, *91* (7), 581-587.

CHAPTER 2. EXPERIMENTAL TECHNIQUES AND INSTRUMENTATION

2.1 Overview

Fluorescence-based spectroscopic techniques are classified into two categories: steady-state and time-resolved. Although time-resolved techniques can probe photophysical processes that occur over times scales from femtosecond to microsecond and longer, it is often necessary and convenient to complement them with steady-state measurements. Steady-state measurements require a constant illumination source and a spectrometer attached to a detector to analyze the transmitted or emitted light. Generally, the steady-state measurements record spectra when rates of excitation and de-excitation reach equilibrium condition and when vibrational and solvent induced relaxations are completed. On the other hand, time-resolved measurements account for various transient phenomena such as solvation, electron transfer, proton transfer, energy transfer, rotational motion and isomerization of excited molecules. Time-resolved techniques require comparatively more elaborate setup and their regular optimization. The light source must be pulsed and the overall time resolution of the instrument should be shorter than the time scale of the process under investigation. With the development of new measurement techniques and availability of ultrafast mode-locked lasers, which can deliver intense short pulses with a temporal width of few femtoseconds, it has become possible to measure transient phenomena down to the femtosecond scale.[1-14]

In this chapter, a few selected steady-state and time-resolved techniques, which are relevant to the experimental methods used in this dissertation, are discussed in detail. Apart from that, some fundamental concepts associated with the photophysical processes, such as Förster resonance energy transfer and fluorescence anisotropy, are also discussed.

2.2 UV-Vis Absorption Spectroscopy

Absorption spectroscopy measures the amount of light absorbed by a molecule at a given wavelength. Particularly, the measurements of absorption in the ultraviolet (UV) and visible (Vis) region of the electromagnetic spectrum are very important since the energy corresponds to this part of the spectrum overlaps with the energy gap between the electronic states of the common fluorophores (many contains C=C, C=O or C=N bonds).[15,16] The wavelength region generally used is from 190 to 1100 nm. The energy of transition is related to the wavelength by the following equation:

$$\Delta E = hc / \lambda \qquad (2.1)$$

where $\Delta E = E_2 - E_1$, the energy difference between the excited state and the ground state of the vibronic levels[17] (the vibrational and the electronic transitions are usually coupled). h, c and λ are the Planck's constant, speed of light and the wavelength of the light that is absorbed. The intensity of the transition is governed by the factors such as selection rules, oscillator strength, an overlap between the states and the population of the molecules.[16] The absorption spectra usually consist of one or more broad bands due to the vibronic coupling of several vibrational states and further broadening of the of each of the transitions.

The intensity of absorption is quantified by the Beer-Lambert law.[18] If a monochromatic light of intensity I_0 incident of a sample of thickness L, the reduction of intensity (dI) after traveling an infinitesimal path (dL) through the sample is given by:

$$dI = -I\sigma\mathcal{N}\, dL \qquad (2.2)$$

where σ is known as the effective cross-section for absorption, $\mathcal{N}$ is the number-density of the molecules. Therefore, the number of photons absorbed is proportional to both the photon density

and the density of the molecules (analogous to the bimolecular reaction). The integrated form of the equation (2.2) is given as:[16]

$$I = I_0 e^{-\sigma \mathcal{N} L} \tag{2.3}$$

The equation is most popularly expressed as:

$$A(\lambda) = \epsilon(\lambda) c L \tag{2.4}$$

where, $A(\lambda)$ is the absorbance at a wavelength λ and given by $\log_{10}(I_0/I)$. c is the molar concentration of the sample in mole dm^{-3} and related to the number density by $\mathcal{N} = N_A c 10^{-3}$, N_A being the Avogadro's number. $\epsilon(\lambda)$ is the decadic molar extinction coefficient expressed in $\mathrm{mole}^{-1}\ \mathrm{cm}^{-1}\ \mathrm{dm}^3$ at a wavelength λ and related to absorption cross-section by $\sigma = 3.81 \times 10^{-19}\epsilon$. The thickness or the pathlength of the sample is usually expressed in cm.

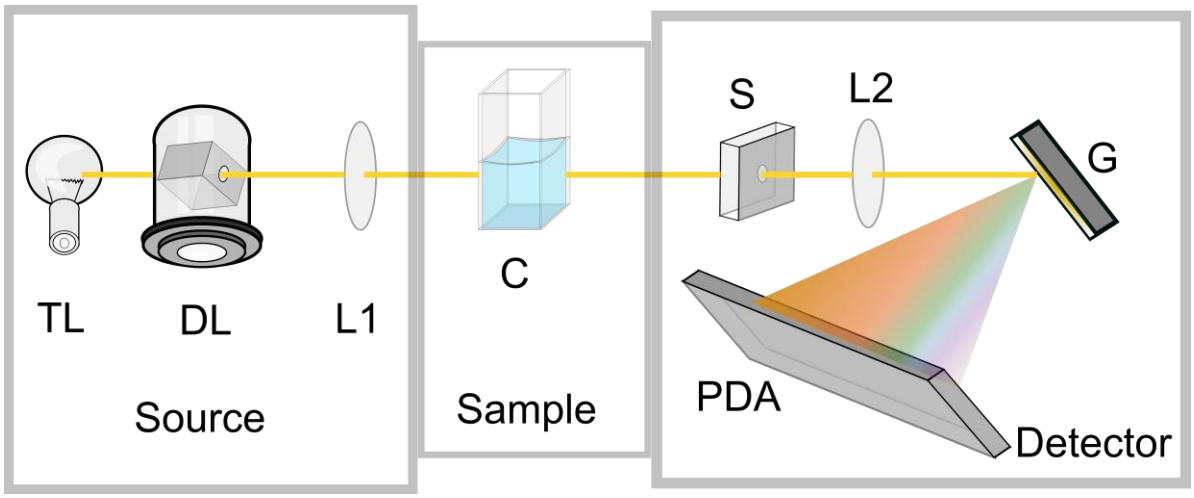

Figure 2.1. Schematic representation of the UV-Visible spectrometer. TL – tungsten lamp, DL – deuterium-discharge lamp, L1 – source lens, C – cuvette, S – slit, L2 – spectrograph lens, G – grating and PDA – photodiode array.[19]

The instrument used in our laboratory to record the absorption spectra is form Agilent Technologies (Agilent 8453 UV-Visible spectrometer). The optical layout of the UV-Visible

spectrometer is given in **Figure 2.1**. The source of light is a combination of a deuterium-discharge lamp (190-800 nm) and a tungsten lamp (370-1100 nm) that share a common axis with the collimating lens. After passing through the sample, the transmitted light is dispersed by a holographic grating at an angle proportional to the wavelength. Subsequently, the dispersed light is detected by an array of 1024 photodiodes, thus providing ~1 nm spectral resolution.[19]

2.3 Fluorescence Spectroscopy

After absorbing a photon, the excited state of a molecule loses its energy via radiative transition (*i.e*. emitting another photon) or by many other nonradiative means.[16,18] The spontaneous radiative transition responsible for the fluorescence usually happens from the ground vibrational state of the excited electronic state (singlet) to the excited vibrational state of ground electronic state (singlet). Thus, fluorescence spectrum is associated with the Stokes' shift and often shows a mirror symmetry with the absorption spectrum.[16] There are other radiative transitions such as phosphorescence that occurs from the triplet excited electronic state to a signet ground electronic state, which is spin forbidden. Resonance energy transfer is a nonradiative process and it is discussed in section **2.6** . The other nonradiative means of deexcitation has been discussed in detail in **Chapter 6**.

The radiative and nonradiative rate constants are related to the fluorescence lifetime and the fluorescence quantum yield. The lifetime of a fluorophore the average time a molecule lived in the excited state. The most simplified case to describe excited state kinetics involves two electronic states and undergo first-order reaction kinetics. Let N_t represent the number of molecules in the excited state at time t. If k_r and k_{nr} are the rate constants for the radiative and nonradiative mode of decay in absence of any external quencher then we can have:[16]

$$-\frac{dN_t}{dt} = (k_r + k_{nr})N_t \tag{2.5}$$

This equation yields

$$N_t = N_0 e^{-(k_r+k_{nr})t} \tag{2.6}$$

where, N_0 is the number of molecules in the excited state at time $t = 0$. The average lifetime of the excited state is given by:

$$\tau = \frac{1}{k_r + k_{nr}} \tag{2.7}$$

The fluorescence quantum yield is defined as the ratio of the number of photons emitted as radiative decay and the number of photons absorbed.[18,20]

$$\phi = \frac{N_{em}}{N_{abs}} \tag{2.8}$$

If we only consider the radiative part of the emission, the rate of the process is given by

$$\frac{dN_{r,t}}{dt} = k_r N_t \tag{2.9}$$

where $N_{r,t}$ is the number of emitted photon at time t. Using equation (2.6) we have:

$$\frac{dN_{r,t}}{dt} = k_r N_0 e^{-(k_r+k_{nr})t} \tag{2.10}$$

Integration of the above equation yields:

$$\Delta N_r = k_r N_0 \frac{1}{k_r + k_{nr}} \tag{2.11}$$

where, ΔN_r is the total number of photons that emitted after the excitation *i.e.* $N_{em} = \Delta N_r$. On the other hand, N_0 is the total number of molecules in the excited state immediately after excitation ($t = 0$) and hence is the number of photons absorbed *i.e.* $N_{abs} = N_0$. Note, a single photon interacts with no more than one molecule and one molecule generates no more than one photon (*i.e.* multiphoton processes are assumed to be absent). Therefore, using equation (2.8) and (2.11) we have:

$$\phi = \frac{k_r}{k_r + k_{nr}} \tag{2.12}$$

Equation (2.7) and (2.12) can be used together to obtain the value of k_r and k_{nr} as follows:

$$k_r = \phi/\tau \quad ; \quad k_{nr} = (1 - \phi)/\tau \tag{2.13}$$

The lifetime of a fluorophore can be measured by time-correlated single-photon counting (TCSPC) techniques, working principle of which has been discussed in section **2.4** . In this section, a brief description of steady-state fluorimeter and measurement of quantum yields are given.

Steady-state fluorescence emission is obtained by exciting the sample at the desired wavelength and subsequently collection the fluorescence signal, usually in a perpendicular geometry to minimize the risk of the source light to reach the detector.[22] The spectrofluorometer used in our laboratory is from Horiba Scientific (FluoroMax-4). The optical layout of a typical fluorimeter is given in **Figure 2.2**.[21] The basic components of a spectrofluorometer are: a 150 W xenon (Xe) arc-lamp (230-1000 nm) as continuous source of visible and ultraviolet light, an excitation monochromator to select the excitation wavelength, a sample compartment, an emission monochromator to select the emission wavelength, a photomultiplier tube (PMT) to detect the fluorescence signal and a system controller that records the data and send it to computer. Since

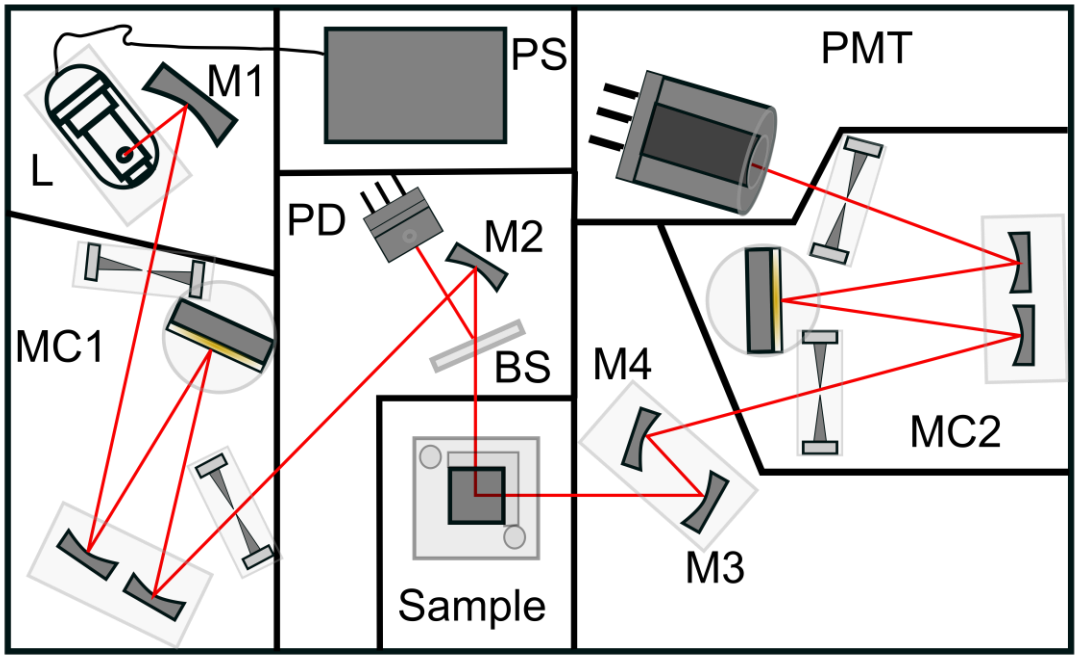

Figure 2.2. Schematic representation of the spectrofluorometer. L – xenon lamp, MC1 – excitation monochromator, MC2 – emission monochromator, M1, M2 and M3 – mirrors, BS – beam splitter, PD – reference photodiode, PMT – photomultiplier tube as the primary detector, PS – power supply for the lamp.[21]

spectrofluorometer is equipped two scanning monochromators, the emission spectrum is recorded by scanning the emission monochromator while keeping the excitation monochromator at a fixed wavelength (λ_{ex}) and the excitation spectrum is obtained by scanning the excitation monochromator while keeping emission monochromator at a fixed wavelength (λ_{em}). The adjustable slits provide controls over the intensity of the spectrum. The primary detector in our spectrofluorometer is a photon counting PMT with a saturation limit of 2×10^6 counts per second, which provides greater sensitivity compared to analog PMT. The variable intensity of the source light over the range of wavelengths and the degradation of the Xe-lamp over time can be corrected by monitoring the lamp spectrum on a reference detector and dividing the primary signal with the reference signal at each wavelength. The transmission efficiency of the monochromator and the

detection efficiency of the PMT also varies with wavelength, which can be corrected by multiplying a correction factor $\gamma(\lambda)$ to the experimental spectrum. Additional corrections, such as correction for the dark offset and subtraction of the blank spectrum are also used. The excitation and the emission monochromators are routinely calibrated with respect to the peak of Xe-lamp spectrum at 467 nm and the peak of Raman scattering spectrum of water at 397 nm for $\lambda_{ex} = 350$ nm, respectively.[21]

The quantum yield of a fluorophore is conveniently determined using the relative measurement techniques.[23,24] A suitable standard is selected which absorbs and emits in the similar wavelength range, soluble in a same or similar solvent as the unknown sample does and whose quantum yield is well established. The relative quantum yield is determined from the fluorescence emission and absorption spectra. Let $F(\lambda_{em})$ and $A(\lambda_{ex})$ denote instrument-corrected fluorescence spectrum and the absorption spectrum of a fluorophore, respectively. Since, the detector of our spectrofluorometer is a photon counting PMT, the total number of photons emitted by the fluorophore is proportional to the integrated area under the fluorescence spectrum.

$$N_{em} \propto \int F(\lambda_{em}) d\lambda_{em} \tag{2.14}$$

The fluorescence photon flux reaching the detector depends on the refractive index (n) of the medium and it is inversely proportional to the n^2. Therefore, a correction is necessary to calculate the total number of emitted photon.

$$N_{em} \propto \left(\int F(\lambda_{em}) d\lambda_{em} \right) n^2 \tag{2.15}$$

When light travels through the medium, the number of photons absorbed is proportional to the drop of the intensity. From the definition of absorbance, $A(\lambda_{ex}) = \log_{10}(I_0/I)$, the number of photons absorbed can be calculated as:

$$N_{abs} \propto \Delta I = (I_0 - I) = I_0\left(1 - 10^{-A(\lambda_{ex})}\right) \tag{2.16}$$

Therefore, from the definition of quantum yield given in equation (2.8) we get:

$$\phi \propto \frac{(\int F(\lambda_{em})d\lambda_{em})n^2}{I_0(1 - 10^{-A(\lambda_{ex})})} \tag{2.17}$$

The relative quantum yield is given by:

$$\frac{\phi_S}{\phi_R} = \frac{(\int F_S(\lambda_{em})d\lambda_{em})}{(\int F_R(\lambda_{em})d\lambda_{em})} \frac{\left(1 - 10^{-A_R(\lambda_{ex})}\right)}{(1 - 10^{-A_S(\lambda_{ex})})} \frac{n_S^2}{n_R^2} \tag{2.18}$$

where, the subscript S and R denote the sample and the reference standard respectively. Choosing the same solvent can eliminate the term involving the refractive index and all the other terms can be measured spectroscopically. The quantum yield of the sample (ϕ_S) can be determined if the quantum yield of the reference (ϕ_R) is known.

2.4 Time-Correlated, Single-Photon Counting (TCSPC)

Time-correlated, single-photon counting is the most important experimental techniques that has been utilized extensively in this dissertation. Unlike the steady-state measurement this technique requires a pulsed laser source. The number of molecules in the excited state after a time t of the pulsed excitation is given by equation (2.6) and the average lifetime of the excited state is given by equation (2.7). Since, the emission from the excited state is random one can only estimate the probability that a single molecule will emit a photon within a certain time interval. The

emission intensity is usually proportional to the number of molecules in the excited state; and therefore, for a single fluorophore one obtains:[25-27]

$$P(t) \propto e^{-\frac{t}{\tau}} \tag{2.19}$$

The excited state decay law can be experimentally obtained by collecting a population of single photon which are correlated to times interval between excitation and emission events, instead of measuring the intensity after a single pulse.[27-30]

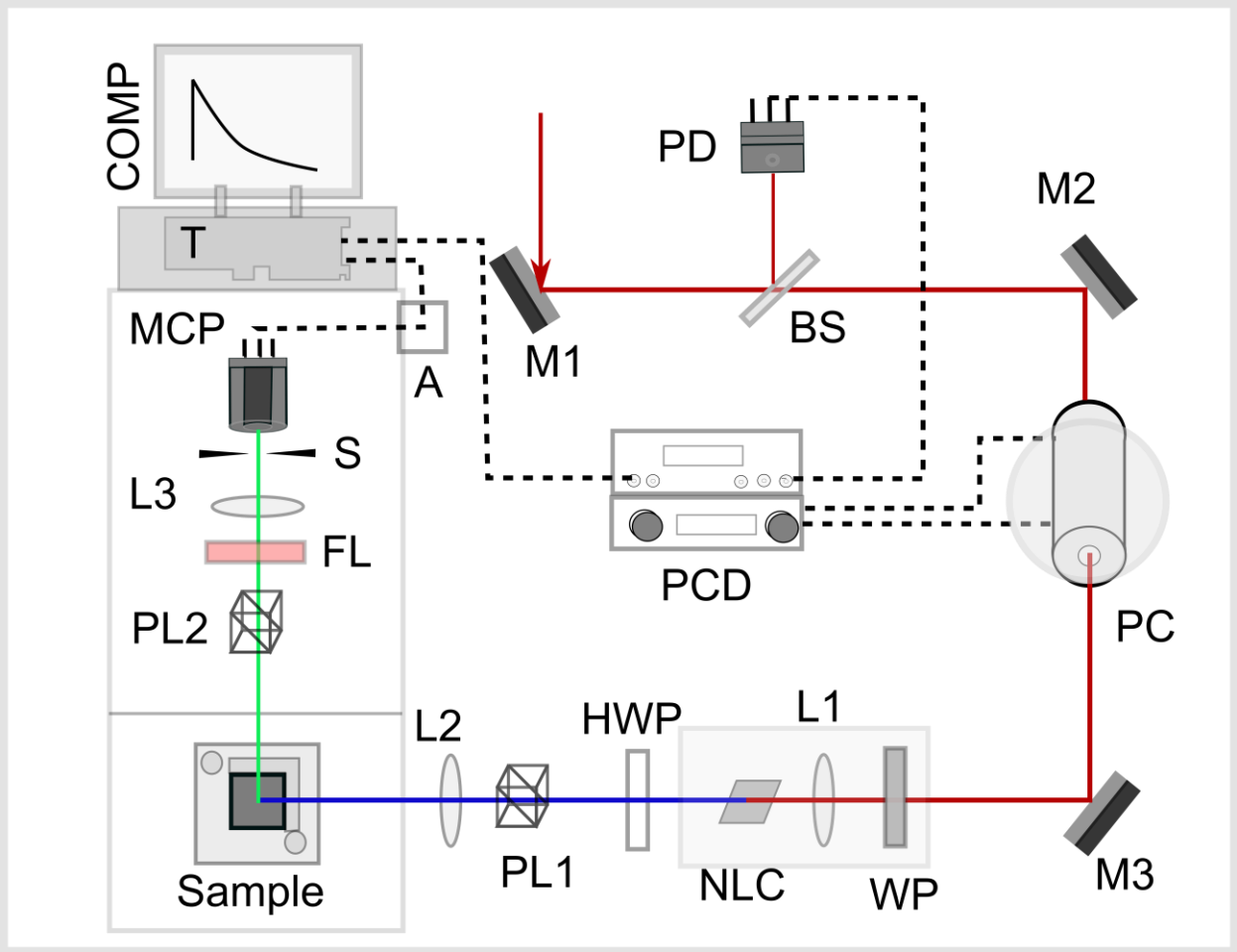

Figure 2.3. Schematic representation of time-correlated single-photon counting (TCSPC) instrument. PD – photodiode, BS – beam splitter, M – mirror, PL – polarizer, HWP – half waveplate, WP – waveplate, L – lens, NLC – nonlinear crystal for SHG, FL – filter, S – slit, A – pre-amplifier, MCP – microchannel plate, PC – Pockel's cell, PCD – Pockel's cell driver, T – timing electronics, COMP – computer.

The TCSPC instrument used in our laboratory is a home-assembled setup. A schematic diagram of the instrument is shown in the **Figure 2.3**. The sample is excited with a high repetition-rate laser. The fluorescence is collected at the perpendicular geometry, similar to the steady-state setup, and subsequently detected by a very sensitive detector, usually micro-channel plate (MCP) operated at a voltage of 3000 V for maximum sensitivity. A secondary reference detector, usually a photodiode (PD), is used to synchronize the excitation pulse and to trigger the "start" (or "stop") of the counting process. At the core of the instrument there a photon counting module from Baker and Hickl GmbH (SPC-630).[32] The essential components of the module are: constant fraction discriminator (CFD) connected to the primary detector (MCP), level trigger form the secondary reference detector (PD), time-to-amplitude converter (TAC), biased amplifier, (AMP), analog-to-digital converter (ADC), histogrammer and memory for temporary data storage (**Figure 2.4**). The CFD reshape the single photon pulse in order to avoid amplitude and time-related jittering due to random amplification mechanism in the detector. The TAC can be considered as a precise stopwatch that can measure time difference in the picosecond. In reverse mode (as in our setup), the TAC is started by the single photon pulse from the primary detector and stopped by the reference pulse. In between a capacitor is charged at a constant rate. Therefore, the final voltage of the capacitor represents the time difference between the fluorescence pulse and reference pulse. The amplifier further changes the slope of the voltage vs time graph, which allow selecting smaller time window within the TAC range. The amplified TAC signal is then measured by the ADC which determine the time-bin address of the detected event. The "histogrammer" receives the detected event into the corresponding bin-addresses and it is held by the memory onboard (16-bit for each channel) until the data is permanently saved. To ensure a single photon detection per

pulse of the laser the count rate at ADC is kept between 1-5 % of the laser repetition rate.[27,30] The relative delay between the reference pulse and the fluorescence pulse is also critical and once needs to adjust them to get a proper time window for the data histogram. The time resolution of the technique is limited by several factors, the most important one is the broadening of the time response when photons travel through the optics and subsequently the ejected photoelectron thought the detector. The transit time spread of the detector (Model R3809U-50, Hamamatsu) in our laboratory is about 25 ps. Therefore, considering that the width of the laser pulse is not the limiting factor, one would expect a 40 ps instrument response function (IRF) for this detector.[27,30] Note that the IRF is collected in the identical setup by replacing the fluorescence sample with a scattering sample and without the filter that cuts the excitation light.

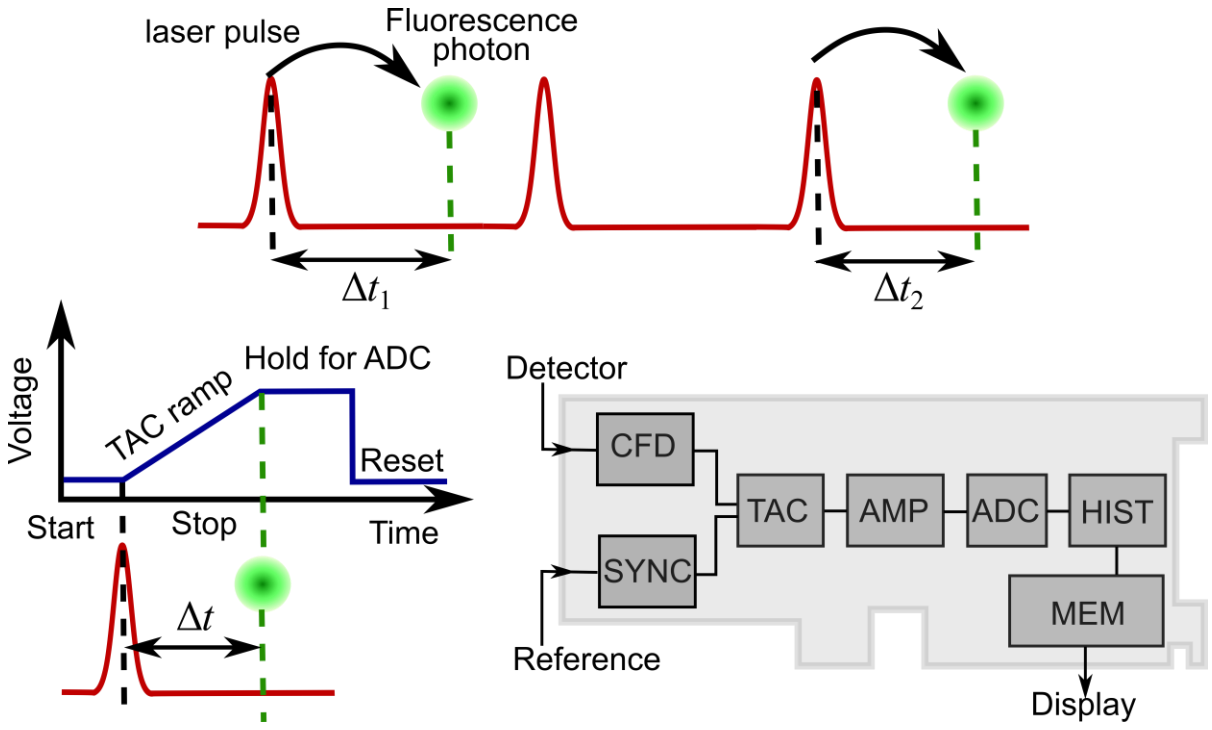

Figure 2.4. Working principle of TCSPC. The delay-time (Δt) for a single fluorescence photon is registered randomly form several excitation pulses. The counting electronics board consists of constant fraction discriminator (CFD), synchronized trigger (SYNC), time-to-amplitude converter (TAC), biased amplifier (AMP), analog-to-digital converter (ADC), histogrammer (HIST), and onboard memory (MEM).[31,32]

2.5 Titanium:sapphire Laser

Titanium sapphire (Ti:sapphire) laser is the most widely used laser in time-resolved applications. The advantages of using Ti:sapphire in TCSPC application are its short pulse-width and its tunability over a range of wavelengths. The sapphire crystal is partially (0.1-0.5 % w/w) doped with titanium oxide (Ti_2O_3) where some aluminium ion is replaced by the titanium ion.[33,34] The Ti^{3+} ion in the crystal environment absorbs light in a broad range of wavelengths center at 490 nm. The crystal is usually pumped with frequency-doubled Nd:YAG or Nd:YVO_4 laser. The lasing action of the Ti:sapphire crystal happens due to the emission from the ground vibrational state of the excited electronic state to the excited vibrational state to the ground electronic state. The emission band of the Ti:sapphire crystal is very broad and has peak ~800 nm. The larger bandwidth allows generation of ultrashort pulses and the tunability of the laser ranges from 675 nm to 1110 nm. The Ti:sapphire laser, also known as Ti:sapphire oscillator, contains the Ti^{3+} doped sapphire crystal as the gain medium and the emission of the fluorescence is trapped between two mirrors which constitute the laser cavity.

2.5.1 Laser modes, pulse-width and repetition rate

The number of longitudinal modes[33] is an important factor that determines the temporal width of the pulses of a laser. For a longitudinal laser mode to persists in the laser cavity, the length (L) of the resonator must be integer (n) multiple of half-wavelength ($\lambda/2$) *i.e.* $L = m(\lambda/2)$ or equivalently, $\nu = mc/2L$, where c is the speed of light, ν is the frequency of the m-th mode. The frequency separation between two consecutive modes is given by:

$$\Delta\nu = \nu_{m+1} - \nu_m = \frac{c}{2L} \tag{2.20}$$

The total number of longitudinal can be obtained from the bandwidth in frequency and the and divide by the frequency separation ($\Delta\nu$). For our system laser system with $L = 170$ cm and emission wavelength range 675-1110 nm, the number of possible modes (N_m) is about 2 million.[35] The superposition of longitudinal modes become narrower as greater number of modes exists. The uncertainty relation for temporal bandwidth ($\Delta\tau_p$) and total frequency bandwidth ($N_m\Delta\nu$) can be written as: $\Delta\tau_p\, N_m\Delta\nu \geq 1/2\pi$. For Ti:sapphire medium the total frequency bandwidth is about 2×10^{14} Hz which corresponds to ~5 femtosecond pulse-width. It can be shown that the maxima of the superposition of the modes are separated by:[36] $T_R = 1/\Delta\nu = 2L/c$. Therefore, the repetition rate is given by: $1/T_R = c/2L$. The transverse electromagnetic mode (TEM) determines the spatial distribution of the intensity around the resonator axis.[36-38] The most import transverse mode of the laser is denoted as TEM_{00} which has Gaussian distribution for a beam with cylindrical symmetry.

$$I_{00}(r) = I_{00}(0)e^{-\frac{2r^2}{w^2}} \tag{2.21}$$

where, r is the distance from the center of the beam, $I_{00}(0)$ is the intensity of the beam at the center and the w is defined as $1/e^2$-radius of the beam (*i.e.* the distance where intensity drops by a factor of e^2 compared to the center).

2.5.2 Kerr-lens mode-locking

The Ti:sapphire laser uses a passive[39,40] Kerr-lens mode-locking (KLM) mechanism to generate ultrashort pulses. The KLM mechanism is based on the optical Kerr effect, a third order nonlinear phenomenon where the effective refractive index changes linearly with the intensity of the electric field.[36,38,41,42]

$$n(I) = n_0 + n_2 \mathrm{I} \tag{2.22}$$

where, $n_2 \propto \chi^{(3)}/n_0^2$ represent the nonlinear coefficient accounts for the change in refractive index, $\chi^{(3)}$ is the third order nonlinear susceptibility and n_0 is the linear refractive index. The TEM_{00} mode of the laser beam has Gaussian intensity distribution with the highest intensity at the center. Thus, the center of the beam experience greater refractive index and travels slower than the edge of the beam i.e. the medium acts as a virtual lens and the beam is self-focused. The superimposed mode-locked pulse will have a higher intensity than the continuous wave as the later consists of some random modes. Therefore, if an aperture is placed in the cavity the high-intensity mode-locked condition is preferentially selected and the CW is blocked (**Figure 2.5**).[43] A small perturbation in the cavity induced fluctuation of modes and large amplitude modulation momentarily. If the modulated intensity is high enough it will initiate mode-locking by preferential selection of the mode-locked part of the beam.

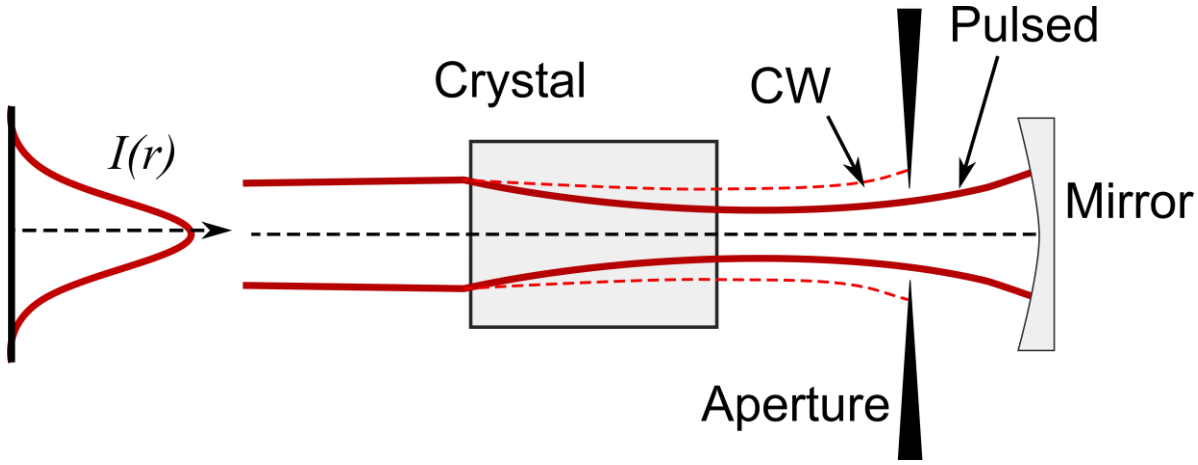

Figure 2.5. Mechanism of Kerr-lens mode-locking in Ti:sapphire crystal. $I(r)$ is the Gaussian intensity profile. The continuous mode (CW) is blocked by the aperture. Pulsed mode generated Kerr-lens effect (self-focusing) and therefore sustained in the cavity.[44]

2.5.3 Group velocity dispersion

When electromagnetic waves enter into a medium with a higher refractive index the longer wavelengths travel faster than the shorter wavelengths. This is due to the frequency dependency of the refractive index. This phenomenon is known as positive group velocity dispersion (GVD).[45,46] The mode-locked pulse consists of a range of frequencies, thus when travels through the gain medium the redder wavelength leads than the bluer wavelength in each trip. This causes boarding of the pulse and eventually breakdown of the mode-lock condition. To compensate the positive GVD a pair of prisms is introduced in the cavity to induce negative GVD. The glass materials itself caused positive GVD but the geometry of the two prisms in the cavity is causing the negative GVD (**Figure 2.6**).[47,48] After dispersion from the first prism the redder wavelengths travel more glass on the second prism than the blue wavelengths. This slows down the redder wavelengths and compensate the positive GVD introduced by the crystals. The degree of negative GVD needs to be controlled in order to get stable mode-lock and ultrashort pulses by changing the inter-prism distance or by moving the second prism into or from the beam.

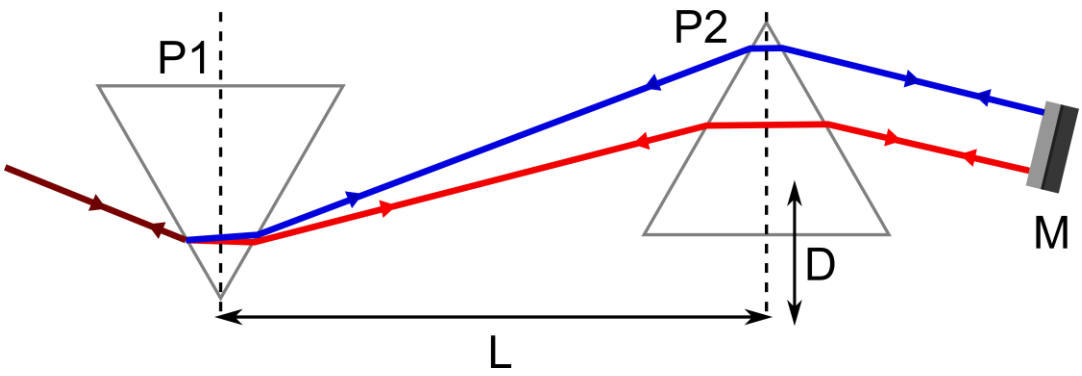

Figure 2.6. Compensation of the positive group velocity dispersion in the cavity by using a pair of prisms.[44]

2.5.4 Nonlinear optical properties, frequency mixing and harmonics generation

The induced polarization (P) on a material varies linearly with the strength of the electric field in weak field regime.[49-51] When the intensity of light is very strong, as in case of an ultrashort laser pulse, the linear relationship between polarization and strength of the field is no longer valid. In that regime we have to consider the higher order term of the Taylor series expansion of the induced polarization (P). Thus, the induced polarization can be express as:

$$P = P^{(1)} + P^{(2)} + P^{(3)} + ... = \chi^{(1)}E + \chi^{(2)}EE + \chi^{(3)}EEE + ... \qquad (2.23)$$

where, $P^{(n)}$ is the n-th order induced polarization and $\chi^{(n)}$ is the n-th order susceptibility. If we consider only the quadratic dependence of electric field, then the nonlinear induced polarization, $P^{(2)}$ is given by:

$$P^{(2)} = \chi^{(2)}EE \qquad (2.24)$$

Let $E(r,t) = E_0 e^{-i(k\cdot r-\omega t)} + cc$ denotes the plane-wave with angular frequency ω and propagation vector k, where cc denotes the complex conjugate. The second order nonlinear polarization is given by:

$$P^{(2)} = \chi^{(2)}E_0^2[e^{i(k.r-\omega t)} + cc][e^{i(k.r-\omega t)} + cc] = \chi^{(2)}[2E_0^2 + E_0^2(e^{i(2k.r-2\omega t)} + cc) \qquad (2.25)$$

Thus, the nonlinear interaction generates two new polarization terms, one is frequency independent and known as optical refraction and another term has a double frequency dependency which is the basis for the second harmonic generation (SHG).

If we have two oscillating fields with different frequency, ω_1 and ω_2 then the resultant applied field is given by:

$$E(r,t) = E_{0,1}[e^{i(k_1.r-\omega_1 t)} + cc] + E_{0,2}[e^{i(k_2.r-\omega_2 t)} + cc] \tag{2.26}$$

where, $E_{0,i}$ and k_i are the amplitude and the propagation vector for i-th component. The second-order nonlinear polarization becomes:[49]

$$\begin{aligned} P^{(2)} = \chi^{(2)}[&E_{0,1}^2(e^{i(2k_1.r-2\omega_1 t)} + cc) + E_{0,2}^2(e^{i(2k_2.r-2\omega_2 t)} + cc) + 2E_{0,1}^2 + 2E_{0,2}^2 \\ &+2E_{0,1}E_{0,2}(e^{i(k_1+k_2)r-i(\omega_1+\omega_2)t} + cc) + 2E_{0,1}E_{0,2}(e^{i(k_1-k_2)r-i(\omega_1-\omega_2)t} + cc)] \end{aligned} \tag{2.27}$$

Therefore, apart from the second harmonics of the two input fields we have two more frequency dependent terms with frequency $\omega_1 + \omega_2$ and $\omega_1 - \omega_2$, which are known as the sum frequency generation (SFG) and the difference frequency generation (DFG) respectively (**Figure 2.7**).

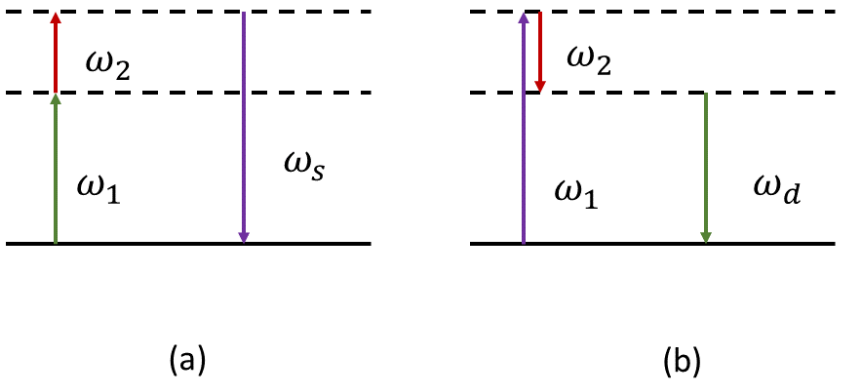

Figure 2.7. Schematic representation of nonlinear optical phenomena. (a) Sum frequency generation (ω_s) (b) Difference frequency generation (ω_d).

In order to observe the nonlinear effect, the second-order nonlinear susceptibility $\chi^{(2)}$ must be nonzero which is true in case of the non-centrosymmetric crystals.[49] Because, the values of $\chi^{(2)}$ is very small and the nonlinear polarization depends quadratically a very high intensity of the field is also required, which is easily obtained from ultrashort pulses. Apart from that the nonlinear output is only efficient if the proper phase matching condition is met. This is due to the frequency

dependency of the phase velocity and the refractive index of the medium. The phase matching condition for three-wave mixing (second-order nonlinear phenomena) is given in terms of the energy ($\hbar\omega$) and momentum ($\hbar k$) conservations.[36,41,52,53]

$$\begin{aligned} \omega &= \omega_1 + \omega_2 \\ k &= k_1 + k_2 \end{aligned} \tag{2.28}$$

For collinear propagation of the waves in a dispersive material the momentum conservation is given as:

$$n(\omega)\omega = n_1(\omega_1)\omega_1 + n_2(\omega_2)\omega_2 \tag{2.29}$$

The energy conservation and momentum conservation cannot be independently satisfied in a normal dispersive medium. In a birefringent medium (e.g. barium borate, lithium niobate, sapphire) the refractive index depends on the frequency, polarization and the direction of propagation of the light through the crystal. Therefore, by selecting proper incident angles, the phase matching condition can be satisfied in such medium.[41,52,53]

2.5.1 Ti:sapphire oscillator for TCSPC application

The optical design of the Ti:sapphire oscillator in our laboratory is given in **Figure 2.8** . The main laser cavity consists of two curved mirrors transparent to the pump-beam and reflective to the laser fundamental, two high-reflective mirror flat mirrors, one optical coupler (10% transmission at lasing wavelength), a Ti:sapphire rod (cut at Brewster angle) as the gain medium, a pair of prism to compensate group velocity dispersion (GVD). The gain medium is pumped at 523 nm with a 5 W frequency-doubled Nd:YAG CW laser from Spectra-Physics (Millennia eV). The pump-beam is focus via a lens through one of the curved mirrors. The fluorescence from the doped crystal is reflected from the curved mirrors and goes to the end mirrors (high reflector and

the optical coupler respectively) of the two arms of the cavity, then it returns to the crystal via the same path. The returning emission causes more stimulated emission if the gain of the medium positive. Therefore, in each round trip the intensity of light is amplified until it reached the saturation limit. The prisms are specially cut to so that the angle of incidence corresponds to the Brewster angle at minimum deviation. The first prism dispersed the laser and the second prism collimate the beam to the high reflector. The laser can be tuned by placing a vertical slit in between the second prism and the high reflector and translating horizontally across the dispersed spectrum.

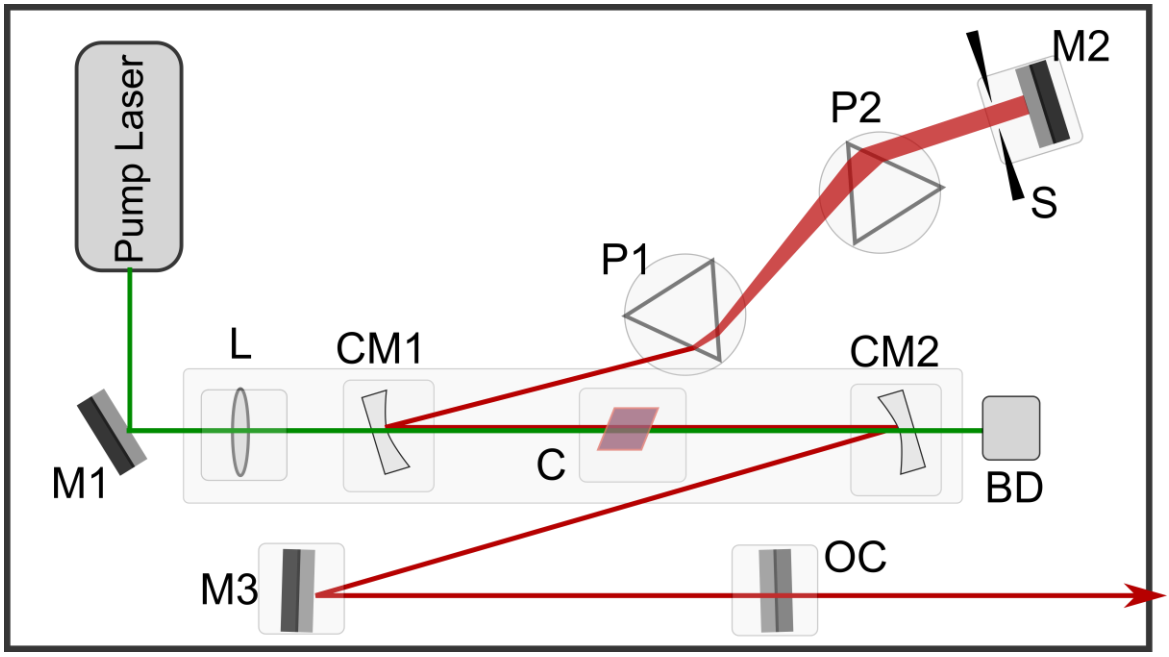

Figure 2.8. Optical layout of Ti:sapphire laser in our laboratory. The pump-laser is a 5 W frequency doubled Nd:YAG with an emission wavelength 532 nm. M1, M2 and M3 – mirrors with high reflectivity, L – focusing lens for the pump-beam. CM1 and CM2 are two curved mirrors transparent to the pump-beam and reflective to the Ti:sapphire fluorescence (675-1100 nm). OC - optical coupler with 10% transmission at 800 nm, C – titanium sapphire crystal. P1 and P2 are the prisms to introduce negative GVD, S – slit to change wavelength and BD – beam dumper.

The asymmetric design of the cavity ensures that the output is high power TEM_{00} mode. The length of the cavity is about 170 cm which corresponds to the 87.5 MHz repetition rate. The

maximum lasing power of ~800 mW can be achieved in CW mode via optimization of the alignment. At optimal alignment, one curved mirror sitting on the spring stage is slid in towards the crystal and gently released to gain mode-locked condition.

The mode-locked output of the laser is usually optimized around 800 nm wavelength. In common practice, the laser is frequency doubled or tripled using SHG and SFG techniques mentioned above to convert the wavelength to 400 nm and 266 nm respectively. This conversion allows us to excite a range of samples which we mostly encounter in our laboratory. The optical setup that we use in our laboratory is a pre-built box (Model TP-2000B THG) form U-Oplaz Technologies, Inc. The input pulse needs to be vertically polarized and the outputs become horizontally and vertically polarized for second and third harmonics respectively.

Another modification of the laser operation is necessary for practical use in TCSPC. In TCSPC technique, use of a laser with high repetition rate is advantageous since it reduces the data acquisition time. The very high repetition rate of Ti:sapphire, however, disadvantageous for samples which have relatively longer fluorescence lifetimes. For example, the in our setup an 87.5 MHz repetition rate corresponds to 11.4 ns time-gap between two pulses. Because of the limitation of the photon counting instruments this 11.4 ns time-gap cannot be fully utilized as the TAC range. In order to get a decay profile that has maximum within 10% of the time window and the tail has counts less than 1% of the maximum, the fluorescence lifetime should be less than 1 ns. This limitation can be avoided by reducing the repetition rate of the laser. In our laboratory, a pre-build pulse selection system form Conoptics Inc is used for the purpose. The pulse selection system is an electro-optic modulator (EOM, Model 350-160) control by a voltage amplifier (Model 25D) in association with a synchronized countdown electronics (Model 305). The EOM acts as a Pockels

medium (KH_2PO_4 crystals) i.e. the refractive index depends on the electric field applied to the material. The two normal components of the linearly polarized light undergo a phase shift due to the application of external electric field. If an appropriate voltage is applied to generate the electric field the EOM can act as a half-waveplate and thus change polarization from horizontal to vertical or vice versa if the linearly polarized light enters at 45° with respect the crystals axis. The countdown device gets the signal from a reference photodiode. The repetition rate is divided by the user set value and the amplifier is triggered at the divided repetition rate, which sends short voltage pulses to the EOM. When no voltage is applied, a horizontally polarized laser pulse enters the EOM, travels unaffected and blocked by the vertical polarizer at the exit of EOM. When the voltage pulse is synchronized with the transit time of a horizontally polarized laser pulse, the polarization is switched to vertical at the exit and thus allowed by the vertical polarizer. Therefore, the assembly can be used to reduce the repetition rate of the Ti:sapphire laser.

2.6 Förster Resonance Energy Transfer

A molecule in excited state may lose its energy through several radiative and non-radiative mechanism. Resonance energy transfer is one of the important mechanism by which a donor (D) molecule returns to its ground state by transferring the energy to an acceptor (A) molecule. The theory of energy transfer was first devolved by Theodor Förster in 1946[54] based on weak dipole-dipole interaction and subsequently verified by Stryer et al.[55] The mechanism is popularly known as Förster resonance energy transfer (FRET). The FRET is a nonradiative process which means it does not involve emission of a photon by the donor and subsequently re-absorption by the acceptor. There are several criteria that need to satisfy in order to FRET to happen. The distance between the donor and the acceptor must be within 10-100 Å. A distance closer than 10 Å leads to electron transfer, another kind of energy transfer mechanism that also contributes to the nonradiative

deexcitation process.[56] The emission spectrum of the donor should have some overlap with the absorption spectrum of the acceptor. The excited state lifetime should be longer than the duration of the energy transfer. The following schematic diagram (**Figure 2.9**) describe the energy transfer process.

The donor (D) molecule absorb a photon and goes to the excited state (D*). The excited donor molecule acts as an oscillating dipole. When the D* and A molecules are close to each other D* induces an oscillation in the acceptor molecule via dipole-dipole interaction. Similar to two

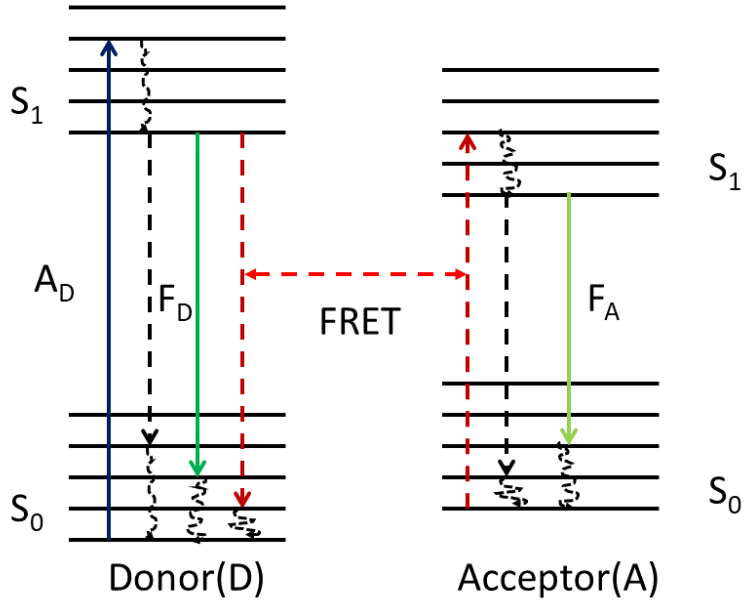

Figure 2.9. Schematic of the resonance energy transfer. A_D is the absorption of photon by the donor, F_D (solid green) is the fluorescence mechanisms of the donor. The nonradiative resonance energy transfer (FRET) is indicated by the dotted red arrows. Fluorescence emission may also take place form acceptor (F_A). All other nonradiative transition are denoted by dotted black arrows. S_0 and S_1 represent the singlet ground and excited electronic states.

mechanically connected pendulums, energy from the D* will transfer completely if the natural frequency of oscillation match, in this case which is indicated by the overlap of the spectra.

Therefore, D* loses its energy and A become A*, the excited acceptor molecule. In order to get the effective interaction between the dipoles of D* and A, they must be oriented favorably to each other i.e. one or both should have a certain degree of rotational freedom.

The rate of dipole-dipole energy transfer is given by:[16,57-59]

$$k_{ET} = \frac{1}{\tau_D}\left(\frac{R_0}{R}\right)^6 \tag{2.30}$$

where, τ_D is the fluorescence lifetime of the donor in absence of the acceptor. R is the distance between donor and acceptor; and R_0 is referred to as the "critical distance," defined by:

$$R_0^6 = \frac{9000\ln(10)\,\phi_D\,\kappa^2}{128\,\pi^5\,n^4 N_A}\int_0^\infty f_D(\bar{\nu})\epsilon_A(\bar{\nu})\bar{\nu}^{-4}d\bar{\nu} \tag{2.31}$$

where $f_D(\bar{\nu}) = F(\bar{\nu})/\int_0^\infty F(\bar{\nu})d\bar{\nu}$, is the fluorescence intensity of the unquenched donor normalized to the unit area on a wavenumber scale. The other parameters are: ϕ_D, the fluorescence quantum yield of the donor; κ^2, the orientation factor, assumed to be 2/3 for randomly oriented donors and acceptors; ϵ_A, the decadic molar extinction coefficient; n, the refractive index of the medium; and N_A, Avogadro's number. The efficiency of the energy transfer is often given as:[18]

$$E_{FRET} = 1 - \frac{\tau_{DA}}{\tau_D} = \frac{R_0^6}{R_0^6 + R^6} \tag{2.32}$$

where, τ_{DA} is the excited state lifetime of the donor in presence of the acceptor. Therefore, R_0 can be defined as the distance at which the efficiency of energy transfer is 50%.

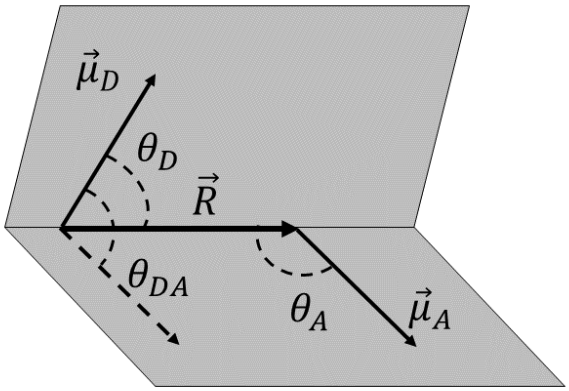

Figure 2.10. Orientation of molecular dipoles of the donor and the acceptor with respect o each other. The average contribution of all possible orientation accounted in the κ^2-factor.

The rate of nonradiative energy transfer given in equation (2.30) can be obtained from the quantum mechanical picture of the weak interaction of dipoles. The energy of weak dipole -dipole interaction is given by:[57]

$$V = \frac{1}{n^2 R^3}[\vec{\mu}_D \cdot \vec{\mu}_A - 3(\vec{\mu}_D \cdot \hat{r})(\hat{r} \cdot \vec{\mu}_A)] \tag{2.33}$$

where, $\vec{\mu}_D$ and $\vec{\mu}_A$ are the dipole moment vector of the donor and the acceptor respectively. $\hat{r}$ denotes the units vector along the distance R between the donor and the acceptor. n is the refractive index of the medium. The term in the square bracket can be written as:[18,57]

$$\begin{aligned}[\mu_D \mu_A \cos\theta_{DA} - 3\mu_D \cos\theta_D \mu_A \cos\theta_A] \\ = [\cos\theta_{DA} - 3\cos\theta_D \cos\theta_A]\mu_D \mu_A = \kappa \mu_D \mu_A\end{aligned} \tag{2.34}$$

where, θ_{DA} is the angle between the transition dipole moments vectors of the donor and the acceptor, θ_D and θ_A are the angles between the unit vector along the distance R and the transition dipole moment vectors of the donor and the acceptor respectively (**Figure 2.10**). The factor, κ, accounts for the orientation of the dipoles and the value of $\kappa^2 = 2/3$ is obtained from the average

contribution from the randomly oriented dipoles. Note that, μ_D and μ_A are the magnitudes of the dipole moment vector. The equation (2.33) can now be written as:

$$V = \frac{\kappa}{n^2 R^3}\mu_D \mu_A \tag{2.35}$$

The rate of nonradiative energy transfer is given by:

$$\begin{aligned} k_{ET} \propto |\langle \mathrm{DA}^* | V | \mathrm{D}^* \mathrm{A} \rangle|^2 \rho(\bar{\nu}) &= \left| \left\langle \mathrm{DA}^* \middle| \frac{\kappa}{n^2 R^3}\mu_D \mu_A \middle| \mathrm{D}^* \mathrm{A} \right\rangle \right|^2 \rho(\bar{\nu}) \\ &= \frac{\kappa^2}{n^4 R^6} |\langle \mathrm{DA}^* | \mu_D | \mathrm{D}^* \mathrm{A} \rangle|^2 |\langle \mathrm{DA}^* | \mu_A | \mathrm{D}^* \mathrm{A} \rangle|^2 \rho(\bar{\nu}) \end{aligned} \tag{2.36}$$

where, $\rho(\bar{\nu})$ is the probability that the transfer energy corresponds to the wavenumber $\bar{\nu}$. Note that the energy transfer takes place from the state $|\mathrm{D}^*\mathrm{A}\rangle$ to the state $|\mathrm{DA}^*\rangle$. This equation indicates that the rate of energy transfer is inversely proportional to the sixth power of the distance between the donor and the acceptor. The first squared term within the vertical bars is the emission transition dipole moment[16,60] and that is proportional to $\bar{\nu}^{-3}\tau_{\mathrm{rad}}^{-1}$, where τ_{rad}^{-1} is the radiative rate constant. The second squared term within the vertical bars is the absorption dipole moment[16] and that is proportional to $\epsilon_A(\bar{\nu})\bar{\nu}^{-1}$, where $\epsilon_A(\bar{\nu})$ is the molar absorptivity as a function of wavenumber. $f_D(\bar{\nu}) = F(\bar{\nu}) / \int_0^\infty F(\bar{\nu}) d\bar{\nu}$ denotes the fraction of the donor fluorescence at wavenumber $\bar{\nu}$ and therefore is equal to $\rho(\bar{\nu})$. Therefore, integrating over the range of wavenumbers the equation (2.36) transform to:

$$k_{ET} \propto \frac{\kappa^2}{n^4 R^6} \int_0^\infty f_D(\bar{\nu}) \bar{\nu}^{-3} \tau_{\mathrm{rad}}^{-1} \epsilon_A(\bar{\nu}) \bar{\nu}^{-1} d\bar{\nu} = \frac{\kappa^2 \tau_{\mathrm{rad}}^{-1}}{n^4 R^6} \int_0^\infty f_D(\bar{\nu}) \epsilon_A(\bar{\nu}) \bar{\nu}^{-4} d\bar{\nu} \tag{2.37}$$

The radiative rate constant, τ_{rad}^{-1}, can be expressed in terms of the fluorescence quantum yield of the donor and the lifetime of the fluorophores using equation (2.13) *i.e.* $\tau_{\text{rad}}^{-1} = \phi_D/\tau_D$. Therefore, we can write:

$$k_{ET} \propto \frac{\kappa^2 \phi_D}{n^4 R^6 \tau_D} \int_0^\infty f_D(\bar{\nu}) \epsilon_A(\bar{\nu}) \bar{\nu}^{-4} d\bar{\nu} \tag{2.38}$$

Using proper proportionality constant one would arrive at the equation (2.30) and (2.31).

Since FRET is dependent on the distance it can be used to study several proximity relationships in proteins, nucleic acid, membranes and other biological systems. The great advantage of the FRET is that it can measure distance in Å resolution and it can be used in *in vivo* condition. In **Chapter 6**, the FRET has been used to estimate the nonradiative quenching of fluorescence of the Cy5 dye by the paramagnetic metal ions.

2.7 Time-Resolved Fluorescence Anisotropy

When a fluorophore absorbs polarized light, the subsequent emission is also polarized in the same direction of the excitation if the photon is emitted instantaneously. However, the excited state of a typical fluorophore has lifetime in the order of 10^{-9} s.[18] This timescale allows the fluorophore to undergo significant angular displacement which affects the polarization of the emitted photon.[61] In an isotropic solution, where the fluorophore molecules are randomly oriented, an incident beam of polarized light preferentially excites molecules with a probability proportional to $\cos^2\theta$, where θ is the angle between the transition dipole moment of the molecule and the polarization of the incident light. This process is known as photoselection.[62] The rotation of the molecules cause depolarization of the anisotropic distribution of molecules and thus the emission is also depolarized. The depolarization of the emitted photon is not only affected by the rotation

of the fluorophore but can also be affected by the intermolecular excitation transfer and relaxation mechanisms.[61]

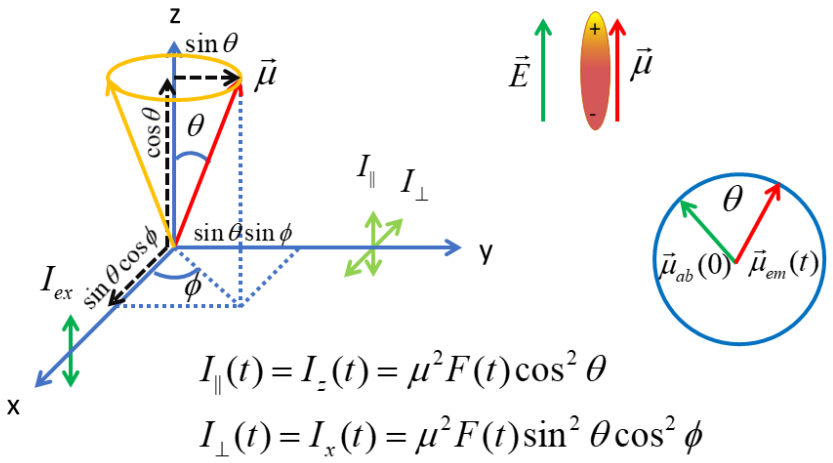

Figure 2.11. General layout of the anisotropy measurement. The excitation beam is vertically polarized (z-axis) by a polarizer and travels along x-axis. The emissions are detected in the perpendicular direction (y-axis). The emission polarizer is set to parallel (z-axis) or perpendicular (x-axis) directions for measurements. Two associated figures represent the electric filed induced dipole and depolarization of emission dipole after certain time.

The basic layout of the anisotropy measurement is given in **Figure 2.11**. The sample is excited with a vertically polarized light using a polarizer (excitation polarizer) and the emission is detected in parallel and perpendicular directions with respect to the excitation using another polarizer (emission polarizer). Let the intensity of emission in parallel and perpendicular directions are given by $I_{\parallel}(t)$ and $I_{\perp}(t)$ respectively. The fluorescence anisotropy, $r(t)$ at time t after the excitation of the fluorophore is defined as:[61,63]

$$r(t) = \frac{I_{\parallel}(t) - I_{\perp}(t)}{I_{\parallel}(t) + 2I_{\perp}(t)} \qquad (2.39)$$

For an ensemble of molecules the time-resolved anisotropy given in equation (2.39) can be expressed in terms of the average orientation of the molecular transition dipoles. The time-dependent angular distribution of the molecular dipoles is given by the rotational diffusion model under certain symmetry condition.[63-65] Let $W(\theta,\phi,t)$ is the probability that a unit dipole $\vec{\mu}(t)$ is oriented at (θ,ϕ) at time t. The rotational diffusion equation is given by:

$$\frac{\partial W(\theta,\phi,t)}{\partial t} = -\hat{H}W(\theta,\phi,t) \tag{2.40}$$

where, $\hat{H} = \sum_{i,j} L_i D_{i,j} L_j$ is the Hamiltonian of the rotational system, $\boldsymbol{L}$ is the angular momentum operator and $\boldsymbol{D}$ is the diffusion tensor.[63,64] By choosing a suitable coordinate system one can transform the Hamiltonian into $\hat{H} = \sum_j D_j L_j^2$. The solution of the equation (2.40) is given by:[61,63]

$$W(\theta,\phi,t) = \int_0^{2\pi} d\phi_0 \int_0^{\pi} \sin\theta_0 d\theta_0 W(\theta_0,\phi_0) G(\theta_0,\phi_0 \mid \theta,\phi,t) \tag{2.41}$$

where, $W(\theta_0,\phi_0) = \frac{1}{4\pi}[1 + 2P_2(\cos\theta_0)]$, is the initial distribution of the orientation of ensemble of randomly oriented dipoles. $P_2(x) = \frac{1}{2}(3x^2 - 1)$ is the second Legendre polynomial. Therefore, we can write:

$$W(\theta_0,\phi_0) = \frac{3}{4\pi} cos^2\theta_0 \tag{2.42}$$

At time $t = 0$, we can assume that the absorption and the emission dipoles are parallel to each other. The normalization condition is given by:

$$\int_0^{2\pi} d\phi_0 \int_0^{\pi} \sin\theta_0 d\theta_0 W(\theta_0,\phi_0) = \int_0^{2\pi} d\phi_0 \int_0^{\pi} \sin\theta_0 d\theta_0 \frac{3}{4\pi} cos^2\theta_0 = 1 \tag{2.43}$$

The Green's function $G(\theta_0, \phi_0|\theta, \phi, t)$ accounts for the time evolution of the orientation probability $W(\theta, \phi, t)$ i.e. the probability that if a dipole is oriented at (θ_0, ϕ_0) at time $t = 0$, it will be oriented at (θ, ϕ) at time t, and it is given by:

$$G(\theta_0, \phi_0 \mid \theta, \phi, t) = \sum_{l=0}^{\infty} \sum_{m=-l}^{+l} C_{l,m}(t) Y_{l,m}^{*}(\theta_0, \phi_0) Y_{l,m}(\theta, \phi) \tag{2.44}$$

where, $Y_{l,m}(\theta, \phi)$ are the spherical harmonics and $C_{l,m}(t)$ is the time-dependent expansion coefficient. The normalization condition requires that:

$$\int_0^{2\pi} d\phi \int_0^{\pi} \sin\theta d\theta G(\theta_0, \phi_0 \mid \theta, \phi, t) = 1 \tag{2.45}$$

and the completeness condition requires that:

$$\begin{aligned} &G(\theta_0, \phi_0 \mid \theta, \phi, t = 0) = \delta(\cos\theta - \cos\theta_0)\delta(\phi - \phi_0) \\ &= \sum_{l=0}^{\infty} \sum_{m=-l}^{+l} Y_{l,m}^{*}(\theta_0, \phi_0) Y_{l,m}(\theta, \phi) \end{aligned} \tag{2.46}$$

Therefore, it can be shown that $C_{l,m}(t = 0) = 1$ for all l and m and $C_{0,0}(t) = 1$ at any time t. Due to the symmetry of rotation, we need to consider the solution only for $l \leq 2$ and the list of spherical harmonics associated with those values of l are given below.

$$
\begin{aligned}
Y_{0,0}(\theta,\phi) &= \sqrt{\frac{1}{4\pi}} \\
Y_{1,0}(\theta,\phi) &= \frac{1}{2}\sqrt{\frac{3}{\pi}}\cos\theta \\
Y_{1,\pm1}(\theta,\phi) &= \pm\frac{1}{2}\sqrt{\frac{3}{2\pi}}\sin\theta e^{\pm i\phi} \\
Y_{2,0}(\theta,\phi) &= \frac{1}{4}\sqrt{\frac{5}{\pi}}(3\cos^2\theta - 1) \\
Y_{2,\pm1}(\theta,\phi) &= \pm\frac{1}{2}\sqrt{\frac{15}{2\pi}}\sin\theta\cos\theta e^{\pm i\phi} \\
Y_{2,\pm2}(\theta,\phi) &= \frac{1}{4}\sqrt{\frac{15}{2\pi}}\sin^2\theta e^{\pm 2i\phi}
\end{aligned}
\tag{2.47}
$$

Because of the orthogonal properties of the spherical harmonics, the only nonzero term will have the coefficient $C_{0,0}$ and $C_{2,0}$ and therefore we have,

$$
\begin{aligned}
W(\theta,\phi,t) &= \int_0^{2\pi} d\phi_0 \int_0^{\pi} \sin\theta_0 d\theta_0 \frac{3}{4\pi} cos^2\theta_0 \\
&\quad \times [C_{0,0}(t)Y^*_{0,0}(\theta_0,\phi_0)Y_{0,0}(\theta,\phi) + C_{2,0}(t)Y^*_{2,0}(\theta_0,\phi_0)Y_{2,0}(\theta,\phi)] \\
&= \frac{1}{4\pi}[1 + 2C_{2,0}(t)P_2(\cos\theta)]
\end{aligned}
\tag{2.48}
$$

Let $f(\theta,\phi,t)$ represent an arbitrary time-dependent function of the orientation of the transition dipoles. Since the molecules orient randomly, the ensemble average of the function should be given by the spatial average over (θ,ϕ):

$$
\begin{aligned}
\langle f(t)\rangle_{\theta,\phi} &= \int_0^{2\pi} d\phi \int_0^{\pi} \sin\theta d\theta f(\theta,\phi,t) W(\theta,\phi,t) \\
&= \int_0^{2\pi} d\phi \int_0^{\pi} \sin\theta d\theta f(\theta,\phi,t) \frac{1}{4\pi}[1 + 2C_{2,0}(t)P_2(\cos\theta)]
\end{aligned}
\tag{2.49}
$$

The intensities of emission at time t in parallel and perpendicular directions from a dipole oriented at (θ,ϕ) are given by:

$$i_{\parallel}(\theta,\phi,t) = \mu^2 F(t)\cos^2\theta$$
$$i_{\perp}(\theta,\phi,t) = \mu^2 F(t)\sin^2\theta\cos^2\phi \tag{2.50}$$

where, $F(t)$ is the fluorescence decay function which represents the probability that a molecule is in the excited state. The measured intensities $I_{\parallel}(t)$ and $I_{\perp}(t)$ are the ensemble average of $i_{\parallel}(\theta,\phi,t)$ and $i_{\perp}(\theta,\phi,t)$ respectively. Then using equation (2.49) and equation (2.50) we have:

$$I_{\parallel}(t) = [\frac{1}{3} + \frac{4}{15}C_{2,0}(t)]\mu^2 F(t)$$
$$I_{\perp}(t) = [\frac{1}{3} - \frac{2}{15}C_{2,0}(t)]\mu^2 F(t) \tag{2.51}$$

It can also be shown that:

$$\left\langle P_2\left(\vec{\mu}(0)\cdot\vec{\mu}(t)\right)\right\rangle = \int_0^{2\pi} d\phi \int_0^{\pi} \sin\theta d\theta P_2\left(\vec{\mu}(0)\cdot\vec{\mu}(t)\right)\frac{1}{4\pi}[1+2C_{2,0}(t)P_2(\cos\theta)]$$
$$= C_{2,0}(t) \tag{2.52}$$

Using the definition of fluorescence anisotropy given in equation (2.39) we can have:

$$r(t) = \frac{2}{5}\left\langle P_2\left(\vec{\mu}(0)\cdot\vec{\mu}(t)\right)\right\rangle = \frac{2}{5}C_{2,0}(t) \tag{2.53}$$

Since, $\vec{\mu}(0)\cdot\vec{\mu}(t) = \cos\theta$, for the unit dipole the above expression can also be written as:

$$r(t) = \frac{2}{5}\left\langle P_2\left(\cos\theta\right)\right\rangle = \frac{2}{5}\left(\frac{3\left\langle\cos^2\theta\right\rangle - 1}{2}\right) \tag{2.54}$$

Using the boundary condition $C_{2,0}(t=0) = 1$, which implies $r(t=0) = 2/5$, the upper limit of the anisotropy. The limiting values of the anisotropy, 0.4 and -0.2, can also be obtained from equation (2.54). Under the assumptions that the molecules behave like a spherical or symmetric rotor and the molecules undergo Brownian motion then anisotropy can be given by:[63]

$$r(t) = \frac{2}{5}\left\langle P_2\left(\vec{\mu}(0)\cdot\vec{\mu}(t)\right)\right\rangle = \frac{2}{5}e^{-6Dt} \tag{2.55}$$

where $D = k_B T/6V_m\eta$ is the rotational diffusion coefficient. k_B, T, V_m and η are the Boltzmann constant, temperature, molecular volume of the fluorophore and the viscosity of the medium respectively.

The anisotropy is often modeled with a sum of exponential functions for a complex type of rotational motion.[66 59]

$$r(t) = \sum_i r_0^{(i)} e^{-t/\tau_r^{(i)}} \tag{2.56}$$

where $\tau_r^{(i)}$ and $r_0^{(i)}$ are rotational correlation time and the anisotropy at time $t = 0$ for the i-th component of the complex rotation. The parallel and the perpendicular component of the intensity can be written as:[66]

$$\begin{aligned} I_{\parallel}(t) &= e^{-t/\tau_F}\left(1+2\sum_i r_0^{(i)} e^{-t/\tau_r^{(i)}}\right) \\ I_{\perp}(t) &= e^{-t/\tau_F}\left(1-\sum_i r_0^{(i)} e^{-t/\tau_r^{(i)}}\right) \end{aligned} \tag{2.57}$$

where τ_F denotes the excited state lifetime of the fluorophore. If the emission polarizer is set to an arbitrary angle α with respect to the excitation polarized the measured intensity is given by:

$$I_{\alpha}(t) = \cos^2\alpha I_{\parallel}(t) + \sin^2\alpha I_{\perp}(t) \tag{2.58}$$

If the angle α is set to 54.7° (also known as "magic angle") then the measured intensity is proportional to the fluorescence decay function, $F(t)$, which eliminate the anisotropy effect.[18,59]

$$F(t) = I_{\parallel}(t) + 2I_{\perp}(t) \propto e^{-t/\tau_F} \tag{2.59}$$

It should be noted that the expression of anisotropy given in equation (2.39) is preferred as compared to the polarization, $p(t) = [I_{\parallel}(t) - I_{\perp}(t)]/[I_{\parallel}(t) + I_{\perp}(t)]$ since the anisotropy expression normalize the difference between the two intensities with the fluorescence decay function and thus eliminated the effect of excited state lifetime on the measurement depolarization.[59] The experimental scheme presented here also applicable to steady-state anisotropy. The sample, however, should be in the solid state for example as film or as in frozen solvent. A correction factor (G) is very often introduced in the anisotropy equation which accounts for the anisotropic response of the optics and the detector towards the parallel and perpendicular polarization of the light. The steady-state anisotropy equation with a correction factor can be written as:[18]

$$r = \frac{I_{\parallel} - GI_{\perp}}{I_{\parallel} + 2GI_{\perp}} \qquad (2.60)$$

Time-resolved depolarization of the fluorescence can be used to study the rotational motion of the molecules in picosecond to nanosecond timescale. The tools are useful in biological and material science to study the structural flexibility of micelles and membranes, molecular orientation and rigidity of composites and films. Both time-resolved and steady-state fluorescence anisotropy has been used to study P3HT films in **Chapter 7**.

2.8 References

1. Cho, M.; Rosenthal, S. J.; Scherer, N. F.; Ziegler, L. D.; Fleming, G. R. Ultrafast Solvent Dynamics: Connection between Time Resolved Fluorescence and Optical Kerr Measurements. *J. Chem. Phys.* **1992**, *96* (7), 5033-5038.

2. Petrich, J. W.; Fleming, G. R. Ultrafast Processes in Biology. *Photochem. Photobiol.* **1984**, *40* (6), 775-780.

3. Gai, F.; Fehr, M. J.; Petrich, J. W. Ultrafast Excited-State Processes in the Antiviral Agent Hypericin. *J. Am. Chem. Soc.* **1993**, *115* (8), 3384-3385.

4. English, D.; Zhang, W.; Kraus, G. A.; Petrich, J. W. Excited-State Photophysics of Hypericin and Its Hexamethoxy Analog: Intramolecular Proton Transfer as a Nonradiative Process in Hypericin. *J. Am. Chem. Soc.* **1997**, *119* (13), 2980-2986.

5. English, D.; Das, K.; Ashby, K.; Park, J.; Petrich, J. W.; Castner, E. Confirmation of Excited-State Proton Transfer and Ground-State Heterogeneity in Hypericin by Fluorescence Upconversion. *J. Am. Chem. Soc.* **1997**, *119* (48), 11585-11590.

6. Das, K.; Smirnov, A. V.; Wen, J.; Miskovsky, P.; Petrich, J. W. Photophysics of Hypericin and Hypocrellin a in Complex with Subcellular Components: Interactions with Human Serum Albumin. *Photochem. Photobiol.* **1999**, *69* (6), 633-645.

7. Petrich, J. W.; Poyart, C.; Martin, J. Photophysics and Reactivity of Heme Proteins: A Femtosecond Absorption Study of Hemoglobin, Myoglobin, and Protoheme. *Biochemistry*. **1988**, *27* (11), 4049-4060.

8. Chen, Y.; Gai, F.; Petrich, J. W. Solvation of 7-Azaindole in Alcohols and Water: Evidence for Concerted, Excited-State, Double-Proton Transfer in Alcohols. *J. Am. Chem. Soc.* **1993**, *115* (22), 10158-10166.

9. Chowdhury, P. K.; Halder, M.; Sanders, L.; Calhoun, T.; Anderson, J. L.; Armstrong, D. W.; Song, X.; Petrich, J. W. Dynamic Solvation in Room-Temperature Ionic Liquids. *J. Phys. Chem. B.* **2004**, *108* (29), 10245-10255.

10. Nisoli, M.; Decleva, P.; Calegari, F.; Palacios, A.; Martín, F. Attosecond Electron Dynamics in Molecules. *Chem. Rev.* **2017**, *117* (16), 10760-10825.

11. Ghosh, A.; Ostrander, J. S.; Zanni, M. T. Watching Proteins Wiggle: Mapping Structures with Two-Dimensional Infrared Spectroscopy. *Chem. Rev.* **2017**, *117* (16), 10726-10759.

12. Laage, D.; Elsaesser, T.; Hynes, J. T. Water Dynamics in the Hydration Shells of Biomolecules. *Chem. Rev.* **2017**, *117* (16), 10694-10725.

13. Nihonyanagi, S.; Yamaguchi, S.; Tahara, T. Ultrafast Dynamics at Water Interfaces Studied by Vibrational Sum Frequency Generation Spectroscopy. *Chem. Rev.* **2017**, *117* (16), 10665-10693.

14. Kraack, J. P.; Hamm, P. Surface-Sensitive and Surface-Specific Ultrafast Two-Dimensional Vibrational Spectroscopy. *Chem. Rev.* **2016**, *117* (16), 10623-10664.

15. Láng, L. Absorption Spectra in the Ultraviolet and Visible Region. **1961**,

16. Birks, J. B. *Photophysics of Aromatic Molecules* Wiley-Interscience: London, New York, 1970.

17. Harris, D. C.; Bertolucci, M. D. *Symmetry and Spectroscopy: An Introduction to Vibrational and Electronic Spectroscopy* Courier Corporation: 1978.

18. Lakowicz, J. R. *Principles of Fluorescence Spectroscopy*, 3rd ed.; Springer: 2011.

19. *Agilent 8453 UV-Visible Spectroscopy System: Operator's Manual* 2011.

20. Murov, S. L.; Carmichael, I.; Hug, G. L. *Handbook of Photochemistry* CRC Press: 1993.

21. *Fluorommax-4 & Fluoromax-4P with USB: Operation Manual Rev. D* 2012.

22. Melhuish, W. Absolute Spectrofluorometry. *J. Res. Nat. Bur. Stand. USA.* **1972**, *76* (6), 547-560.

23. Brouwer, A. M. Standards for Photoluminescence Quantum Yield Measurements in Solution (IUPAC Technical Report). *Pure Appl. Chem.* **2011**, *83* (12), 2213-2228.

24. Würth, C.; Grabolle, M.; Pauli, J.; Spieles, M.; Resch-Genger, U. Relative and Absolute Determination of Fluorescence Quantum Yields of Transparent Samples. *Nat. Protoc.* **2013**, *8* (8), 1535.

25. Darvey, I.; Staff, P. Stochastic Approach to First-Order Chemical Reaction Kinetics. *J. Chem. Phys.* **1966**, *44* (3), 990-997.

26. McQuarrie, D. A. Stochastic Approach to Chemical Kinetics. *Journal of applied probability*. **1967**, *4* (3), 413-478.

27. O'Connor, D. V.; Phillips, D. *Time Correlated Single Photon Counting* Academic Press Inc.: London, 1984.

28. Becker, W. *Advanced Time-Correlated Single Photon Counting Applications* Springer: 2016.

29. Peter, K.; Wahl, M.; Erdmann, R. *Advanced Photon Counting: Applications, Methods, Instrumentation* Springer: 2015.

30. Becker, W. *Advanced Time-Correlated Single Photon Counting Techniques* Springer Science & Business Media: 2005.

31. Wahl, M. *Technical Note: Time-Correlated Single Photon Counting*

PicoQuant GmbH: Berlin, Germany,

32. Becker, W. *The Bh Tcspc Handbook, (Becker & Hickl Gmbh)* 2015.

33. Schulz, P. A. Fast Electro-Optic Wavelength Selection and Frequency Modulation in Solid State Lasers. *Lincoln Laboratory Journal;(USA).* **1990**, *3*

34. Dutt, G.; Doraiswamy, S.; Periasamy, N.; Venkataraman, B. Rotational Reorientation Dynamics of Polar Dye Molecular Probes by Picosecond Laser Spectroscopic Technique. *J. Chem. Phys.* **1990**, *93* (12), 8498-8513.

35. Diels, J.-C.; Rudolph, W. *Ultrashort Laser Pulse Phenomena: Fundamentals, Techniques, and Applications on a Femtosecond Time Scale* Elsevier: 2006.

36. Abramczyk, H. *Introduction to Laser Spectroscopy* Elsevier: 2005.

37. Siegman, A. E. *Lasers (Mill Valley, Ca* University Science Books: 1986.

38. Svelto, O.; Hanna, D. C. Principles of Lasers. **1998**,

39. Spence, D. E.; Kean, P. N.; Sibbett, W. 60-Fsec Pulse Generation from a Self-Mode-Locked Ti: Sapphire Laser. *Opt. Lett.* **1991**, *16* (1), 42-44.

40. Herink, G.; Jalali, B.; Ropers, C.; Solli, D. Resolving the Build-up of Femtosecond Mode-Locking with Single-Shot Spectroscopy at 90 Mhz Frame Rate. *Nat. Photonics*. **2016**, *10* (5), 321.

41. Saleh, B. E.; Teich, M. C.; Saleh, B. E. *Fundamentals of Photonics* Wiley New York: 1991.

42. Träger, F. *Springer Handbook of Lasers and Optics* Springer Science & Business Media: 2012.

43. Silfvast, W. T. *Laser Fundamentals* Cambridge university press: 2004.

44. Adhikary, R. Application of Fluorescence Spectroscopy: Excited-State Dynamics, Food-Safety, and Disease Diagnosis. **2010**,

45. Hecht, E. *Optics* Pearson Education: 2016.

46. Pedrotti, F. L.; Pedrotti, L. M.; Pedrotti, L. S. *Introduction to Optics*, 3rd ed.; Pearson Prentice Hall: Upper Saddle River, N.J., 2007.

47. Martinez, O.; Gordon, J.; Fork, R. Negative Group-Velocity Dispersion Using Refraction. *JOSA A.* **1984**, *1* (10), 1003-1006.

48. Milonni, P. W.; Eberly, J. H. *Introduction to Laser Operation*, 1st ed.; Wiley & Sons, Inc. : 2010.

49. Verbiest, T.; Clays, K.; Rodriguez, V. *Second-Order Nonlinear Optical Characterization Techniques: An Introduction* CRC press: 2009.

50. Papadopoulos, M. G.; Sadlej, A. J.; Leszczynski, J. *Non-Linear Optical Properties of Matter* Springer: 2006.

51. Boyd, R. W. *Nonlinear Optics* Academic press: 2003.

52. Rosencher, E.; Vinter, B. *Optoelectronics* Cambridge University Press: 2002.

53. Ghatak, A. K.; Thyagarajan, K. *Optical Electronics* Cambridge University Press: 1989.

54. Förster, T. Zwischenmolekulare Energiewanderung Und Fluoreszenz. *Annalen der Physik*. **1948**, *437* (1-2), 55-75.

55. Stryer, L.; Haugland, R. P. Energy Transfer: A Spectroscopic Ruler. *Proceedings of the National Academy of Sciences*. **1967**, *58* (2), 719-726.

56. Dexter, D. L. A Theory of Sensitized Luminescence in Solids. *J. Chem. Phys.* **1953**, *21* (5), 836-850.

57. Van Der Meer, B. W.; Coker, G.; Chen, S.-Y. S. *Resonance Energy Transfer:Theory and Data* VCH New York: 1994.

58. Förster, T. *Intermolecular Energy Transfer and Fluorescence* National Research Council of Canada: 1955.

59. Fleming, G. R. *Chemical Application of Ultrafast Spectroscopy* Oxford University Press: New York, 1986.

60. Hilborn, R. C. Einstein Coefficients, Cross Sections, F Values, Dipole Moments, and All That. *arXiv preprint physics/0202029*. **2002**,

61. Fleming, G. R.; Morris, J. M.; Robinson, G. Direct Observation of Rotational Diffusion by Picosecond Spectroscopy. *Chem. Phys.* **1976**, *17* (1), 91-100.

62. Jameson, D. M.; Seifried, S. E. Quantification of Protein–Protein Interactions Using Fluorescence Polarization. *Methods*. **1999**, *19* (2), 222-233.

63. Tao, T. Time-Dependent Fluorescence Depolarization and Brownian Rotational Diffusion Coefficients of Macromolecules. *Biopolymers*. **1969**, *8* (5), 609-632.

64. Chuang, T.; Eisenthal, K. Theory of Fluorescence Depolarization by Anisotropic Rotational Diffusion. *J. Chem. Phys.* **1972**, *57* (12), 5094-5097.

65. Weber, G. Theory of Fluorescence Depolarization by Anisotropic Brownian Rotations. Discontinuous Distribution Approach. *J. Chem. Phys.* **1971**, *55* (5), 2399-2407.

66. Cross, A. J.; Fleming, G. R. Analysis of Time-Resolved Fluorescence Anisotropy Decays. *Biophys. J.* **1984**, *46* (1), 45-56.

CHAPTER 3. WHAT IS THE BEST METHOD TO FIT TIME-RESOLVED DATA? A COMPARISON OF THE RESIDUAL MINIMIZATION AND THE MAXIMUM LIKELIHOOD TECHNIQUES AS APPLIED TO EXPERIMENTAL TIME-CORRELATED, SINGLE-PHOTON COUNTING DATA

A paper published in the Journal of Physical Chemistry B

Kalyan Santra,[1,2] Jinchun Zhan,[3] Xueyu Song,[1,2] Emily A. Smith,[1,2] Namrata Vaswani,[3] and Jacob W. Petrich*[,1,2]

3.1 Abstract

The need for measuring fluorescence lifetimes of species in subdiffraction-limited volumes in, for example, stimulated emission depletion (STED) microscopy, entails the dual challenge of probing a small number of fluorophores and fitting the concomitant sparse data set to the appropriate excited-state decay function. This need has stimulated a further investigation into the relative merits of two fitting techniques commonly referred to as "residual minimization," RM, and "maximum likelihood," ML. Fluorescence decays of the well-characterized standard, rose bengal

---

Reprinted with permission from *The Journal of Physical Chemistry B* **2016**, 120(9): 2484-90

*To whom correspondence should be addressed. Email: jwp@iastate.edu

[1]Department of Chemistry, Iowa State University, Ames, Iowa 50011, USA

[2]U. S. Department of Energy, Ames Laboratory, Ames, Iowa 50011, USA

[3]Department of Electrical and Computer Engineering, Iowa State University, Ames, Iowa 50011, USA

in methanol at room temperature (530 ± 10 ps), were acquired in a set of five experiments in which the total number of "photon counts" was approximately 20, 200, 1000, 3000, and 6000; and there were from about 2 to 200 counts at the maxima of the respective decays. Each set of experiments was repeated 50 times in order to generate the appropriate statistics. Each of the 250 data sets was analyzed by ML and two different RM methods (differing in the weighting of residuals) using in-house routines and compared with a frequently-used commercial RM routine. Convolution with a real instrument response function was always included in the fitting. While RM using Pearson's weighting of residuals can recover the correct mean result with a total number of counts of 1000 or more, ML distinguishes itself by yielding, in all cases, the same mean lifetime within 2% of the accepted value. For 200 total counts and greater, ML always provides a standard deviation of less than 10% of the mean lifetime; and even at 20 total counts there is only 20% error in the mean lifetime. The robustness of ML advocates its use for sparse data sets such as those acquired in some subdiffraction-limited microscopies, such as STED, and, more importantly, provides greater motivation for exploiting the time-resolved capacities of this technique to acquire and analyze fluorescence lifetime data.

3.2 Introduction

Time-resolved spectroscopic techniques provide an important portfolio of tools for investigating fundamental processes in chemistry, physics, and biology as well as for evaluating the properties of a wide range of materials.[1,2] One of the most powerful time-resolved techniques is that of time-correlated, single-photon counting (TCSPC), which is explained in detail in the texts by Fleming[1] and O'Conner and Phillips.[2] Traditionally, this method requires constructing a histogram of arrival time differences between an excitation pulse and pulse resulting from an

emitted photon and fitting this histogram to an exponential decay (or perhaps, a sum of exponential decays in more complicated systems). We shall refer to this method of analysis as the Residual Minimization technique (RM). Phase fluorometry is an exception.[3-5] The quality of the histogram directly determines the quality of the fit, and hence, the accuracy of the extracted decay time. Thus, if the sample does not have a high fluorescence quantum yield (number of photons emitted per number of photons absorbed), one must collect data for a longer period of time in order to obtain a histogram of commensurate quality. This, however, is not always practical. For example, the sample may not have a high fluorescence quantum yield, or it may degrade after prolonged exposure to light. **Figure 3.1** provides examples of such histograms.

The difficulties cited above are illustrated by a certain class of fluorescence microscopy experiments, in particular, those involving subdiffraction-limited spatial resolution, which usually require rapid data acquisition times and the use of fluorescent probes that may not be stable at the high laser powers that these techniques often require.[6,7] The experimental technique also limits the probe volume, thus reducing the concentration of excited-state fluorophores, and thereby contributing to the reduction of the fluorescence signal. One of the ways to overcome this is to bin the adjacent pixels of the image to increase the number of photons in the time channels. This, however, compromises the spatial resolution, which is clearly undesirable in an experiment whose objective is super resolution imaging. We have recently discussed these difficulties as they pertain to stimulated emission depletion (STED) microscopy.[7] In particular, a major challenge in STED fluorescence lifetime imaging has been, as we have indicated above, collecting a sufficient number of photons with which to construct a histogram of photon arrival times from which a fluorescence lifetime may be extracted. We discussed[7] the utility of binning time channels in order to convert a sparse data set, whose histogram may bear a faint resemblance to an exponential decay, into a

histogram that may be fit with sufficient accuracy to an exponential decay with a well-resolved time constant. An example of binning is given in the inset of the 200-count data set of **Figure 3.1.** One difficulty presented by binning time channels, however, is that it reduces the dynamic range over which the data are fit and thus renders the accurate determination of a time constant--or several time constants in a heterogeneous system--problematic.

An alternative to RM exists, however, in recognizing that given a certain model for the fluorescence decay, there is a well-defined probability of detecting a certain number of photons in a given bin (or channel) of the histogram. The time constant for fluorescence decay can thus be extracted by comparing this probability distribution function with the number of photons in the set of bins. In this technique, it is advantageous to maximize the number of bins used to construct the histogram. This method of analysis is referred to as the Maximum Likelihood technique (ML).[8]

Here we present a detailed and systematic comparison of RM with ML using the very-well characterized dye, rose bengal in methanol, as our standard (**Figure 3.1.**). The excited state lifetime, τ, at 20°C in methanol is 530 ± 10 ps.[1] A more recent study gives 516 ps (with no error estimate).[9] The fluorescence decay of rose bengal is collected over a total of 1024 bins in a set of five experiments in which the total number of arrival times (counts) in all the bins is approximately 20, 200, 1000, 3000, and 6000, respectively. Each set of experiments was repeated 50 times in order to obtain appropriate statistics. Each of the 250 fluorescence decays was analyzed using both RM and ML.

Analyzing data via RM and ML methods has, of course, been previously discussed.[8,10-29] With a few exceptions,[19,20,22,26] these analyses were limited to simulated data. Our work has been stimulated by the efforts of Maus *et al.*[20], who provided a careful and detailed comparison of the RM (to which they refer as LS, "least squares") and ML methods using experimental data. Maus

et al. used Neyman[12,30,31] weighting in their RM analysis. They find that such weighting underestimates the mean lifetime. In addition, they find that ML effectively generates the correct lifetime down to about 1000 total counts, the lowest number of total counts that they considered. We have extended their analysis in two significant ways. In order to push the comparison between RM and ML as far as possible, our data sets were designed to be considerably sparser than those considered before, ranging from about 2 to 200 counts at the maximum of the respective fluorescence decays, whereas those of Maus *et al*. range from about 60 to 1300. We note that from 200 total counts and below, the data bear little or no resemblance to an exponential decay (**Figure 3.1.**); and this is precisely where one might expect the distinction between RM and ML to be most marked. We also employ two different methods of weighting residuals in RM, that of Neyman and that of Pearson.[12,30,31] Our results are consistent with those of Maus et al. in that we also observe that Neyman weighting, except in one instance, underestimates the target answer. We find, however, that at 1000 total counts and greater, Pearson weighting affords an acceptable answer. Furthermore, and most importantly, we too find that ML can be an effective analysis tool, but that its utility can be extended down to 200 total counts and even fewer. For example, at 20 total counts, the correct target lifetime is recovered with 20% error, which in some cases may be sufficiently accurate. Finally, we explicitly point out that the ML method (estimating the parameters that maximize the data likelihood under the assumed model) as it is traditionally and originally formulated[32] yields the exact same maximizers as the modified method introduced by Baker and Cousins[12] and employed by others,[19,20,22,25] which invokes a "likelihood ratio." Finally, we note for completeness that there are other methods of analysis[2,33-37], such as, for example, Bayesian[33,34], Laguerre expansion[35], and Laplace transform[2] analyses.

3.3 Materials and Methods

3.3.1 Experimental procedure

Rose bengal (Sigma) was purified by thin-layer chromatography using silica-gel plates and a solvent system of ethanol, chloroform, and ethyl acetate in a ratio of 25:15:30 by volume. Solvents were used without further purification. The R_f (retardation factor) value of the pure dye in this mixture was approximately 0.51. The purified dye was stored in methanol. Rose bengal absorbs in the region of 460-590 nm. Time-resolved data were collected using a home-made time-correlated, single-photon counting (TCSPC) instrument that employs a SPC-830 TCSPC module from Becker & Hickl GmbH. A Fianium pulsed laser (Fianium Ltd, Southampton, UK) operating at 570 nm and 2 MHz was used for the excitation of the sample. Emission was collected using a 590 nm long-pass filter. The instrumental response function was measured by collecting scattered light at 570 nm from the pure methanol solvent. The full-width at half-maximum of the instrument function was typically ~120 ps. Sparser data sets were obtained by attenuating the excitation laser beam with neutral density filters. The TCSPC data were collected in 1024 channels, providing a time resolution of 19.51 ps/channel, and a full-scale time window of 19.98 ns. Experiments were performed at 19.7 ± 0.2°C. Five different data sets consisting of 50 fluorescence decays were collected with total counts of approximately 20, 200, 1000, 3000, and 6000, respectively. The photon arrival times are used to build histograms comprised of 1024 bins (channels).

3.3.2 Data analysis

Modeling the time-correlated, single-photon counting data

Let t_j, j=1, 2,…, 1024 represent the center of the jth bin (or channel); and ϵ=19.51 ps, the time width of each bin in the histogram. Then, $t_1 = \epsilon/2$, $t_2 = t_1 + \epsilon$,... $t_j = t_1 + (j\text{-}1)\ \epsilon$,…, $t_{max} = t_{1024} = t_1 + 1023\epsilon$. Let $C(t)=\{c_1, c_2,\ldots, c_{1024}\}$ represent the set of counts obtained experimentally in all

1024 bins. Similarly, we can have $I(t)=\{ I_1, I_2,\ldots, I_{1024}\}$ as the set of counts for the experimentally measured IRF. We thus assume that the IRF consists of a series of 1024 delta pluses (δ-IRFs) having intensity $I_1, I_2,\ldots, I_{1024}$, respectively.

The probability that a photon is detected in the jth bin, p_j, is proportional to the convolution of the IRF and the model for the fluorescence decay.

$$p_j \propto \sum_{i=1}^{j-j_0} I_i e^{-\frac{t_{j-j_0}-t_i}{\tau}} \tag{3.1}$$

where, j_0 is given by $b = j_0\epsilon$. b is a linear shift between the instrument response function and the fluorescence decay. This shift parameter is necessary because the lower energy ("redder") fluorescence photons travel at a different speed through dispersive optics than the higher energy ("bluer") excitation photons that are used to generate the IRF in a scattering experiment.[1,38,39]

The probability that a photon is detected in the range $t_1 \leq t \leq t_{max} = t_{1024}$ must be $\sum_j p_j = 1$. We have, therefore:

$$p_j = \frac{\sum_{i=1}^{j-j_0} I_i e^{-\frac{t_{j-j_0}-t_i}{\tau}}}{\sum_{j=1}^{1024}\left(\sum_{i=1}^{j-j_0} I_i e^{-\frac{t_{j-j_0}-t_i}{\tau}}\right)} = \frac{\sum_{i=1}^{j-j_0} I_i e^{-\frac{t_{j-j_0}-t_i}{\tau}}}{\sum_{k=1}^{1024}\left(\sum_{i=1}^{k-j_0} I_i e^{-\frac{t_{k-j_0}-t_i}{\tau}}\right)} \tag{3.2}$$

The denominator acts as the normalization factor for the probability and it is independent of the index j. We can, therefore, change the dummy index, j, to another dummy index, k, for clarity, while retaining j_0, as this is a constant unknown shift applied for all bins. The denominator is proportional to the total convoluted counts generated from the IRF.

Let $\hat{c}_j$ represent the number of predicted counts from the single-exponential model in the jth bin, taking into account convolution. The number of predicted counts in a given bin is directly

proportional to the probability that a photon is detected in that bin: $\hat{c}_j \propto p_j$. Thus, the sequence $\{\hat{c}_1, \hat{c}_2, \ldots, \hat{c}_{1024}\}$ is the predicted data for a decay. The area under the decay curves obtained from the observed counts $C(t)$ and from the predicted counts $\hat{C}(t)$ must be conserved during optimization of the fitting parameters. In other words, the total number of predicted counts must be equal to the total number of observed photon counts. Therefore, the number of predicted counts in the jth bin is given by:

$$\hat{c}_j = C_T \frac{\sum_{i=1}^{j-j_0} I_i e^{-\frac{t_{j-j_0}-t_i}{\tau}}}{\sum_{k=1}^{1024}\left(\sum_{i=1}^{k-j_0} I_i e^{-\frac{t_{k-j_0}-t_i}{\tau}}\right)} \tag{3.3}$$

where $C_T = \sum_j c_j$.

Finally, we note that the shift parameter, b, need not be an integral multiple of ϵ. If we assume that b can take continuous values, then we can always find an integer, j_0, such that $b = j_0\epsilon + \zeta$, where ζ lies between 0 and ϵ, the time width of the bin. The probability, p_j, and predicted number of counts, $\hat{c}_j$, are thus given by:

$$p_j = \frac{\sum_{i=1}^{j-j_0-1} I_i e^{-\frac{t_j-t_i-b}{\tau}}}{\sum_{k=1}^{1024}\left(\sum_{i=1}^{k-j_0-1} I_i e^{-\frac{t_k-t_i-b}{\tau}}\right)} \quad ; \quad \hat{c}_j = C_T \frac{\sum_{i=1}^{j-j_0-1} I_i e^{-\frac{t_j-t_i-b}{\tau}}}{\sum_{k=1}^{1024}\left(\sum_{i=1}^{k-j_0-1} I_i e^{-\frac{t_k-t_i-b}{\tau}}\right)} \tag{3.4}$$

Residual minimization method (RM)

In this method, the sum of the squares of the residuals, as given in equation (3.5), is minimized over the parameters, τ and b, to obtain the optimal values.

$$S = \sum_{j=1}^{1024} (c_j - \hat{c}_j)^2 \tag{3.5}$$

It is well established that minimization of the weighted square of the residuals provides a better fit than minimization of the unweighted square of the residuals.[12,19,40] We, therefore, construct a weighted square of the residuals:

$$S_w = \sum_j w_j (c_j - \hat{c}_j)^2 \tag{3.6}$$

where w_j is the weighting factor. Depending on the choice of w_j, equation (3.6) often takes the form of the classical chi squared, for example :[12,16,19,20,25,30,31,40]

$$\chi_P^2 = \text{Pearson's}\chi^2 = \sum_{j=1}^{1024} (c_j - \hat{c}_j)^2 / \hat{c}_j \tag{3.7}$$

or,

$$\chi_N^2 = \text{Neyman's}\chi^2 = \sum_{j=1}^{1024} (c_j - \hat{c}_j)^2 / c_j \tag{3.8}$$

The reduced χ^2 is obtained by dividing by the number of degrees of freedom:

$$\chi_{red}^2 = \frac{1}{n-p} \chi^2 \tag{3.9}$$

where n is the number of data points; and p, the number of parameters and constraints in the model. For example, in our case we have 1024 data points, two parameters (τ and b), and one constraint, $C_T = \hat{C}_T$. This gives $n - p$ =1021. For an ideal case, χ_{red}^2 will be unity; and $\chi_{red}^2 < 1$ signifies overfitting the data. Therefore, the closer χ_{red}^2 is to unity (without being less than unity), the better the fit. The program is run so as to vary τ and b in such a manner as to minimize χ_{red}^2.

Maximum likelihood method (ML)

The total probability of having a sequence $\{c_1, c_2,\ldots, c_{1024}\}$ subject to the condition, $C_T = \sum_j c_j$, follows the multinomial distribution:

$$Pr(c_1, c_2, \ldots c_{1024}) = \frac{C_T!}{c_1! c_2! \ldots c_{1024}!} \prod_{j=1}^{1024} (p_j)^{c_j} = C_T! \prod_{j=1}^{1024} \frac{(p_j)^{c_j}}{c_j!} \tag{3.10}$$

We can define a likelihood function as the joint probability density function above: $\mathcal{L}(\hat{c}, c) = Pr(c_1, c_2, \cdots, c_{1024})$.

Substituting the expression for the probability using equation (3.4), we have:

$$\mathcal{L}(\hat{c}, c) = C_T! \prod_{j=1}^{1024} \frac{(\hat{c}_j / C_T)^{c_j}}{c_j!} \tag{3.11}$$

Following the treatment of Baker and Cousins,[12] we let $\{c'\}$ represent the true value of $\{c\}$ given by the model. A likelihood ratio, λ, can be defined as:

$$\lambda = \mathcal{L}(\hat{c}, c) / \mathcal{L}(c', c) \tag{3.12}$$

According to the likelihood ratio test theorem,[20,25,41,42] the "likelihood χ^2" is defined by

$$\chi^2_\lambda = -2 \ln \lambda \tag{3.13}$$

which obeys a chi-squared distribution as the sample size (or number of total counts) increases.

For the multinomial distribution, we may replace the unknown $\{c'\}$ by the experimentally observed {c}.[12] This gives:

$$\lambda = \left[C_T ! \prod_{j=1}^{1024} \frac{(\hat{c}_j / C_T)^{c_j}}{c_j !} \right] / \left[C_T ! \prod_{j=1}^{1024} \frac{(c_j / C_T)^{c_j}}{c_j !} \right] = \prod_{j=1}^{1024} \left(\frac{\hat{c}_j}{c_j} \right)^{c_j} \tag{3.14}$$

And the "likelihood χ^2" becomes:

$$\chi^2_\lambda = -2 \ln \lambda = -2 \ln \prod_{j=1}^{1024} \left(\frac{\hat{c}_j}{c_j} \right)^{c_j} = 2 \sum_{j=1}^{1024} c_j \ln \left(\frac{c_j}{\hat{c}_j} \right) \tag{3.15}$$

The minimization of the "likelihood χ^2," described in equation (3.15) , is thus performed to obtain the optimum values of τ and b.

It is important to stress that the form of the maximum likelihood method given in equation (3.10) is used widely by statisticians [32] and that equation (3.15), popularized by Baker and Cousins[12] and used in several instances to fit photon-counting data [19,20,22,25] is formally identical to it, as Baker and Cousins themselves point out. Namely, maximizing equation (3.10) is equivalent to minimizing equation (3.15). Specifically, from equation (3.10):

$$Pr(c_1, c_2, \ldots c_{1024}) = C_T ! \prod_{j=1}^{1024} \frac{(p_j)^{c_j}}{c_j !}$$

$$\ln Pr(c_1, c_2, \ldots c_{1024}) = const. + \sum_{j=1}^{1024} c_j \ln p_j = const. + \sum_{j=1}^{1024} c_j \ln \hat{c}_j$$

since, $p_j = \hat{c}_j / C_T$. The *const.* includes the terms involving only C_T or c_j, as they are experimentally observed numbers and independent of the parameters τ and b. From equation (3.15):

$$\chi^2_\lambda = 2 \sum_{j=1}^{1024} c_j \ln \left(\frac{c_j}{\hat{c}_j} \right) = 2 \sum_{j=1}^{1024} c_j \ln c_j - 2 \sum_{j=1}^{1024} c_j \ln \hat{c}_j = const. - 2 \sum_{j=1}^{1024} c_j \ln \hat{c}_j$$

Again the *const.* includes the terms which are independent of the parameters τ and *b*. equation (3.10) may be considered to be simpler in form than equation (3.15) and, for some models, may prove to be less computationally expensive as well.

For completeness, we mention the Bayesian analysis, which offers another approach in terms of a likelihood function. The Bayesian analysis starts with a prior distribution of the parameters in the appropriate range. The "posterior distribution" is calculated using the likelihood of the observed distribution for a given "prior distribution."[33,34] In the case of our model system, let $P(\tau,b)$ represent the prior distribution of the parameters. We can write the likelihood of having an observed distribution, $\{c\}=\{c_1, c_2,\ldots, c_{1024}\}$, subject to the prior distribution as $Pr(\{c\}|\ \tau,b)$. Therefore, the posterior distribution is given by:

$$P(\tau,b\,|\,\{c\}) = \frac{P(\tau,b)Pr(\{c\}\,|\,\tau,b)}{\int d\tau' db' P(\tau',b')Pr(\{c\}\,|\,\tau',b')} \qquad (3.16)$$

where the denominator is acting as the normalization factor. Maximization of the posterior distribution will furnish the desired value of the parameters. The results are often greatly affected by the choice of the prior distribution. Usually the prior distribution is chosen in such a way that the entropy of the distribution is maximized.

Computational tools

The RM and ML analyses described above are performed using codes written in MATLAB. We employ the GlobalSearch toolbox, which uses the "fmincon" solver. In each calculation, a global minimum was found. Finally, for comparison, the data were also analyzed with the proprietary SPCImage software v. 4.9.7 (SPCI), provided by Becker & Hickl GmbH. As this program is based upon a method of RM, it should, in principle, perform identically to our in-house code. In all the fitting comparisons to be discussed, there are only two variable parameters,

the lifetime (τ), and the shift parameter (b), see below. With our in-house routines, we experimented with different initial values of the lifetime and shift parameters, ranging from 0.3 to 0.7 ns and from -0.02 to 0.02 ns, respectively. In all cases, we retrieved the same fit results through the third decimal place.

3.4 Results and Discussion

Each of the 250 fluorescence decays for the five sets of data (taken with approximately 20, 200, 1000, 3000, and 6000 total counts) is analyzed by the four methods described above: ML; RM-Neyman; RM-Pearson; and the commercial SPCI. As noted, the ML results obtained from equation (3.10) and equation (3.15) are formally identical; and the fits obtained using the two equations yield the same results. **Figure 3.1.** presents a sample decay from each of the five data sets. **Figure 3.2(a)** provides a scatter plot of each lifetime obtained for each method of fitting. The horizontal red dashed line represents the value of a recently acquired lifetime of rose bengal in methanol at room temperature of 516 ps,[9] which we use as reference. Histograms of lifetimes obtained for the different fitting methods are presented in **Figures 3.2(b)-(f).** The mean (average) lifetime plus or minus one standard deviation, $< \tau > \pm \sigma$, obtained from the results are computed and summarized in **Table 3.1**.

The salient results are the following. Concerning the RM methods, we note that because the SPCI source code is not available, the details of the differences arising between it and our code cannot be determined. One noticeable and important difference between SPCI and our RM (**Table 3.1**) is that SPCI does not converge for the 20-total-counts data set. On the other hand, our RM-Neyman and RM-Pearson methods fit the data in all cases, but with varying degrees of success. Except for the case of 200 counts, RM-Neyman consistently underestimates the target value. For

200 counts, all RM methods overestimate the target value, and SPCI yields an aberrant result of 600 ± 700 ps. From 1000 counts onward, RM-Pearson provides results close to those of the target value and similar to those of SPCI. RM-Pearson appears to be more robust and reliable than either RM-Neyman or SPCI.

In contrast, at 20 counts, ML yields 500 ± 100 ps, which brackets the target result and which is to be compared with 320 ± 30 ps for RM-Neyman and with 460 ± 70 ps for RM-Pearson. For 200 total counts and greater, ML always provides an acceptable result with a standard deviation of less than 10% of the mean lifetime. The RM techniques achieve this level of precision only as of 1000 counts; and, as mentioned above, RM-Neyman generally underestimates the target value. Perhaps the most significant difference among the ML and the RM methods is that ML, within 2%, always produces the same mean lifetime, whereas this is not the case for RM, especially for total counts of 1000 and less.

In the Introduction, we commented on the careful comparison of the RM and ML methods by Maus *et al.*[20] and noted that our results presented here are not only consistent with theirs but also suggest that the ML method can be extended to considerably fewer counts than they explored in their study. We summarize some of the more important differences between our work and that of Maus *et al*.

1. Our data sets were designed to be considerably sparser than those considered before, ranging from about 2 to 200 counts *at the maximum* of the respective fluorescence decays, whereas those of Maus *et al*. range from about 60 to 1300. From 200 total counts and below, the data bear little or no resemblance to an exponential decay (**Figure 3.1.**); and this is precisely where one might expect the distinction between RM and ML to be the greatest—and the most useful.

2. Maus *et al.* use only 180 time channels (140 ps/channel) to study a molecule (hexaphenylbenzene-perylenemonoimide) whose lifetime is ~4500 ps, whereas we have used 1024 time channels (19.51 ps/channel) to study rose bengal, whose lifetime is ~530 ps. In other words, our experimental conditions (both the time window and the excited-state lifetime under consideration) are determined to distribute the data over as many time channels as possible in order to minimize the effects of time-binning, which we have discussed elsewhere[7] and to highlight instances where the differences between ML and RM might be the most pronounced.

3. There are some subtle but significant differences in the details of the fitting procedures. For example, we argue that it is necessary to conserve the total number of counts (which is proportional to the area under the fitted curve) during the optimization process. Maus *et al.*, however, permit the amplitude (our total counts) to vary for RM but keep it fixed for ML. Also, all of our fitting comparisons involve two variable parameters, the lifetime and the shift, τ and b. Maus *et al*. only have one variable parameter for ML, τ; but they employ two for RM, τ and the amplitude. We suggest that a close comparison between the methods should maintain as many similarities as possible.

In addition, we note that Köllner and Wolfrum[8] have discussed the use of ML. They suggested, based on simulations (some including 20% of a constant background), that one needs to have at least 185 photon counts in a time window of 8 ns with 256 time channels to measure a 2.5-ns lifetime with 10% variance without background.

3.5 Conclusions

We have performed a comparison of the maximum likelihood (ML) and residual minimization (RM) fitting methods by applying them to experimental data incorporating a

convoluted instrument function. While RM using Pearson's weighting of residuals can recover the correct mean result with a total number of counts of 1000 or more, ML distinguishes itself by yielding, in all cases, the same mean lifetime within 2% of the accepted value. For total counts of 200 and higher, ML always provides a standard deviation of less than 10% of the mean lifetime. Even at 20 total counts, ML provides a 20% error. The robustness of ML advocates its use for sparse data sets such as those acquired in some subdiffraction-limited microscopies, such as STED, and, more importantly, provides greater motivation for exploiting the time-resolved capacities of this technique to acquire and analyze fluorescence lifetime data.

3.6 Acknowledgments

We thank Mr. Ujjal Bhattacharjee for assistance in the early stages of this work. The work performed by K. Santra, E. A. Smith, and J. W. Petrich was supported by the U.S. Department of Energy, Office of Basic Energy Sciences, Division of Chemical Sciences, Geosciences, and Biosciences through the Ames Laboratory. The Ames Laboratory is operated for the U.S. Department of Energy by Iowa State University under Contract No. DE-AC02-07CH11358. X. Song was supported by The Division of Material Sciences and Engineering, Office of Basic Energy Sciences, U.S. Department of Energy, under Contact No. W-7405-430 ENG-82 with Iowa State University. The work of J. Zhan and N. Vaswani was partly supported by grant CCF-1117125 from the National Science Foundation.

3.7 References

1. Fleming, G. R. *Chemical Application of Ultrafast Spectroscopy* Oxford University Press: New York, 1986.

2. O'Connor, D. V.; Phillips, D. *Time Correlated Single Photon Counting* Academic Press Inc.: London, 1984.

3. Lakowicz, J. R. *Principles of Fluorescence Spectroscopy*, 3rd ed.; Springer: 2011.

4. Stringari, C.; Cinquin, A.; Cinquin, O.; Digman, M. A.; Donovan, P. J.; Gratton, E. Phasor Approach to Fluorescence Lifetime Microscopy Distinguishes Different Metabolic States of Germ Cells in a Live Tissue. *Proc. Natl. Acad. Sci. U. S. A.* **2011**, *108* (33), 13582-13587.

5. Colyer, R. A.; Lee, C.; Gratton, E. A Novel Fluorescence Lifetime Imaging System That Optimizes Photon Efficiency. *Microsc. Res. Techniq.* **2008**, *71* (3), 201-213.

6. Lesoine, M. D.; Bose, S.; Petrich, J. W.; Smith, E. A. Supercontinuum Stimulated Emission Depletion Fluorescence Lifetime Imaging. *J. Phys. Chem. B.* **2012**, *116* (27), 7821-7826.

7. Syed, A.; Lesoine, M. D.; Bhattacharjee, U.; Petrich, J. W.; Smith, E. A. The Number of Accumulated Photons and the Quality of Stimulated Emission Depletion Lifetime Images. *Photochem. Photobiol.* **2014**, *90* (4), 767-772.

8. Köllner, M.; Wolfrum, J. How Many Photons Are Necessary for Fluorescence-Lifetime Measurements? *Chem. Phys. Lett.* **1992**, *200* (1), 199-204.

9. Luchowski, R.; Szabelski, M.; Sarkar, P.; Apicella, E.; Midde, K.; Raut, S.; Borejdo, J.; Gryczynski, Z.; Gryczynski, I. Fluorescence Instrument Response Standards in Two-Photon Time-Resolved Spectroscopy. *Appl. Spectrosc.* **2010**, *64* (8), 918-922.

10. Ankjærgaard, C.; Jain, M.; Hansen, P. C.; Nielsen, H. B. Towards Multi-Exponential Analysis in Optically Stimulated Luminescence. *J. Phys. D: Appl. Phys.* **2010**, *43* (19), 195501.

11. Bajzer, Ž.; Therneau, T. M.; Sharp, J. C.; Prendergast, F. G. Maximum Likelihood Method for the Analysis of Time-Resolved Fluorescence Decay Curves. *Eur. Biophys. J.* **1991**, *20* (5), 247-262.

12. Baker, S.; Cousins, R. D. Clarification of the Use of Chi-Square and Likelihood Functions in Fits to Histograms. *Nucl. Instr. Meth. Phys. Res.* **1984**, *221* (2), 437-442.

13. Bevington, P.; Robinson, D. K. *Data Reduction and Error Analysis for the Physical Sciences*, 3rd ed.; McGraw-Hill: New York, 2002.

14. Grinvald, A.; Steinberg, I. Z. On the Analysis of Fluorescence Decay Kinetics by the Method of Least-Squares. *Anal. Biochem.* **1974**, *59* (2), 583-598.

15. Hall, P.; Selinger, B. Better Estimates of Exponential Decay Parameters. *J. Phys. Chem.* **1981**, *85* (20), 2941-2946.

16. Hauschild, T.; Jentschel, M. Comparison of Maximum Likelihood Estimation and Chi-Square Statistics Applied to Counting Experiments. *Nucl. Instr. Meth. Phys. Res. A.* **2001**, *457* (1), 384-401.

17. Hinde, A. L.; Selinger, B.; Nott, P. On the Reliability of Fluorescence Decay Data. *Aust. J. Chem.* **1977**, *30* (11), 2383-2394.

18. Kim, G.-H.; Legresley, S. E.; Snyder, N.; Aubry, P. D.; Antonik, M. Single-Molecule Analysis and Lifetime Estimates of Heterogeneous Low-Count-Rate Time-Correlated Fluorescence Data. *Appl. Spectrosc.* **2011**, *65* (9), 981-990.

19. Laurence, T. A.; Chromy, B. A. Efficient Maximum Likelihood Estimator Fitting of Histograms. *Nat. Methods*. **2010**, *7* (5), 338-339.

20. Maus, M.; Cotlet, M.; Hofkens, J.; Gensch, T.; De Schryver, F. C.; Schaffer, J.; Seidel, C. An Experimental Comparison of the Maximum Likelihood Estimation and Nonlinear Least-Squares Fluorescence Lifetime Analysis of Single Molecules. *Anal. Chem.* **2001**, *73* (9), 2078-2086.

21. Moore, C.; Chan, S. P.; Demas, J.; DeGraff, B. Comparison of Methods for Rapid Evaluation of Lifetimes of Exponential Decays. *Appl. Spectrosc.* **2004**, *58* (5), 603-607.

22. Nishimura, G.; Tamura, M. Artefacts in the Analysis of Temporal Response Functions Measured by Photon Counting. *Phys. Med. Biol.* **2005**, *50* (6), 1327.

23. Periasamy, N. Analysis of Fluorescence Decay by the Nonlinear Least Squares Method. *Biophys. J.* **1988**, *54* (5), 961-967.

24. Sharman, K. K.; Periasamy, A.; Ashworth, H.; Demas, J. Error Analysis of the Rapid Lifetime Determination Method for Double-Exponential Decays and New Windowing Schemes. *Anal. Chem.* **1999**, *71* (5), 947-952.

25. Turton, D. A.; Reid, G. D.; Beddard, G. S. Accurate Analysis of Fluorescence Decays from Single Molecules in Photon Counting Experiments. *Anal. Chem.* **2003**, *75* (16), 4182-4187.

26. Tellinghuisen, J.; Goodwin, P. M.; Ambrose, W. P.; Martin, J. C.; Keller, R. A. Analysis of Fluorescence Lifetime Data for Single Rhodamine Molecules in Flowing Sample Streams. *Anal. Chem.* **1994**, *66* (1), 64-72.

27. Enderlein, J.; Köllner, M. Comparison between Time-Correlated Single Photon Counting and Fluorescence Correlation Spectroscopy in Single Molecule Identification. *Bioimaging.* **1998**, *6* (1), 3-13.

28. Bialkowski, S. E. Data Analysis in the Shot Noise Limit. 1. Single Parameter Estimation with Poisson and Normal Probability Density Functions. *Anal. Chem.* **1989**, *61* (22), 2479-2483.

29. Bialkowski, S. E. Data Analysis in the Shot Noise Limit. 2. Methods for Data Regression. *Anal. Chem.* **1989**, *61* (22), 2483-2489.

30. Neyman, J.; Pearson, E. S. On the Use and Interpretation of Certain Test Criteria for Purposes of Statistical Inference: Part I. *Biometrika.* **1928**, *20A* (1/2), 175-240.

31. Neyman, J.; Pearson, E. S. On the Use and Interpretation of Certain Test Criteria for Purposes of Statistical Inference: Part II. *Biometrika.* **1928**, *20A* (3/4), 263-294.

32. Poor, H. V. An Introduction to Signal Detection and Estimation, 2nd ed.; Springer: 1994.

33. Barber, P.; Ameer-Beg, S.; Pathmananthan, S.; Rowley, M.; Coolen, A. A Bayesian Method for Single Molecule, Fluorescence Burst Analysis. *Biomed. Opt. Express.* **2010**, *1* (4), 1148-1158.

34. Rowley, M. I.; Barber, P. R.; Coolen, A. C.; Vojnovic, B. Bayesian Analysis of Fluorescence Lifetime Imaging Data. *SPIE BiOS* International Society for Optics and Photonics: 2011, 790325-790325-790312.

35. Jo, J. A.; Fang, Q.; Marcu, L. Ultrafast Method for the Analysis of Fluorescence Lifetime Imaging Microscopy Data Based on the Laguerre Expansion Technique. *IEEE J. Sel. Top. Quantum Electron.* **2005**, *11* (4), 835-845.

36. Večeř, J.; Kowalczyk, A.; Davenport, L.; Dale, R. Reconvolution Analysis in Time-Resolved Fluorescence Experiments--an Alternative Approach: Reference-to-Excitation-to-Fluorescence Reconvolution. *Rev. Sci. Instrum.* **1993**, *64* 3413-3424.

37. Istratov, A. A.; Vyvenko, O. F. Exponential Analysis in Physical Phenomena. *Rev. Sci. Instrum.* **1999**, *70* (2), 1233-1257.

38. Calligaris, F.; Ciuti, P.; Gabrielli, I.; Giamcomich, R.; Mosetti, R. Wavelength Dependence of Timing Properties of the Xp 2020 Photomultiplier. *Nucl. Instr. Meth.* **1978**, *157* (3), 611-613.

39. Sipp, B.; Miehe, J.; Lopez-Delgado, R. Wavelength Dependence of the Time Resolution of High-Speed Photomultipliers Used in Single-Photon Timing Experiments. *Opt. Commun.* **1976**, *16* (1), 202-204.

40. Jading, Y.; Riisager, K. Systematic Errors in X 2-Fitting of Poisson Distributions. *Nucl. Instr. Meth. Phys. Res. A.* **1996**, *372* (1), 289-292.

41. Wilks, S. The Likelihood Test of Independence in Contingency Tables. *Ann. Math. Stat.* **1935**, *6* (4), 190-196.

42. Wilks, S. S. The Large-Sample Distribution of the Likelihood Ratio for Testing Composite Hypotheses. *Ann. Math. Stat.* **1938**, *9* (1), 60-62.

3.8 Tables and Figures

Table 3.1.
Mean lifetime ± One Standard Deviation (ps) Associated with Each Method of Analysis ML, maximum likelihood method; RM-Neyman, residual minimization method weighting the residuals by $1/c_j$, where c_j is the number of counts in a channel (equation (3.8)); RM- Pearson, residual minimization method weighting the residuals by $1/\hat{c}_j$, where $\hat{c}_j$ is the predicted number of counts in a channel (equation (3.7)); SPCI, commercially supplied residual minimization software.

Total counts	ML	RM		SPCI
		Neyman	Pearson	
20	500 ± 100	320 ± 30	460 ± 70	
200	510 ± 40	690 ± 20	600 ± 50	600 ± 700
1000	510 ± 20	490 ± 30	560 ± 20	520 ± 30
3000	510 ± 10	480 ± 20	540 ± 10	520 ± 20
6000	501 ± 8	480 ± 10	520 ± 20	520 ± 10

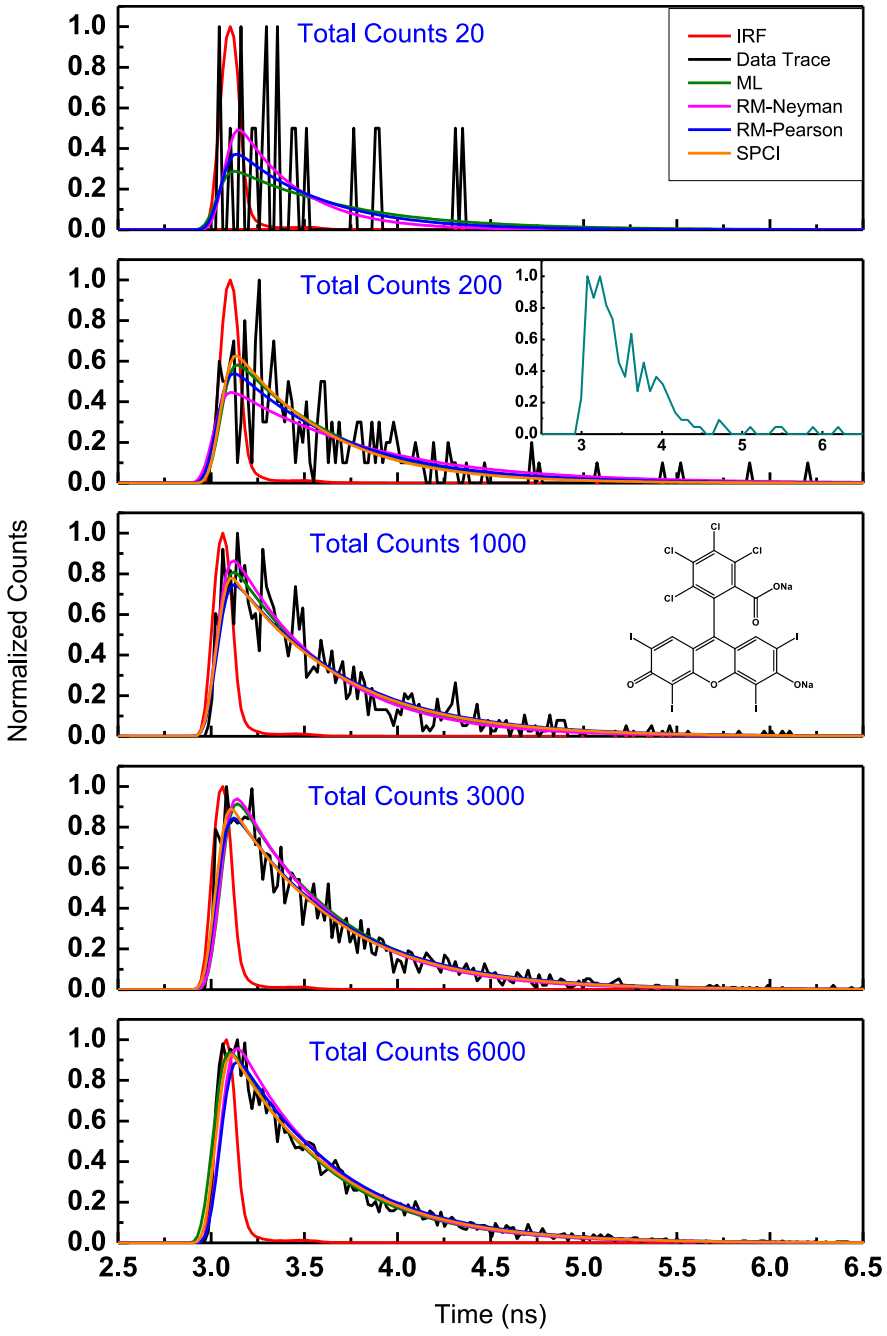

Figure 3.1. A representative histogram for a given number of total counts is presented. Each panel gives the raw data (black), the instrument response function (IRF, red), the ML fit (green), the RM-Neyman fit (magenta), the RM-Pearson fit (blue), and the SPCI fit (orange). The inset in the 200-count panel gives the result of binning four contiguous time channels, reducing the number from 1024 to 256. The inset in the 1000-count panel presents the structure of the sodium salt of rose bengal.

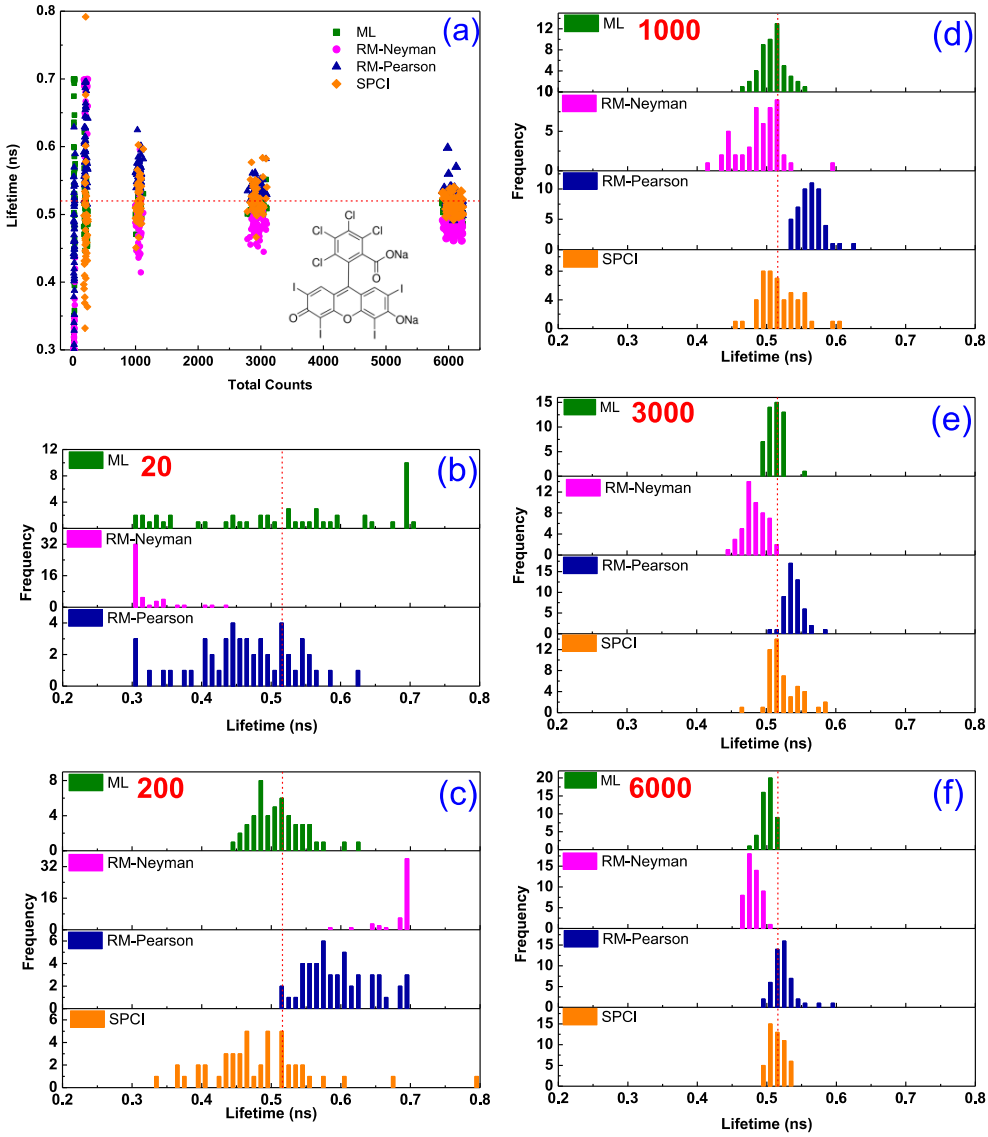

Figure 3.2. Estimated lifetime of rose bengal by ML (green), RM-Neyman (magenta), RM-Pearson (blue) and SPCI (orange). (a) The scatter plot of the lifetime with respect to the total counts in a decay. (b)-(f) Histograms of the lifetimes obtained by the above four methods for total counts of 20, 200, 1000, 3000, and 6000 respectively. The bins for all of the histograms are 10 ps wide. The red dashed lines give, as a benchmark, a recent value of $\tau = 516$ ps.[9]

CHAPTER 4. PHOTON COUNTING DATA ANALYSIS: APPLICATION OF THE MAXIMUM LIKELIHOOD AND RELATED METHODS FOR THE DETERMINATION OF LIFETIMES IN MIXTURES OF ROSE BENGAL AND RHODAMINE B

A paper published in the *Journal of Physical Chemistry A*

Kalyan Santra, Emily A. Smith, Jacob W. Petrich, and Xueyu Song*

4.1 Abstract

It is often convenient to know the minimum amount of data needed in order to obtain a result of desired accuracy and precision. It is a necessity in the case of subdiffraction-limited microscopies, such as stimulated emission depletion (STED) microscopy, owing to the limited sample volumes and the extreme sensitivity of the samples to photobleaching and photodamage. We present a detailed comparison of probability-based techniques (the maximum likelihood method and methods based on the binomial and the Poisson distributions) with residual minimization-based techniques for retrieving the fluorescence decay parameters for various two-fluorophore mixtures, as a function of the total number of photon counts, in time-correlated, single-

---

*To whom correspondence should be addressed. Email: xsong@iastate.edu

Department of Chemistry, Iowa State University, Ames, Iowa 50011, USA

U. S. Department of Energy, Ames Laboratory, Ames, Iowa 50011, USA

photon counting experiments. The probability-based techniques proved to be the most robust (insensitive to initial values) in retrieving the target parameters and, in fact, performed equivalently to 2-3 significant figures. This is to be expected, as we demonstrate that the three methods are fundamentally related. Furthermore, methods based on the Poisson and binomial distributions have the desirable feature of providing a bin-by-bin analysis of a single fluorescence decay trace, which thus permits statistics to be acquired using only the one trace for not only the mean and median values of the fluorescence decay parameters but also for the associated standard deviations. These probability-based methods lend themselves well to the analysis of the sparse data sets that are encountered in subdiffraction-limited microscopies.

4.2 Introduction

Time-resolved spectroscopic techniques have a wide range of applications in the physical and biological sciences. Owing to, for example, its ease of use, high sensitivity, large dynamic range, applicability to imaging and subdiffraction-limited microscopies, one of the most widely used techniques is time-correlated, single-photon counting (TCSPC).[1,2] A major challenge in analyzing the data obtained in these experiments arises from sparse data sets, such as those that may often be encountered in super-resolution microscopies, such as stimulated emission depletion (STED) microscopy.[3-6] Typically, in a TCSPC experiment, a fluorescence lifetime is determined by acquiring a histogram of arrival time differences between an excitation pulse and the pulse resulting from a detected photon. As we have noted, [3,4] when a histogram of sufficient quality cannot be obtained to provide a good fit by means of minimizing the residuals (RM) between the experimental data and a given functional form, the maximum likelihood (ML) technique is particularly effective, namely when the total number of counts is very low.[3] As we have shown in

the case of rose bengal, ML retrieved the correct mean lifetime to within 2% of the accepted value with total counts as low as 20; and it retrieved the correct mean lifetime with less than 10% standard deviation with total counts as low as 200.

There are several comparisons of the ML and RM techniques,[7-27] but most of them have been limited to simulated data. In those cases where the techniques were applied to real experimental data, the comparisons were limited by several factors such as the exclusion of a real instrument response function (IRF), the bin size for the time channels of the histogram, the exclusion of a shift parameter that accounts for the wavelength difference between the instrument response function and the fluorescence signal, and, most importantly, by not determining the minimum number of counts at which the respective techniques provide an acceptable result. In our recent work,[3] we addressed all of these issues for a single fluorophore, rose bengal. Here, we extend these efforts by studying mixtures of fluorophores, which is more relevant to the type of data that can be extracted from a STED experiment capable of extracting fluorescence lifetimes.[6] In such experiments, heterogeneity in the lifetimes of the emitting fluorophores is expected; and such heterogeneity can provide insight into the processes being probed in the subdiffraction-limited spot under interrogation. To this end, we examined mixtures of the well-characterized dyes, rose bengal (Rb) and rhodamine B (RhB), in methanol. The excited-state lifetime, τ, of Rb is 0.49 ± 0.01 ns.[3] Some reported values are 0.53 ± 0.01 ns[1] and 0.512 ns,[28] with no error estimate. We have measured the excited-state lifetime of RhB to be 2.45 ± 0.01 ns. Reported values are 2.42 ± 0.08 ns,[29] 2.3 ns,[30] and 2.6 ns[31] in methanol at room temperature. We studied five different sets of mixtures with varying compositions. The fluorescence decays were collected over a total of 1024 bins (channels). The fluorescence decay of each of the five sets of mixtures

was collected fifty times, with a total number of counts of 20, 100, 200, 500, 1000, 3000, 6000, 10000, and 20000. Thus, a total of 2250 fluorescence decay profiles were analyzed.

We furthermore examined the performance and utility of other methods related to ML. For example, though analysis of fifty decays gives sufficient statistics to retrieve the two lifetime and amplitude components of the fluorescence decay using the ML method (or the RM method under certain conditions), in a subdiffraction-limited imaging experiment it is usually not practical to perform multiple measurements of the same sample. These other methods are related to ML in that they are based on the binomial and Poisson distributions and have the interesting and useful properties of yielding statistics from only one measurement of the fluorescence decay. In particular, since we know that there is a well-defined probability that a certain number of photons will be accumulated in a given bin of the histogram, we can apply a Poisson distribution or a binomial distribution to the random arrival of photons to estimate the decay constant of the sample by analyzing only one bin. Therefore, photon counts in each bin will furnish a decay constant corresponding the position of the bin. We, thus, demonstrate the ability to analyze a single experimental fluorescence decay within a given range of accuracy while at the same time providing statistics.

4.3 Materials and Methods

4.3.1 Experimental procedure

Rose bengal (Rb) and rhodamine B (RhB) were obtained from Sigma and Eastman, respectively, and were purified by thin-layer chromatography using silica-gel plates and a solvent system of ethanol, chloroform, and ethyl acetate in a ratio of 25:15:30 by volume. Solvents were used without further purification. The purified dyes were stored in methanol in the dark. Rb

absorbs in the region 460-590 nm; RhB, 440-590 nm. 550 nm was thus selected as the excitation wavelength. Five sets of samples were prepared so that they had an absorption ratio of Rb:RhB at 550 nm of: 100:0; 75:25; 50:50; 25:75; and 0:100 respectively. The net absorbance of each of the five solutions was kept near 0.3 (**Figure 4.1a**). Time-resolved data were collected using a home-made, time-correlated, single-photon counting (TCSPC) instrument using a SPC-630 TCSPC module (Becker & Hickl GmbH). A collimated Fianium pulsed laser (Fianium Ltd, Southampton, UK) at a 2 MHz repetition rate, was used to excite the sample at 550 nm. The excitation beam was vertically polarized. Emission was detected at the "magic angle" (54.7°) with respect to the excitation using a 590-nm, long-pass filter (**Figure 4.1b**). The instrument response function (IRF) was measured by collecting scattered light at 550 nm (without the emission filter) from the pure methanol solvent. The full-width at half-maximum of the instrument function was typically ~120 ps. The TCSPC data were collected in 1024 channels (bins), providing a time resolution of 19.51 ps/channel, and a full-scale time window of 19.98 ns. Nine different data sets consisting of 50 fluorescence decays were collected with a total number of counts of approximately 20, 100, 200, 500, 1000, 3000, 6000, 10000, and 20000, respectively.

4.3.2 Data analysis

Modeling the time-correlated, single-photon counting data

When there is more than one emitting species, a multi-exponential model can be applied:

$$F(t_j) = \sum_n a_n e^{-(\frac{t_j}{\tau_n})} . \qquad (4.1)$$

where $\sum a_n = 1$; and a_n are the fractions of the *n*th species in the sample mixture. In the case of the two-component system of Rb and RhB:

$$F(t_j) = a_1 e^{-(\frac{t_j}{\tau_1})} + (1-a_1) e^{-(\frac{t_j}{\tau_2})} \tag{4.2}$$

where τ_1 and τ_2 are the lifetimes of the two species, and a_1 is the fraction of the species with lifetime τ_1.

Let $\boldsymbol{t} = \{t_1, t_2, \ldots, t_{1024}\}$ represent the time axis, where the center of the *j*th bin (or channel) is given by t_j; and $\epsilon = 19.51$ ps is the time width of each bin in the histogram. Let $\boldsymbol{C} = \{c_1, c_2, \ldots, c_{1024}\}$ be the set of counts obtained in the 1024 bins. Similarly, we experimentally measure the instrument response function (IRF) and represent it as $\boldsymbol{I} = \{I_1, I_2, \ldots, I_{1024}\}$, where the I_j are the number of counts in the *j*th bin.

The probability that a photon is detected in the *j*th bin, p_j, is proportional to the discrete convolution of the IRF and the model for the fluorescence decay given in equation (4.2).

$$p_j \propto \sum_{i=1}^{j-j_0} I_i F(t_{j-j_0} - t_i) = \sum_{i=1}^{j-j_0} I_i \left(a_1 e^{-(\frac{t_{j-j_0}-t_i}{\tau_1})} + (1-a_1) e^{-(\frac{t_{j-j_0}-t_i}{\tau_2})} \right) \tag{4.3}$$

where, j_0 is given by $b = j_0 \epsilon$. The parameter *b* describes the linear shift between the instrument response function and the fluorescence decay.[1,3,32,33] The probability that a photon is detected in the range $t_1 \leq t \leq t_{max} = t_{1024}$ must be $\sum_j p_j = 1$. We have, therefore:

$$p_j = \frac{\sum_{i=1}^{j-j_0} I_i \left(a_1 e^{-(\frac{t_{j-j_0}-t_i}{\tau_1})} + (1-a_1) e^{-(\frac{t_{j-j_0}-t_i}{\tau_2})} \right)}{\sum_{k=1}^{1024} \left(\sum_{i=1}^{k-j_0} I_i \left(a_1 e^{-(\frac{t_{k-j_0}-t_i}{\tau_1})} + (1-a_1) e^{-(\frac{t_{k-j_0}-t_i}{\tau_2})} \right) \right)} \tag{4.4}$$

The normalization factor in the denominator is independent of the index, *j*; and, hence, the "dummy index," *k*, is inserted while retaining j_0, as this constant, unknown shift applies for all bins. The denominator is proportional to the total number of convoluted counts generated with the IRF.

Let $\hat{c}_j$ represent the number of predicted counts from the multi-exponential model in the *j*th bin, taking into account convolution. The number of predicted counts in a given bin is directly proportional to the probability that a photon is detected in that bin: $\hat{c}_j \propto p_j$. Thus, we can write the predicted counts as $\widehat{\boldsymbol{C}} = \{\hat{c}_1, \hat{c}_2, \ldots, \hat{c}_{1024}\}$. The area under the decay curves obtained from the observed counts $\boldsymbol{C}$ and from the predicted counts $\widehat{\boldsymbol{C}}$ must be conserved during optimization of the fitting parameters. In other words, the total number of predicted counts must be equal to the total number of observed photon counts. The number, therefore, of predicted counts in the *j*th bin is given by:

$$\hat{c}_j = C_T \frac{\sum_{i=1}^{j-j_0-1} I_i \left(a_1 e^{-\left(\frac{t_j - t_i - b}{\tau_1}\right)} + (1-a_1) e^{-\left(\frac{t_j - t_i - b}{\tau_2}\right)} \right)}{\sum_{k=1}^{1024} \left(\sum_{i=1}^{k-j_0-1} I_i \left(a_1 e^{-\left(\frac{t_k - t_i - b}{\tau_1}\right)} + (1-a_1) e^{-\left(\frac{t_k - t_i - b}{\tau_2}\right)} \right) \right)} \tag{4.5}$$

where $C_T = \sum_j c_j$. It should be noted that in the above equation we allowed the shift parameter, *b*, to assume continuous values. Therefore, we always find an integer, j_0, such that $b = j_0\epsilon + \zeta$, where ζ lies between 0 and ϵ, the time width of the bin. In the case of a single-exponential model, the expressions for the probability, p_j, and the predicted number of counts, $\hat{c}_j$ are obtained by substituting $a_1 = 1$:

$$p_j = \frac{\sum_{i=1}^{j-j_0-1} I_i e^{-\left(\frac{t_j - t_i - b}{\tau_1}\right)}}{\sum_{k=1}^{1024} \left(\sum_{i=1}^{k-j_0-1} I_i e^{-\left(\frac{t_k - t_i - b}{\tau_1}\right)} \right)} \quad ; \quad \hat{c}_j = C_T \frac{\sum_{i=1}^{j-j_0-1} I_i e^{-\left(\frac{t_j - t_i - b}{\tau_1}\right)}}{\sum_{k=1}^{1024} \left(\sum_{i=1}^{k-j_0-1} I_i e^{-\left(\frac{t_k - t_i - b}{\tau_1}\right)} \right)}. \tag{4.6}$$

Residual minimization method (RM)

The traditional method of RM uses the sum of the square of the differences (residuals) between the experimentally obtained counts and the predicted counts to optimize the fit. It is also well known[9,20,34] that minimization of the weighted square of the residuals provides a better fit than does the unweighted square of the residuals. We, therefore, used the sum of the weighted squares of the residuals and minimized it over the parameters, τ_1, τ_2, a_1 and b, to obtain the optimal values:

$$S_w = \sum_j w_j (c_j - \hat{c}_j)^2 \tag{4.7}$$

where w_j is the weighting factor. Depending on the choice of w_j, equation (3.6) can take the following forms of the classical chi-squared (χ^2), for example:[9,16,20,21,27,34-36]

$$\chi_P^2 = \text{Pearson's}\chi^2 = \sum_{j=1}^{1024} (c_j - \hat{c}_j)^2 / \hat{c}_j \tag{4.8}$$

or,

$$\chi_N^2 = \text{Neyman's}\chi^2 = \sum_{j=1}^{1024} (c_j - \hat{c}_j)^2 / c_j \tag{4.9}$$

The reduced χ^2 is obtained by dividing by the number of degrees of freedom:

$$\chi_{red}^2 = \frac{1}{n-p}\chi^2 \tag{4.10}$$

where n is the number of data points; and p, the number of parameters and constraints in the model. For example, in our case we have 1024 data points, two or four parameters (τ_1, b or τ_1, τ_2, a_1, b) depending on whether one or two exponentials are used to describe the decay, and one constraint,

$C_T = \hat{C}_T$. This gives $n - p$ = 1021 or 1019, respectively. For an ideal case, χ^2_{red} is unity. $\chi^2_{red} <$ 1 implies overfitting of the data. Therefore, the closer χ^2_{red} is to unity (without being less than unity), the better the fit. The minimization program is run over the parameters to minimize χ^2_{red}.

Binomial distribution

In a time-correlated, single-photon counting experiment, the random events are independent of each other; and each pulse, by experimental design, can only give one photon in any of the 1024 bins. The next photon is detected in a completely different cycle that depends on an identical but different pulse. It can, therefore, be concluded that the successive detection of a photon in any particular bin is independent of the detection of any other photon.

The probability distribution of *discrete events*, such as occurring in the TCSPC experiment, can be described by several well-known probability distributions. The binomial probability distribution is one example where the probability distribution of the number of successes is described for a series of independent experiments. In each experiment, the probability of success or failure is identical.[37] (This is also known as a Bernoulli trial).

Let the probability that a photon is detected (success) in the *j*th bin be p_j. Depending on whether the fluorescence decay is described by two or one decaying exponentials, the expression for p_j is given by either equation (4.4) or equation (4.6). The probability that the photon is not detected (failure) in the *j*th bin is given by $q_j = 1 - p_j$. Let c_j be the number of photons that is accumulated in *j*th bin in an experiment, where the total number of counts is C_T. The binomial probability function is thus given by:

$$P_j^{binom}(c_j \mid C_T) = \binom{C_T}{c_j} p_j^{c_j} q_j^{C_T - c_j} = \binom{C_T}{c_j} p_j^{c_j} \left(1 - p_j\right)^{C_T - c_j}, \qquad (4.11)$$

where the factor on the right in the curved bracket is the binomial coefficient. It is important to note that the binomial probability is independent of all indices except *j* and that, therefore, the distribution of the number of photons over all the other channels, $(C_T - c_j)$, which do not accumulate in the *j*th bin, does not affect the binomial probability. This independent but identical binomial probability can be maximized with respect to the parameters (τ_1, b *or* τ_1, τ_2, a_1, b), depending on the model used to describe the fluorescence decay. This procedure thus generates a lifetime value for every channel for one fluorescence decay experiment, from which a histogram of lifetime values can be obtained. From this histogram, the mean and standard deviation of the lifetime parameters can be extracted. Furthermore, we can construct a joint probability distribution to obtain a best possible value of the lifetime corresponding to a single decay curve. The joint probability is given by:

$$P^{binom}(c_1, c_2, ..., c_{1024}) = \prod_{j=1}^{1024} \binom{C_T}{c_j} p_j^{c_j} \left(1 - p_j\right)^{C_T - c_j} \tag{4.12}$$

Maximization of the probability P^{binom} can be performed over the parameters used to describe the fluorescence decay function.

Poisson distribution

Another well-known probability distribution that describes the occurrence of discrete events is the Poisson distribution.[37] The Poisson distribution gives the probability of the occurrence of a certain number of events for a given average number of events in that time interval. The Poisson distribution can be applied if the successive occurrences of the events are independent of each other and the numbers of occurrences are integers. (For our case, we are not interested in the number of events that do not occur). Since successive photon counts are independent and since a photon count in a bin is an integer, the time-correlated, single-photon counting experiment

conforms to the criteria necessary for its being able to be described by a Poisson distribution. Whereas the binomial distribution incorporates the probability that a photon is accumulated (success) or not accumulated (failure) in a given bin directly, the Poisson distribution requires the average number of photons that accumulates is a certain bin in order to estimate the probability of having a certain number of photons in a given bin in the same time interval. The Poisson distribution is an approximation of the binomial distribution in the limit where the number of trials is relatively large and (or) the probability of success of each trial is very small (which is the case in all of our experiments).[37]

In order for the Poisson distribution to be applied, one must know beforehand that the fluorescence decay is indeed an exponential (or sum of exponentials) because the Poisson distribution employs the mean or the average number of counts in a bin. For example, consider a given decay, where we have a number, C_T , of photons collected over a time window, *T*. Now, to estimate the average number of photons in a bin within that time window, *T*, we can simply use the multiexponential function, even though the true nature of the probability distribution of the emission may not be known owing to collection of only a small number of photons, because we require only the average number of predicted counts.

Let us assume that we continue collecting the fluorescence decay until it becomes smooth enough to be fit with the usual residual minimization methods. A full decay will have 65535 photons in the peak channel (a 16-bit memory sets the limit of the number of counts to 2^{16}-1 in a channel). If this process takes a time period of $T_m = mT$, then the total number of photons is C_{T_m}. If the rate of the data acquisition remains constant within the time period, then we have $C_{T_m} = mC_T$. Now we can apply the multiexponential model to estimate the average number of predicated counts in a bin:

$$\hat{c}_{jm} = C_{Tm} \frac{\sum_{i=1}^{j-j_0-1} I_i \left(a_1 e^{-(\frac{t_j - t_i - b}{\tau_1})} + (1-a_1) e^{-(\frac{t_j - t_i - b}{\tau_2})} \right)}{\sum_{k=1}^{1024} \left(\sum_{i=1}^{k-j_0-1} I_i \left(a_1 e^{-(\frac{t_k - t_i - b}{\tau_1})} + (1-a_1) e^{-(\frac{t_k - t_i - b}{\tau_2})} \right) \right)} = C_{T_m} p_j \,. \tag{4.13}$$

The average number of counts in the time period T is given by:

$$\begin{aligned} \hat{c}_j = \frac{T}{T_m} \hat{c}_{jm} &= \frac{T}{T_m} C_{Tm} \frac{\sum_{i=1}^{j-j_0-1} I_i \left(a_1 e^{-(\frac{t_j - t_i - b}{\tau_1})} + (1-a_1) e^{-(\frac{t_j - t_i - b}{\tau_2})} \right)}{\sum_{k=1}^{1024} \left(\sum_{i=1}^{k-j_0-1} I_i \left(a_1 e^{-(\frac{t_k - t_i - b}{\tau_1})} + (1-a_1) e^{-(\frac{t_k - t_i - b}{\tau_2})} \right) \right)} \\ &= C_T \frac{\sum_{i=1}^{j-j_0-1} I_i \left(a_1 e^{-(\frac{t_j - t_i - b}{\tau_1})} + (1-a_1) e^{-(\frac{t_j - t_i - b}{\tau_2})} \right)}{\sum_{k=1}^{1024} \left(\sum_{i=1}^{k-j_0-1} I_i \left(a_1 e^{-(\frac{t_k - t_i - b}{\tau_1})} + (1-a_1) e^{-(\frac{t_k - t_i - b}{\tau_2})} \right) \right)} \end{aligned} \tag{4.14}$$

Now, the Poisson distribution is given by:

$$p_j(c_j \text{ number of success}) = \frac{\lambda_j^{c_j} e^{-\lambda_j}}{c_j!} \tag{4.15}$$

where λ_j is the average number of success at jth bin in the same time interval and is given by $\lambda_j = \hat{c}_j$. The important point here is that given the above, we can conclude that each bin follows an identical and independent Poisson distribution and that we can maximize the probability of having a number, c_j, of "successes" to obtain the estimated lifetime of the sample at the corresponding time bin. We can define the joint probability distribution of a sequence of counts in a single decay in the same manner as we defined it in the case of the binomial distribution.

$$P(c_1, c_2, ..., c_{1024}) = \prod_{j=1}^{1024} \frac{\lambda_j{}^{c_j} e^{-\lambda_j}}{c_j!} \tag{4.16}$$

Maximization of the probability *P* can be performed over the parameters, τ_1, τ_2, a_1, and *b*.

Maximum likelihood method (ML)

Another approach to describe the joint probability distribution is to express it in terms of a multinomial form and to apply the maximum likelihood technique on the resulting distribution function. The total probability of having a sequence $\{c_1, c_2, \ldots, c_{1024}\}$ subject to the condition, $C_T = \sum_j c_j$, follows the multinomial distribution:

$$Pr(c_1, c_2, \ldots c_{1024}) = \frac{C_T!}{c_1! c_2! \ldots c_{1024}!} \prod_{j=1}^{1024} (p_j)^{c_j} = C_T! \prod_{j=1}^{1024} \frac{(p_j)^{c_j}}{c_j!} \tag{4.17}$$

We can define a likelihood function as the joint probability density function above: $L(\hat{c}, c) = Pr(c_1, c_2, \cdots, c_{1024})$. We substitute the expression for the probability as $p_j = \hat{c}_j / C_T$ to obtain:

$$L(\hat{c}, c) = C_T! \prod_{j=1}^{1024} \frac{(\hat{c}_j / C_T)^{c_j}}{c_j!} \tag{4.18}$$

Following the treatment of Baker and Cousins,[9] we let $\{c'\}$ represent the true value of $\{c\}$ given by the model. A likelihood ratio, λ, can be defined as:

$$\lambda = L(\hat{c}, c) / L(c', c) \tag{4.19}$$

According to the likelihood ratio test theorem, the "likelihood χ^2" is defined by

$$\chi^2_\lambda = -2 \ln \lambda \tag{4.20}$$

which obeys a chi-squared distribution as the sample size (or number of total counts) increases.

For the multinomial distribution, we may replace the unknown $\{c'\}$ by the experimentally observed $\{c\}$. This gives:

$$\lambda = \left[C_T ! \prod_{j=1}^{1024} \frac{(\hat{c}_j / C_T)^{c_j}}{c_j !} \right] / \left[C_T ! \prod_{j=1}^{1024} \frac{(c_j / C_T)^{c_j}}{c_j !} \right] = \prod_{j=1}^{1024} \left(\frac{\hat{c}_j}{c_j} \right)^{c_j} \tag{4.21}$$

and the "likelihood χ^2" becomes:

$$\chi^2_\lambda = -2 \ln \lambda = -2 \ln \prod_{j=1}^{1024} \left(\frac{\hat{c}_j}{c_j} \right)^{c_j} = 2 \sum_{j=1}^{1024} c_j \ln \left(\frac{c_j}{\hat{c}_j} \right) \tag{4.22}$$

The minimization of the "likelihood χ^2," is done by varying the parameters τ_1, τ_2, a_1 and b.

It is important to recognize that the multinomial form given in equation (4.17) and the "likelihood χ^2" form given in equation (4.22), popularized by Baker and Cousins[9] and used by several others[20,21,23,27], are formally identical to each other. Maximization of the probability in equation (4.17) is equivalent to minimization of χ^2_λ in equation (4.22).

Furthermore, we note that all the probability-based methods are equivalent under certain assumptions. It has already been pointed out in the previous section that the Poisson distribution is related to the binomial distribution in the limit where the number of trials is relatively large and (or) the probability of success of each trial is very small. The joint Poisson probability distribution given in equation (4.16) can be written as:

$$P(c_1, c_2, ..., c_{1024}) = \prod_{j=1}^{1024} \frac{\hat{c}_j^{\,c_j} e^{-\hat{c}_j}}{c_j !} \tag{4.23}$$

since $\lambda_j = \hat{c}_j$. This equation can be transformed to:

$$\begin{aligned}\ln P(c_1, c_2, ..., c_{1024}) &= \ln\left(\prod_{j=1}^{1024} \frac{\hat{c}_j^{\,c_j} e^{-\hat{c}_j}}{c_j!}\right) \\ &= \sum_{j=1}^{1024} c_j \ln \hat{c}_j - \sum_{j=1}^{1024} \hat{c}_j - \sum_{j=1}^{1024} \ln c_j!\end{aligned} \tag{4.24}$$

Under the assumption that the total number of predicted counts is equal to the total number of observed photon counts ($\sum_j \hat{c}_j = \sum_j c_j = C_T$), we have:

$$\ln P(c_1, c_2, ..., c_{1024}) = \sum_{j=1}^{1024} c_j \ln \hat{c}_j - C_T - \sum_{j=1}^{1024} \ln c_j! \tag{4.25}$$

Now, because $\hat{c}_j = C_T p_j$, equation (4.25) can be written as:

$$\ln P(c_1, c_2, ..., c_{1024}) = \sum_{j=1}^{1024} c_j \ln p_j + \beta_1 \tag{4.26}$$

where β_1 is independent of the parameters τ_1, τ_2, a_1 and b, and thus remains constant during optimization. Furthermore, from equation (4.17), it can also be shown that

$$\begin{aligned}\ln Pr(c_1, c_2, \ldots c_{1024}) &= \ln C_T! + \sum_{j=1}^{1024} c_j \ln p_j - \sum_{j=1}^{1024} \ln c_j! \\ &= \sum_{j=1}^{1024} c_j \ln p_j + \beta_2\end{aligned} \tag{4.27}$$

where β_2 is another constant independent of the parameters τ_1, τ_2, a_1 and b. Therefore, the maximization of the probability given in equation (4.26) and (4.27) will be at the same point in the parameter space. In the ensuing discussion, for simplicity and economy, we shall, however, primarily discuss ML as representative of the probability-based methods unless otherwise noted.

Computational methods

The RM, ML, binomial, and Poisson analyses described above are performed using codes written in MATLAB that were run on a machine equipped with a quad-core Intel® Core™ i7

processor and 16 Gigabytes of memory. We employ the GlobalSearch toolbox, which uses the "fmincon" solver to minimize the objective function in the respective cases. In each calculation, a global minimum was found. In the case of a single-component system, we have two parameters, τ_1 and b. For a two-component system, there are four parameters: τ_1, τ_2, $a_{1,}$ and b. With our in-house routines, we experimented with different initial values in the following ranges for τ_1, τ_2, a_1, and b : 0.01-1.5 ns, 1.5-3.5 ns, 0.0-1.0, and -0.1 to 0.1 ns, respectively. Within the specified ranges, we always retrieved the same fit results through the third decimal place. Since the binomial and the Poisson distributions can be defined for individual channels in a single fluorescence data trace by equations (4.11) and (4.15), we have estimated the parameters for given traces for each individual channel and subsequently constructed histograms of the parameter values to obtain statistics for those values. For purposes of illustration, we have arbitrarily chosen three individual florescence decays from total-count data sets for a 50:50 mixture for 200, 6000, and 20000 total counts. (Experiments for all the mixtures for all the total counts numbers were performed, and a large selection of the results are presented in the supporting information). Finally, for comparison, the data were also analyzed with the proprietary SPCImage software v. 4.9.7 (SPCI), provided by Becker & Hickl GmbH.

4.4 Results and Discussion

4.4.1 Complete fluorescence decay analyses

Each of the fluorescence decays was analyzed by the RM-Pearson (equation 4.8), RM-Neyman (equation 4.9), ML (equation 4.22), binomial (equation 4.12), and the Poisson (equation 4.16) methods. For purposes of comparison, the commercial software (SPCI) was also used. **Figure 4.2** presents the sample decay traces for Rb:RhB 50:50 along with the fit obtained with the

ML method. Histograms of the lifetime parameters (τ_1, τ_2 and a_1) for the 50:50 mixture obtained using all the methods are given in **Figure 4.3a-c.** The vertical dotted dark gray line in each panel represents the target value for the parameter. The results of the mean and the standard deviation for τ_1, τ_2, and a_1 computed from the different methods are summarized in **Tables 4.1**, **4.2**, and **4.3**, respectively for the 50:50 mixture. **Tables 4.4**, **4.5**, and **4.6** present a concise summary of the results for all of the mixtures for all of the techniques employed at which a minimum number of total counts provided mean values within ~ 10% of the target values with standard deviations of ~ 20% of the target value.

These results indicate that the probability-based methods (ML, Poisson and binomial) are very effective in recovering the target fluorescence decay parameters. These three methods yield very similar results (indeed, identical through the second or third decimal place), as might be expected, given their similarity. A few salient points can be noted. When data for the mixtures are analyzed using the probability-based methods, the lower limit of the number of total counts where one retrieves the target mean with ~ 20% standard deviation is higher than that of pure compound (for which the total number of counts is about 20) in general. For the lifetime of rose bengal (τ_1), the mean target lifetime can be retrieved to less than 20 % of standard deviation with a total number of counts as low as 6000 in the case of the 50:50 mixture. For the lifetime of rhodamine B (τ_2), the mean target lifetime can be retrieved to about 20% of the standard deviation with only 100 total counts for the same mixture. The amplitude of the rose bengal lifetime (a_1) can be obtained with the same degree of precision with only 1000 total counts for the same mixture.

The minimum number of total counts required to estimate the lifetime of rose bengal increases as the fraction of rhodamine B increases. For example, in order to retrieve the target lifetime of rose bengal (τ_1) with a standard deviation of ~ 20% or less, 20, 1000, 6000, and 10000

total counts are required for the mixtures Rb:RhB 100:0, Rb:RhB 75:25, Rb:RhB 50:50, and Rb:RhB 25:75 respectively. The same trend is also reflected for the amplitude of the rose bengal lifetime, a_1. A minimum of 200, 1000, and 10000 total counts are required for the mixtures Rb:RhB 75:25, Rb:RhB 50:50, and Rb:RhB 25:75, respectively, to retrieve the correct result with a standard deviation of ~20% or less. Finally, for the lifetime of rhodamine B (τ_2), the minimum number of total counts required are 100, 100, 100, and 20 for the mixtures Rb:RhB 75:25, Rb:RhB 50:50, Rb:RhB 25:75, and Rb:RhB 0:100, respectively, to obtain the target lifetime with a standard deviation of ~20% or less.

We note that the lifetime of rose bengal becomes 10-20 ps (2-4%) shorter on average while the mean lifetime of rhodamine B becomes 70-110 ps (3-5%) shorter in the limit of 20000 total counts in the case of mixtures. The extent to which this shortening occurs depends roughly on the concentration of the other component. This observation has been confirmed from an independent experiment where the decay traces are collected to the highest quality supported by the memory.

With regard to the relative merits of the techniques, the residual minimization methods (RM-Pearson and RM-Neyman) proved to be markedly inferior to the ML and probability-based methods in retrieving the fluorescence lifetime parameters (**Figures 4.3** and **Tables 4.1-4.3**). In this context, we also note that the commercial software (SPCI), which is also based on a residual minimization method, has its own peculiarities. Some of these are summarized here. Except for the pure rose bengal data sets, one needs at least 500 total counts in order for the software even to initiate the analysis. In the case of pure rose bengal, one needs at least 200 total counts. In almost all cases, SPCI retrieves significantly different target values with larger standard deviations compared to all of the other methods, especially for mixtures where the total number of counts is less than 20000 (**Tables 4.1-4.3**). And even with 20000 total counts for the 50:50 mixture, SPCI

grossly overestimates the lifetime of rose bengal as 0.9 ns. Because SPCI is propriety, we are unable to obtain the source code to discern the origins of this behavior.

4.4.2 A bin-by-bin analyses of a single fluorescence decay trace to yield statistics

As noted above, the probability distribution for the number of photon counts in *each individual bin* can be obtained using the binomial (equation 4.11) and the Poisson (equation 4.15) probability distributions. This property permits the analysis of a single florescence decay trace, bin-by-bin, and of constructing frequency histograms of the various fluorescence decay parameters. From the histograms, the mean, median, and standard deviations of the parameters can be obtained. To demonstrate this, we have arbitrarily chosen three individual fluorescence decay traces from the sets of experiments with total counts 200, 6000, and 20000, respectively. Each trace has been analyzed by using the Poisson and the binomial methods, which have been applied to all five Rb:RhB mixtures examined (see supporting information). For purposes of illustration, the histograms obtained using the Poisson distribution method are presented in **Figure 4.4** for the Rb:RhB 50:50 mixture. A normalized Gaussian line (red) has been overlaid in each histogram using the calculated mean and standard derivation of (τ_1, τ_2, or a_1). As one might expect, the distribution becomes narrower and more well-defined as we progress from 200 to 20000 total counts.

4.5 Conclusions

We have presented a detailed comparison of probability-based methods (ML, binomial and the Poisson) with residual minimization-based methods (RM-Pearson, RM-Neyman, and SPCI) to retrieve the fluorescence decay parameters for various two-component mixtures in time-correlated, single-photon counting experiments. The maximum likelihood (ML) proved to be the most robust way to retrieve the target parameters. All the probability-based methods, however, have performed

equivalently to 2-3 significant figures. This is to be expected, as the three methods are all fundamentally related. ML consistently outperforms the RM methods. In some cases, RM-based methods did not converge to the expected values for a given number of total counts. RM-Pearson tends to overestimate parameters while RM-Neyman tends to underestimate them, both giving larger standard deviations than ML. We have discussed a bin-by-bin analysis of a single fluorescence decay trace and have shown that it is possible to retrieve not only their mean and median values but also the associated standard deviations by constructing frequency histograms from the analysis of the fluorescence decay at each bin. In conclusion, the ML technique or a bin-by-bin analysis provide robust methods (insensitive to initial conditions) of analyzing time-correlated, single-photon counting data for sparse data sets, and, in the case of bin-by-bin analysis, providing statistics from one fluorescence decay. These methods lend themselves well to the sparse data sets that can be encountered in subdiffraction-limited microscopies, such as STED.

4.6 Acknowledgments

The work performed by K. Santra, E. A. Smith, and J. W. Petrich was supported by the U.S. Department of Energy, Office of Basic Energy Sciences, Division of Chemical Sciences, Geosciences, and Biosciences through the Ames Laboratory. The Ames Laboratory is operated for the U.S. Department of Energy by Iowa State University under Contract No. DE-AC02-07CH11358. X. Song was supported by The Division of Material Sciences and Engineering, Office of Basic Energy Sciences, U.S. Department of Energy, under Contact No. W-7405-430 ENG-82 with Iowa State University. We acknowledge the assistance of Mr. Zhitao Zhao, a visiting undergraduate student from Beijing Normal University, Beijing.

4.7 References

1. Fleming, G. R. *Chemical Application of Ultrafast Spectroscopy* Oxford University Press: New York, 1986.

2. O'Connor, D. V.; Phillips, D. *Time Correlated Single Photon Counting* Academic Press Inc.: London, 1984.

3. Santra, K.; Zhan, J.; Song, X.; Smith, E. A.; Vaswani, N.; Petrich, J. W. What Is the Best Method to Fit Time-Resolved Data? A Comparison of the Residual Minimization and the Maximum Likelihood Techniques as Applied to Experimental Time-Correlated, Single-Photon Counting Data. *J. Phys. Chem. B.* **2016**, *120* (9), 2484-2490.

4. Syed, A.; Lesoine, M. D.; Bhattacharjee, U.; Petrich, J. W.; Smith, E. A. The Number of Accumulated Photons and the Quality of Stimulated Emission Depletion Lifetime Images. *Photochem. Photobiol.* **2014**, *90* (4), 767-772.

5. Lesoine, M. D.; Bhattacharjee, U.; Guo, Y.; Vela, J.; Petrich, J. W.; Smith, E. A. Subdiffraction, Luminescence-Depletion Imaging of Isolated, Giant, CdSe/CdS Nanocrystal Quantum Dots. *J. Phys. Chem. C.* **2013**, *117* (7), 3662-3667.

6. Lesoine, M. D.; Bose, S.; Petrich, J. W.; Smith, E. A. Supercontinuum Stimulated Emission Depletion Fluorescence Lifetime Imaging. *J. Phys. Chem. B.* **2012**, *116* (27), 7821-7826.

7. Ankjærgaard, C.; Jain, M.; Hansen, P. C.; Nielsen, H. B. Towards Multi-Exponential Analysis in Optically Stimulated Luminescence. *J. Phys. D: Appl. Phys.* **2010**, *43* (19), 195501.

8. Bajzer, Ž.; Therneau, T. M.; Sharp, J. C.; Prendergast, F. G. Maximum Likelihood Method for the Analysis of Time-Resolved Fluorescence Decay Curves. *Eur. Biophys. J.* **1991**, *20* (5), 247-262.

9. Baker, S.; Cousins, R. D. Clarification of the Use of Chi-Square and Likelihood Functions in Fits to Histograms. *Nucl. Instr. Meth. Phys. Res.* **1984**, *221* (2), 437-442.

10. Bevington, P.; Robinson, D. K. *Data Reduction and Error Analysis for the Physical Sciences*, 3rd ed.; McGraw-Hill: New York, 2002.

11. Bialkowski, S. E. Data Analysis in the Shot Noise Limit. 1. Single Parameter Estimation with Poisson and Normal Probability Density Functions. *Anal. Chem.* **1989**, *61* (22), 2479-2483.

12. Bialkowski, S. E. Data Analysis in the Shot Noise Limit. 2. Methods for Data Regression. *Anal. Chem.* **1989**, *61* (22), 2483-2489.

13. Enderlein, J.; Köllner, M. Comparison between Time-Correlated Single Photon Counting and Fluorescence Correlation Spectroscopy in Single Molecule Identification. *Bioimaging.* **1998**, *6* (1), 3-13.

14. Grinvald, A.; Steinberg, I. Z. On the Analysis of Fluorescence Decay Kinetics by the Method of Least-Squares. *Anal. Biochem.* **1974**, *59* (2), 583-598.

15. Hall, P.; Selinger, B. Better Estimates of Exponential Decay Parameters. *J. Phys. Chem.* **1981**, *85* (20), 2941-2946.

16. Hauschild, T.; Jentschel, M. Comparison of Maximum Likelihood Estimation and Chi-Square Statistics Applied to Counting Experiments. *Nucl. Instr. Meth. Phys. Res. A.* **2001**, *457* (1), 384-401.

17. Hinde, A. L.; Selinger, B.; Nott, P. On the Reliability of Fluorescence Decay Data. *Aust. J. Chem.* **1977**, *30* (11), 2383-2394.

18. Kim, G.-H.; Legresley, S. E.; Snyder, N.; Aubry, P. D.; Antonik, M. Single-Molecule Analysis and Lifetime Estimates of Heterogeneous Low-Count-Rate Time-Correlated Fluorescence Data. *Appl. Spectrosc.* **2011**, *65* (9), 981-990.

19. Köllner, M.; Wolfrum, J. How Many Photons Are Necessary for Fluorescence-Lifetime Measurements? *Chem. Phys. Lett.* **1992**, *200* (1), 199-204.

20. Laurence, T. A.; Chromy, B. A. Efficient Maximum Likelihood Estimator Fitting of Histograms. *Nat. Methods*. **2010**, *7* (5), 338-339.

21. Maus, M.; Cotlet, M.; Hofkens, J.; Gensch, T.; De Schryver, F. C.; Schaffer, J.; Seidel, C. An Experimental Comparison of the Maximum Likelihood Estimation and Nonlinear Least-Squares Fluorescence Lifetime Analysis of Single Molecules. *Anal. Chem.* **2001**, *73* (9), 2078-2086.

22. Moore, C.; Chan, S. P.; Demas, J.; DeGraff, B. Comparison of Methods for Rapid Evaluation of Lifetimes of Exponential Decays. *Appl. Spectrosc.* **2004**, *58* (5), 603-607.

23. Nishimura, G.; Tamura, M. Artefacts in the Analysis of Temporal Response Functions Measured by Photon Counting. *Phys. Med. Biol.* **2005**, *50* (6), 1327.

24. Periasamy, N. Analysis of Fluorescence Decay by the Nonlinear Least Squares Method. *Biophys. J.* **1988**, *54* (5), 961-967.

25. Sharman, K. K.; Periasamy, A.; Ashworth, H.; Demas, J. Error Analysis of the Rapid Lifetime Determination Method for Double-Exponential Decays and New Windowing Schemes. *Anal. Chem.* **1999**, *71* (5), 947-952.

26. Tellinghuisen, J.; Goodwin, P. M.; Ambrose, W. P.; Martin, J. C.; Keller, R. A. Analysis of Fluorescence Lifetime Data for Single Rhodamine Molecules in Flowing Sample Streams. *Anal. Chem.* **1994**, *66* (1), 64-72.

27. Turton, D. A.; Reid, G. D.; Beddard, G. S. Accurate Analysis of Fluorescence Decays from Single Molecules in Photon Counting Experiments. *Anal. Chem.* **2003**, *75* (16), 4182-4187.

28. Luchowski, R.; Szabelski, M.; Sarkar, P.; Apicella, E.; Midde, K.; Raut, S.; Borejdo, J.; Gryczynski, Z.; Gryczynski, I. Fluorescence Instrument Response Standards in Two-Photon Time-Resolved Spectroscopy. *Appl. Spectrosc.* **2010**, *64* (8), 918-922.

29. Kristoffersen, A. S.; Erga, S. R.; Hamre, B.; Frette, Ø. Testing Fluorescence Lifetime Standards Using Two-Photon Excitation and Time-Domain Instrumentation: Rhodamine B, Coumarin 6 and Lucifer Yellow. *J. Fluoresc.* **2014**, *24* (4), 1015-1024.

30. Snare, M. J.; Treloar, F. E.; Ghiggino, K. P.; Thistlethwaite, P. J. The Photophysics of Rhodamine B. *J. Photochem.* **1982**, *18* (4), 335-346.

31. Beaumont, P. C.; Johnson, D. G.; Parsons, B. J. Photophysical Properties of Laser Dyes: Picosecond Laser Flash Photolysis Studies of Rhodamine 6G, Rhodamine B and Rhodamine 101. *J. Chem. Soc., Faraday Trans.* **1993**, *89* (23), 4185-4191.

32. Calligaris, F.; Ciuti, P.; Gabrielli, I.; Giamcomich, R.; Mosetti, R. Wavelength Dependence of Timing Properties of the Xp 2020 Photomultiplier. *Nucl. Instr. Meth.* **1978**, *157* (3), 611-613.

33. Sipp, B.; Miehe, J.; Lopez-Delgado, R. Wavelength Dependence of the Time Resolution of High-Speed Photomultipliers Used in Single-Photon Timing Experiments. *Opt. Commun.* **1976**, *16* (1), 202-204.

34. Jading, Y.; Riisager, K. Systematic Errors in χ^2-Fitting of Poisson Distributions. *Nucl. Instr. Meth. Phys. Res. A.* **1996**, *372* (1), 289-292.

35. Neyman, J.; Pearson, E. S. On the Use and Interpretation of Certain Test Criteria for Purposes of Statistical Inference: Part I. *Biometrika.* **1928**, *20A* (1/2), 175-240.

36. Neyman, J.; Pearson, E. S. On the Use and Interpretation of Certain Test Criteria for Purposes of Statistical Inference: Part II. *Biometrika.* **1928**, *20A* (3/4), 263-294.

37. Feller, W. *An Introduction to Probability Theory and Its Applications: Volume I*, 3rd ed.; John Wiley & Sons, Inc. London-New York-Sydney-Toronto: 1968.

4.8 Tables and Figures

Table 4.1

Rose bengal (τ_1): mean lifetime (ns) ± standard deviation (ns) for a Rb:RhB 50:50 mixture

Total counts	ML	Poisson	Binomial	RM-Pearson	RM-Neyman	SPCI
20	0.5 ± 0.5	0.5 ± 0.5	0.5 ± 0.5	0.3 ± 0.4	0.4 ± 0.3	0 ± 0
100	0.6 ± 0.5	0.6 ± 0.5	0.6 ± 0.5	0.2 ± 0.2	1.1 ± 0.6	0 ± 0
200	0.6 ± 0.5	0.7 ± 0.5	0.7 ± 0.5	0.3 ± 0.2	0.2 ± 0.3	0 ± 0
500	0.5 ± 0.3	0.5 ± 0.3	0.5 ± 0.3	0.5 ± 0.2	0.3 ± 0.1	1.4 ± 1.0
1000	0.5 ± 0.3	0.5 ± 0.3	0.5 ± 0.3	0.7 ± 0.2	0.43 ± 0.08	1.3 ± 0.5
3000	0.5 ± 0.2	0.5 ± 0.2	0.5 ± 0.2	0.9 ± 0.2	0.87 ± 0.08	1.5 ± 0.4
6000	0.5 ± 0.1	0.5 ± 0.1	0.5 ± 0.1	0.9 ± 0.2	1.1 ± 0.1	1.2 ± 0.2
10000	0.48 ± 0.06	0.48 ± 0.06	0.48 ± 0.06	0.8 ± 0.2	0.8 ± 0.4	1.5 ± 0.3
20000	0.47 ± 0.04	0.47 ± 0.04	0.47 ± 0.04	0.6 ± 0.1	0.47 ± 0.05	0.9 ± 0.1

Table 4.2

Rhodamine B (τ_2): mean lifetime (ns) ± standard deviation (ns) for a Rb:RhB 50:50 mixture

Total counts	ML	Poisson	Binomial	RM-Pearson	RM-Neyman	SPCI
20	2.7 ± 0.7	2.6 ± 0.8	2.6 ± 0.7	3.1 ± 0.6	2.1 ± 0.6	0 ± 0
100	2.6 ± 0.5	2.6 ± 0.5	2.6 ± 0.5	3.48 ± 0.08	1.6 ± 0.2	0 ± 0
200	2.7 ± 0.5	2.7 ± 0.5	2.7 ± 0.5	3.48 ± 0.08	2.3 ± 0.2	0 ± 0
500	2.4 ± 0.2	2.4 ± 0.2	2.4 ± 0.2	3.48 ± 0.07	3.47 ± 0.08	6 ± 7
1000	2.4 ± 0.2	2.4 ± 0.2	2.4 ± 0.2	3.48 ± 0.07	3.5 ± 0	3 ± 2
3000	2.4 ± 0.1	2.4 ± 0.1	2.4 ± 0.1	3.4 ± 0.1	3.5 ± 0	2.9 ± 0.6
6000	2.39 ± 0.06	2.39 ± 0.06	2.39 ± 0.06	3.1 ± 0.2	3.5 ± 0.2	3.7 ± 0.6
10000	2.39 ± 0.04	2.39 ± 0.04	2.39 ± 0.04	2.9 ± 0.2	2.7 ± 0.5	3.8 ± 0.9
20000	2.38 ± 0.03	2.38 ± 0.03	2.38 ± 0.03	2.61 ± 0.06	2.28 ± 0.04	2.45 ± 0.08

Table 4.3

Rose bengal (a_1): mean value of the amplitude of the component of rose bengal emission ± standard deviation for a Rb:RhB 50:50 mixture

Total counts	ML	Poisson	Binomial	RM-Pearson	RM-Neyman	SPCI
20	0.8 ± 0.3	0.8 ± 0.3	0.8 ± 0.3	0.4 ± 0.4	0.999 ± 0.009	0 ± 0
100	0.6 ± 0.2	0.6 ± 0.2	0.6 ± 0.2	0.5 ± 0.3	0.6 ± 0.4	0 ± 0
200	0.6 ± 0.2	0.6 ± 0.2	0.6 ± 0.2	0.5 ± 0.2	0.4 ± 0.3	0 ± 0
500	0.5 ± 0.1	0.5 ± 0.1	0.5 ± 0.1	0.6 ± 0.1	0.5 ± 0.2	0.7 ± 0.3
1000	0.49 ± 0.09	0.49 ± 0.09	0.48 ± 0.09	0.58 ± 0.05	0.64 ± 0.05	0.7 ± 0.1
3000	0.45 ± 0.06	0.45 ± 0.05	0.45 ± 0.05	0.64 ± 0.04	0.72 ± 0.02	0.7 ± 0.1
6000	0.44 ± 0.03	0.44 ± 0.03	0.44 ± 0.03	0.61 ± 0.06	0.76 ± 0.05	0.77 ± 0.09
10000	0.44 ± 0.02	0.44 ± 0.02	0.44 ± 0.02	0.57 ± 0.05	0.6 ± 0.2	0.8 ± 0.2
20000	0.44 ± 0.02	0.44 ± 0.02	0.44 ± 0.02	0.5 ± 0.02	0.42 ± 0.02	0.42 ± 0.05

Table 4.4

Rose bengal lifetime (τ_1): The total number of counts required for a given method to obtain a mean value within ~ 10% of the target value ($\tau_1 = 0.49$ ns) with a standard deviation of ~ 20% [a]

	ML		RM-Pearson		RM-Neyman		SPCI	
Sets	**Lifetime (ns)**	**Min Total Counts**	**Lifetime (ns)**	**Min Total Counts**	**Lifetime (ns)**	**Min Total Counts**	**Lifetime (ns)**	**Min Total Counts**
Rb:RhB 100:0	0.5 ± 0.1	20	0.54 ± 0.02	6000	0.53 ± 0.06	500	0.48 ± 0.04	500
Rb:RhB 75:25	0.5 ± 0.1	1000	0.53 ± 0.03	20000	0.49 ± 0.03	20000	0.52 ± 0.06	20000
Rb:RhB 50:50	0.5 ± 0.1	6000	0.6 ± 0.1	20000	0.47 ± 0.05	20000	0.9 ± 0.1	20000
Rb:RhB 25:75	0.5 ± 0.1	10000	1.0 ± 0.3	20000	0.5 ± 0.3	20000	1.9 ± 0.1	20000
Rb:RhB 0:100								

[a] In those cases where the results are not within ~10% of the mean with ~20% SD even with 20000 counts, a result is nevertheless still reported.

Table 4.5

Rhodamine B lifetime (τ_2): The number of total counts required for a given method to obtain a mean value within ~ 10% of the target value ($\tau_2 = 2.45$ ns) with a standard deviation of ~ 20%

	ML		**RM-Pearson**		**RM-Neyman**		**SPCI**	
Sets	**Lifetime (ns)**	**Min Total Counts**	**Lifetime (ns)**	**Min Total Counts**	**Lifetime (ns)**	**Min Total Counts**	**Lifetime (ns)**	**Min Total Counts**
Rb:RhB 100:0								
Rb:RhB 75:25	2.5 ± 0.5	100	2.61 ± 0.04	20000	2.4 ± 0.1	10000	2.4 ± 0.2	20000
Rb:RhB 50:50	2.6 ± 0.5	100	2.61 ± 0.06	20000	2.7 ± 0.5	10000	2.45 ± 0.08	20000
Rb:RhB 25:75	2.7 ± 0.5	100	2.8 ± 0.1	20000	2.36 ± 0.09	20000	2.9 ± 0.1	20000
Rb:RhB 0:100	2.4 ± 0.5	20	2.74 ± 0.03	6000	2.48 ± 0.09	3000	2.4 ± 0.5	1000

Table 4.6

Amplitude of the rose bengal contribution to the fluorescence decay (a_1): The total number of counts required for a given method to obtain a mean value within ~ 10% of the target value ($a_1 = 0.68$, 0.44 and 0.22 for Rb:RhB 75:25, Rb:RhB 50:50 and Rb:RhB 25:75 respectively) with a standard deviation of ~ 20%

	ML		**RM-Pearson**		**RM-Neyman**		**SPCI**	
Sets	**Fraction of τ_1**	**Min Total Counts**	**Fraction of τ_1**	**Min Total Counts**	**Fraction of τ_1**	**Min Total Counts**	**Fraction of τ_1**	**Min Total Counts**
Rb:RhB 100:0								
Rb:RhB 75:25	0.7 ± 0.1	200	0.75 ± 0.01	10000	0.72 ± 0.03	10000	0.70 ± 0.03	20000
Rb:RhB 50:50	0.49 ± 0.09	1000	0.50 ± 0.02	20000	0.42 ± 0.02	20000	0.42 ± 0.05	20000
Rb:RhB 25:75	0.23 ± 0.04	10000	0.38 ± 0.08	20000	0.23 ± 0.08	20000	0.65 ± 0.07	20000
Rb:RhB 0:100								

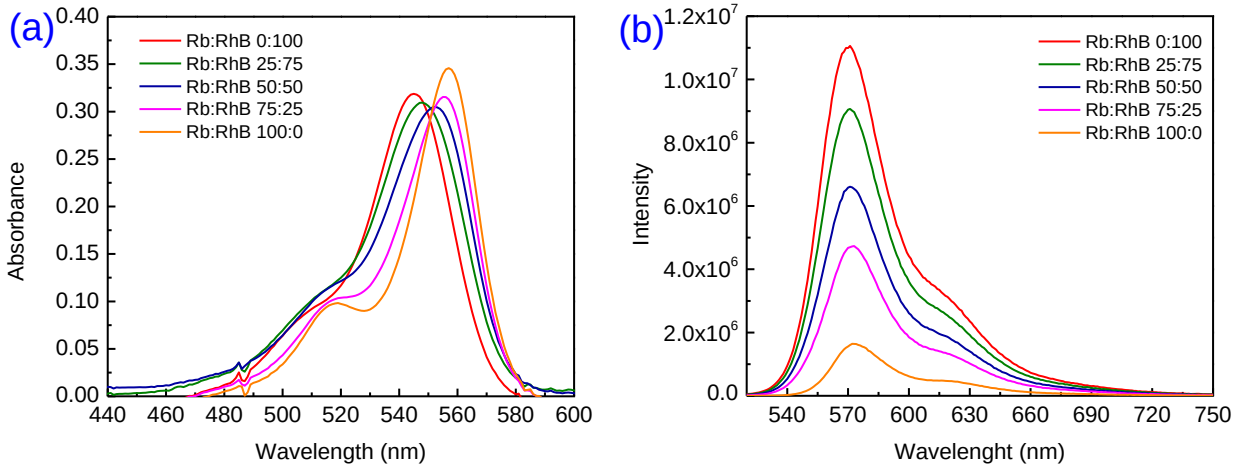

Figure 4.1. (a) Absorption spectra and (b) emission spectra for mixtures of rose bengal (Rb) and rhodamine B (RhB) with "composition ratios," Rb:Rhb of: 100:0; approximately 75:25, 50:50, 25:75; and 0:100. The "composition ratio" is the ratio of the optical density of one to the other at 550 nm, where this ratio is adjusted such that the sums of the individual optical densities are ~0.3, as indicated in panel (a). The exact contribution of the optical density of rose bengal is given by the amplitude of its lifetime component, a_1, which is cited in the Tables and Figures.

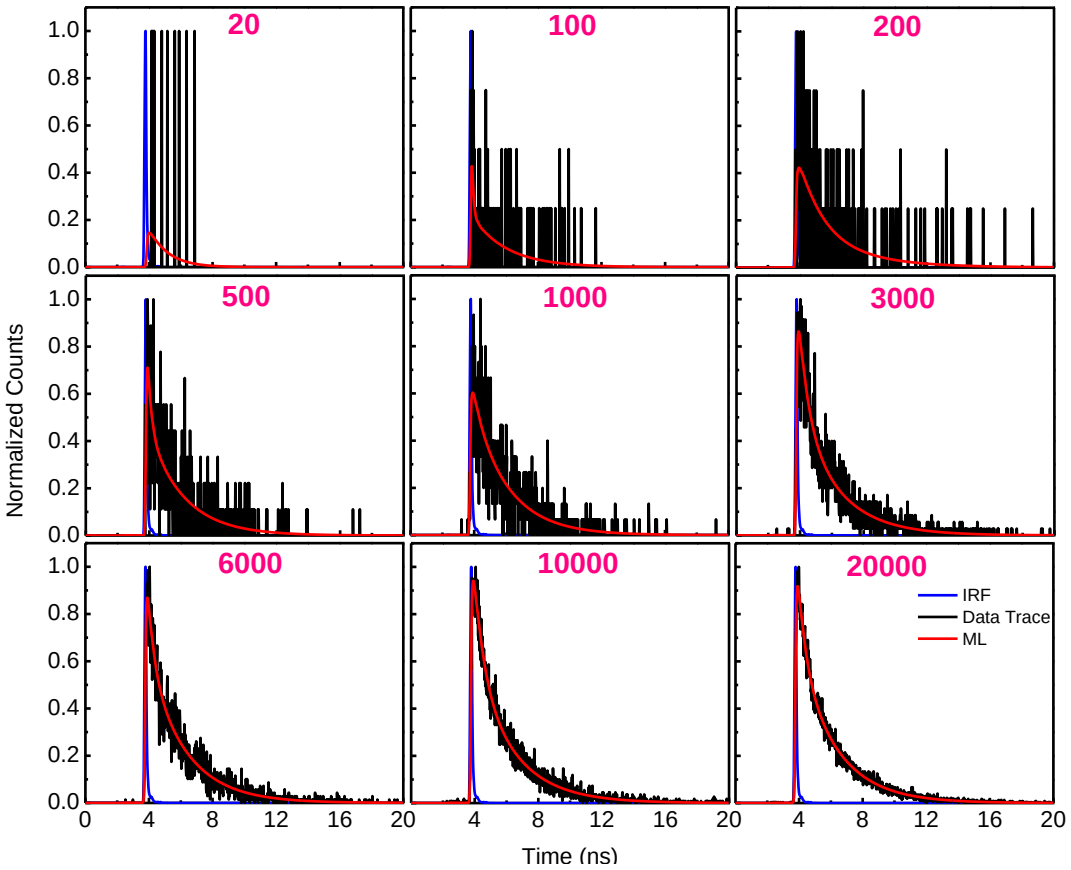

Figure 4.2. Representative fluorescence decay for a given number of total counts (as indicated in each panel) for a 50:50 Rb:RhB mixture. Experimental data are given by the black traces; the fits, by the red curves; and the instrument response functions (IRFs), by the blue traces.

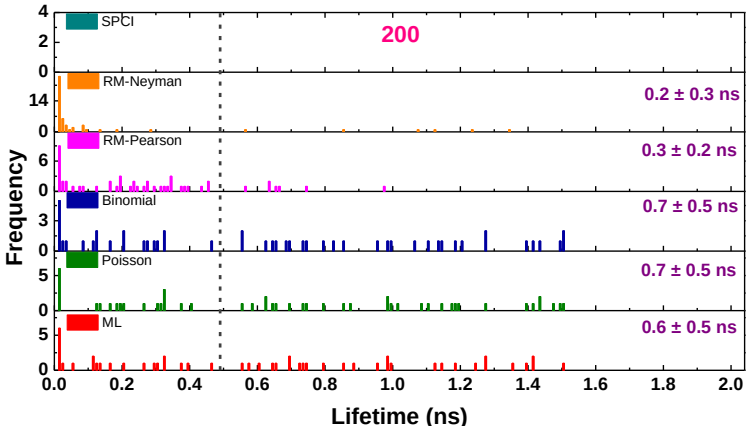

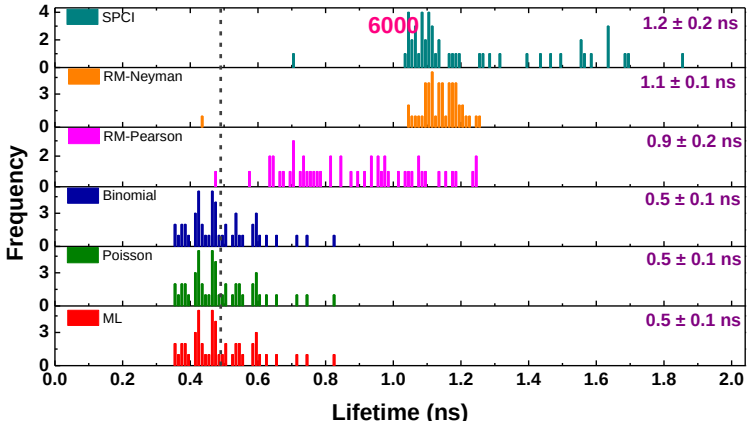

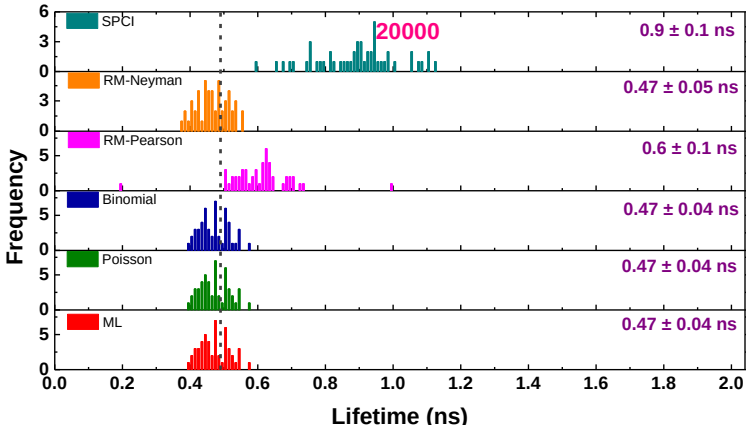

(a)

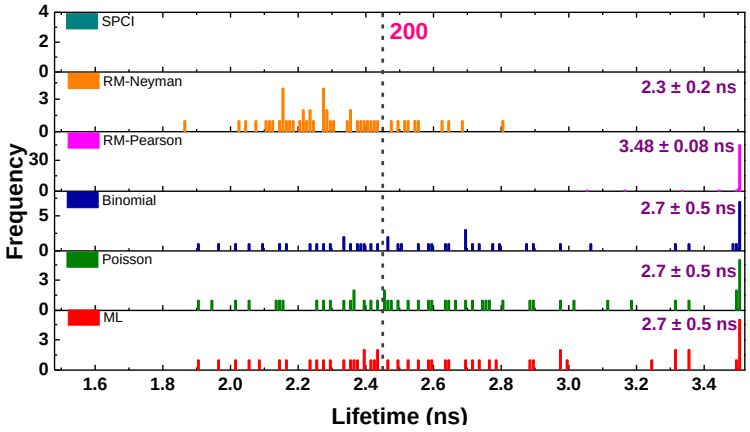

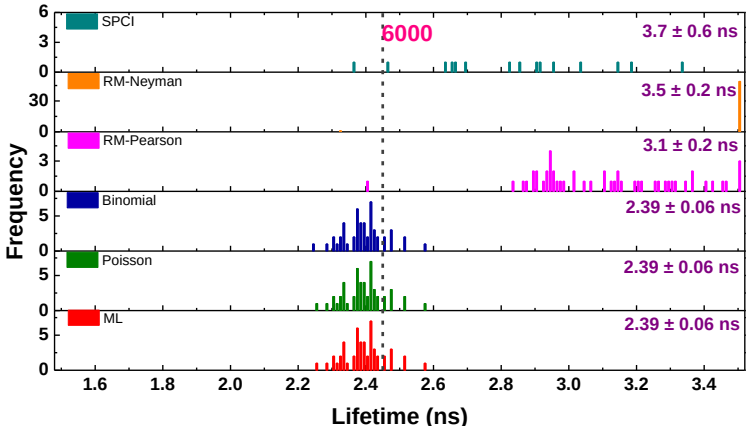

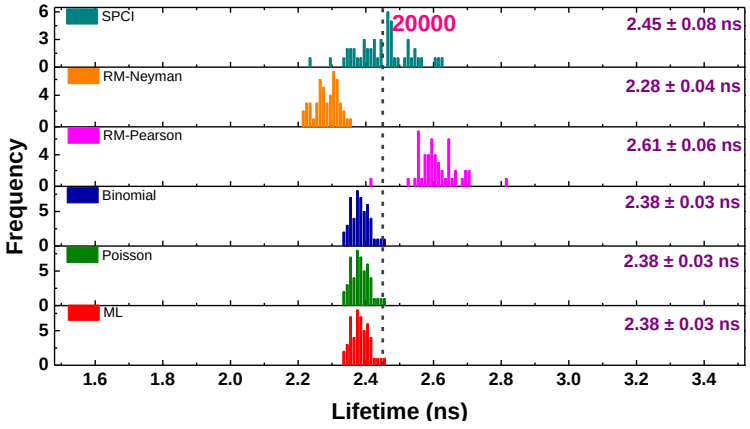

(b)

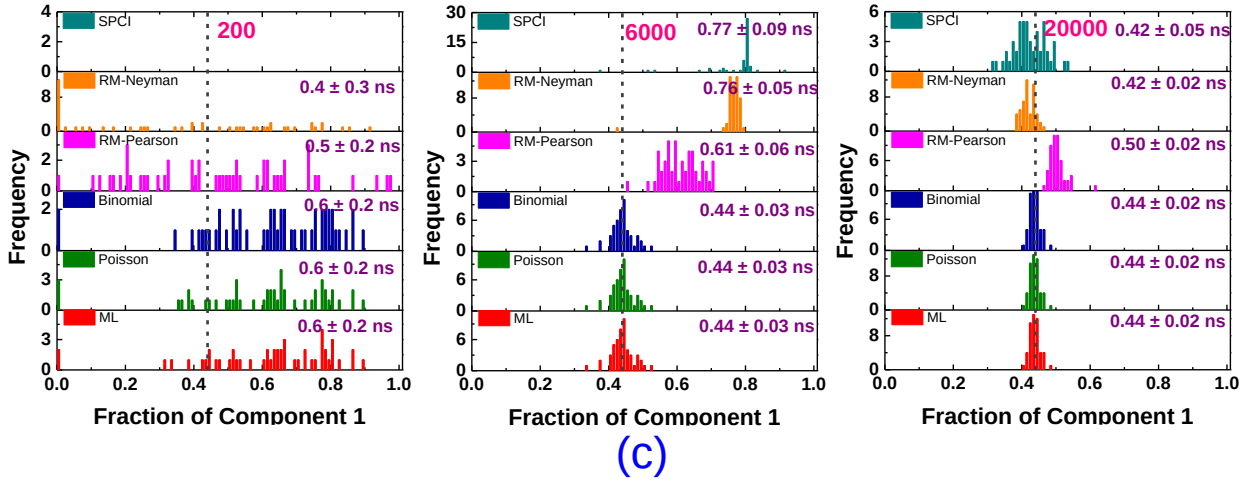

Figure 4.3. Histograms of the (a) lifetime of rose bengal (τ_1), (b) lifetime of rhodamine B (τ_2), and (c) the amplitude of the lifetime of the short lifetime of rose bengal (a_1) estimated by ML (red), Poisson (green), binomial (blue), RM-Pearson (magenta), RM-Neyman (orange), and SPCI (cyan) methods for the total counts of 200, 6000, and 20000 in the Rb:RhB 50:50 data sets. The bins for all of the histograms are 10 ps wide. The vertical dark gray dashed lines give the target values: $\tau_1 = 0.49$ ns; $\tau_2 = 2.45$ ns; and $a_1 = 0.44$ in (a), (b), and (c) respectively.

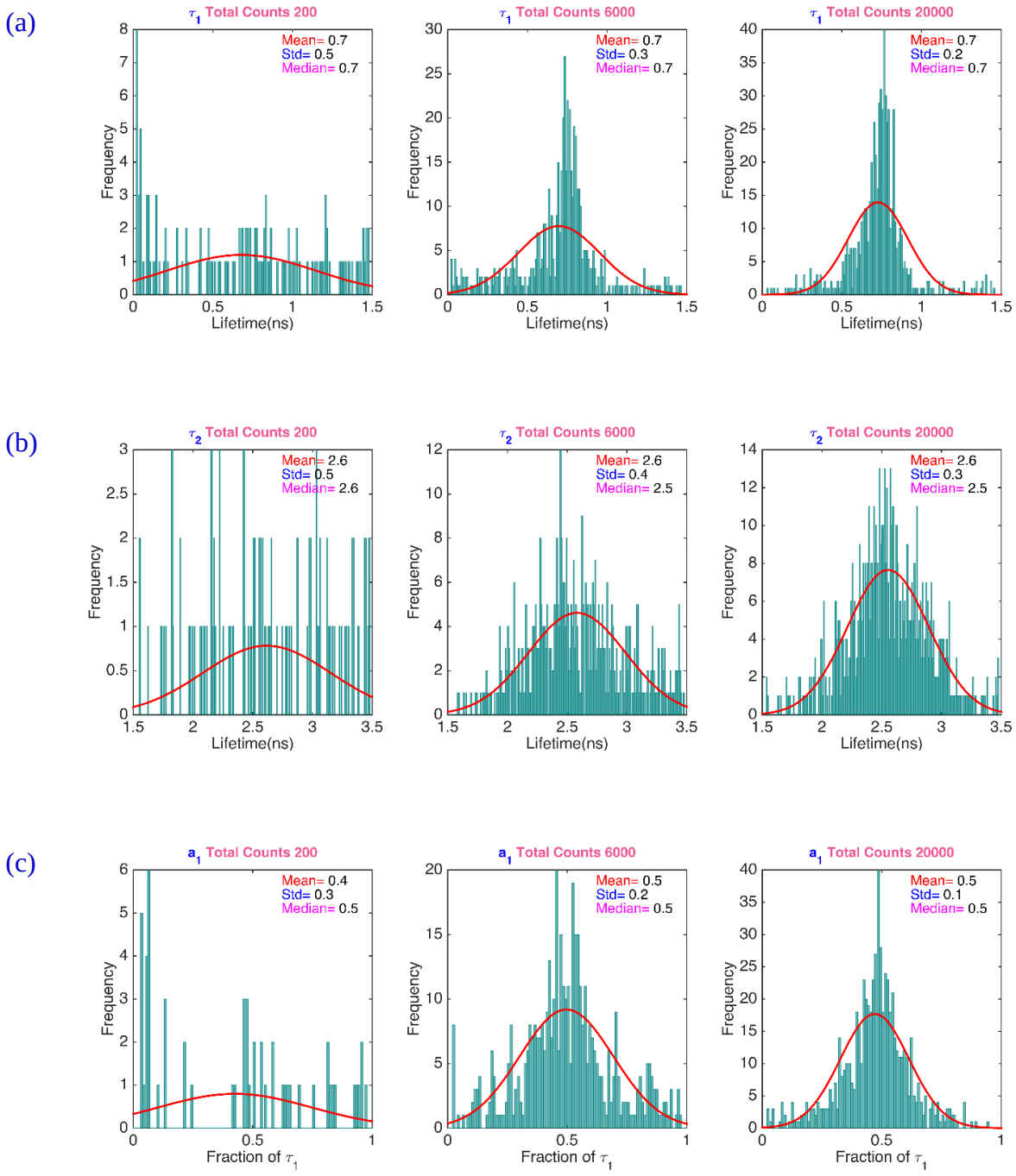

Figure 4.4. Histograms of the frequencies of obtaining values of the fluorescence decay parameters for τ_1, τ_2, and a_1, are presented in panels (a), (b), and (c), respectively. The histograms are obtained from a bin-by-bin analysis using the Poisson distribution of a representative, single fluorescence decay trace from a 50:50 mixture of Rb and RhB with total counts of 200, 6000, and 20000. The histograms are fit to Gaussians using the values of the mean and standard deviation obtained from them.

4.9 Supplementary Information

4.9.1 Complete fluorescence decay analyses

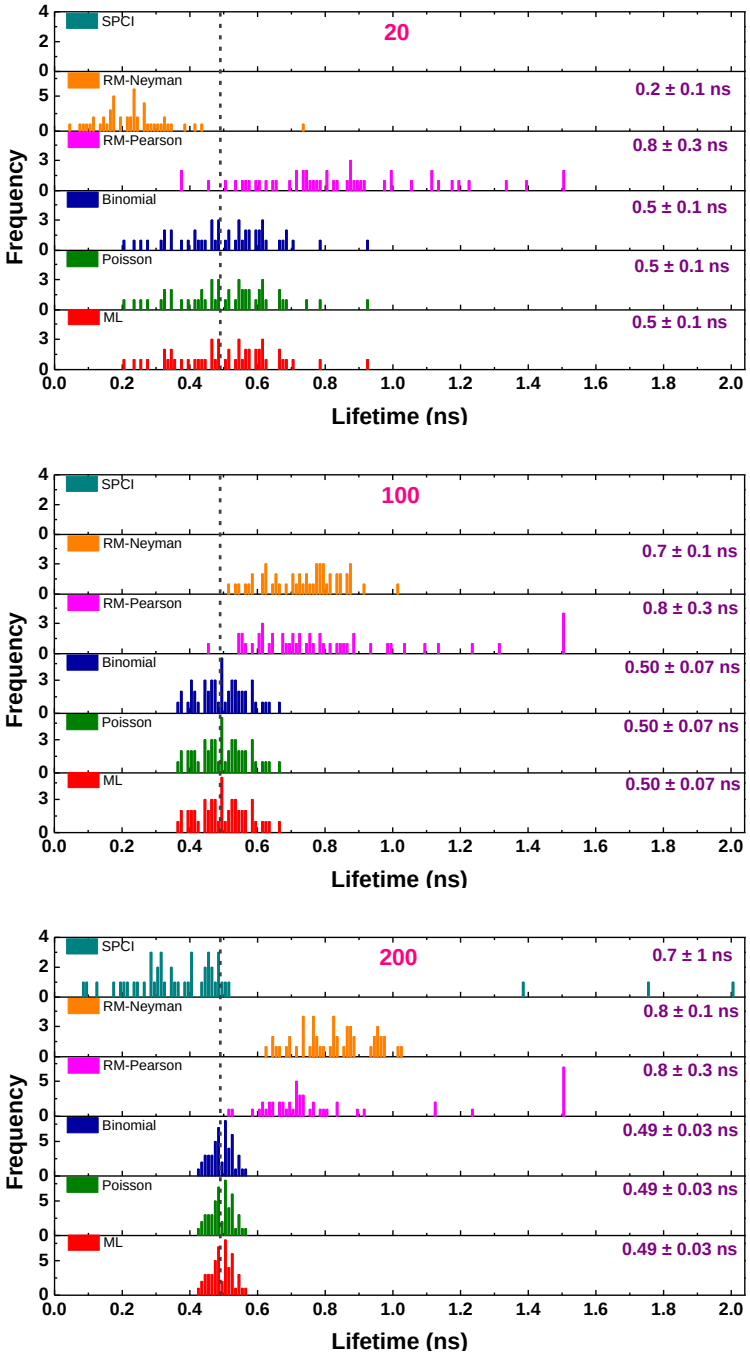

(a-i)

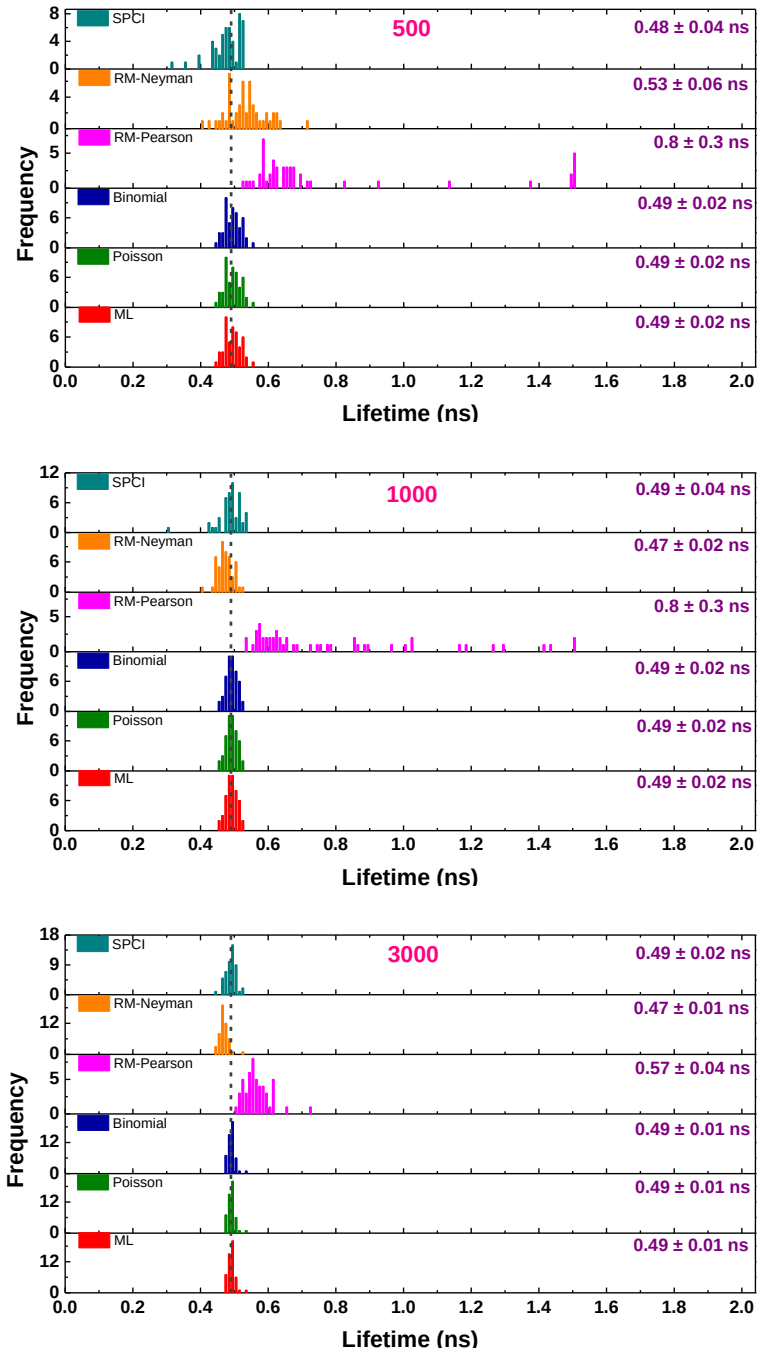

(a-ii)

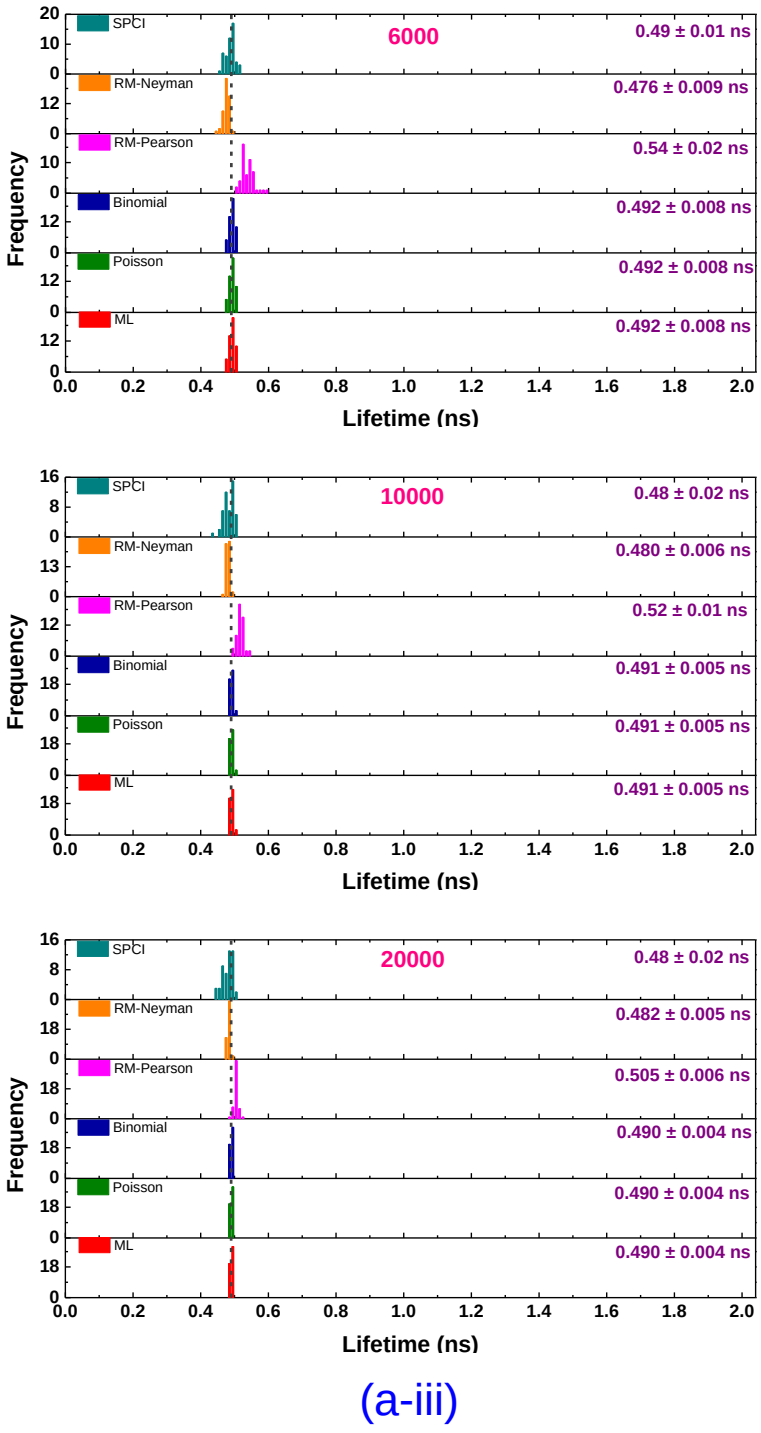

Figure S4.1. Histograms of the lifetime of rose bengal (τ_1) estimated by ML (red), Poisson (green), Binomial (blue), RM-Pearson (magenta), RM-Neyman (orange) and SPCI (cyan) methods for the total counts indicated in each panel in the Rb:RhB 100:0 data sets are presented in (a-i)-(a-iii). The bins for all of the histograms are 10 ps wide. The vertical dark gray dash lines give target values $\tau_1 = 0.49$ ns.

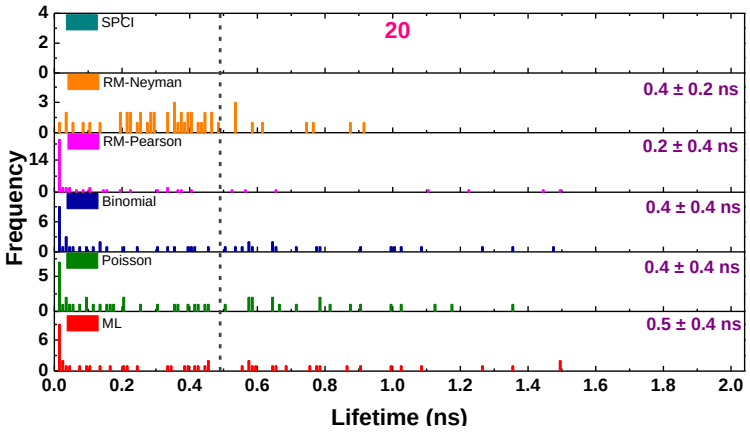

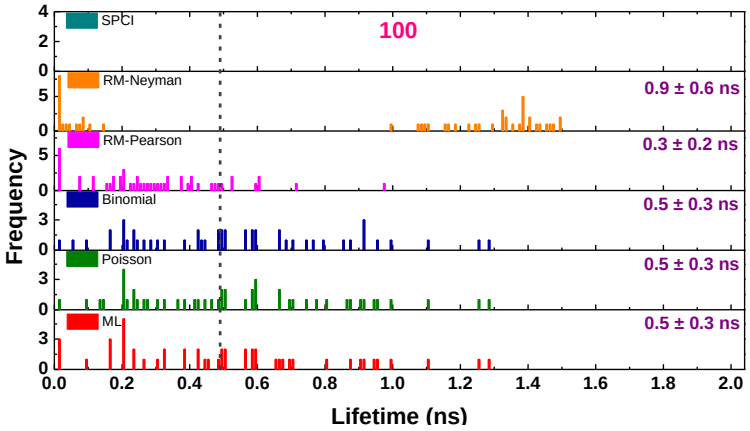

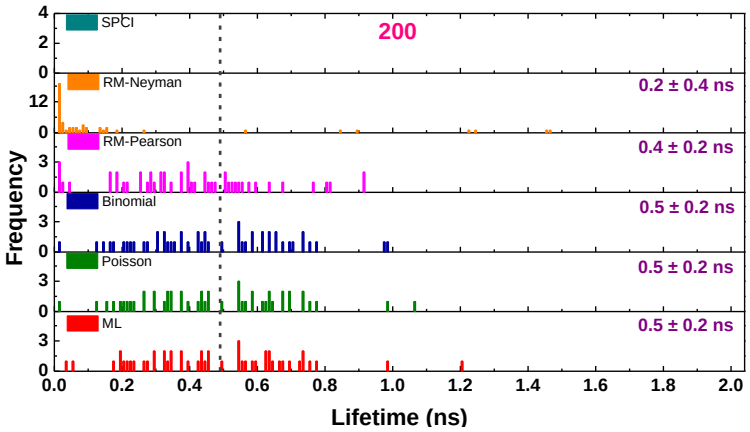

(a-i)

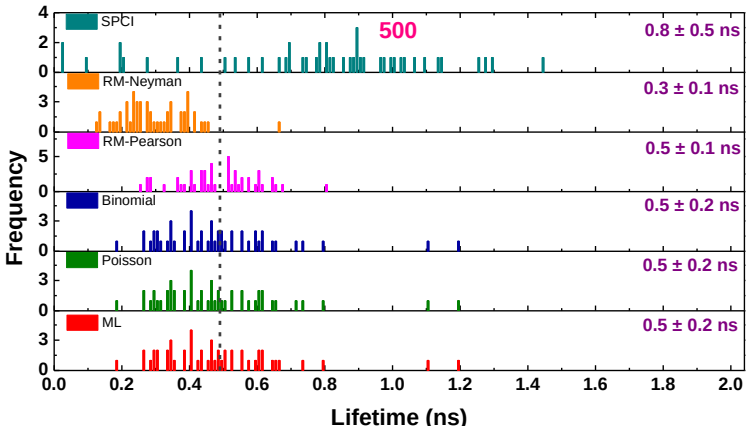

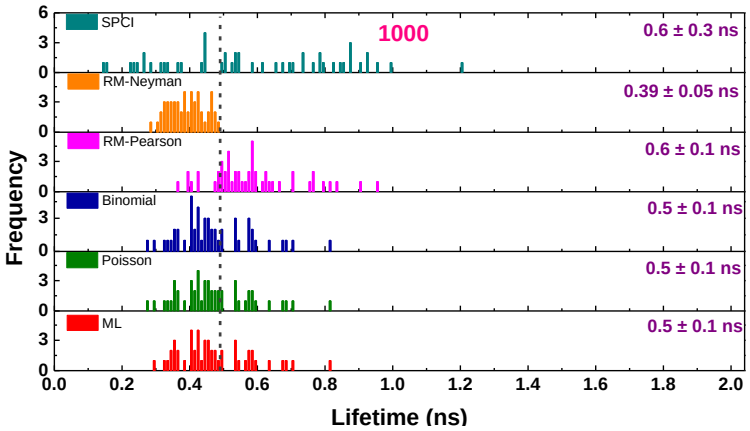

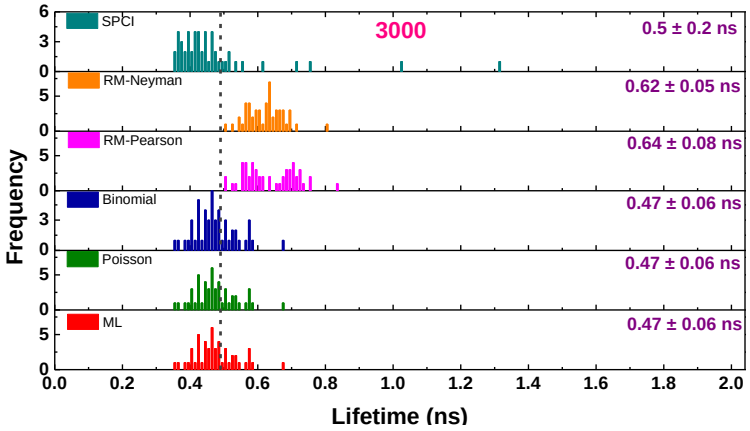

(a-ii)

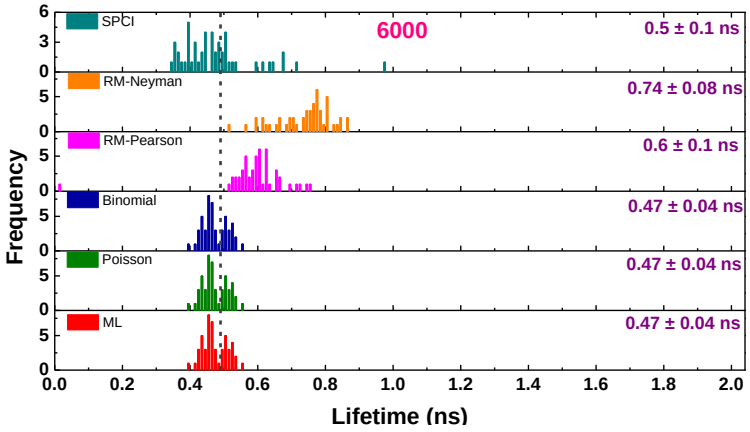

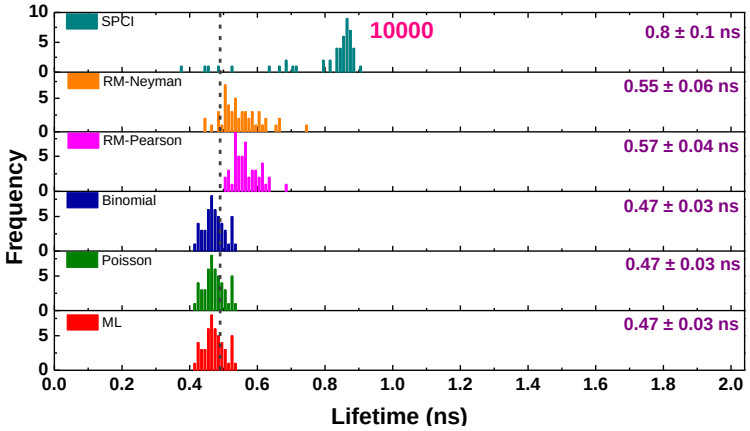

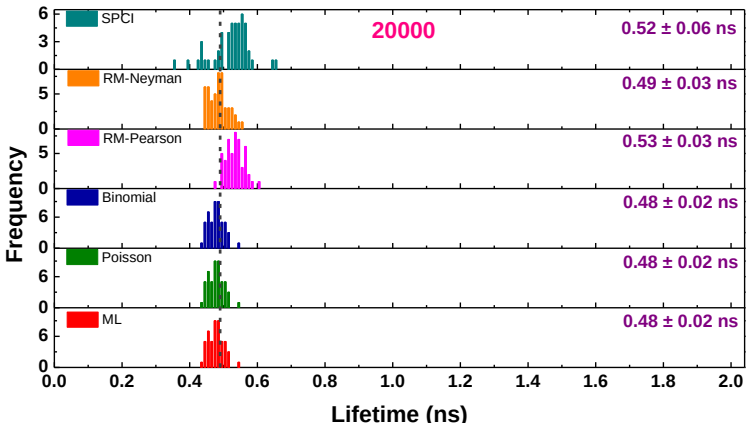

(a-iii)

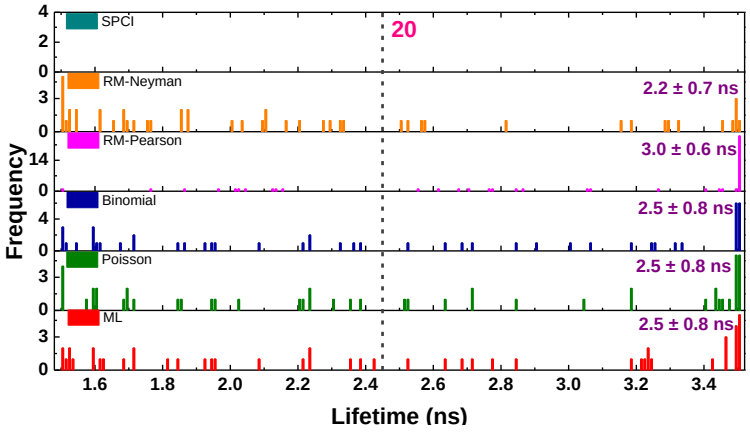

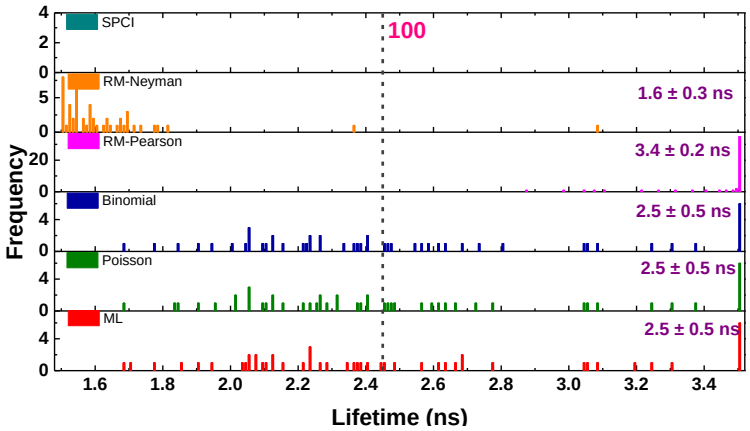

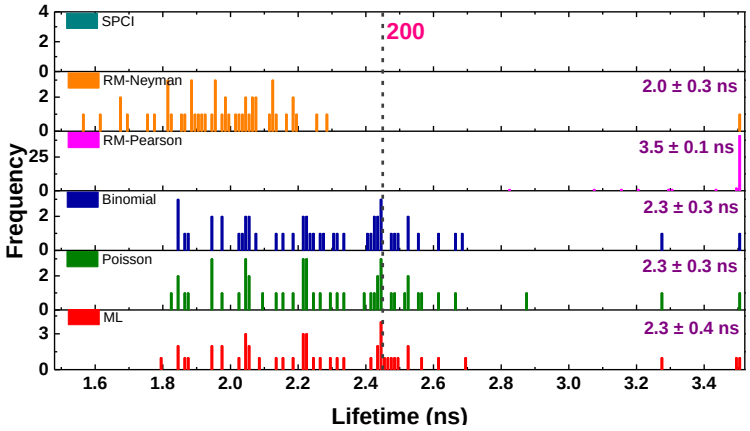

(b-i)

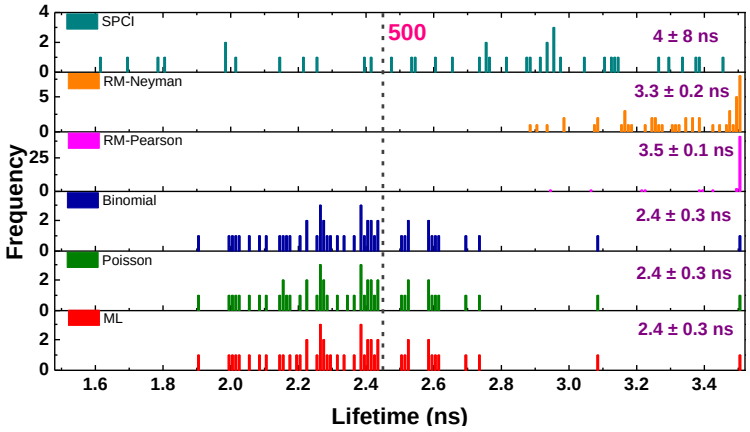

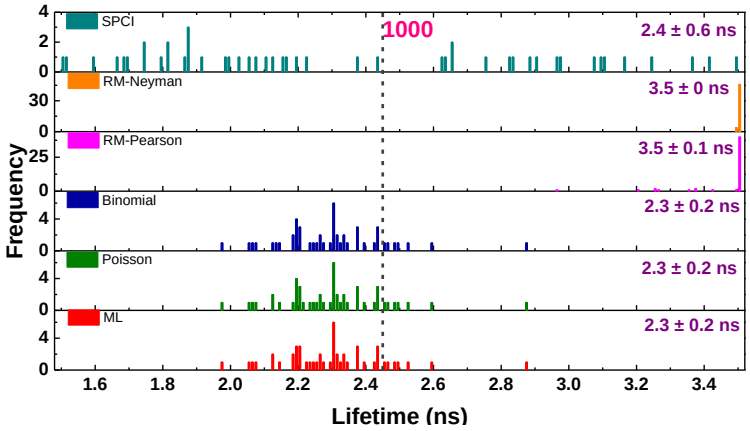

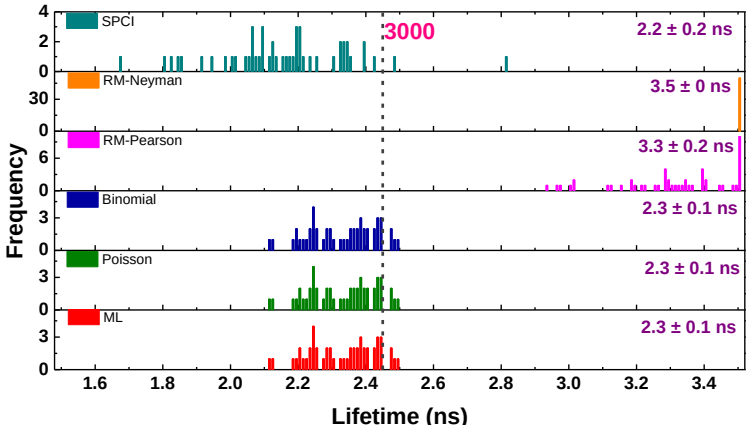

(b-ii)

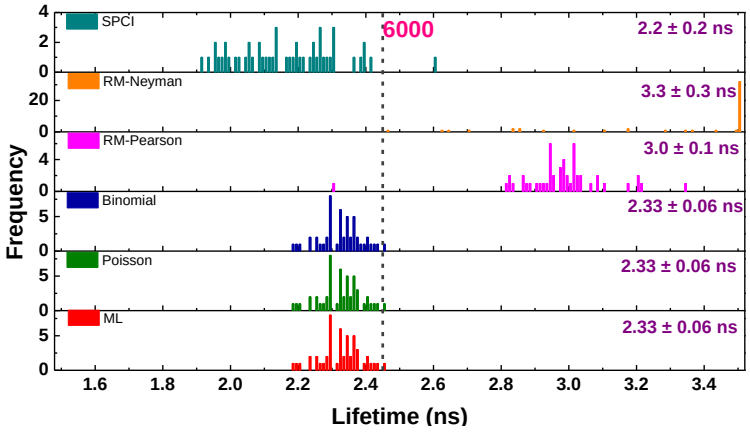

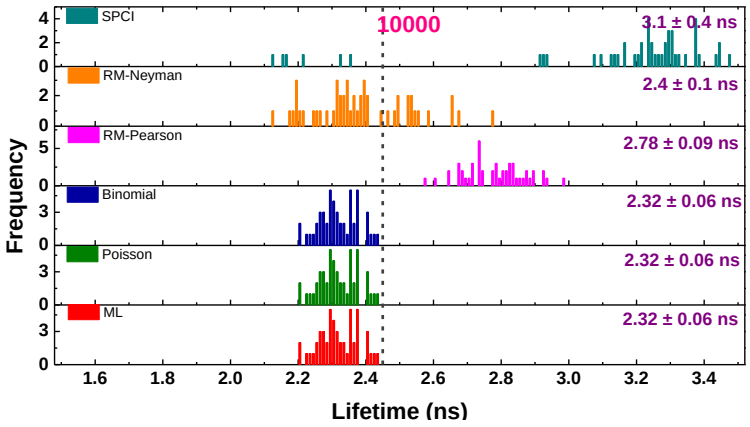

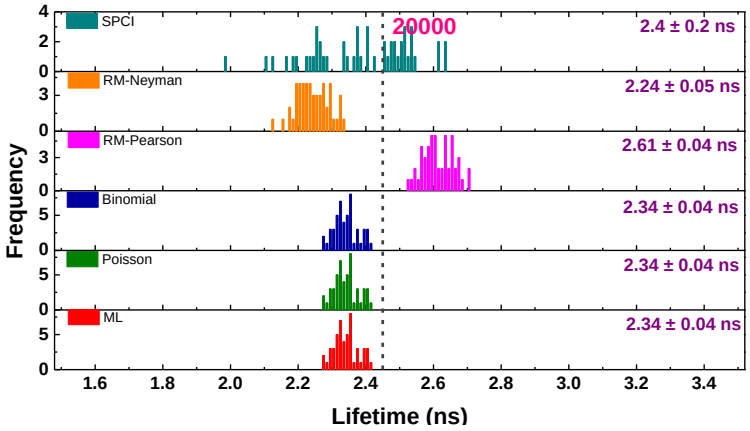

(b-iii)

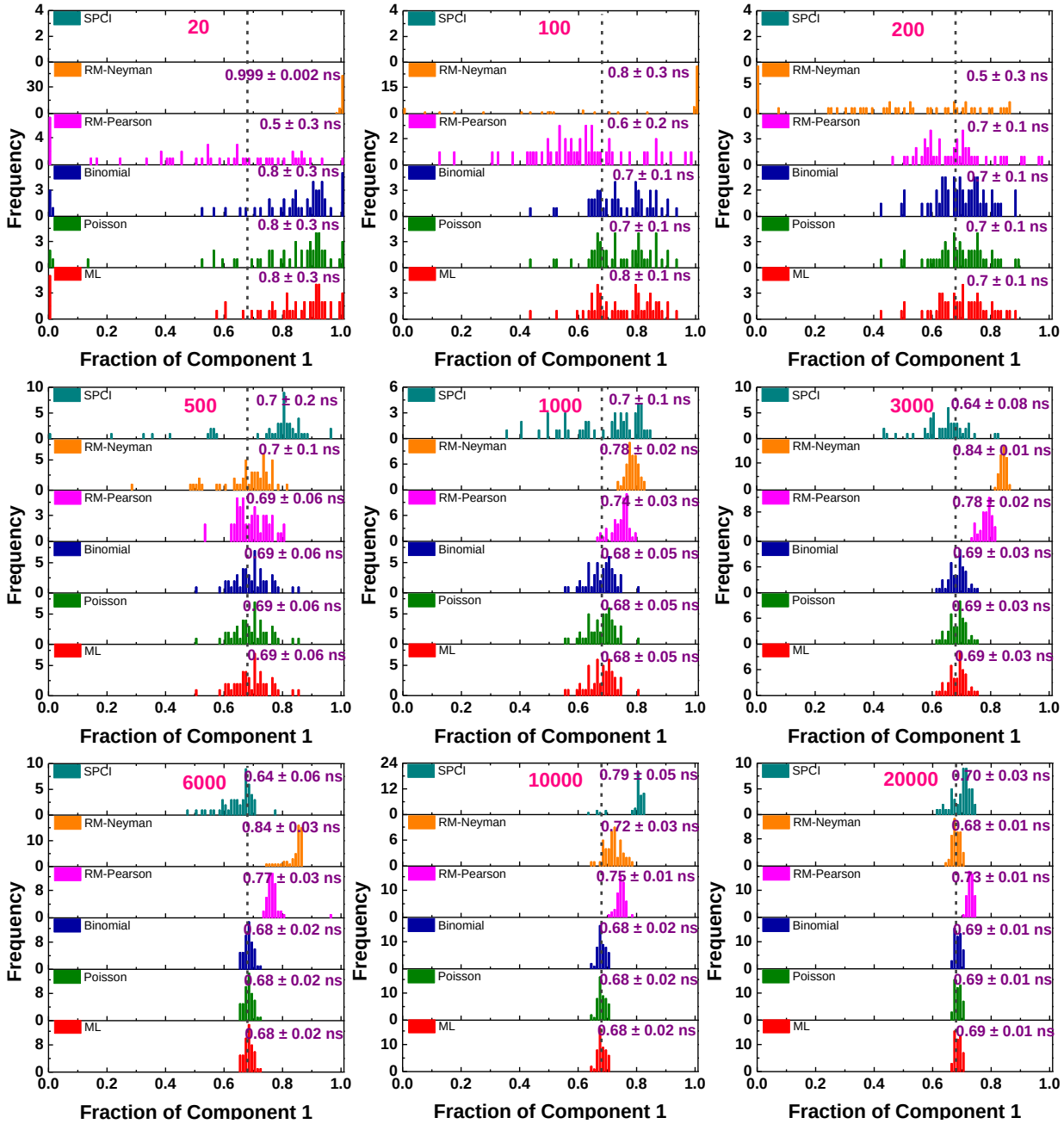

Figure S4.2. Histograms of the (a-i)-(a-iii) lifetime of rose bengal (τ_1), (b-i)-(b-iii) lifetime of rhodamine B (τ_2) and (c) the amplitude of the lifetime of the short lifetime of rose bengal (a_1) estimated by ML (red), Poisson (green), Binomial (blue), RM-Pearson (magenta), RM-Neyman (orange) and SPCI (cyan) methods for the total counts indicated in each panel in the Rb:RhB 75:25 data sets are presented. The bins for all of the histograms are 10 ps wide. The vertical dark gray dash lines give target values $\tau_1 = 0.49$ ns, $\tau_2 = 2.45$ ns and $a_1 = 0.68$ in (a), (b) and (c) respectively.

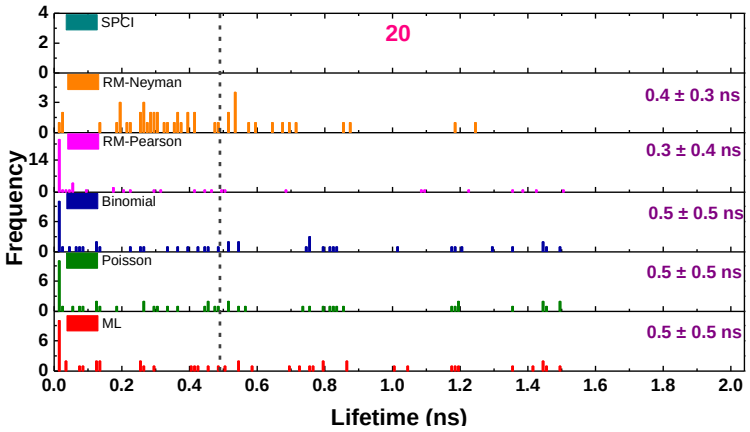

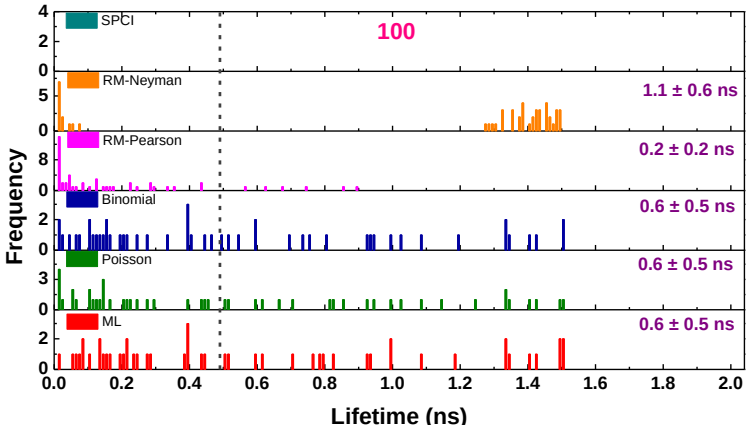

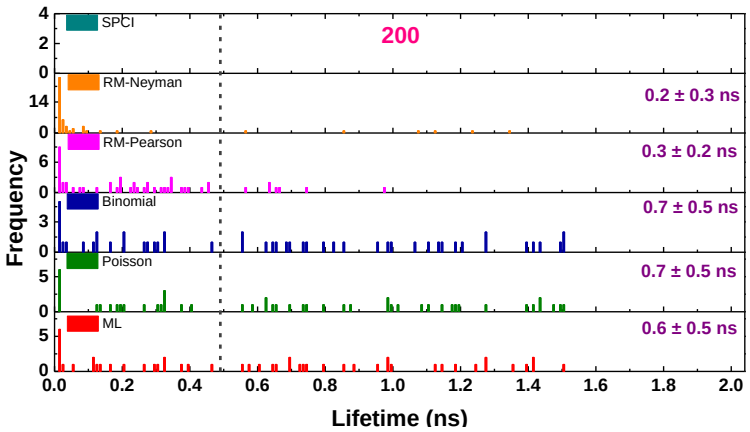

(a-i)

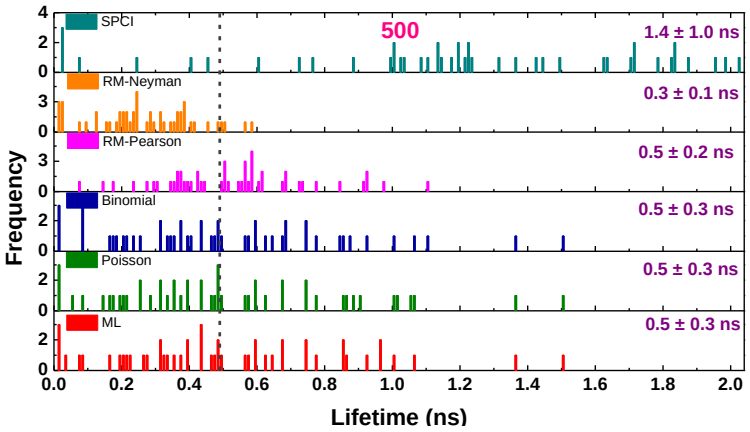

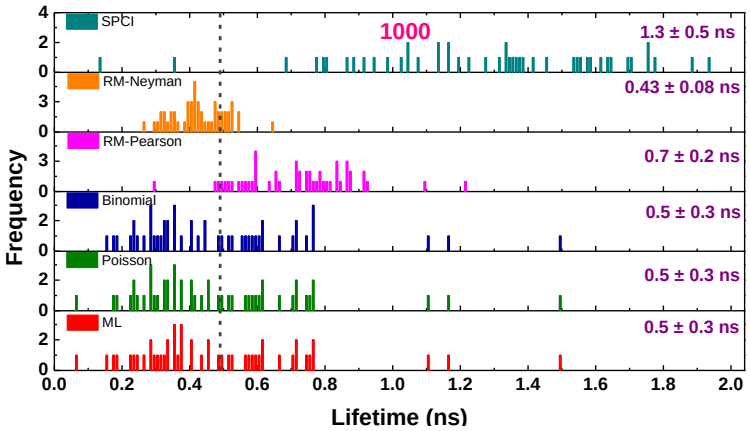

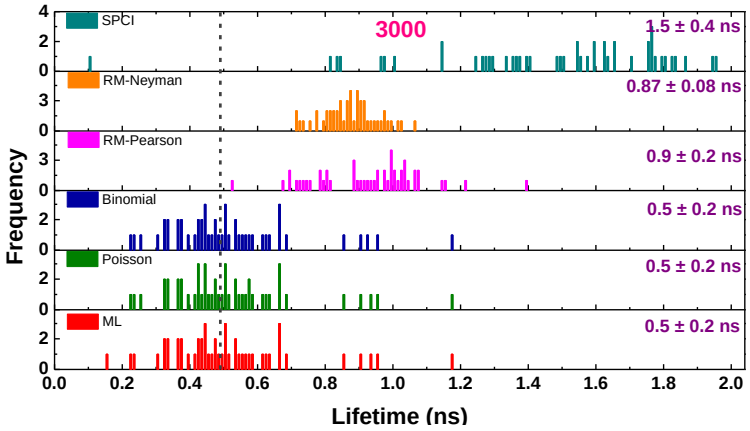

(a-ii)

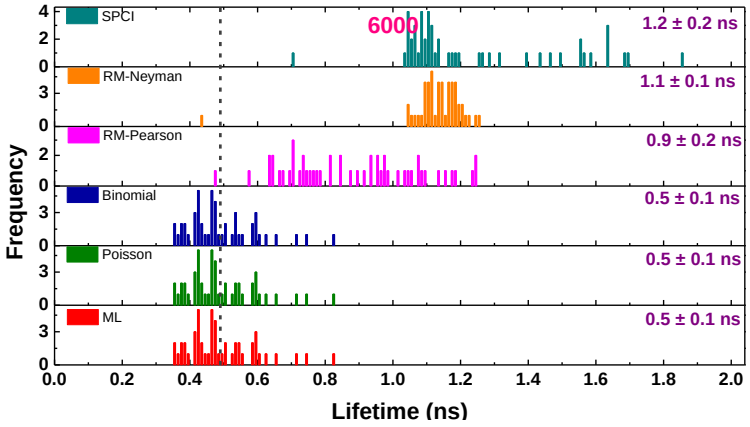

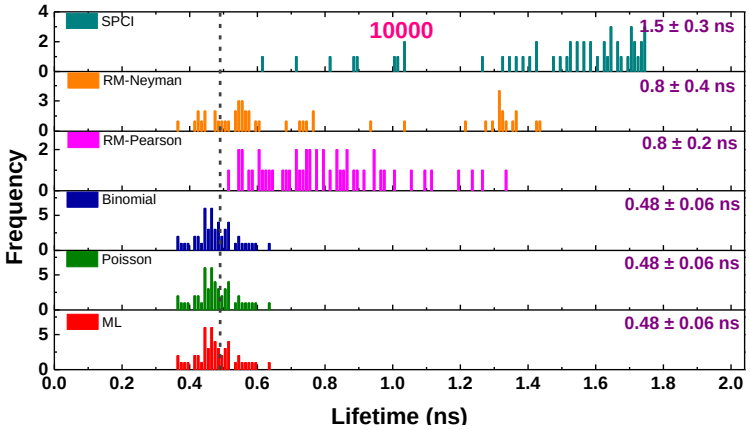

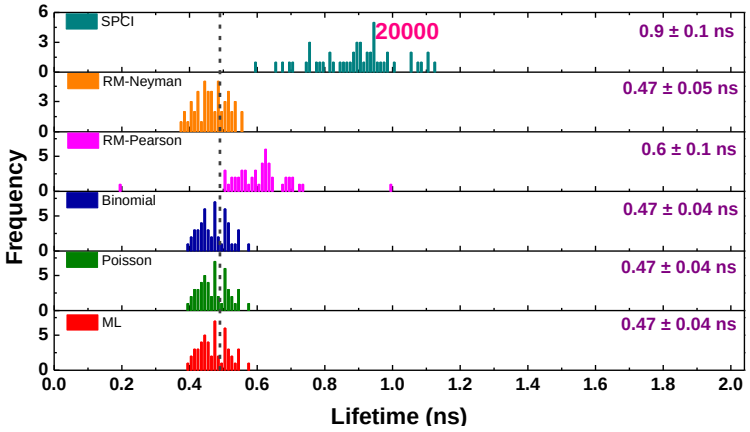

(a-iii)

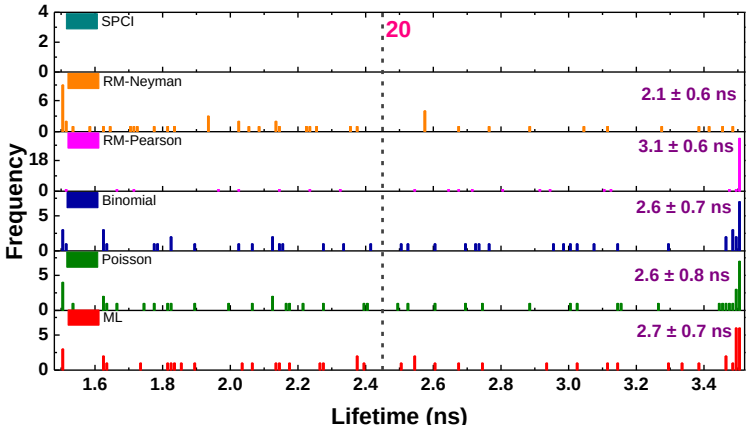

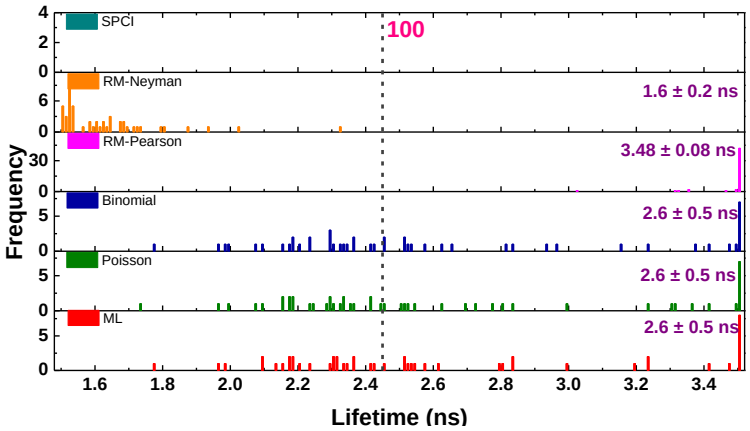

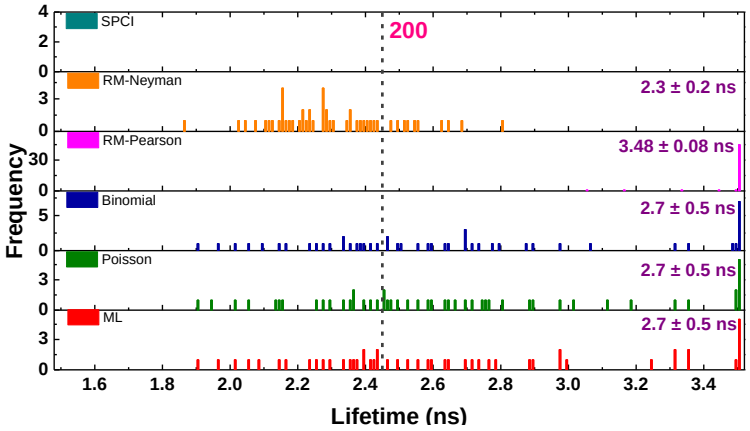

(b-i)

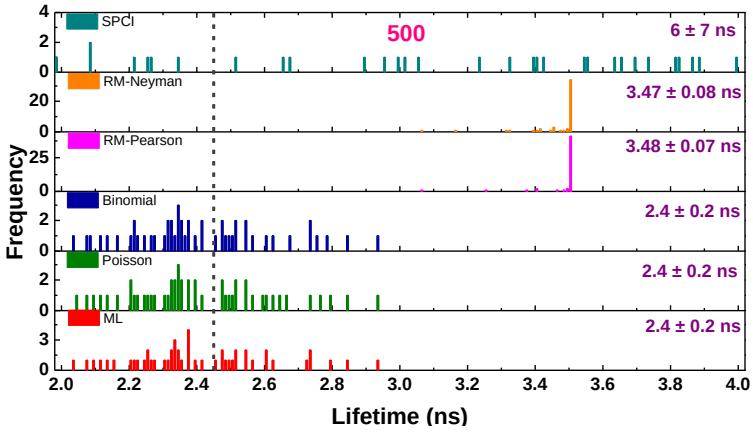

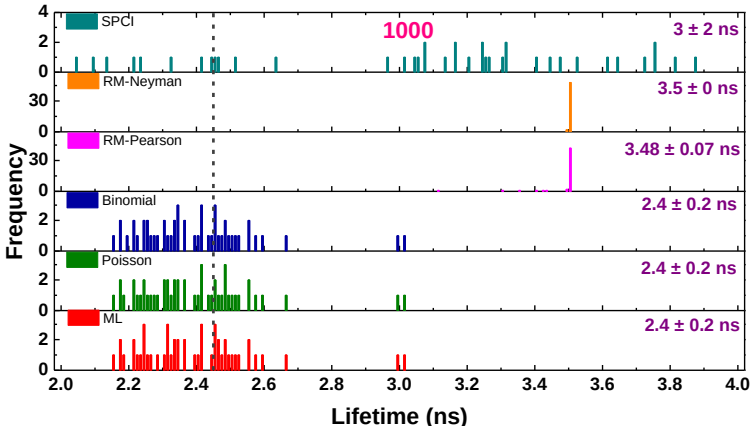

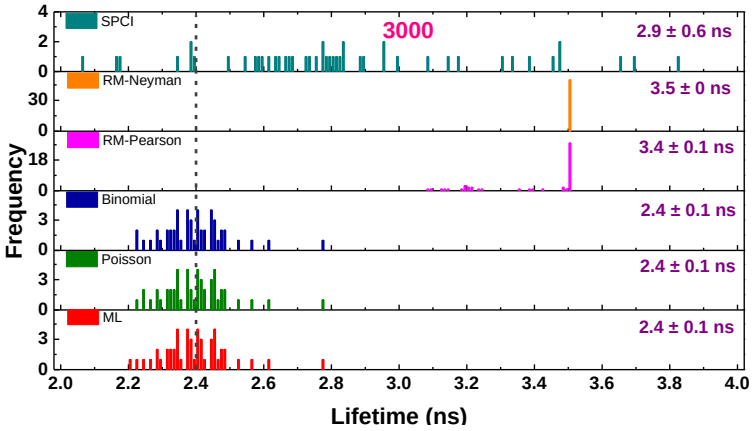

(b-ii)

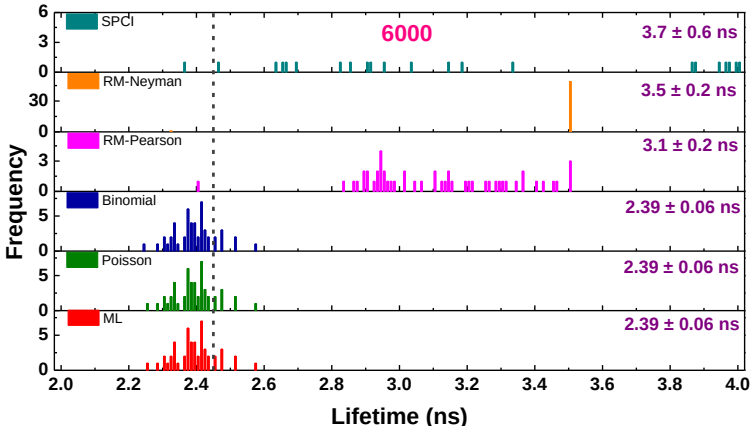

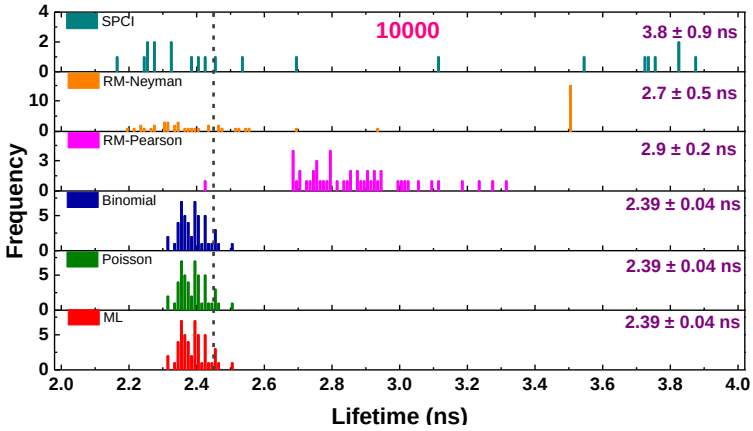

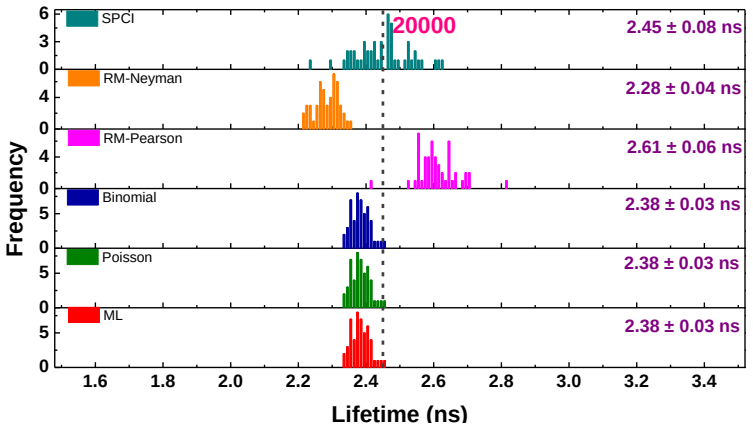

(b-iii)

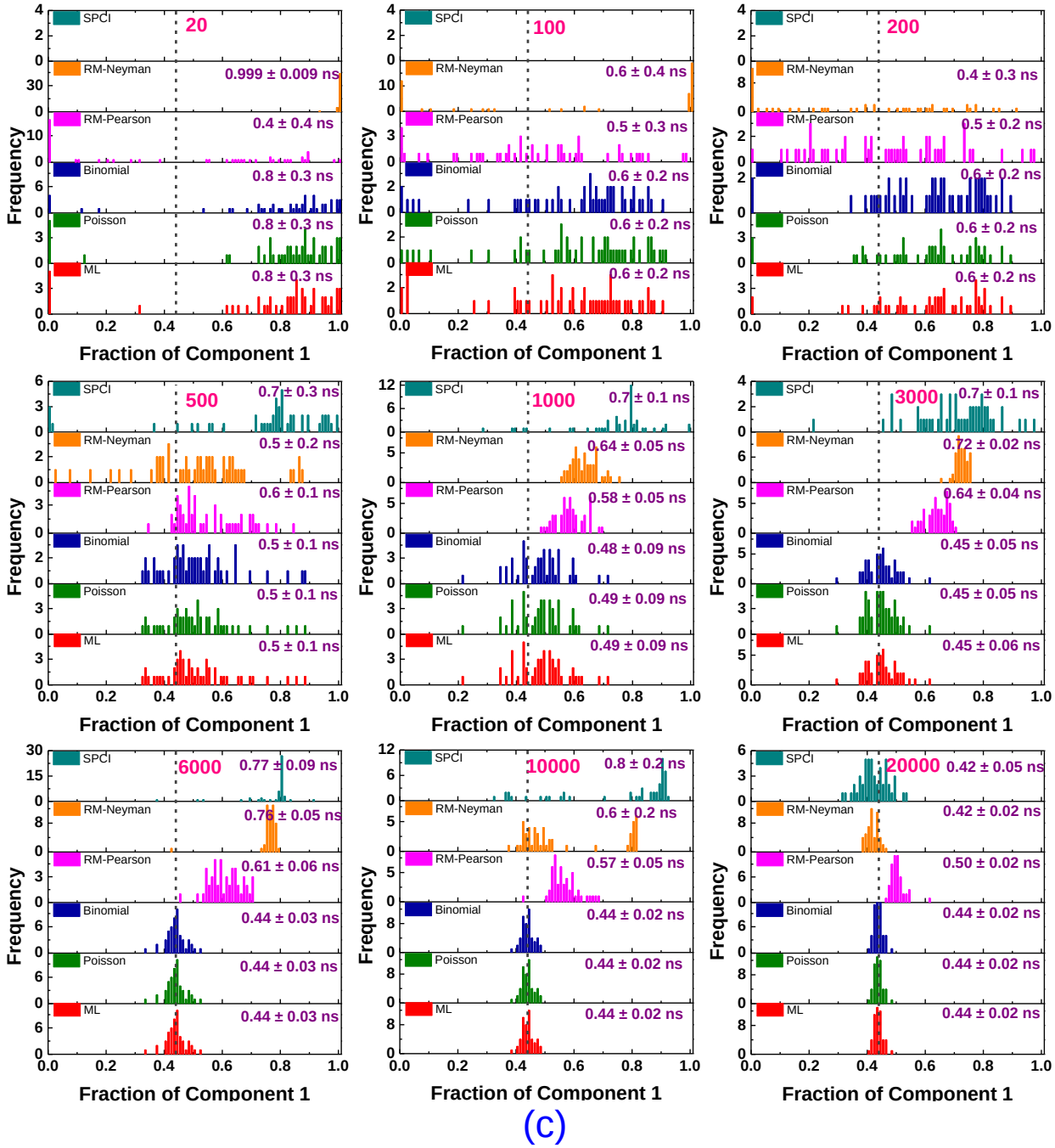

Figure S4.3. Histograms of the (a-i)-(a-iii) lifetime of rose bengal (τ_1), (b-i)-(b-iii) lifetime of rhodamine B (τ_2) and (c) the amplitude of the lifetime of the short lifetime of rose bengal (a_1) estimated by ML (red), Poisson (green), Binomial (blue), RM-Pearson (magenta), RM-Neyman (orange) and SPCI (cyan) methods for the total counts indicated in each panel in the Rb:RhB 50:50 data sets are presented. *Note that the 500-10000-count panels in part (b) have different scales for the abscissa.* The bins for all of the histograms are 10 ps wide. The vertical dark gray dash lines give target values $\tau_1 = 0.49$ ns, $\tau_2 = 2.45$ ns and $a_1 = 0.44$ in (a), (b) and (c) respectively.

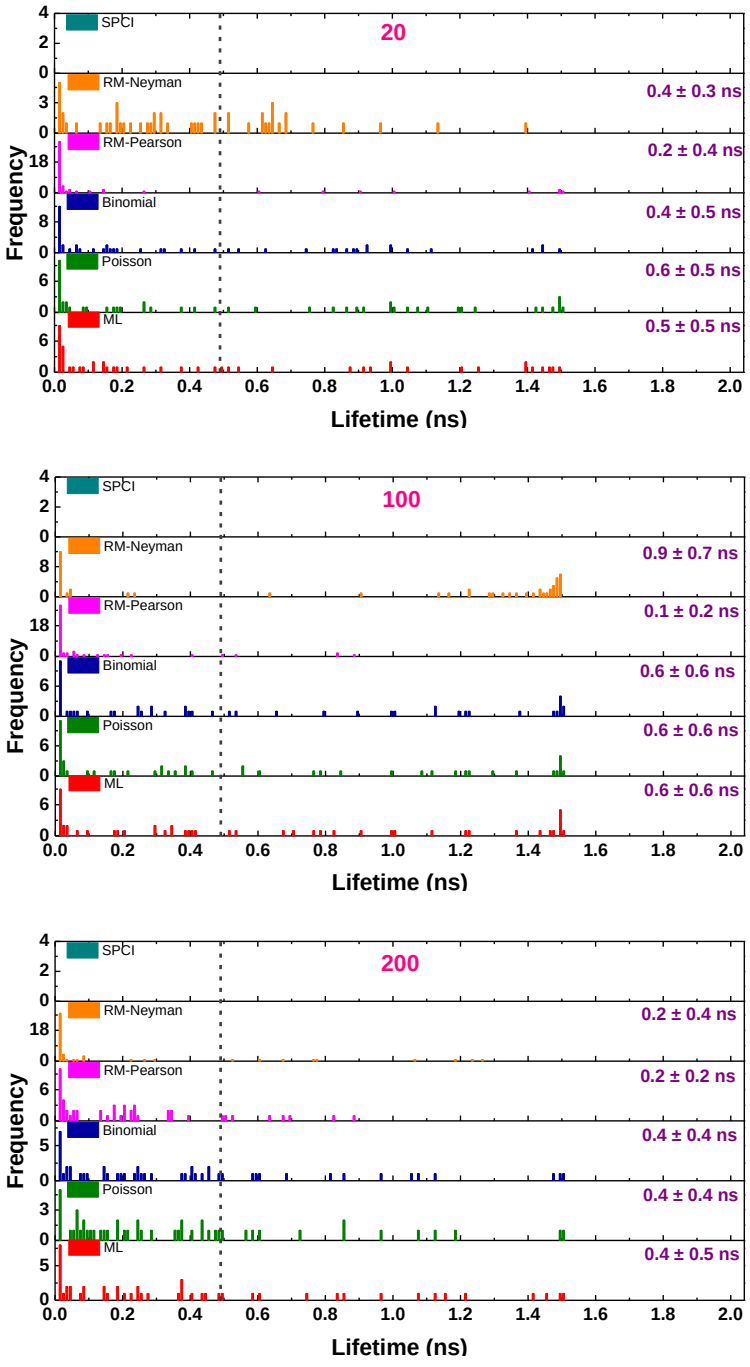

(a-i)

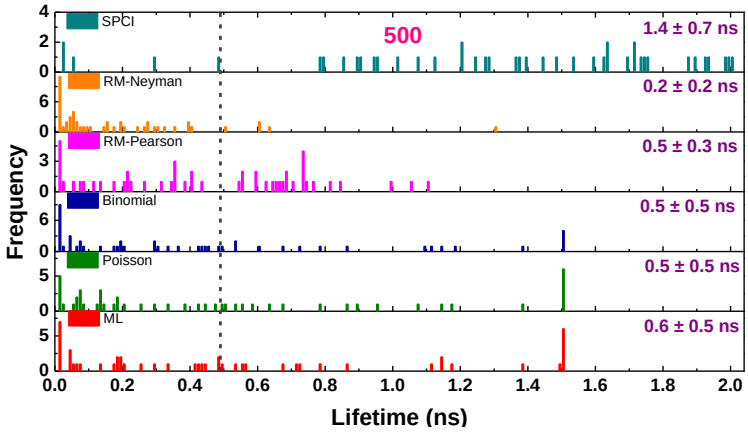

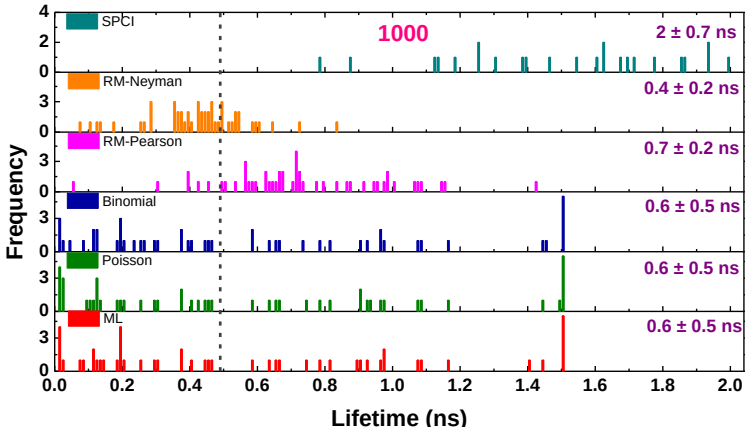

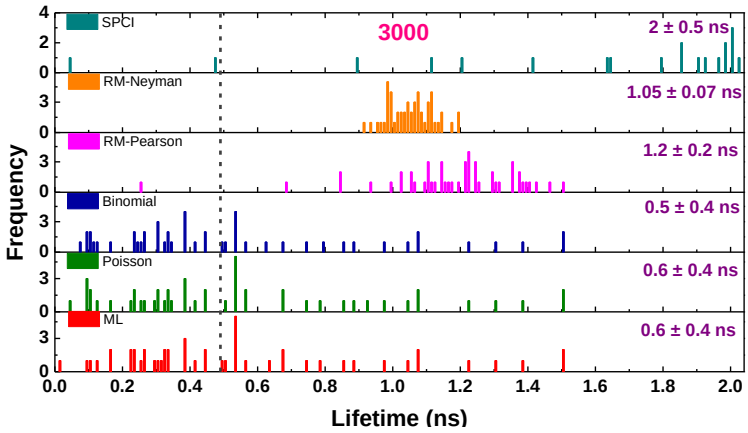

(a-ii)

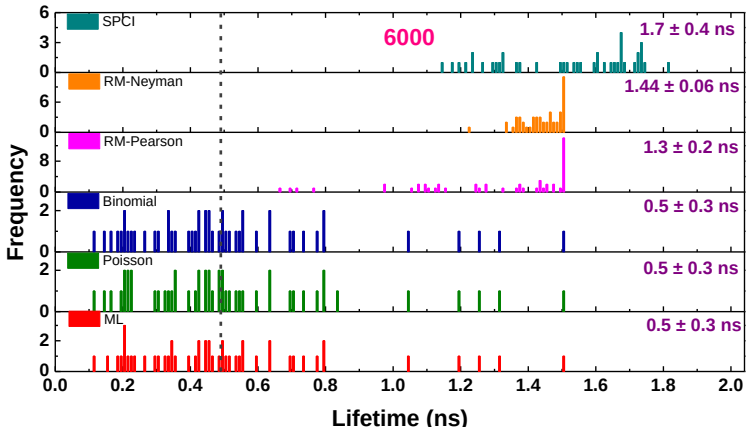

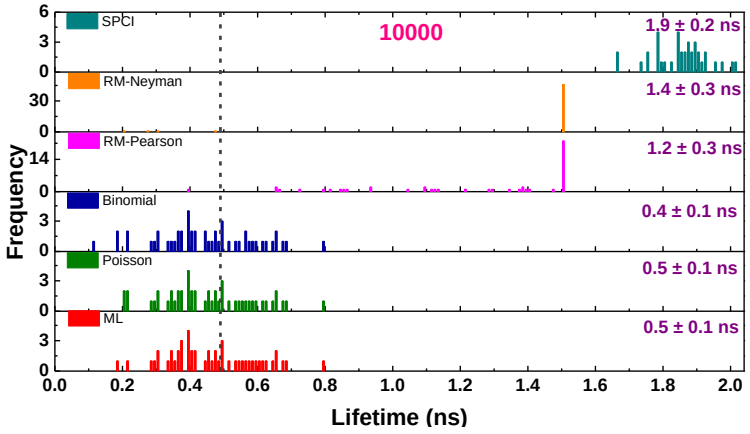

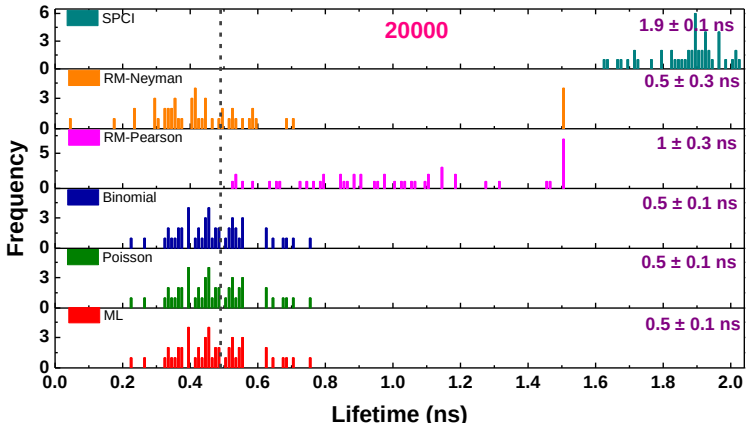

(a-iii)

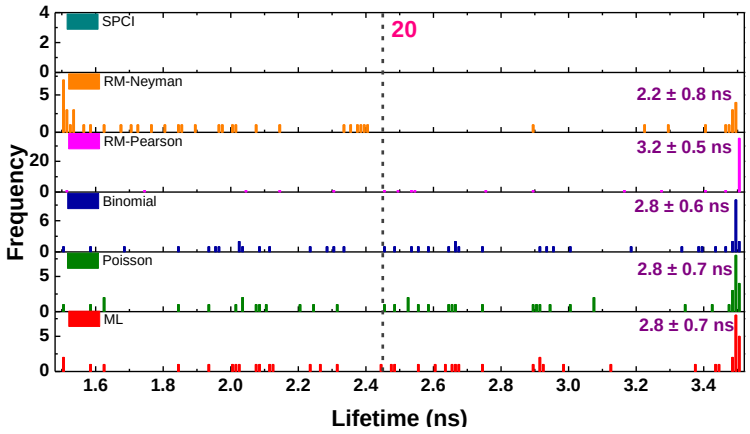

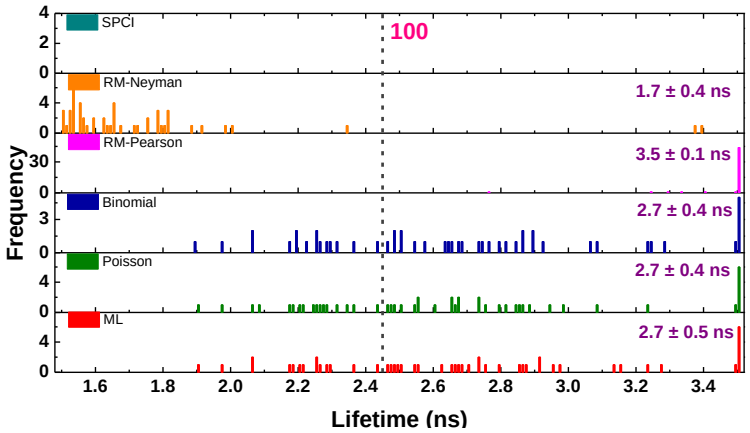

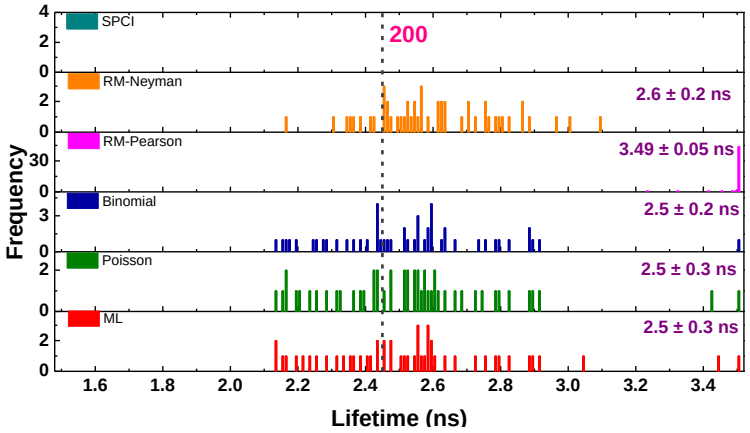

(b-i)

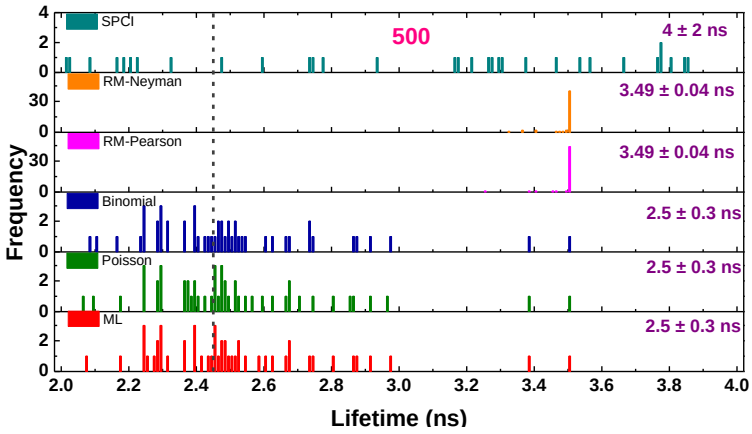

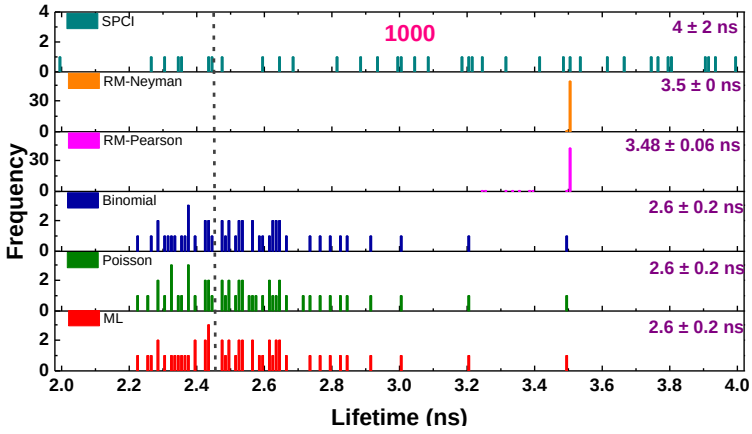

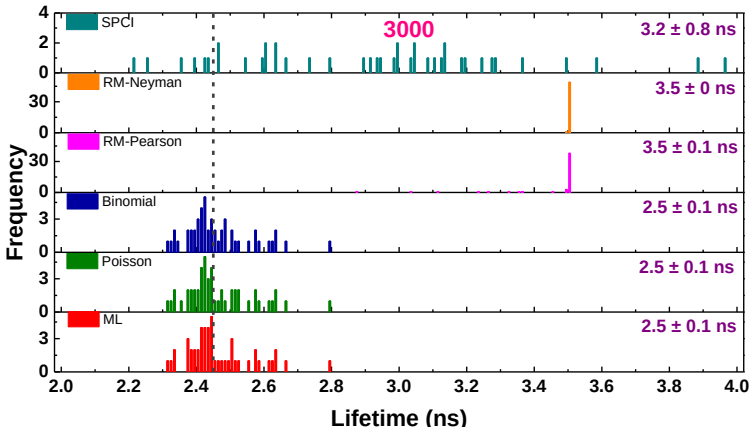

(b-ii)

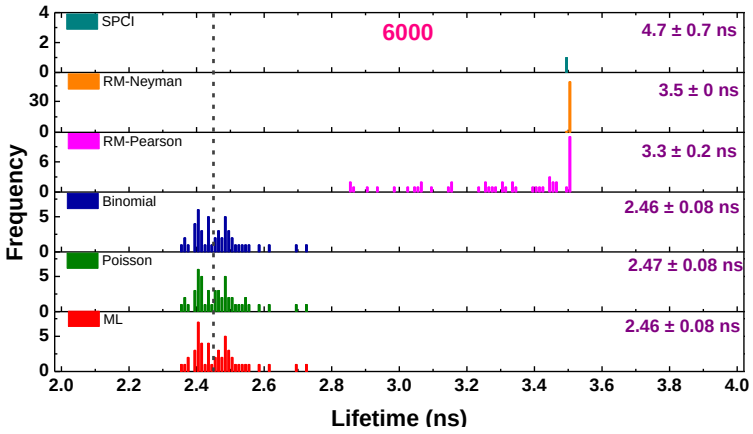

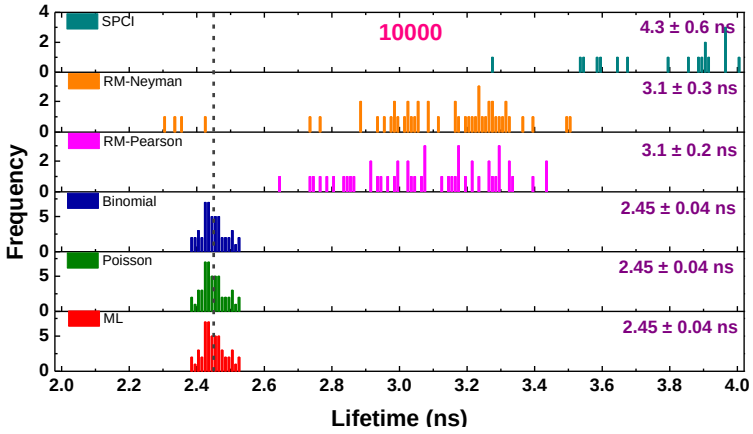

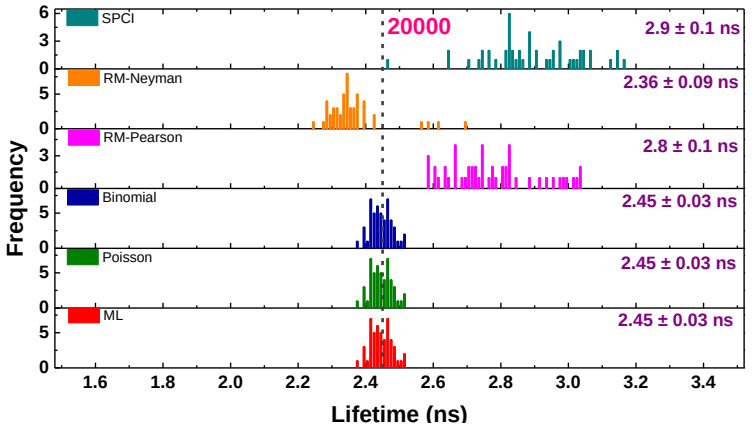

(b-iii)

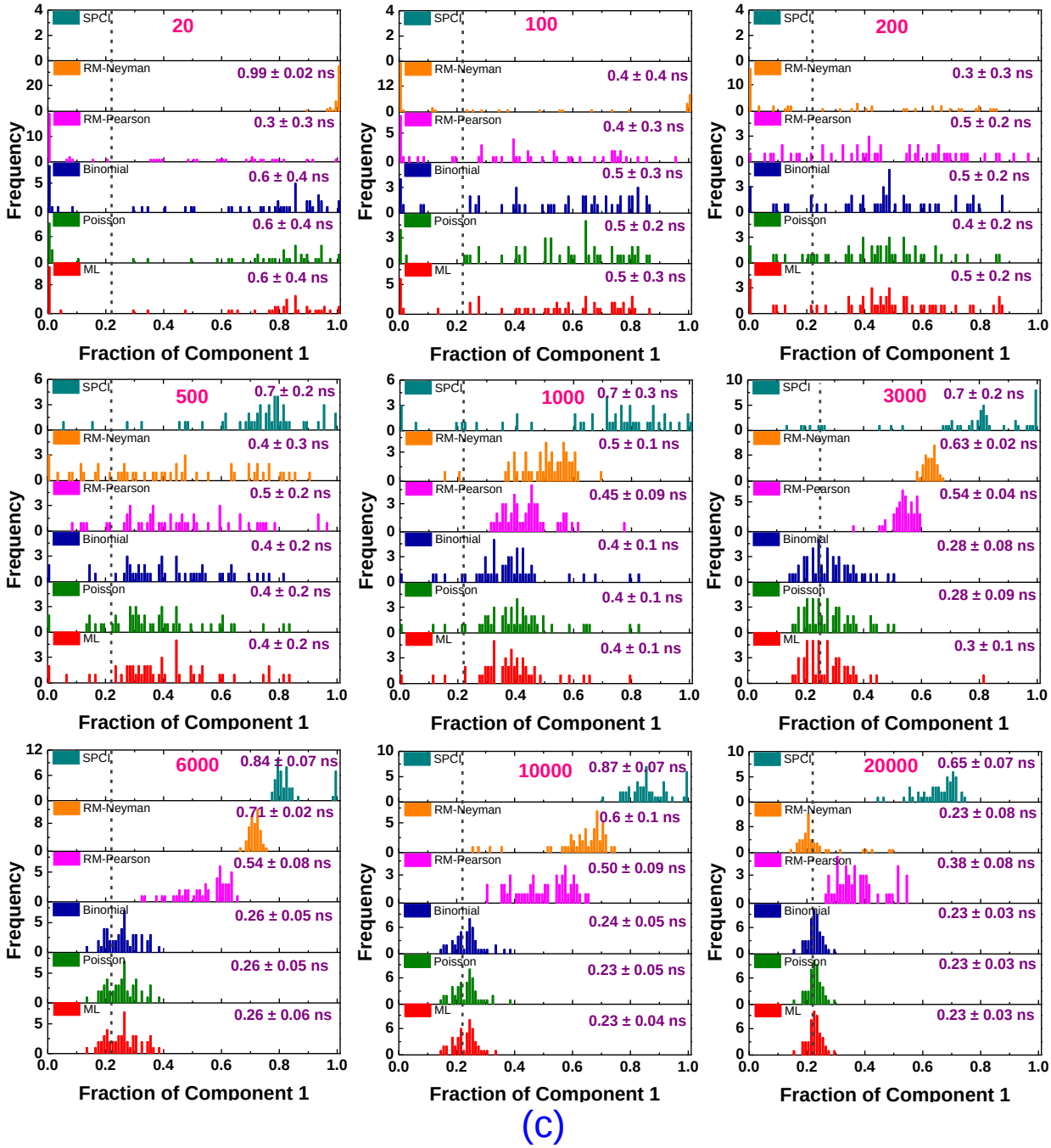

Figure S4.4. Histograms of the (a-i)-(a-iii) lifetime of rose bengal (τ_1), (b-i)-(b-iii) lifetime of rhodamine B (τ_2) and (c) the amplitude of the lifetime of the short lifetime of rose bengal (a_1) estimated by ML (red), Poisson (green), Binomial (blue), RM-Pearson (magenta), RM-Neyman (orange) and SPCI (cyan) methods for the total counts indicated in each panel in the Rb:RhB 25:75 data sets are presented. *Note that the 500-10000-count panels in part (b) have different scales for the abscissa.* The bins for all of the histograms are 10 ps wide. The vertical dark gray dash lines give target values $\tau_1 = 0.49$ ns, $\tau_2 = 2.45$ ns and $a_1 = 0.22$ in (a), (b) and (c) respectively.

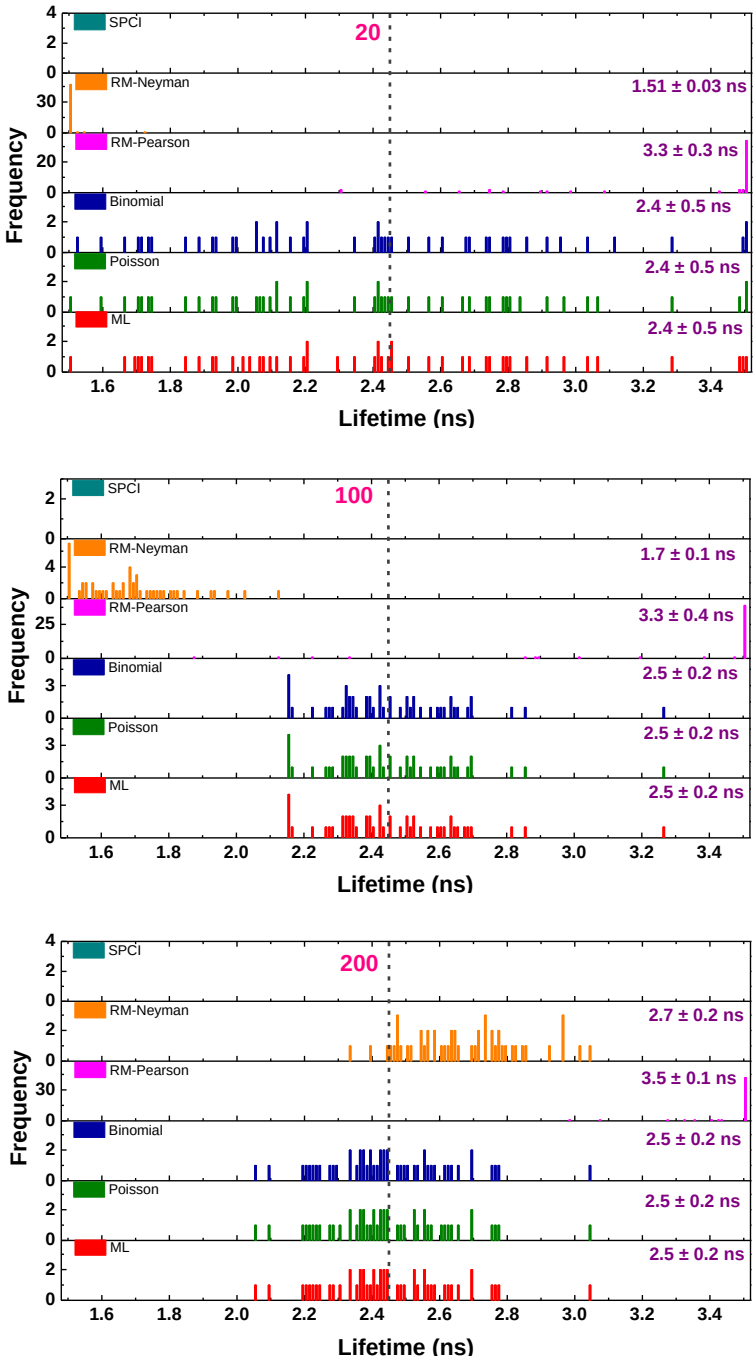

(a-i)

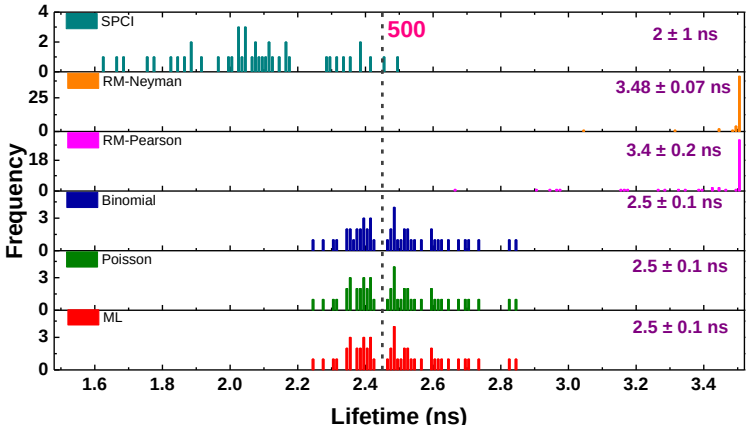

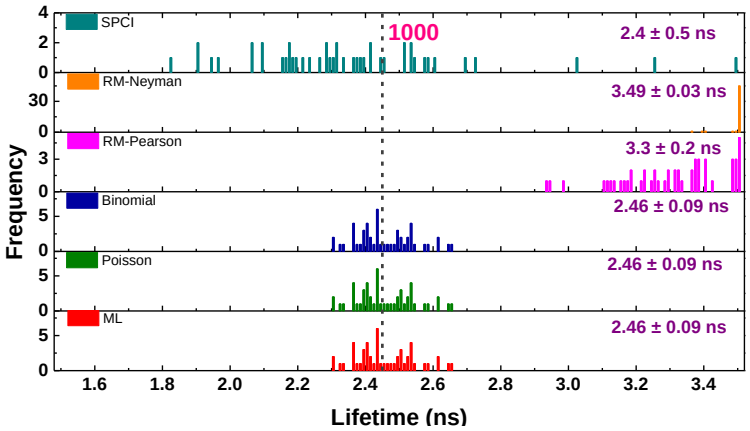

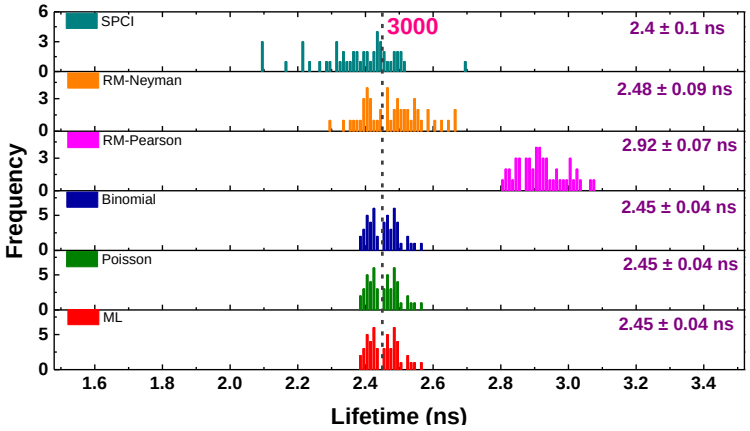

(a-ii)

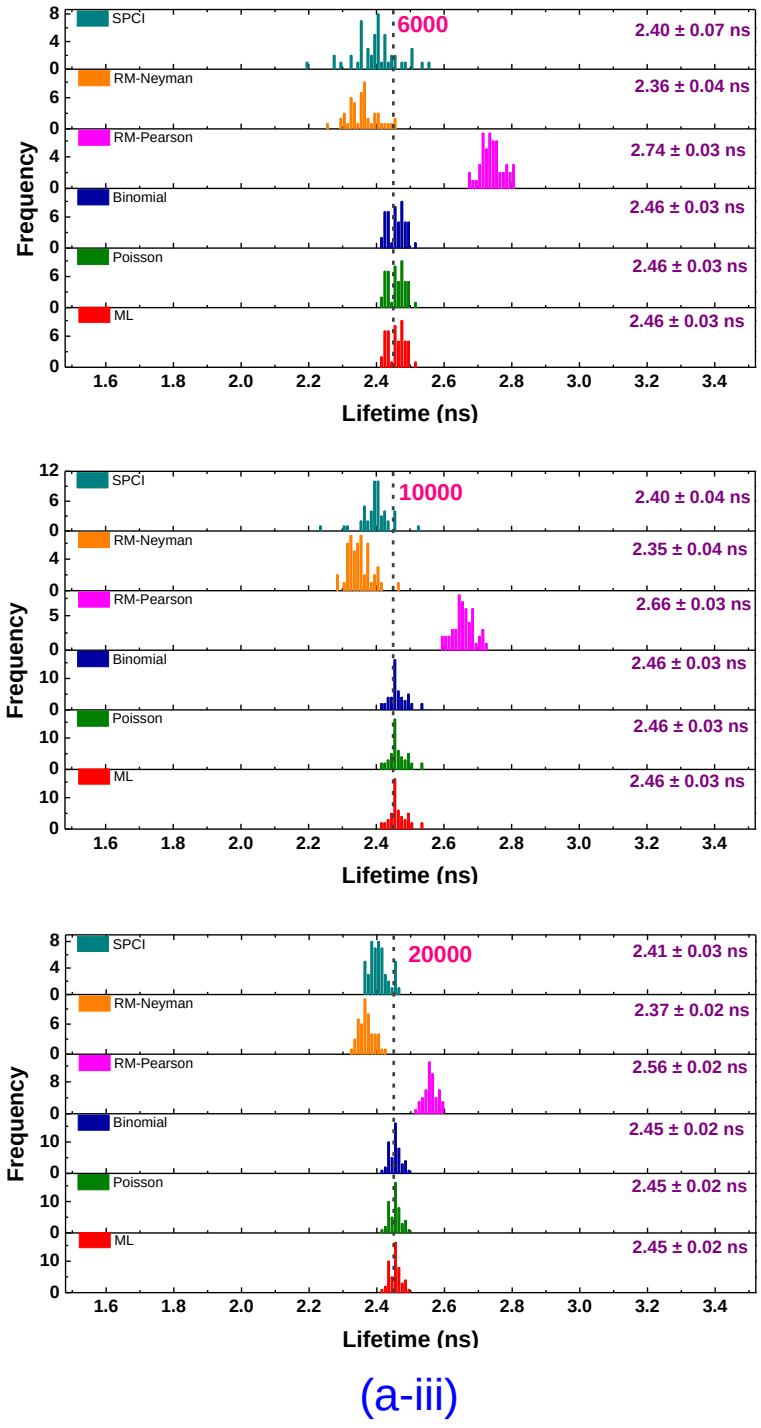

Figure S4.5. Histograms of the lifetime of rhodamine B (τ_2) estimated by ML (red), Poisson (green), Binomial (blue), RM-Pearson (magenta), RM-Neyman (orange) and SPCI (cyan) methods for the total counts indicated in each panel in the Rb:RhB 0:100 data sets are presented in (a-i)-(a-iii). The bins for all of the histograms are 10 ps wide. The vertical dark gray dash lines give target values $\tau_2 = 2.45$ ns.

Table S4.1

Rose bengal (τ_1): mean lifetime (ns) ± standard deviation (ns) for a Rb:RhB 100:0 mixture

Total counts	ML	Poisson	Binomial	RM-Pearson	RM-Neyman	SPCI
20	0.5 ± 0.1	0.5 ± 0.1	0.5 ± 0.1	0.8 ± 0.3	0.2 ± 0.1	0 ± 0
100	0.5 ± 0.07	0.5 ± 0.07	0.5 ± 0.07	0.8 ± 0.3	0.7 ± 0.1	0 ± 0
200	0.49 ± 0.03	0.49 ± 0.03	0.49 ± 0.03	0.8 ± 0.3	0.8 ± 0.1	0.7 ± 1
500	0.49 ± 0.02	0.49 ± 0.02	0.49 ± 0.02	0.8 ± 0.3	0.53 ± 0.06	0.48 ± 0.04
1000	0.49 ± 0.02	0.49 ± 0.02	0.49 ± 0.02	0.8 ± 0.3	0.47 ± 0.02	0.49 ± 0.04
3000	0.49 ± 0.01	0.49 ± 0.01	0.49 ± 0.01	0.57 ± 0.04	0.47 ± 0.01	0.49 ± 0.02
6000	0.492 ± 0.008	0.492 ± 0.008	0.492 ± 0.008	0.54 ± 0.02	0.476 ± 0.009	0.49 ± 0.01
10000	0.491 ± 0.005	0.491 ± 0.005	0.491 ± 0.005	0.52 ± 0.01	0.48 ± 0.006	0.48 ± 0.02
20000	0.49 ± 0.004	0.49 ± 0.004	0.49 ± 0.004	0.505 ± 0.006	0.482 ± 0.005	0.48 ± 0.02

Table S4.2(a)

Rose bengal (τ_1): mean lifetime (ns) ± standard deviation (ns) for a Rb:RhB 75:25 mixture

Total counts	ML	Poisson	Binomial	RM-Pearson	RM-Neyman	SPCI
20	0.5 ± 0.4	0.4 ± 0.4	0.4 ± 0.4	0.2 ± 0.4	0.4 ± 0.2	0 ± 0
100	0.5 ± 0.3	0.5 ± 0.3	0.5 ± 0.3	0.3 ± 0.2	0.9 ± 0.6	0 ± 0
200	0.5 ± 0.2	0.5 ± 0.2	0.5 ± 0.2	0.4 ± 0.2	0.2 ± 0.4	0 ± 0
500	0.5 ± 0.2	0.5 ± 0.2	0.5 ± 0.2	0.5 ± 0.1	0.3 ± 0.1	0.8 ± 0.5
1000	0.5 ± 0.1	0.5 ± 0.1	0.5 ± 0.1	0.6 ± 0.1	0.39 ± 0.05	0.6 ± 0.3
3000	0.47 ± 0.06	0.47 ± 0.06	0.47 ± 0.06	0.64 ± 0.08	0.62 ± 0.05	0.5 ± 0.2
6000	0.47 ± 0.04	0.47 ± 0.04	0.47 ± 0.04	0.6 ± 0.1	0.74 ± 0.08	0.5 ± 0.1
10000	0.47 ± 0.03	0.47 ± 0.03	0.47 ± 0.03	0.57 ± 0.04	0.55 ± 0.06	0.8 ± 0.1
20000	0.48 ± 0.02	0.48 ± 0.02	0.48 ± 0.02	0.53 ± 0.03	0.49 ± 0.03	0.52 ± 0.06

Table S4.2(b)

Rhodamine B (τ_2): mean lifetime (ns) ± standard deviation (ns) for a Rb:RhB 75:25 mixture

Total counts	ML	Poisson	Binomial	RM-Pearson	RM-Neyman	SPCI
20	2.5 ± 0.8	2.5 ± 0.8	2.5 ± 0.8	3 ± 0.6	2.2 ± 0.7	0 ± 0
100	2.5 ± 0.5	2.5 ± 0.5	2.5 ± 0.5	3.4 ± 0.2	1.6 ± 0.3	0 ± 0
200	2.3 ± 0.4	2.3 ± 0.3	2.3 ± 0.3	3.5 ± 0.1	2 ± 0.3	0 ± 0
500	2.4 ± 0.3	2.4 ± 0.3	2.4 ± 0.3	3.5 ± 0.1	3.3 ± 0.2	4 ± 8
1000	2.3 ± 0.2	2.3 ± 0.2	2.3 ± 0.2	3.5 ± 0.1	3.5 ± 0	2.4 ± 0.6
3000	2.3 ± 0.1	2.3 ± 0.1	2.3 ± 0.1	3.3 ± 0.2	3.5 ± 0	2.2 ± 0.2
6000	2.33 ± 0.06	2.33 ± 0.06	2.33 ± 0.06	3 ± 0.1	3.3 ± 0.3	2.2 ± 0.2
10000	2.32 ± 0.06	2.32 ± 0.06	2.32 ± 0.06	2.78 ± 0.09	2.4 ± 0.1	3.1 ± 0.4
20000	2.34 ± 0.04	2.34 ± 0.04	2.34 ± 0.04	2.61 ± 0.04	2.24 ± 0.05	2.4 ± 0.2

Table S4.2(c)

Rose bengal (a_1): mean value of the amplitude of the component of rose bengal emission ± standard deviation for a Rb:RhB 75:25 mixture

Total counts	ML	Poisson	Binomial	RM-Pearson	RM-Neyman	SPCI
20	0.8 ± 0.3	0.8 ± 0.3	0.8 ± 0.3	0.5 ± 0.3	0.999 ± 0.002	0 ± 0
100	0.8 ± 0.1	0.7 ± 0.1	0.7 ± 0.1	0.6 ± 0.2	0.8 ± 0.3	0 ± 0
200	0.7 ± 0.1	0.7 ± 0.1	0.7 ± 0.1	0.7 ± 0.1	0.5 ± 0.3	0 ± 0
500	0.69 ± 0.06	0.69 ± 0.06	0.69 ± 0.06	0.69 ± 0.06	0.7 ± 0.1	0.7 ± 0.2
1000	0.68 ± 0.05	0.68 ± 0.05	0.68 ± 0.05	0.74 ± 0.03	0.78 ± 0.02	0.7 ± 0.1
3000	0.69 ± 0.03	0.69 ± 0.03	0.69 ± 0.03	0.78 ± 0.02	0.84 ± 0.01	0.64 ± 0.08
6000	0.68 ± 0.02	0.68 ± 0.02	0.68 ± 0.02	0.77 ± 0.03	0.84 ± 0.03	0.64 ± 0.06
10000	0.68 ± 0.02	0.68 ± 0.02	0.68 ± 0.02	0.75 ± 0.01	0.72 ± 0.03	0.79 ± 0.05
20000	0.69 ± 0.01	0.69 ± 0.01	0.69 ± 0.01	0.73 ± 0.01	0.68 ± 0.01	0.7 ± 0.03

Table S4.3(a)

Rose bengal (τ_1): mean lifetime (ns) ± standard deviation (ns) for a Rb:RhB 50:50 mixture

Total counts	ML	Poisson	Binomial	RM-Pearson	RM-Neyman	SPCI
20	0.5 ± 0.5	0.5 ± 0.5	0.5 ± 0.5	0.3 ± 0.4	0.4 ± 0.3	0 ± 0
100	0.6 ± 0.5	0.6 ± 0.5	0.6 ± 0.5	0.2 ± 0.2	1.1 ± 0.6	0 ± 0
200	0.6 ± 0.5	0.7 ± 0.5	0.7 ± 0.5	0.3 ± 0.2	0.2 ± 0.3	0 ± 0
500	0.5 ± 0.3	0.5 ± 0.3	0.5 ± 0.3	0.5 ± 0.2	0.3 ± 0.1	1.4 ± 1.0
1000	0.5 ± 0.3	0.5 ± 0.3	0.5 ± 0.3	0.7 ± 0.2	0.43 ± 0.08	1.3 ± 0.5
3000	0.5 ± 0.2	0.5 ± 0.2	0.5 ± 0.2	0.9 ± 0.2	0.87 ± 0.08	1.5 ± 0.4
6000	0.5 ± 0.1	0.5 ± 0.1	0.5 ± 0.1	0.9 ± 0.2	1.1 ± 0.1	1.2 ± 0.2
10000	0.48 ± 0.06	0.48 ± 0.06	0.48 ± 0.06	0.8 ± 0.2	0.8 ± 0.4	1.5 ± 0.3
20000	0.47 ± 0.04	0.47 ± 0.04	0.47 ± 0.04	0.6 ± 0.1	0.47 ± 0.05	0.9 ± 0.1

Table S4.3(b)

Rhodamine B (τ_2): mean lifetime (ns) ± standard deviation (ns) for a Rb:RhB 50:50 mixture

Total counts	ML	Poisson	Binomial	RM-Pearson	RM-Neyman	SPCI
20	2.7 ± 0.7	2.6 ± 0.8	2.6 ± 0.7	3.1 ± 0.6	2.1 ± 0.6	0 ± 0
100	2.6 ± 0.5	2.6 ± 0.5	2.6 ± 0.5	3.48 ± 0.08	1.6 ± 0.2	0 ± 0
200	2.7 ± 0.5	2.7 ± 0.5	2.7 ± 0.5	3.48 ± 0.08	2.3 ± 0.2	0 ± 0
500	2.4 ± 0.2	2.4 ± 0.2	2.4 ± 0.2	3.48 ± 0.07	3.47 ± 0.08	6 ± 7
1000	2.4 ± 0.2	2.4 ± 0.2	2.4 ± 0.2	3.48 ± 0.07	3.5 ± 0	3 ± 2
3000	2.4 ± 0.1	2.4 ± 0.1	2.4 ± 0.1	3.4 ± 0.1	3.5 ± 0	2.9 ± 0.6
6000	2.39 ± 0.06	2.39 ± 0.06	2.39 ± 0.06	3.1 ± 0.2	3.5 ± 0.2	3.7 ± 0.6
10000	2.39 ± 0.04	2.39 ± 0.04	2.39 ± 0.04	2.9 ± 0.2	2.7 ± 0.5	3.8 ± 0.9
20000	2.38 ± 0.03	2.38 ± 0.03	2.38 ± 0.03	2.61 ± 0.06	2.28 ± 0.04	2.45 ± 0.08

Table S4.3(c)

Rose bengal (a_1): mean value of the amplitude of the component of rose bengal emission ± standard deviation for a Rb:RhB 50:50 mixture

Total counts	ML	Poisson	Binomial	RM-Pearson	RM-Neyman	SPCI
20	0.8 ± 0.3	0.8 ± 0.3	0.8 ± 0.3	0.4 ± 0.4	0.999 ± 0.009	0 ± 0
100	0.6 ± 0.2	0.6 ± 0.2	0.6 ± 0.2	0.5 ± 0.3	0.6 ± 0.4	0 ± 0
200	0.6 ± 0.2	0.6 ± 0.2	0.6 ± 0.2	0.5 ± 0.2	0.4 ± 0.3	0 ± 0
500	0.5 ± 0.1	0.5 ± 0.1	0.5 ± 0.1	0.6 ± 0.1	0.5 ± 0.2	0.7 ± 0.3
1000	0.49 ± 0.09	0.49 ± 0.09	0.48 ± 0.09	0.58 ± 0.05	0.64 ± 0.05	0.7 ± 0.1
3000	0.45 ± 0.06	0.45 ± 0.05	0.45 ± 0.05	0.64 ± 0.04	0.72 ± 0.02	0.7 ± 0.1
6000	0.44 ± 0.03	0.44 ± 0.03	0.44 ± 0.03	0.61 ± 0.06	0.76 ± 0.05	0.77 ± 0.09
10000	0.44 ± 0.02	0.44 ± 0.02	0.44 ± 0.02	0.57 ± 0.05	0.6 ± 0.2	0.8 ± 0.2
20000	0.44 ± 0.02	0.44 ± 0.02	0.44 ± 0.02	0.5 ± 0.02	0.42 ± 0.02	0.42 ± 0.05

Table S4.4(a)

Rose bengal (τ_1): mean lifetime (ns) ± standard deviation (ns) for a Rb:RhB 25:75 mixture

Total counts	ML	Poisson	Binomial	RM-Pearson	RM-Neyman	SPCI
20	0.5 ± 0.5	0.6 ± 0.5	0.4 ± 0.5	0.2 ± 0.4	0.4 ± 0.3	0 ± 0
100	0.6 ± 0.6	0.6 ± 0.6	0.6 ± 0.6	0.1 ± 0.2	0.9 ± 0.7	0 ± 0
200	0.4 ± 0.5	0.4 ± 0.4	0.4 ± 0.4	0.2 ± 0.2	0.2 ± 0.4	0 ± 0
500	0.6 ± 0.5	0.5 ± 0.5	0.5 ± 0.5	0.5 ± 0.3	0.2 ± 0.2	1.4 ± 0.7
1000	0.6 ± 0.5	0.6 ± 0.5	0.6 ± 0.5	0.7 ± 0.2	0.4 ± 0.2	2 ± 0.7
3000	0.6 ± 0.4	0.6 ± 0.4	0.5 ± 0.4	1.2 ± 0.2	1.05 ± 0.07	2 ± 0.5
6000	0.5 ± 0.3	0.5 ± 0.3	0.5 ± 0.3	1.3 ± 0.2	1.44 ± 0.06	1.7 ± 0.4
10000	0.5 ± 0.1	0.5 ± 0.1	0.4 ± 0.1	1.2 ± 0.3	1.4 ± 0.3	1.9 ± 0.2
20000	0.5 ± 0.1	0.5 ± 0.1	0.5 ± 0.1	1 ± 0.3	0.5 ± 0.3	1.9 ± 0.1

Table S4.4(b)

Rhodamine B (τ_2): mean lifetime (ns) ± standard deviation (ns) for a Rb:RhB 25:75 mixture

Total counts	ML	Poisson	Binomial	RM-Pearson	RM-Neyman	SPCI
20	2.8 ± 0.7	2.8 ± 0.7	2.8 ± 0.6	3.2 ± 0.5	2.2 ± 0.8	0 ± 0
100	2.7 ± 0.5	2.7 ± 0.4	2.7 ± 0.4	3.5 ± 0.1	1.7 ± 0.4	0 ± 0
200	2.5 ± 0.3	2.5 ± 0.3	2.5 ± 0.2	3.49 ± 0.05	2.6 ± 0.2	0 ± 0
500	2.5 ± 0.3	2.5 ± 0.3	2.5 ± 0.3	3.49 ± 0.04	3.49 ± 0.04	4 ± 2
1000	2.6 ± 0.2	2.6 ± 0.2	2.6 ± 0.2	3.48 ± 0.06	3.5 ± 0	4 ± 2
3000	2.5 ± 0.1	2.5 ± 0.1	2.5 ± 0.1	3.5 ± 0.1	3.5 ± 0	3.2 ± 0.8
6000	2.46 ± 0.08	2.47 ± 0.08	2.46 ± 0.08	3.3 ± 0.2	3.5 ± 0	4.7 ± 0.7
10000	2.45 ± 0.04	2.45 ± 0.04	2.45 ± 0.04	3.1 ± 0.2	3.1 ± 0.3	4.3 ± 0.6
20000	2.45 ± 0.03	2.45 ± 0.03	2.45 ± 0.03	2.8 ± 0.1	2.36 ± 0.09	2.9 ± 0.1

Table S4.4(c)

Rose bengal (a_1): mean value of the amplitude of the component of rose bengal emission ± standard deviation for a Rb:RhB 25:75 mixture

Total counts	ML	Poisson	Binomial	RM-Pearson	RM-Neyman	SPCI
20	0.6 ± 0.4	0.6 ± 0.4	0.6 ± 0.4	0.3 ± 0.3	0.99 ± 0.02	0 ± 0
100	0.5 ± 0.3	0.5 ± 0.2	0.5 ± 0.3	0.4 ± 0.3	0.4 ± 0.4	0 ± 0
200	0.5 ± 0.2	0.4 ± 0.2	0.5 ± 0.2	0.5 ± 0.2	0.3 ± 0.3	0 ± 0
500	0.4 ± 0.2	0.4 ± 0.2	0.4 ± 0.2	0.5 ± 0.2	0.4 ± 0.3	0.7 ± 0.2
1000	0.4 ± 0.1	0.4 ± 0.1	0.4 ± 0.1	0.45 ± 0.09	0.5 ± 0.1	0.7 ± 0.3
3000	0.3 ± 0.1	0.28 ± 0.09	0.28 ± 0.08	0.54 ± 0.04	0.63 ± 0.02	0.7 ± 0.2
6000	0.26 ± 0.06	0.26 ± 0.05	0.26 ± 0.05	0.54 ± 0.08	0.71 ± 0.02	0.84 ± 0.07
10000	0.23 ± 0.04	0.23 ± 0.05	0.24 ± 0.05	0.5 ± 0.09	0.6 ± 0.1	0.87 ± 0.07
20000	0.23 ± 0.03	0.23 ± 0.03	0.23 ± 0.03	0.38 ± 0.08	0.23 ± 0.08	0.65 ± 0.07

Table S4.5

Rhodamine B (τ_2): mean lifetime (ns) ± standard deviation (ns) for a Rb:RhB 0:100 mixture

Total counts	ML	Poisson	Binomial	RM-Pearson	RM-Neyman	SPCI
20	2.4 ± 0.5	2.4 ± 0.5	2.4 ± 0.5	3.3 ± 0.3	1.51 ± 0.03	0 ± 0
100	2.5 ± 0.2	2.5 ± 0.2	2.5 ± 0.2	3.3 ± 0.4	1.7 ± 0.1	0 ± 0
200	2.5 ± 0.2	2.5 ± 0.2	2.5 ± 0.2	3.5 ± 0.1	2.7 ± 0.2	0 ± 0
500	2.5 ± 0.1	2.5 ± 0.1	2.5 ± 0.1	3.4 ± 0.2	3.48 ± 0.07	2 ± 1
1000	2.46 ± 0.09	2.46 ± 0.09	2.46 ± 0.09	3.3 ± 0.2	3.49 ± 0.03	2.4 ± 0.5
3000	2.45 ± 0.04	2.45 ± 0.04	2.45 ± 0.04	2.92 ± 0.07	2.48 ± 0.09	2.4 ± 0.1
6000	2.46 ± 0.03	2.46 ± 0.03	2.46 ± 0.03	2.74 ± 0.03	2.36 ± 0.04	2.4 ± 0.07
10000	2.46 ± 0.03	2.46 ± 0.03	2.46 ± 0.03	2.66 ± 0.03	2.35 ± 0.04	2.4 ± 0.04
20000	2.45 ± 0.02	2.45 ± 0.02	2.45 ± 0.02	2.56 ± 0.02	2.37 ± 0.02	2.41 ± 0.03

4.9.2 Bin-by-bin analyses of a single fluorescence decay

Poisson distribution

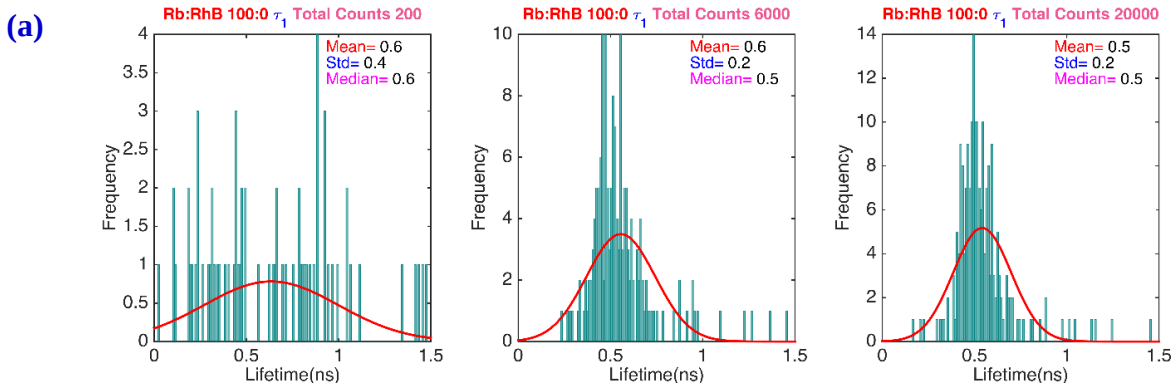

Figure S4.6. Histograms of the frequencies of obtaining values of the fluorescence decay parameter for τ_1 is presented in panels (a). The histograms are obtained from a bin-by-bin analysis using the Poisson distribution of a representative, single fluorescence decay trace from a 100:0 mixture of Rb and RhB with total counts of 200, 6000, and 20000. The histograms are fit to Gaussians using the values of the mean and standard deviation obtained from them.

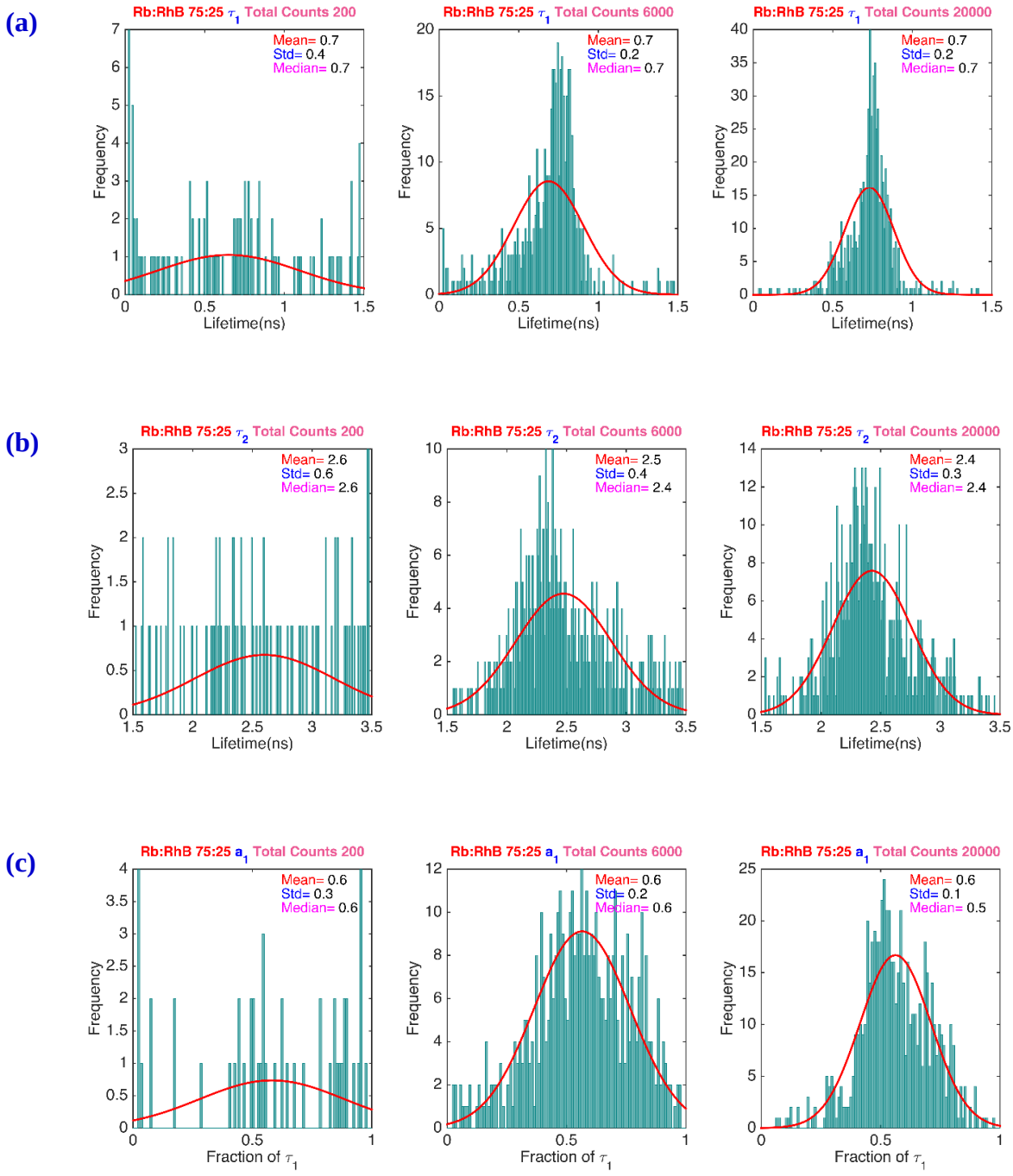

Figure S4.7. Histograms of the frequencies of obtaining values of the fluorescence decay parameters for τ_1, τ_2, and a_1 are presented in panels (a), (b), and (c), respectively. The histograms are obtained from a bin-by-bin analysis using the Poisson distribution of a representative, single fluorescence decay trace from a 75:25 mixture of Rb and RhB with total counts of 200, 6000, and 20000. The histograms are fit to Gaussians using the values of the mean and standard deviation obtained from them.

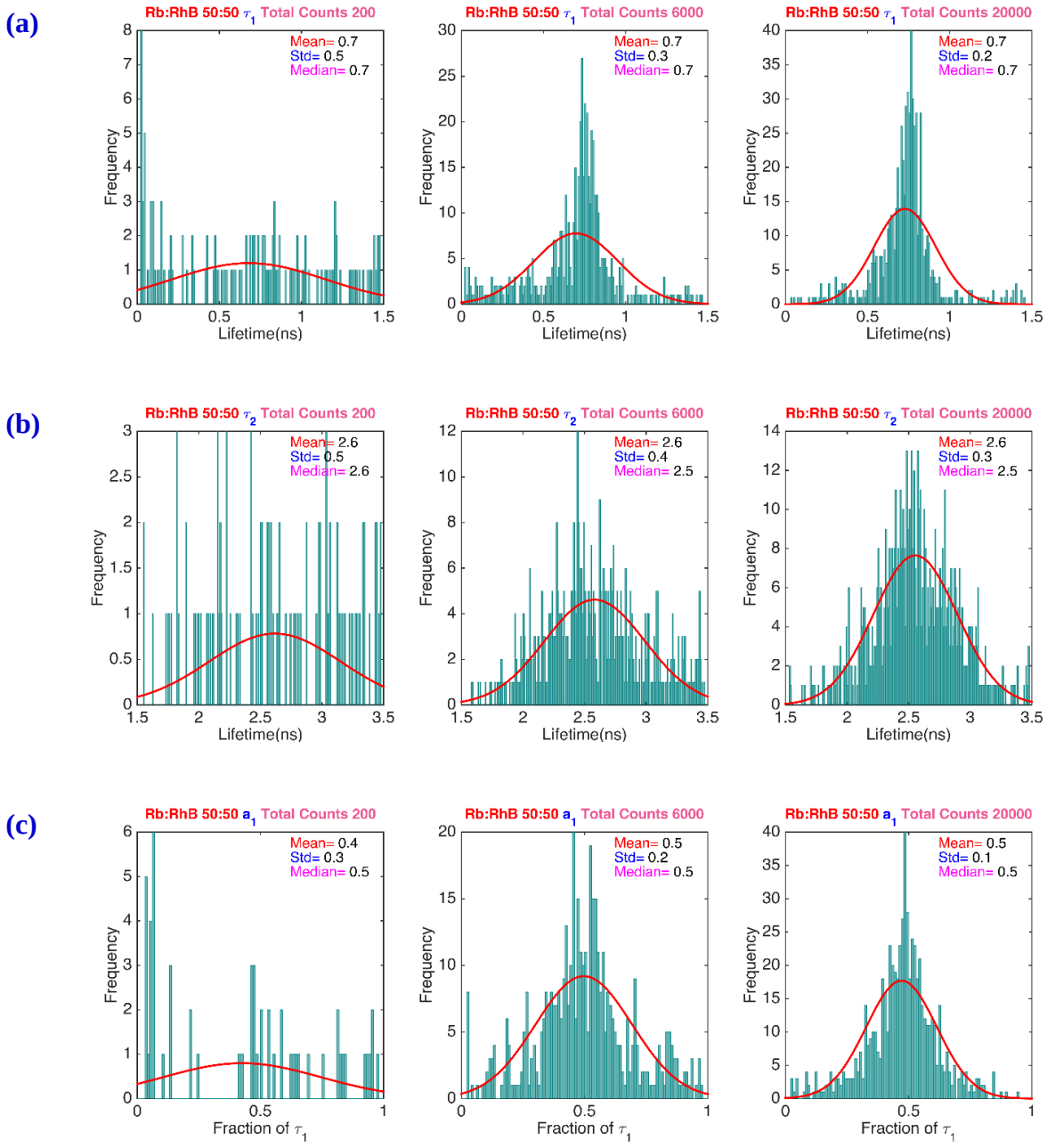

Figure S4.8. Histograms of the frequencies of obtaining values of the fluorescence decay parameters for τ_1, τ_2, and a_1 are presented in panels (a), (b), and (c), respectively. The histograms are obtained from a bin-by-bin analysis using the Poisson distribution of a representative, single fluorescence decay trace from a 50:50 mixture of Rb and RhB with total counts of 200, 6000, and 20000. The histograms are fit to Gaussians using the values of the mean and standard deviation obtained from them.

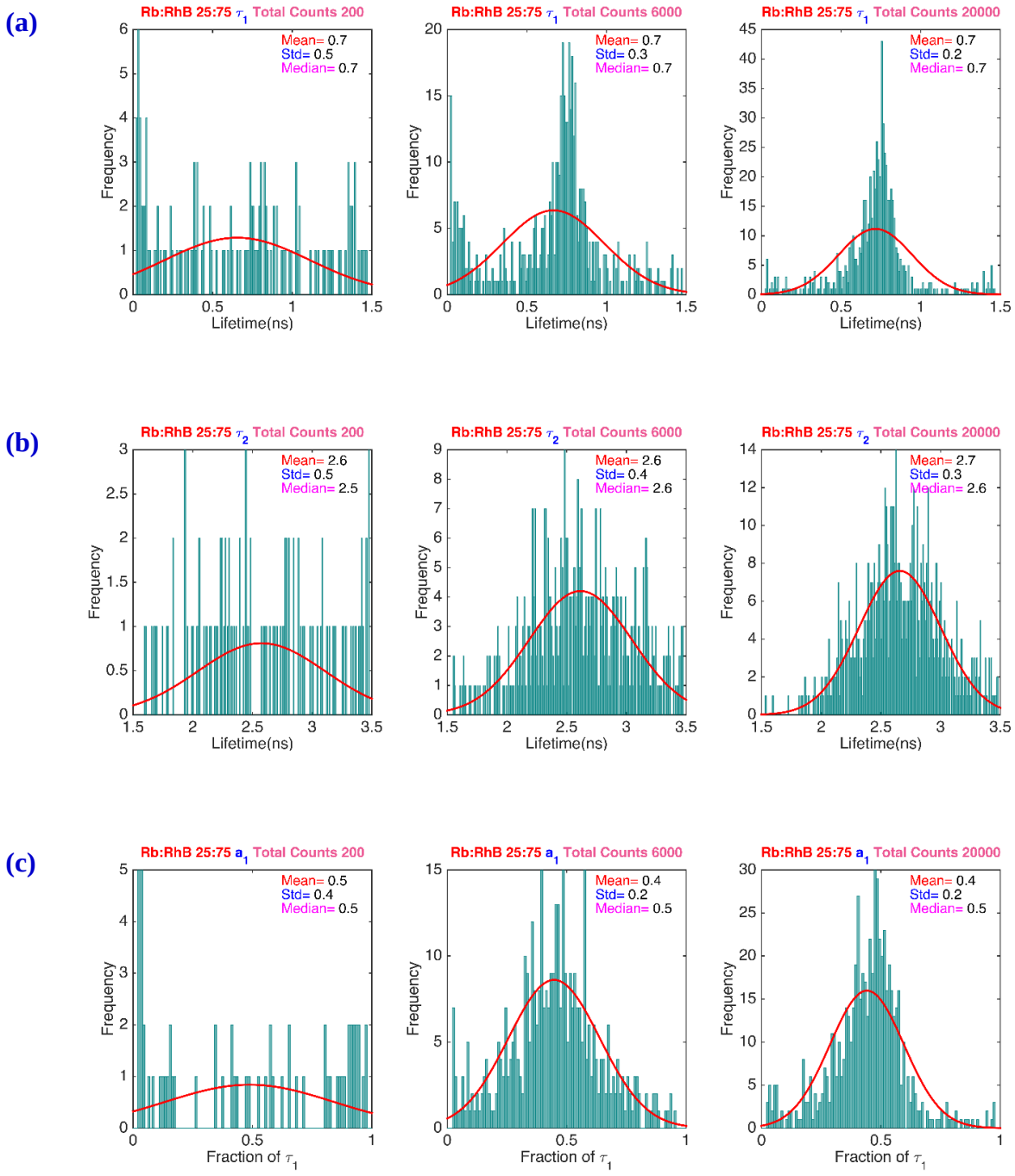

Figure S4.9. Histograms of the frequencies of obtaining values of the fluorescence decay parameters for τ_1, τ_2, and a_1 are presented in panels (a), (b), and (c), respectively. The histograms are obtained from a bin-by-bin analysis using the Poisson distribution of a representative, single fluorescence decay trace from a 25:75 mixture of Rb and RhB with total counts of 200, 6000, and 20000. The histograms are fit to Gaussians using the values of the mean and standard deviation obtained from them.

(a)

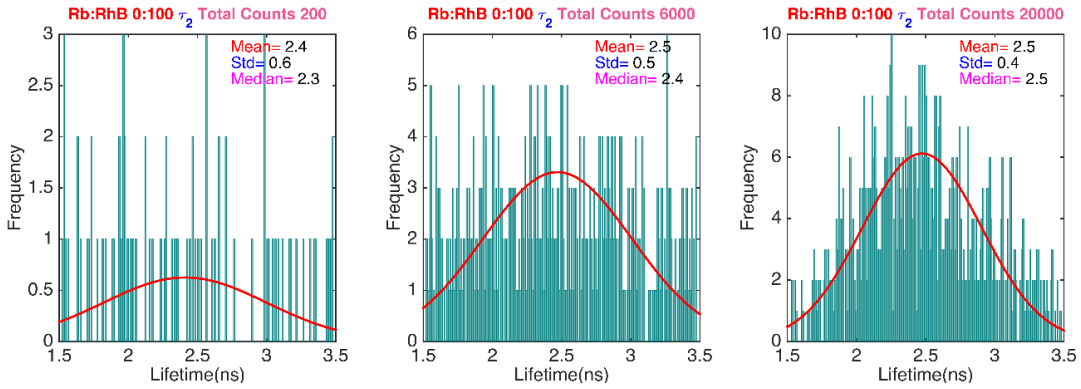

Figure S4.10. Histograms of the frequencies of obtaining values of the fluorescence decay parameters τ_2 is presented in panels (a). The histograms are obtained from a bin-by-bin analysis using the Poisson distribution of a representative, single fluorescence decay trace from a 0:100 mixture of Rb and RhB with total counts of 200, 6000, and 20000. The histograms are fit to Gaussians using the values of the mean and standard deviation obtained from them.

Binomial distribution

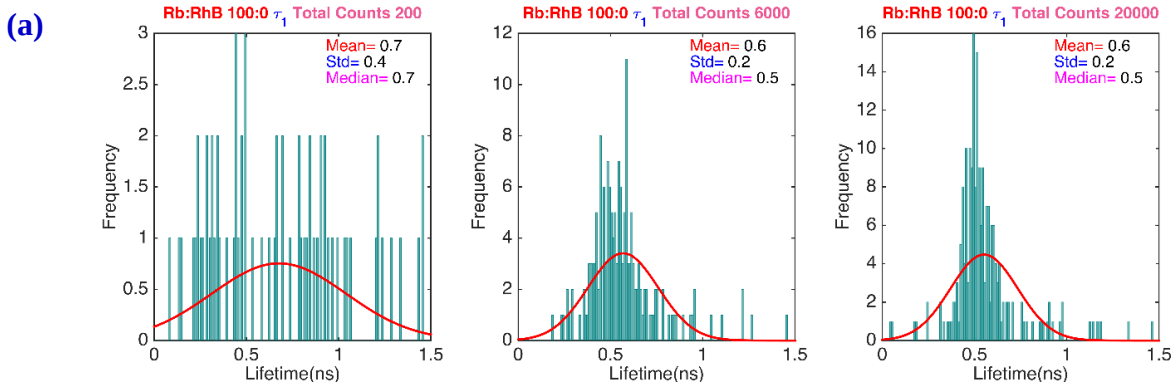

Figure S4.11. Histograms of the frequencies of obtaining values of the fluorescence decay parameter τ_1 is presented in panels (a). The histograms are obtained from a bin-by-bin analysis using the binomial distribution of a representative, single fluorescence decay trace from a 100:0 mixture of Rb and RhB with total counts of 200, 6000, and 20000. The histograms are fit to Gaussians using the values of the mean and standard deviation obtained from them.

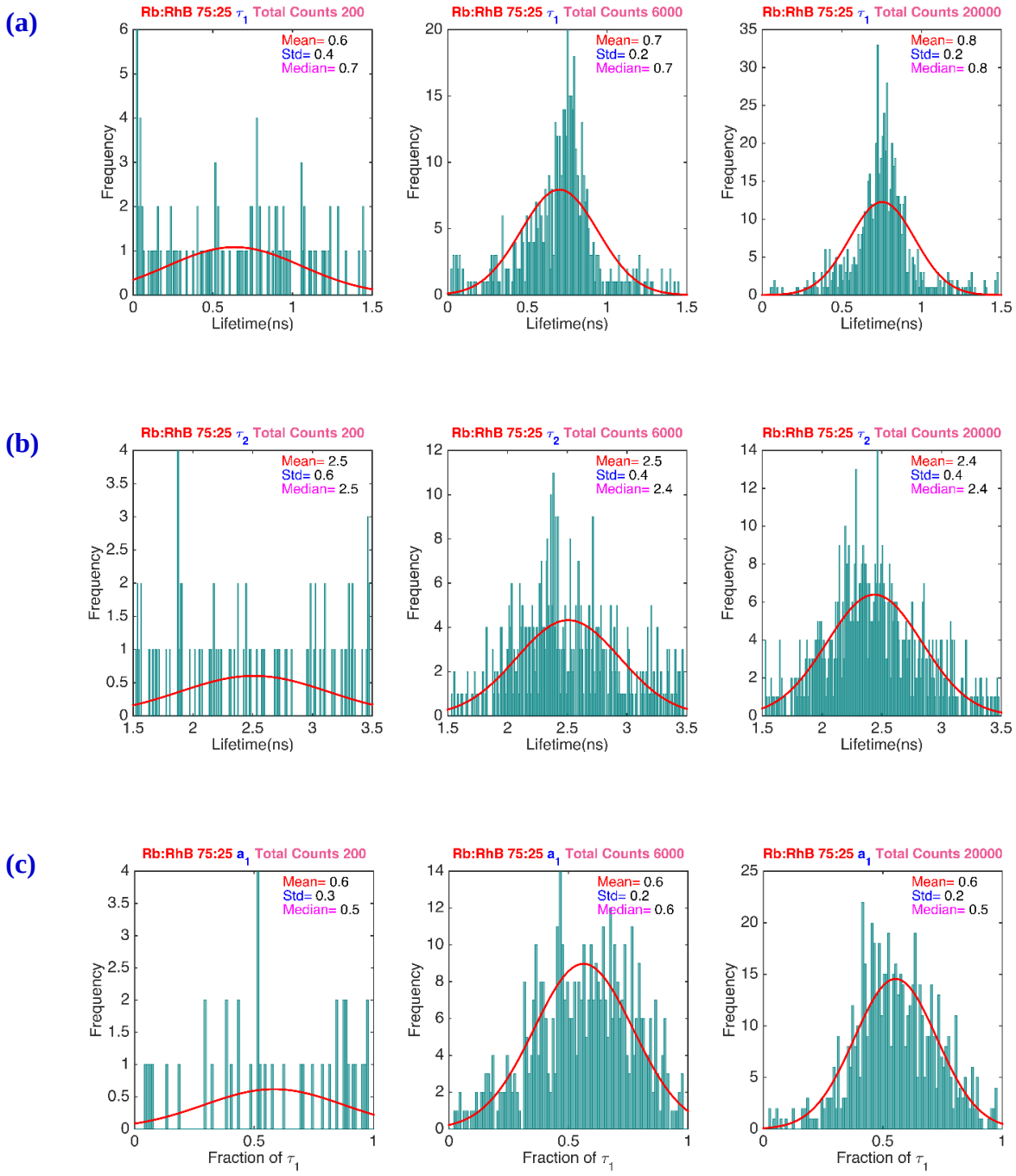

Figure S4.12. Histograms of the frequencies of obtaining values of the fluorescence decay parameters for τ_1, τ_2, and a_1 are presented in panels (a), (b), and (c), respectively. The histograms are obtained from a bin-by-bin analysis using the binomial distribution of a representative, single fluorescence decay trace from a 75:25 mixture of Rb and RhB with total counts of 200, 6000, and 20000. The histograms are fit to Gaussians using the values of the mean and standard deviation obtained from them.

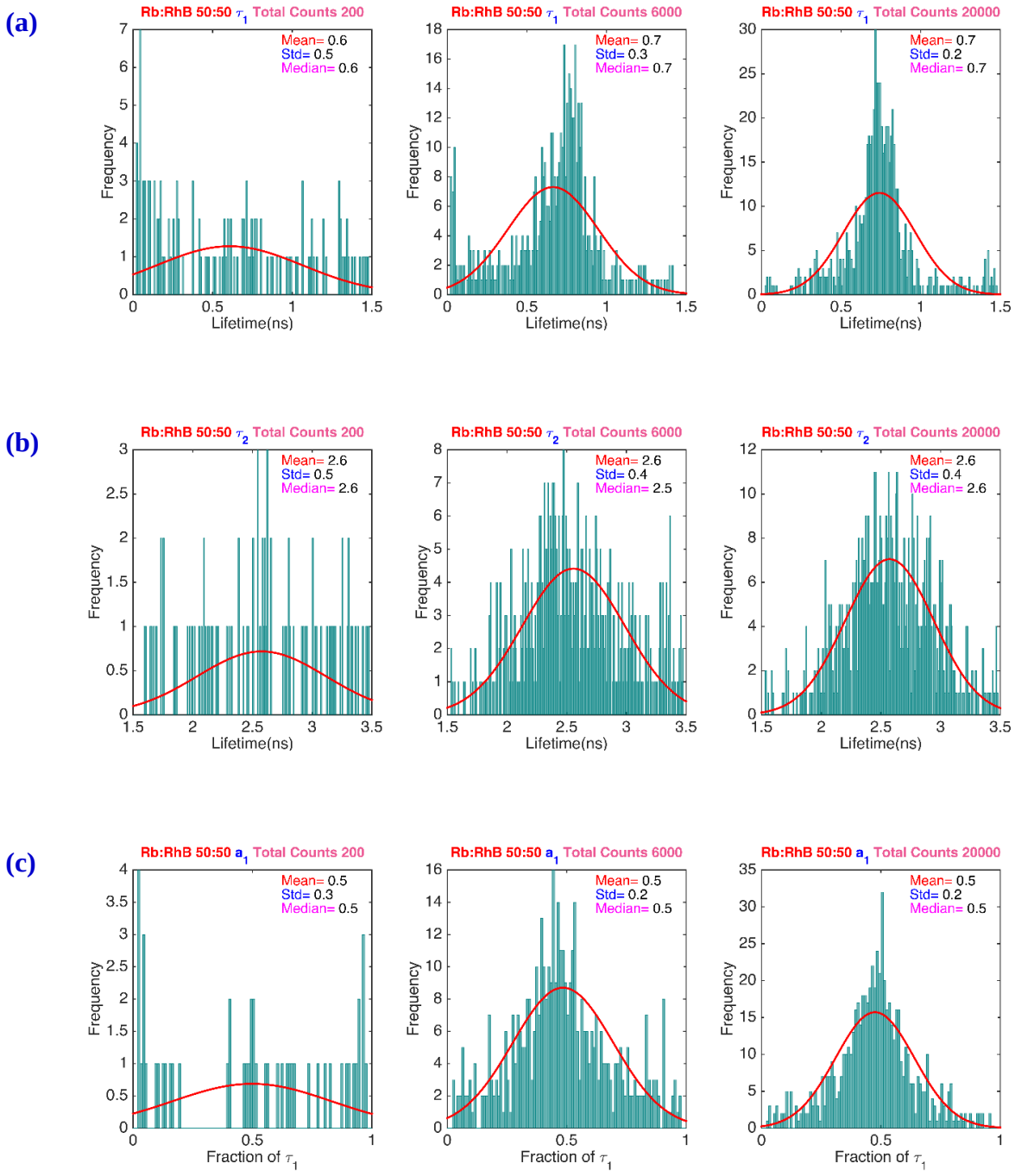

Figure S4.13. Histograms of the frequencies of obtaining values of the fluorescence decay parameters for τ_1, τ_2, and a_1 are presented in panels (a), (b), and (c), respectively. The histograms are obtained from a bin-by-bin analysis using the binomial distribution of a representative, single fluorescence decay trace from a 50:50 mixture of Rb and RhB with total counts of 200, 6000, and 20000. The histograms are fit to Gaussians using the values of the mean and standard deviation obtained from them.

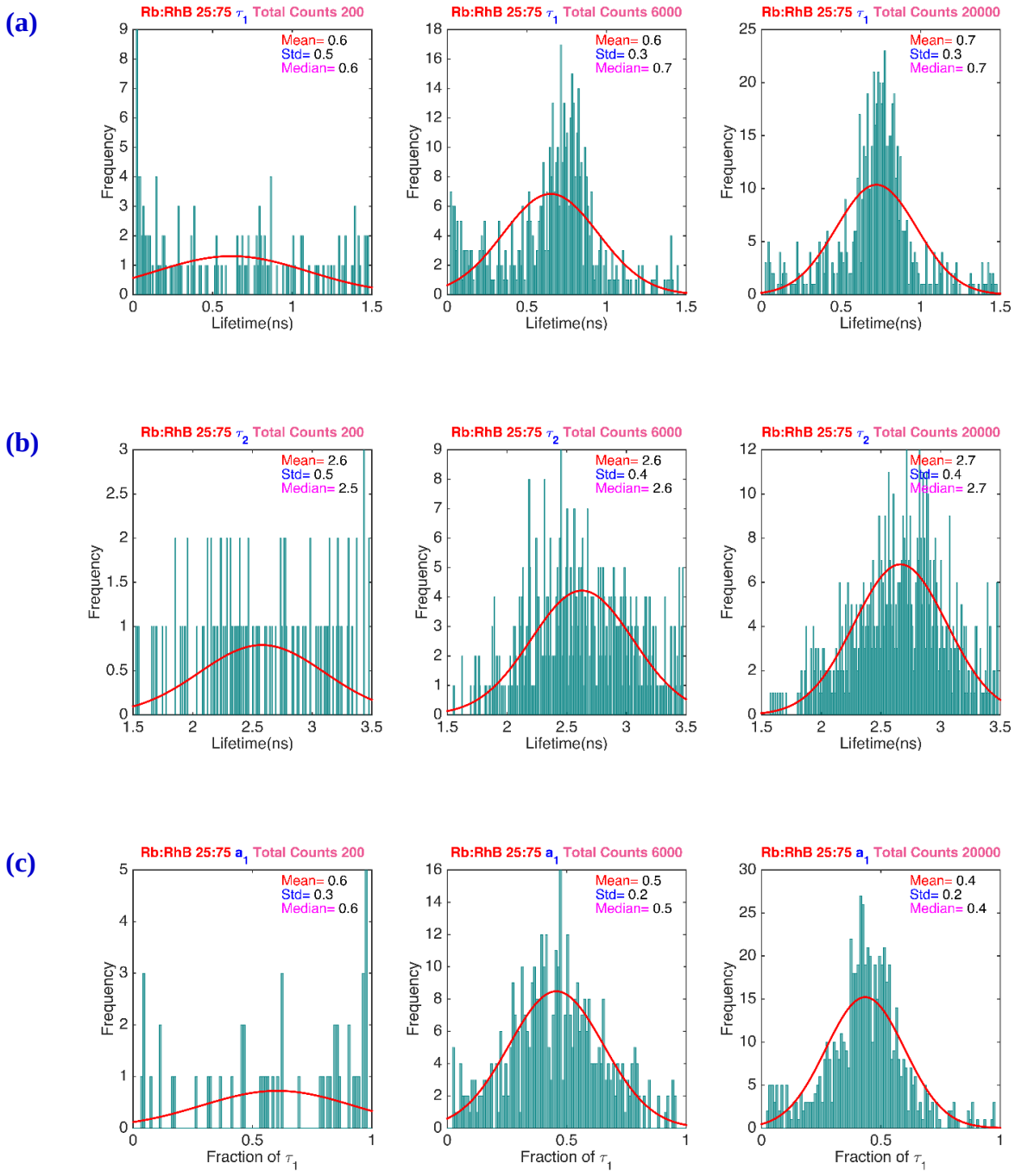

Figure S4.14. Histograms of the frequencies of obtaining values of the fluorescence decay parameters for τ_1, τ_2, and a_1 are presented in panels (a), (b), and (c), respectively. The histograms are obtained from a bin-by-bin analysis using the binomial distribution of a representative, single fluorescence decay trace from a 25:75 mixture of Rb and RhB with total counts of 200, 6000, and 20000. The histograms are fit to Gaussians using the values of the mean and standard deviation obtained from them.

(a)

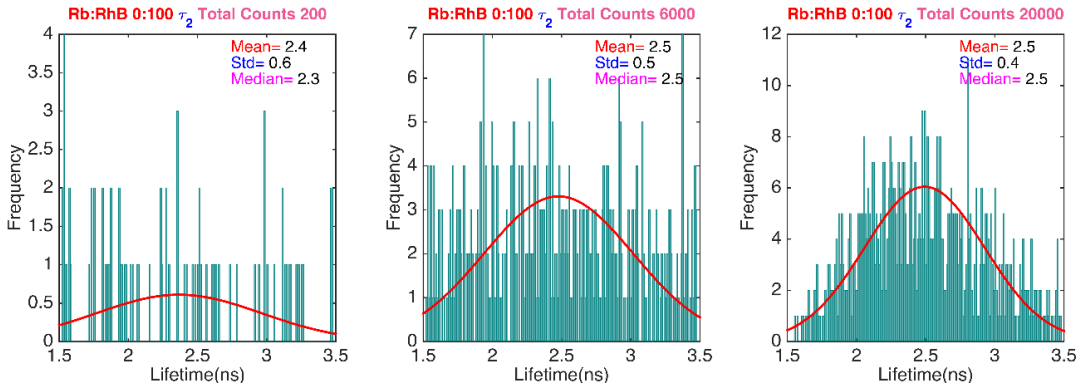

Figure S4.15. Histograms of the frequencies of obtaining values of the fluorescence decay parameters τ_2 is presented in panels (a). The histograms are obtained from a bin-by-bin analysis using the binomial distribution of a representative, single fluorescence decay trace from a 0:100 mixture of Rb and RhB with total counts of 200, 6000, and 20000. The histograms are fit to Gaussians using the values of the mean and standard deviation obtained from them.

CHAPTER 5. A BAYESIAN APPROACH FOR EXTRACTING FLUORESCENCE LIFETIMES FROM SPARSE DATA SETS AND ITS SIGNIFICANCE FOR SUBDIFFRACTION-LIMITED IMAGING

The modified content of this chapter to be submitted for publication

Kalyan Santra [1], Emily A. Smith [1], Xueyu Song [1], and Jacob W. Petrich *,[1]

5.1 Abstract

The measurement of fluorescence lifetimes in subdiffraction-limited volumes presents the dual challenge of probing a small number of fluorophores and fitting the concomitant sparse data set to the appropriate excited-state decay function. A common method of analysis, such as the Maximum Likelihood (ML) technique, assumes a *uniform* probability distribution of the parameters describing the fluorescence decay function. An improvement is thus suggested by implementing a suitable *nonuniform* distribution, as is provided by a Bayesian framework, where the distribution of parameters is obtained from both their prior knowledge and the evidence-based likelihood of an event for a given set of parameters. We have also considered the Dirichlet prior distribution, whose great advantage and utility is that its form enables analytical solutions of the fitting parameters to be rapidly obtained. If Gaussian and exponential prior distributions are

---

*To whom correspondence should be addressed. Email: jwp@iastate.edu

[1]Department of Chemistry, Iowa State University, and U. S. Department of Energy, Ames Laboratory, Ames, Iowa 50011, USA

judiciously chosen, they reproduce the experimental target lifetime to within 20% with as few as 20 total photon counts for the data set, as does the Dirichlet prior distribution. But because of the analytical solutions afforded by the Dirichlet prior distribution, it is proposed to employ a Dirichlet prior to search parameter space rapidly to provide, if necessary, appropriate parameters for subsequent employment of a Gaussian or exponential prior distribution.

5.2 Introduction

Time-correlated, single-photon counting has become an integral part of techniques such as fluorescence-lifetime imaging microscopy[1-5], Förster resonance-energy transfer[6-8], and fluorescence-correlation spectroscopy[9-11]. The technique records the time difference between the arrival times of an excitation pulse and a pulse resulting from a photon detected from fluorescence emission. A histogram of arrival-time differences is accumulated and fit to a model function for the fluorescence decay. The most frequently used fitting method (Residual Minimization, RM) minimizes the weighted squares of the residuals of the experimental data and the continuously optimized fitting function. RM requires a histogram of very high quality to extract the mean lifetime with high accuracy, and such a histogram is only obtained with a large number of total photon counts (~20000 for rose bengal). In super-resolution microscopies, however, such as stimulated-emission depletion microscopy[12-14], high spatial resolution is only obtained at the expense of the fluorescence signal, as the latter decreases with decreasing detection volume. Additional factors such as a low intrinsic fluorescence quantum yield or photodegradation of the sample contribute to reducing the magnitude of the total photon counts, thus making it more difficult to generate a histogram of high quality. Unless there is a certain number of total counts, RM yields a poor estimate of the mean lifetime.[15,16] In these cases[15-17], probability-based methods,

such as Maximum Likelihood (ML), provide considerable improvement over RM. One of the limitations of ML, however, is that it assumes a uniform probability distribution of the parameters describing the fluorescence decay function. Thus, ML can be further improved by implementing a suitable *nonuniform* distribution.

Here, we consider photon-counting data analysis using a Bayesian framework, where the distribution of parameters is obtained from both their prior knowledge and the evidence-based likelihood of an event for a given set of parameters. If $\boldsymbol{\beta}$ and $\boldsymbol{E}$ represent the parameter space and the evidence (*i.e.*, experimental observations), respectively, then the *posterior* distribution of the parameters for $\boldsymbol{E}$, $P(\boldsymbol{\beta}|\boldsymbol{E})$, is given by the Bayes' theorem[18-20]:

$$P(\boldsymbol{\beta}|\boldsymbol{E}) = \frac{P(\boldsymbol{\beta})P(\boldsymbol{E}|\boldsymbol{\beta})}{P(\boldsymbol{E})} \tag{5.1}$$

$P(\boldsymbol{E}|\boldsymbol{\beta})$ is the likelihood of evidence given the set of parameters $\boldsymbol{\beta}$; and $P(\boldsymbol{\beta})$ is the *prior* distribution of the parameters, which is obtained from the prior knowledge of the parameters. As the evidence is collected, the prior knowledge can be updated for the prediction of the parameters. $P(\boldsymbol{E})$ is the total likelihood (also known as the marginal likelihood) of the evidence at all possible points in the parameter space and acts as a normalization.

The Bayesian method is employed[19,21-34] to estimate parameters where there are insufficient evidences. It has been used in fluorescence-lifetime imaging[26,28,33], Förster resonance-energy transfer[26], and fluorescence-correlation spectroscopy[31,32] experiments. The choices, however, of the parameters to which priors are assigned and the functional form of the priors themselves varied widely. In some cases, an *exponential* prior has been assigned to "the relaxation time of the photon-generating emission process" based on the argument that it has the maximum entropy within the allowed parameter range[33]. In other cases, a uniform prior was assigned for the fraction of mean lifetime components; but this defeats the point of implementing the Bayesian approach

because it becomes reduced to the ML method[26]. Thus, one of the major challenges in implementing a Bayesian analysis of photon-counting data is determining the choice of the prior distribution and updating it as more evidence is successively acquired. In this work, we compare *Gaussian* and *exponential* prior distributions, where the lifetime parameter is directly incorporated in the posterior that is to be optimized, as well as *Dirichlet* prior distribution, where the lifetime parameter is indirectly calculated using the estimated probability of the bins. For the Gaussian and exponential prior, two analysis schemes were employed. In one, an identical prior was used for every data trace collected for a fixed number of counts. In the other, the prior is calculated and updated using the statistics of the results obtained from a data trace having a similar number of counts. As the latter method is preferable, the discussion of the former is given in the SI.

These prior distributions and the utility of the Bayesian approach were tested by analyzing photon-counting data obtained from the very well-characterized fluorophore, rose bengal. Rose bengal in methanol has an excited-state lifetime of 0.49 ± 0.01 ns at room temperature.[16] Three sets of data were collected, each consisting of 50 individual traces, with a total number of counts of approximately 20, 200, and 20000, respectively. In all the analyses, we incorporated the real instrument response function (IRF), a very narrow ~20-ps time channel (to avoid the limitations incurred from binning time channels[16]), and a shift parameter.

5.3 Materials and Methods

Rose bengal (Sigma-Aldrich, St. Louis) was purified by thin-layer chromatography.[16] 550 nm was the excitation wavelength. Time-resolved data were collected using a home-made instrument.[16] The full-width at half-maximum of the instrument function was typically ~120 ps. The data were collected in 1024 channels (bins), providing a time resolution of 19.51 ps/channel and a full-scale time window of 19.98 ns. Three different data sets consisting of 50 fluorescence

decay traces were collected with a total number of counts of approximately 20, 200, and 20000, respectively.

The signal from the excited state of the fluorophore is represented by a single-exponential decay. Let $\boldsymbol{C} = (c_1, c_2, \dots, c_K)$ be the counts obtained in the K (1024) bins represented by the time axis, $\boldsymbol{t} = (t_1, t_2, \dots, t_K)$, where the center of the jth bin is given by t_j and the corresponding counts are given by c_j. In a discretized data collection system, as in time-correlated, single-photon counting, the probability that a photon is detected in the jth bin, p_j, is proportional to the discrete convolution of the IRF and the model for the fluorescence decay function.

$$p_j(\tau, b) \propto \sum_{i=1}^{j-j_0-1} I_i F(t_j - t_i - b) = \sum_{i=1}^{j-j_0-1} I_i e^{-\left(\frac{t_j - t_i - b}{\tau}\right)} \tag{2}$$

where, b is a parameter that assumes continuous values, j_0 is an integer and the relation between them is given by $b = j_0\epsilon + \zeta$, where ζ lies between 0 and ϵ, the time width of the bin. b describes the linear shift between the instrument response function and the fluorescence decay.[16] If $\widehat{\boldsymbol{C}} = (\hat{c}_1, \hat{c}_2, \dots, \hat{c}_K)$ represents the predicted counts from the convoluted exponential model, then the number of predicted counts in the jth bin, $\hat{c}_j$, is given by:

$$\hat{c}_j = C_T\, p_j(\tau, b) = C_T \frac{\sum_{i=1}^{j-j_0-1} I_i e^{-\left(\frac{t_j - t_i - b}{\tau}\right)}}{\sum_{k=1}^{K}\left(\sum_{i=1}^{k-j_0-1} I_i e^{-\left(\frac{t_k - t_i - b}{\tau}\right)}\right)} \tag{5.3}$$

where $C_T = \sum_j c_j$, the total number of counts.

5.3.1 The likelihood of the collected data and the Bayesian formulation

The likelihood of observing a sequence of counts $(c_1, c_2, \dots, c_K)$ with probability $(p_1, p_2, \dots, p_K)$ for a given set of parameters (τ, b) and subject to the condition, $C_T = \sum_j c_j$, is given by the multinomial form[15-17]:

$$P(c_1, c_2, \ldots, c_K \mid \tau, b) = \frac{C_T!}{c_1! c_2! \ldots c_K!} \prod_{j=1}^{K} (p_j)^{c_j} = C_T! \prod_{j=1}^{K} \frac{(p_j)^{c_j}}{c_j!} \tag{5.4}$$

Using equation (5.5.3) and the probability, $p_j = \hat{c}_j / C_T$, we obtain:

$$P(c_1, c_2, \ldots, c_K \mid \tau, b) = C_T! \prod_{j=1}^{K} \frac{(\hat{c}_j / C_T)^{c_j}}{c_j!} \tag{5.5}$$

Note that both the probability of a photon being detected in the *j*th channel, p_j, and the predicted counts, $\hat{c}_j$, in that channel are functions of the parameters τ and b. The experimental data, the "evidence" of photon counting events for a given parameter space $\boldsymbol{\beta} \equiv (\tau, b)$, are the observed counts. Therefore, we have $\boldsymbol{E} \equiv \boldsymbol{C} = (c_1, c_2, \ldots, c_K)$; and equation (5.4.17) can be rewritten as:

$$P(\boldsymbol{E} \mid \boldsymbol{\beta}) = C_T! \prod_{j=1}^{K} \frac{(\hat{c}_j / C_T)^{c_j}}{c_j!} . \tag{5.6}$$

Gaussian and exponential prior distributions

The critical part of the Bayesian analysis is identifying and selecting a suitable prior distribution for the parameters. Since our analysis includes two independent parameters, τ and b, the prior distribution is:

$$P(\boldsymbol{\beta}) = P(\tau) P(b) . \tag{5.7}$$

We have shown that the estimated mean lifetime of a fluorophore approximately follows a normal distribution.[15,16] This conclusion is also obtained from the central limit theorem[35,36], which states that with a sufficiently large number of samples or of observations the distribution will converge to a normal distribution. Therefore, a Gaussian function with a pre-selected mean and variance is arguably a good choice for a prior distribution:

$$P(\tau) = (2\pi\sigma_0^2)^{-1/2} e^{-\left[\frac{(\tau-\mu_0)^2}{2\sigma_0^2}\right]}. \tag{5.8}$$

The "hyperparameters" (*i.e.*, the parameters determining the distribution of the parameter τ) μ_0 and σ_0 are the mean and the standard deviation of the prior distribution for τ. We also have tested the exponential prior distribution for the mean lifetime with known hyperparameter, λ_0:

$$P(\tau) = \lambda_0 e^{-\lambda_0 \tau}, \tag{5.9}$$

where $\langle\tau\rangle = 1/\lambda_0$ is the mean of the prior distribution. For the shift parameters, b, since we limit ourselves to a small range, -0.1 to 0.1 ns, it is convenient to assume that their distribution is uniform. Therefore, we take $P(b) = 1/(b_{max} - b_{min})$, which is a constant and does not affect the overall prior distribution, $P(\boldsymbol{\beta})$. From equation (5.5.1), we write:

$$P(\boldsymbol{\beta} \mid \boldsymbol{E}) = \frac{P(\tau)P(b)P(\boldsymbol{E} \mid \boldsymbol{\beta})}{P(\boldsymbol{E})} \tag{5.10}$$

The marginal likelihood, $P(\boldsymbol{E})$, is given its name from the process of "marginalization," which is an integration over all the parameters[23]:

$$P(\boldsymbol{\beta} \mid \boldsymbol{E}) = \frac{P(\tau)P(b)P(\boldsymbol{E} \mid \boldsymbol{\beta})}{\int d\tau db P(\tau)P(b)P(\boldsymbol{E} \mid \tau, b)} \tag{5.11}$$

Since $P(b)$ is a constant, it can be eliminated from equation (5.5.11). Substituting $P(\tau)$ from equation (5.5.8) and the expression for $P(\boldsymbol{E}|\boldsymbol{\beta})$ from equation (5.5.6), the logarithm of the posterior for the Gaussian prior distribution can be written as:

$$\ln P(\boldsymbol{\beta} \mid \boldsymbol{E}) = \gamma_1 - \frac{(\tau - \mu_0)^2}{2\sigma_0^2} + \sum_{j=1}^{K} c_j \ln \hat{c}_j. \tag{5.12}$$

where all the terms that are independent of the parameters τ and b are condensed into the constant γ_1. Similarly, if we choose the exponential prior distribution for the mean lifetime given in equation (5.5.9), we have:

$$\ln P(\boldsymbol{\beta} \mid \boldsymbol{E}) = \gamma_2 - \lambda_0 \tau + \sum_{j=1}^{K} c_j \ln \hat{c}_j , \tag{5.13}$$

where γ_2 is another constant, independent of the parameters τ and b. Maximization, therefore, of the logarithm of the posterior probability distribution in equation (5.5.12) and (5.5.13) provides the optimum values of the parameters.

Dirichlet prior distribution

Since the joint probability distribution given in equation (5.5.4) is in multinomial form, the Dirichlet prior[37-43] distribution is a natural choice for estimating the probability of the channels because it forms a conjugate prior[42,43] with the multinomial distribution insofar as it combines with the likelihood function to form a posterior distribution that belongs to same Dirichlet family. Thus, analytical solutions for the parameters can be easily formulated. The process for extracting the lifetime from the estimated probabilities of the channels is the following. We rewrite the likelihood distribution function from equation (5.5.4) as $P(\boldsymbol{c}|\boldsymbol{\pi})$ in the following by considering the probabilities of the channels as unknown parameters given by $\boldsymbol{\pi} = (\pi_1, \pi_2, \dots, \pi_K)$, where $\sum \pi_j = 1$.

$$P(\boldsymbol{c} \mid \boldsymbol{\pi}) = C_T ! \prod_{j=1}^{K} \frac{(\pi_j)^{c_j}}{c_j !} . \tag{5.14}$$

Let $\boldsymbol{\alpha} = (\alpha_1, \alpha_2, \dots, \alpha_K)$ be the "pre-counts" (virtual counts[42] or pseudo counts[43]) of the channels with probabilities $(\pi_1, \pi_2, \dots, \pi_K)$ before the evidence is collected; and let the sum of all "pre-counts" be $\sum \alpha_j = \mathrm{A}_T$. Then, the Dirichlet prior distribution is:

$$P(\boldsymbol{\pi}\,|\,\boldsymbol{\alpha}) \sim D(\alpha_1, \alpha_2, ..., \alpha_K) = \frac{\Gamma(\mathrm{A}_T)}{\prod_{j=1}^{K}\Gamma(\alpha_j)} \prod_{j=1}^{K} \pi_j^{\alpha_j - 1} \tag{5.15}$$

The "pre-counts," $\boldsymbol{\alpha}$, act as hyperparameters for the $\boldsymbol{\pi}$. The Dirichlet prior mean and variance are given by $E(\pi_j) = \alpha_j/\mathrm{A}_T$ and $\mathrm{Var}(\pi_j) = \alpha_j(\mathrm{A}_T - \alpha_j)/\mathrm{A}_T^2(\mathrm{A}_T + 1)$, respectively.[37]

The posterior is given by

$$\begin{aligned} &P(\boldsymbol{\pi}\,|\,\boldsymbol{c},\boldsymbol{\alpha}) \propto P(\boldsymbol{\pi}\,|\,\boldsymbol{\alpha})P(\boldsymbol{c}\,|\,\boldsymbol{\pi}) \sim D(\alpha_1 + c_1, \alpha_2 + c_2, ..., \alpha_K + c_K) \\ &= \frac{\Gamma(\mathrm{A}_T + C_T)}{\prod_{j=1}^{K}\Gamma(\alpha_j + c_j)} \prod_{j=1}^{K} \pi_j^{\alpha_j + c_j - 1} \end{aligned} \tag{5.16}$$

and the posterior mean is given by

$$E(\pi_j\,|\,\boldsymbol{c}) = \frac{\alpha_j + c_j}{\mathrm{A}_T + C_T} = \frac{\mathrm{A}_T}{\mathrm{A}_T + C_T}\theta_j + \frac{C_T}{\mathrm{A}_T + C_T}\phi_j \tag{5.17}$$

where, $\theta_j = E(\pi_j) = \alpha_j/\mathrm{A}_T$ and $\phi_j = c_j/C_T$. The posterior mean is thus the weighted average of the prior mean θ_j and the sample mean ϕ_j with respect to the total "pre-counts" and the total experimental counts, respectively.[37,39] The most important point aspect of the Dirichlet prior is that, unlike the Gaussian and exponential priors, it does not combine the prior distribution of the lifetime parameter (τ) directly in the estimation. Rather, the method of employing a Dirichlet prior evaluates the expected probability of the channels given the experimental counts.

In order to find the lifetime parameter, the bin-averaged time of the photon counts data was evaluated from the posterior and then compared with the sample quantity calculated from the convoluted model. In order to do this, first, one needs to estimate the "pre-counts" of the channels. For a given set of initial parameters (τ_{int}, b_{int}), we propose to distribute the total number of experimental counts C_T into the K bins to estimate $\boldsymbol{\alpha} = (\alpha_1, \alpha_2, \ldots, \alpha_K)$ as follows, using equation (5.5.3):

$$\alpha_j = C_T\, p_j(\tau_{\text{int}}, b_{\text{int}}) = C_T \frac{\sum_{i=1}^{j-j_0-1} I_i e^{-\left(\frac{t_j - t_i - b_{\text{int}}}{\tau_{\text{int}}}\right)}}{\sum_{k=1}^{K}\left(\sum_{i=1}^{k-j_0-1} I_i e^{-\left(\frac{t_k - t_i - b_{\text{int}}}{\tau_{\text{int}}}\right)}\right)} \tag{5.18}$$

where, $\sum \alpha_j = \mathrm{A}_T = C_T$. The expectation values of the bin probabilities π_j are then calculated using equation (5.5.17) for all the channels. Let t_{av} represent the bin-averaged time calculated from the expectation value of the bin probability. Therefore,

$$t_{av} = \sum_{j=1}^{K} t_j E(\pi_j \mid \boldsymbol{c}) = \sum_{j=1}^{K} t_j \frac{\alpha_j + c_j}{\mathrm{A}_T + C_T} \tag{5.19}$$

Similarly, for a given set of values of the parameters (τ, b), we can define another bin-averaged time (t'_{av}) for the convoluted model using the form of the probability p_j given in equation (5.5.3):

$$t'_{av} = \sum_{j=1}^{K} t_j\, p_j(\tau, b) = \sum_{j=1}^{K} t_j \frac{\sum_{i=1}^{j-j_0-1} I_i e^{-\left(\frac{t_j - t_i - b}{\tau}\right)}}{\sum_{k=1}^{K}\left(\sum_{i=1}^{k-j_0-1} I_i e^{-\left(\frac{t_k - t_i - b}{\tau}\right)}\right)} \tag{5.20}$$

Theoretically, the values of these two bin-averaged times (t_{av} and t'_{av}) should be equal for the ideal data without any noise. Therefore, for experimental data we can minimize the absolute difference (Δ_{abs}) between t_{av} and t'_{av}as shown in equation (5.5.21) to obtain the optimum values of the parameters, (τ_{opt}, b_{opt}).

$$\Delta_{abs} = \left| t_{av} - t'_{av} \right| \tag{5.21}$$

The obtained optimal values are set as the new initial parameters, $(\tau_{int}, b_{int}) = (\tau_{opt}, b_{opt})$ and the entire procedure is repeated for several iterations until the results converge to a preset tolerance.

5.3.2 Computational methods

The optimizations of the posterior distributions given in equations (5.5.12) and (5.5.13) are performed using codes written in MATLAB. The GlobalSearch toolbox in MATLAB uses the "fmincon" solver to minimize the objective function with respect to the parameters; and in each calculation, a global minimum is reached. The ranges of the parameters τ and b are assigned as 0.01 to 1.5 ns and -0.1 to 0.1 ns, respectively. Within the specified ranges, we run our in-house routine with different initial values of the parameters and always retrieve the same results through the third decimal place.

Gaussian and exponential priors

Both equations (5.5.12) and (5.5.13) depend on the initial values of the hyperparameters. We employ two schemes to assign the values of the hyperparameters. In the first, we use identical prior hyperparameters (*i.e.*, fixed μ_0 and σ_0 for the Gaussian prior or fixed λ_0 for the exponential prior) for all the fifty decay traces in a set. In the second, we update the prior hyperparameters for the analysis of Nth decay trace using the calculated statistics of the results obtained from all the analyzed $N-1$ decay traces of that set according to the equation (5.5.22) given below. In the second scheme we update the mean and the standard deviation after the analysis of 1 and 5 decay traces, respectively, to obtain sufficient statistics:

$$\begin{aligned}(\mu_0)_N &= \frac{1}{N-1}\sum_{r=1}^{N-1}\tau_r \ ; \text{for all } N>1 \\ (\sigma_0)_N &= \sqrt{\frac{1}{N-1}\sum_{r=1}^{N-1}\left[\tau_r-(\mu_0)_N\right]^2} \ ; \text{for all } N>5 \\ (\lambda_0)_N &= 1/(\mu_0)_N \ ; \text{for all } N>1\end{aligned} \tag{5.22}$$

In both schemes, different combinations of the initial values of the hyperparameters are assigned.

Dirichlet prior

As shown in equation (5.5.21), the absolute difference between t_{av} and t'_{av} is minimized to obtain the new set of initial parameters $(\tau_{int}, b_{int}) = (\tau_{opt}, b_{opt})$. The change of the value of the lifetime parameter is monitored; and convergence is obtained if the change between two successive iterations, $\delta\tau$, is less than a preset tolerance value, which we set to $\delta\tau_{tol} = 10^{-4}$ ns. If $b < 10^{-4}$ in an iteration, then b is set to zero. (We find $b \approx 0$ using the maximum likelihood estimation and other Bayesian analyses considered here for our data sets. Setting $b = 0$ simplifies the computation.) All the calculations converged in ≤ 50 iterations. To test the influence of the initial conditions the parameter space for the lifetime has been expanded (0.001 to 15 ns), and various initial values of τ_{int} are chosen within that range. In all cases, the results converge to the same lifetime value.

5.4 Results and Discussion

5.4.1 Gaussian and exponential priors

We assign the initial values of the hyperparameters for a decay trace and those values are mentioned in the corresponding figures and tables. After obtaining the results from a certain number of traces, we calculate the statistics of the results for all the decay traces considered up to that point using equation (5.5.22). The calculated statistics provide the hyperparameters for the subsequent analysis of the remaining decay traces. After each step, a new set of hyperparameters is obtained. Estimated lifetimes using this scheme are presented in **Figure 5.1** for all 50 decay traces for each set of data having a total number of 20, 200, and 20000 counts, respectively. Each panel is labeled with the initial values of μ_0 and σ_0. The histograms of the lifetimes obtained by

using Gaussian and exponential priors with different sets of initial hyperparameters are given in **Figure 5.2.** Statistics are summarized in **Table 5.1**.

For a Gaussian prior, where σ_0 = 0.5 ns, the results converge to the correct mean value as more and more decay traces are analyzed for a data set. As a result, the distribution of the estimated lifetimes becomes very narrow, with standard deviations of 8%, 2%, and less than 1% of the mean lifetime for the data sets with total number of 20, 200, and 20000 counts, respectively, as shown in **Figure 5.2a** and **Table 5.1**. The identical-prior counterpart (see SI) has much wider distributions, as noted in the previous section. As in the identical-prior counterpart, however, the estimated lifetime is not very sensitive to the initial values of the prior mean, μ_0, when the initial value of the prior standard deviation σ_0 is wide. For an exponential prior, the convergence is not as rapid as in the case of the Gaussian prior using this strategy (**Figure 5.2b**). Again, the initial choice of λ_0 has no influence on the estimated lifetime for the three data sets. These results also suggest that the Gaussian prior is preferable to the exponential prior.

This example of updating the prior distribution using the results from data sets with the same number of total counts is purely illustrative. The point is that the fitting results can be improved by employing data collected using similar experimental conditions and choosing the prior hyperparameter accordingly. Once obtained, higher-quality data (*e.g.*, from a decay trace having 20000 total counts) can be used to extract the hyperparameters for the prior when analyzing lesser-quality data (*e.g.*, from a decay trace having 20 total photon counts). Further updating of the prior might even be unnecessary, since it is possible that one data set of sufficiently high quality can provide a suitable prior. Such higher-quality data sets may be obtained from bulk solutions or from imaging data from STED experiments, for example, using pixels of higher intensity where the experimental conditions and fluorophore environment are similar.

5.4.2 Dirichlet Prior

Using the strategy of minimization of the absolute difference between two bin-average time (t_{av} and t'_{av}) given in equation (5.5.21) for the Dirichlet prior, each of the decay traces was analyzed; and convergence was obtained when $\delta\tau < 10^{-4}$ ns. The lifetimes of the individual traces are given in **Figure S5.3** for all the decay traces. The histograms of the lifetimes obtained from an analysis employing the Dirichlet prior are given in **Figure 5.3** for all the data traces for a given initial condition. The statistics of the results for the fifty decay traces of each set are summarized in **Table 5.2**. The value of the initial lifetime (τ_{int}), which has been used to estimate the "pre-counts" ($\boldsymbol{\alpha}$) for the Dirichlet prior at the beginning of the iteration, is 0.4 ns; and it is given in **Figure 5.3**, **Figure S5.3**, and **Table 5.2**.

To test the influence of the initial value, the parameter space for the lifetime was expanded (0.001 ns $\leq \tau_{int} \leq$ 15 ns), and various initial values of τ_{int} are chosen within that range. In all cases, the results converge to the same lifetime value. An example is shown in **Figure S5.4**, where the convergence is tested with various initial conditions (τ_{int}) for a representative data trace randomly chosen from each of the data set with total number of counts 20, 200 and 20000 respectively.

It can be seen (**Tables 5.2 and S5.1**) that the mean and the standard deviation of the lifetimes obtained for all the fifty decay traces in a set using a Dirichlet prior are comparable to those obtained using a Gaussian prior when σ_0 is 0.5 ns in the case of the three values (0.2 ns, 0.5 ns and 1.0 ns) of μ_0. When σ_0 is 0.3 ns, the statistical results of the lifetimes are comparable to those we obtained from the Dirichlet prior for all cases except that where μ_0 is 1.0 ns and the data set has 20 total counts. Here, the Gaussian prior yields 0.6 ± 0.1 ns and the Dirichlet prior yields 0.5 ± 0.1 ns. As mentioned above, the statistical results of the lifetimes for the Gaussian prior

analysis depends on the value of μ_0 when σ_0 is 0.1 ns for the data set with a total number of counts of 200 or less. On the other hand, the statistical results of the lifetimes obtained from the Dirichlet prior analysis are comparable to those we obtained using an exponential prior for all cases except that where the exponential prior parameter (λ_0) is 5.0 ns^{-1} and the data set has 20 total counts. Here, the exponential prior yields 0.4 ± 0.1 ns.

Thus, the advantage of employing a Dirichlet prior is not so much for the result it yields but rather because its use does not require any *a priori* knowledge of the lifetime of the sample. The change of the value of the lifetime parameter between two successive iteration, $\delta\tau$, should converge to yield the optimized results from any given starting point (initial value) for all the three data sets we have considered with total number of counts 20, 200, and 20000, respectively. The Gaussian prior, on the other hand, can yield much smaller standard deviations; but its use requires prior knowledge of the parameters. In the case of the exponential prior, the initial condition (the value of the hyperparameter, λ_0) has little influence on the estimated lifetimes for the data set with a total count number of 20. The Dirichlet prior, being a natural conjugate prior for the multinomial distribution, combines with the joint probability of the data obtained in the photon counting experiments to estimate the posterior of channel probability parameters analytically. It also differs significantly from the Gaussian and exponential prior cases in how the parameters are evaluated.

5.5 Conclusions

We have formulated and demonstrated the usefulness of a Bayesian approach for analyzing time-correlated, single-photon counting data to estimate the mean fluorescence lifetime of a well-characterized fluorophore, rose bengal. Although the exponential prior is less sensitive to the initial values of the hyperparameters, the Gaussian prior yields a much narrower distribution of the estimated lifetime, and thus, a more precise value of the retrieved value of the fluorescence

lifetime. The greatest advantage, however, of the Dirichlet prior is that for the cases we investigated, the same optimized results are obtained *regardless of the initial conditions* for the prior parameters. Thus, an analysis strategy is suggested in which parameter space can rapidly be searched with the Dirichlet prior; and a subsequent, more refined search may be carried out with a Gaussian or exponential prior, if necessary. Such a strategy may assist in the design and analysis of imaging experiments, especially those that are subdiffraction-limited, where small sample volumes and the possibility of photodamage necessitate the collection of sparse data sets

5.6 Acknowledgments

Support was provided by the U.S. Department of Energy, Office of Science, Office of Biological and Environmental Research, through the Ames Laboratory, under Contract No. DE-AC02-07CH11358. The Ames Laboratory is operated for the U.S. Department of Energy by Iowa State University. We thank Dr. Hyung Jun Woo for encouraging the consideration of the Dirichlet prior and for his helpful comments.

5.7 References

1. O'Connor, D. V.; Phillips, D. *Time Correlated Single Photon Counting* Academic Press Inc.: London, 1984.

2. Bastiaens, P. I.; Squire, A. Fluorescence Lifetime Imaging Microscopy: Spatial Resolution of Biochemical Processes in the Cell. *Trends Cell Biol.* **1999**, *9* (2), 48-52.

3. Elangovan, M.; Day, R.; Periasamy, A. Nanosecond Fluorescence Resonance Energy Transfer-Fluorescence Lifetime Imaging Microscopy to Localize the Protein Interactions in a Single Living Cell. *J. Microsc.* **2002**, *205* (1), 3-14.

4. Tinnefeld, P.; Buschmann, V.; Herten, D. P.; Han, K. T.; Sauer, M. Confocal Fluorescence Lifetime Imaging Microscopy (FLIM) at the Single Molecule Level. *Single Mol.* **2000**, *1* (3), 215-223.

5. Gerritsen, H.; Asselbergs, M.; Agronskaia, A.; Van Sark, W. Fluorescence Lifetime Imaging in Scanning Microscopes: Acquisition Speed, Photon Economy and Lifetime Resolution. *J. Microsc.* **2002**, *206* (3), 218-224.

6. Lee, M.; Tang, J.; Hochstrasser, R. M. Fluorescence Lifetime Distribution of Single Molecules Undergoing Förster Energy Transfer. *Chem. Phys. Lett.* **2001**, *344* (5), 501-508.

7. Scholes, G. D. Long-Range Resonance Energy Transfer in Molecular Systems. *Annu. Rev. Phys. Chem.* **2003**, *54* (1), 57-87.

8. Van Der Meer, B. W.; Coker, G.; Chen, S.-Y. S. *Resonance Energy Transfer:Theory and Data* VCH New York: 1994.

9. Thompson, N. L. *Fluorescence Correlation Spectroscopy* Springer: 2002.

10. Elson, E. L.; Magde, D. Fluorescence Correlation Spectroscopy. I. Conceptual Basis and Theory. *Biopolymers*. **1974**, *13* (1), 1-27.

11. Magde, D.; Elson, E. L.; Webb, W. W. Fluorescence Correlation Spectroscopy. II. An Experimental Realization. *Biopolymers*. **1974**, *13* (1), 29-61.

12. Lesoine, M. D.; Bhattacharjee, U.; Guo, Y.; Vela, J.; Petrich, J. W.; Smith, E. A. Subdiffraction, Luminescence-Depletion Imaging of Isolated, Giant, CdSe/CdS Nanocrystal Quantum Dots. *J. Phys. Chem. C*. **2013**, *117* (7), 3662-3667.

13. Lesoine, M. D.; Bose, S.; Petrich, J. W.; Smith, E. A. Supercontinuum Stimulated Emission Depletion Fluorescence Lifetime Imaging. *J. Phys. Chem. B*. **2012**, *116* (27), 7821-7826.

14. Syed, A.; Lesoine, M. D.; Bhattacharjee, U.; Petrich, J. W.; Smith, E. A. The Number of Accumulated Photons and the Quality of Stimulated Emission Depletion Lifetime Images. *Photochem. Photobiol.* **2014**, *90* (4), 767-772.

15. Santra, K.; Smith, E. A.; Petrich, J. W.; Song, X. Photon Counting Data Analysis: Application of the Maximum Likelihood and Related Methods for the Determination of Lifetimes in Mixtures of Rose Bengal and Rhodamine B. *J. Phys. Chem. A.* **2016**, *121* (1), 122-132.

16. Santra, K.; Zhan, J.; Song, X.; Smith, E. A.; Vaswani, N.; Petrich, J. W. What Is the Best Method to Fit Time-Resolved Data? A Comparison of the Residual Minimization and the Maximum Likelihood Techniques as Applied to Experimental Time-Correlated, Single-Photon Counting Data. *J. Phys. Chem. B.* **2016**, *120* (9), 2484-2490.

17. Baker, S.; Cousins, R. D. Clarification of the Use of Chi-Square and Likelihood Functions in Fits to Histograms. *Nucl. Instr. Meth. Phys. Res.* **1984**, *221* (2), 437-442.

18. Koch, K.-R. *Bayes' Theorem* Springer: 1990.

19. Bishop, C. M. *Pattern Recognition and Machine Learning* Springer: 2006.

20. Lindley, D. V. *Making Decisions*, 2nd ed.; Wiley: 1991.

21. Bretthorst, G. L.; Toussaint, U. V. The Maximum Entropy Method of Moments and Bayesian Probability Theory. *AIP Conf. Proc.* AIP: 2013, 3-15.

22. Wakefield, J. The Bayesian Analysis of Population Pharmacokinetic Models. *J. Am. Stat. Assoc.* **1996**, *91* (433), 62-75.

23. Bretthorst, G. L. *An Introduction to Parameter Estimation Using Bayesian Probability Theory* Springer: 1990.

24. Lai, W.; Liu, X.; Chen, W.; Lei, X.; Tang, X.; Zang, Z. Transient Multiexponential Signals Analysis Using Bayesian Deconvolution. *Appl. Math. Comp.* **2015**, *265* 486-493.

25. Barber, P.; Ameer-Beg, S.; Pathmananthan, S.; Rowley, M.; Coolen, A. A Bayesian Method for Single Molecule, Fluorescence Burst Analysis. *Biomed. Opt. Express.* **2010**, *1* (4), 1148-1158.

26. Kaye, B.; Foster, P. J.; Yoo, T. Y.; Needleman, D. J. Developing and Testing a Bayesian Analysis of Fluorescence Lifetime Measurements. *PLoS One.* **2017**, *12* (1), e0169337.

27. Van Dyk, D. A.; Connors, A.; Kashyap, V. L.; Siemiginowska, A. Analysis of Energy Spectra with Low Photon Counts Via Bayesian Posterior Simulation. *Astrophys. J.* **2001**, *548* (1), 224.

28. Rowley, M. I.; Coolen, A. C.; Vojnovic, B.; Barber, P. R. Robust Bayesian Fluorescence Lifetime Estimation, Decay Model Selection and Instrument Response Determination for Low-Intensity FLIM Imaging. *PLoS One*. **2016**, *11* (6), e0158404.

29. Malave, P.; Sitek, A. Bayesian Analysis of a One-Compartment Kinetic Model Used in Medical Imaging. *J. Appl. Stat.* **2015**, *42* (1), 98-113.

30. Borsuk, M. E.; Stow, C. A. Bayesian Parameter Estimation in a Mixed-Order Model of BOD Decay. *Water Res.* **2000**, *34* (6), 1830-1836.

31. Guo, S.-M.; He, J.; Monnier, N.; Sun, G.; Wohland, T.; Bathe, M. Bayesian Approach to the Analysis of Fluorescence Correlation Spectroscopy Data II: Application to Simulated and in Vitro Data. *Anal. Chem.* **2012**, *84* (9), 3880-3888.

32. He, J.; Guo, S.-M.; Bathe, M. Bayesian Approach to the Analysis of Fluorescence Correlation Spectroscopy Data I: Theory. *Anal. Chem.* **2012**, *84* (9), 3871-3879.

33. Rowley, M. I.; Barber, P. R.; Coolen, A. C.; Vojnovic, B. Bayesian Analysis of Fluorescence Lifetime Imaging Data. *SPIE BiOS* International Society for Optics and Photonics: 2011, 790325-790325.

34. Lubrano, M. Bayesian Analysis of Nonlinear Time Series Models with a Threshold. *Nonlinear Econometric Modeling in Time Series: Proceedings of the Eleventh International Symposium in Economic Theory* Cambridge University Press: 2000, 79.

35. Dobrushin, R. L. Central Limit Theorem for Nonstationary Markov Chains. I. *Theory of Probability & Its Applications*. **1956**, *1* (1), 65-80.

36. Feller, W. *An Introduction to Probability Theory and Its Applications: Volume I*, 3rd ed.; John Wiley & Sons, Inc. London-New York-Sydney-Toronto: 1968.

37. Agresti, A. *Analysis of Ordinal Categorical Data*, 2nd ed.; John Wiley & Sons: 2010.

38. Minka, T. P. *Estimating a Dirichlet Distribution* Technical report, MIT: 2000.

39. Agresti, A.; Hitchcock, D. B. Bayesian Inference for Categorical Data Analysis. *Stat. Meth. & Appl.* **2005**, *14* (3), 297-330.

40. Basu, D.; Pereira, C. A. d. B. On the Bayesian Analysis of Categorical Data: The Problem of Nonresponse. *J. Stat. Plan. Infer.* **1982**, *6* (4), 345-362.

41. Huang, J. Maximum Likelihood Estimation of Dirichlet Distribution Parameters. *CMU Techniq. Rep.* **2005**,

42. Minka, T. P. Bayesian Inference, Entropy, and the Multinomial Distribution. *Online tutorial*. **2003**,

43. Murphy, K. P. *Binomial and Multinomial Distributions* University of British Columbia, Tech. Rep.: 2006.

5.8 Tables and Figures

Table 5.1

Fitting results for three sets of 50 decay traces employing a Bayesian analysis using updated prior distributions.

total number of counts	**mean lifetime $\pm$ one standard deviation (ns)***		
Gaussian prior	$\mu_0 = 0.2$ ns, $\sigma_0 = 0.5$ ns	$\mu_0 = 0.5$ ns, $\sigma_0 = 0.5$ ns	$\mu_0 = 1.0$ ns, $\sigma_0 = 0.5$ ns
20	0.48 ± 0.04	0.48 ± 0.04	0.49 ± 0.04
200	0.49 ± 0.01	0.49 ± 0.01	0.49 ± 0.01
20000	0.489 ± 0.001	0.489 ± 0.001	0.489 ± 0.001
Exponential prior	$\lambda_0 = 5.0$ ns^{-1}	$\lambda_0 = 2.0$ ns^{-1}	$\lambda_0 = 1.0$ ns^{-1}
20	0.5 ± 0.1	0.5 ± 0.1	0.5 ± 0.1
200	0.49 ± 0.03	0.49 ± 0.03	0.49 ± 0.03
20000	0.490 ± 0.004	0.490 ± 0.004	0.490 ± 0.004

* Mean lifetime $\pm$ one standard deviation (ns) of fifty decay traces calculated using a Bayesian analysis for three data sets with a total number of counts of 20, 200, and 20000, respectively. The priors for a data trace in a set are updated using the statistics of the results of all the analyzed decay traces of that set, as given in equation (5.5.22). The type of prior and the initial values of the hyperparameters are given in the shaded rows.

Table 5.2

Fitting results for three sets of 50 decay traces employing a Bayesian analysis using Dirichlet prior distributions.

total number of counts	**mean lifetime $\pm$ one standard deviation (ns)***
Dirichlet prior	$\tau_{int} = 0.4$ ns, $\alpha_j = C_T p_j$
20	0.5 ± 0.1
200	0.50 ± 0.04
20000	0.489 ± 0.004

* Mean lifetime $\pm$ one standard deviation (ns) of fifty decay traces calculated using a Bayesian analysis for three data sets with a total number of counts of 20, 200, and 20000, respectively. The absolute difference between t_{av} and t'_{av} shown in equation (5.5.21) is minimized to obtain optimum values of the lifetime and the convergence is obtained if the change between two successive iteration, $\delta\tau < 10^{-4}$ ns. The initial parameter, τ_{int}, and the estimation of "pre-counts" are given in the second row.

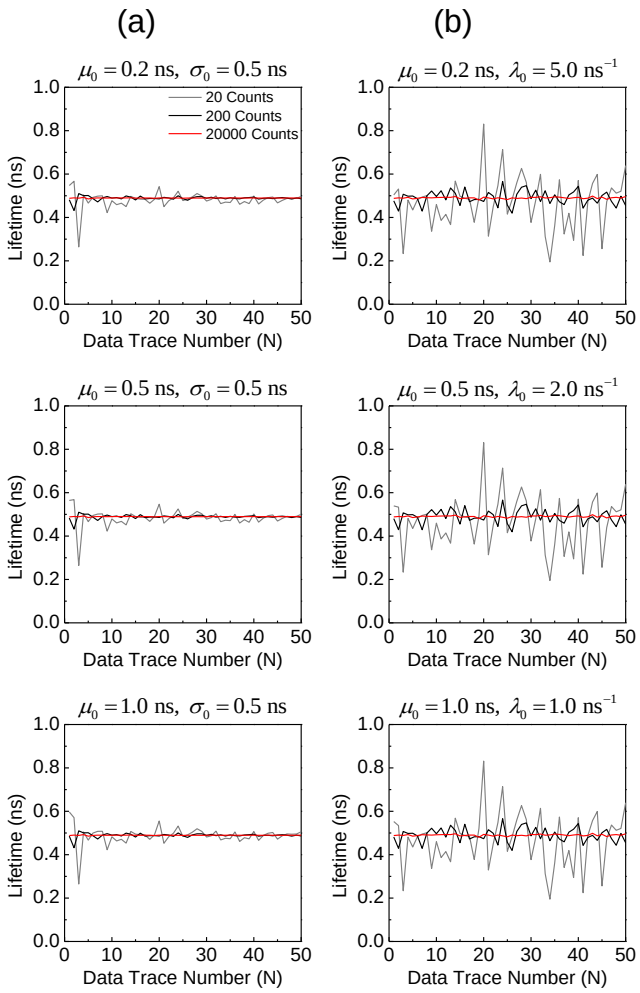

Figure 5.1. Estimated lifetimes of all fifty decay traces obtained by the Bayesian analysis where priors are updated following equation (5.5.22). The results using a Gaussian prior are shown in column (a); and the results from an exponential prior, in column (b). Corresponding hyperparameters are given at the top of each panel.

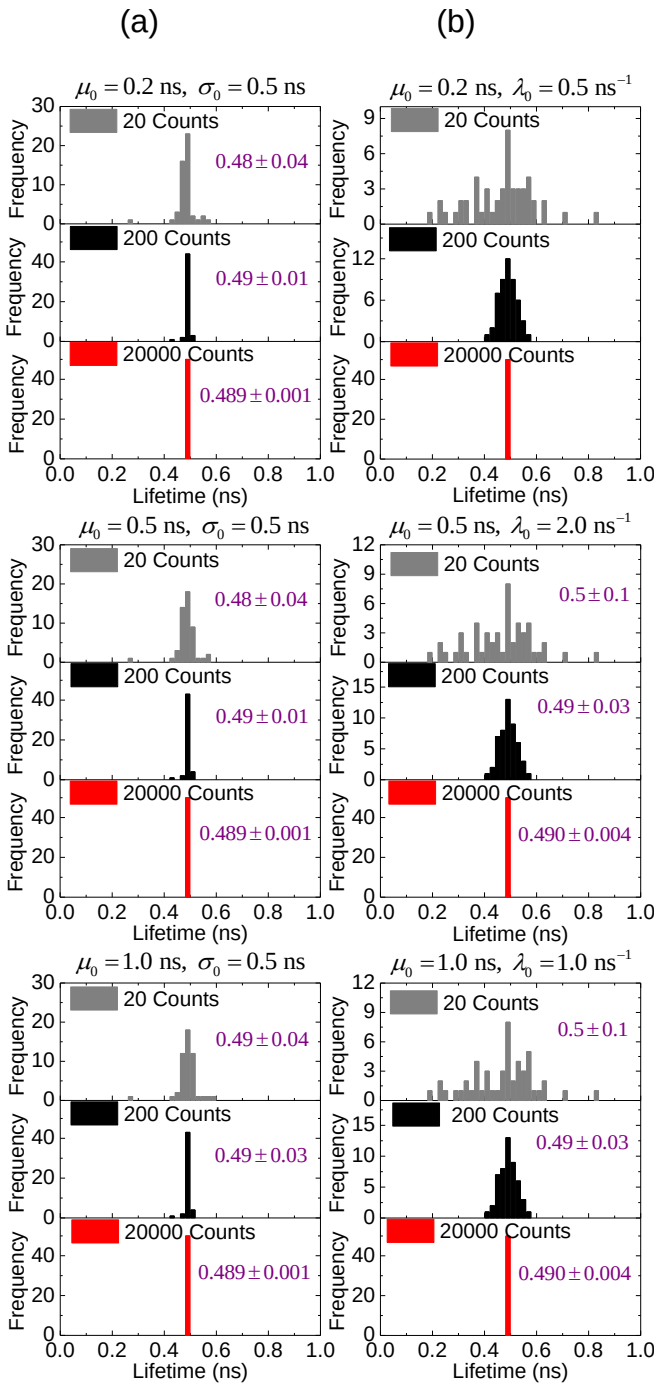

Figure 5.2. Histograms of the estimated lifetimes of all fifty decay traces obtained by the Bayesian analysis using updated priors following equation (5.5.22). Column (a) represents the results using a Gaussian prior; and column (b), the results using an exponential prior. Corresponding hyperparameters are given at the top of each panel. The mean and the standard deviation of the estimated lifetime are given in each histogram.

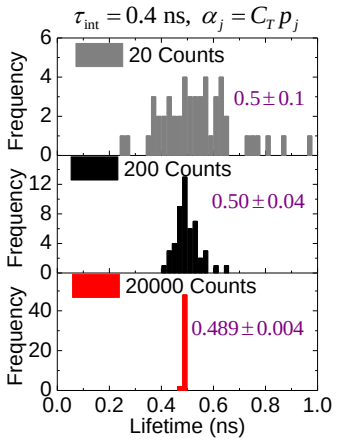

Figure 5.3. Histograms of the estimated lifetimes of all fifty decay traces obtained by the Bayesian analysis using a Dirichlet prior distribution. The initial values of the lifetime, τ_{int} , and the estimation of the "pre-counts" are given at the top of the panel. The mean and the standard deviation of the estimated lifetimes are given in each histogram.

5.9 Supplementary Information

5.9.1 Derivation of the probability and the estimated counts in a bin

It can be assumed that for a single emissive species the signal from an excited state fluorophore follows a single exponential decay law. If t_j is the time after the excitation corresponding to the *j*th time channel, then the fluorescence signal corresponding to that time is

$$F(t_j) \propto e^{-(\frac{t_j}{\tau})} \tag{S5.1}$$

where τ is the mean excited-state lifetime (*i.e.*, the lifetime) of the fluorophore. Let $\boldsymbol{C} = (c_1, c_2, \ldots, c_K)$ be the set of counts obtained in the K (1024) bins represented by the time axis, $\boldsymbol{t} = (t_1, t_2, \ldots, t_K)$, where the center of the *j*th bin is given by t_j and the corresponding counts are given by c_j. Similarly, we experimentally measure the instrument response function (IRF) and represent it as $\boldsymbol{I} = (I_1, I_2, \ldots, I_K)$, where the I_j are the number of counts in the *j*th bin. The width of each bin is given by $\epsilon = 19.51$ ps. The probability that a photon is detected in the *j*th bin, p_j, is

proportional to the discrete convolution of the IRF and the model for the fluorescence decay given in equation (S5.1).

$$p_j(\tau, b) \propto \sum_{i=1}^{j-j_0-1} I_i F(t_j - t_i - b) = \sum_{i=1}^{j-j_0-1} I_i e^{-\left(\frac{t_j - t_i - b}{\tau}\right)} \tag{S5.2}$$

where, b is a parameter that assumes continuous values, j_0 is an integer, and the relation between them is given by $b = j_0\epsilon + \zeta$, where ζ lies between 0 and ϵ. b describes the linear shift between the instrument response function and the fluorescence decay.[1-4] The probability that a photon is detected in the range $t_1 \leq t \leq t_{max} = t_K$ must be $\sum_j p_j = 1$. We have, therefore:

$$p_j(\tau, b) = \frac{\sum_{i=1}^{j-j_0-1} I_i e^{-\left(\frac{t_j - t_i - b}{\tau}\right)}}{\sum_{k=1}^{K}\left(\sum_{i=1}^{k-j_0-1} I_i e^{-\left(\frac{t_k - t_i - b}{\tau}\right)}\right)} \tag{S5.3}$$

The normalization factor in the denominator is independent of j; and, hence, the "dummy index," k, is inserted while retaining j_0, as this constant, unknown shift applies for all bins. The denominator is proportional to the total number of convoluted counts generated with the IRF.

Let the set of predicted counts from the convoluted exponential model be represented as $\widehat{\boldsymbol{C}} = (\hat{c}_1, \hat{c}_2, \ldots, \hat{c}_K)$, where $\hat{c}_j$ is the predicted number of counts in the jth bin. $\hat{c}_j$ is directly proportional to the probability that a photon is detected in that bin. The area under the decay curves obtained from the observed counts $\boldsymbol{C}$ and from the predicted counts $\widehat{\boldsymbol{C}}$ must be conserved during optimization of the fitting parameters. In other words, the total number of predicted counts must be equal to the total number of observed photon counts. The number, therefore, of predicted counts in the jth bin is given by:

$$\hat{c}_j = C_T\, p_j(\tau, b) = C_T \frac{\sum_{i=1}^{j-j_0-1} I_i e^{-\left(\frac{t_j - t_i - b}{\tau}\right)}}{\sum_{k=1}^{K}\left(\sum_{i=1}^{k-j_0-1} I_i e^{-\left(\frac{t_k - t_i - b}{\tau}\right)}\right)} \tag{S5.4}$$

where $C_T = \sum_j c_j$.

5.9.2 Posterior probability of the parameters in the Bayesian framework

The posterior distribution of the parameters $\boldsymbol{\beta}$ for the given "evidence", $\boldsymbol{E}$ is given by:

$$P(\boldsymbol{\beta} \mid \boldsymbol{E}) = \frac{P(\tau)P(b)P(\boldsymbol{E} \mid \boldsymbol{\beta})}{\int d\tau db P(\tau)P(b)P(\boldsymbol{E} \mid \tau, b)} \tag{S5.5}$$

Since $P(b)$ is constant, it can be eliminated leaving another constant in the denominator, *e.g.*, $P'(\boldsymbol{E})$. If we substitute the Gaussian prior distribution from equation (5.8) and the expression for $P(\boldsymbol{E}|\boldsymbol{\beta})$ from equation (5.6), we obtain:

$$P(\boldsymbol{\beta} \mid \boldsymbol{E}) = \frac{(2\pi\sigma_0^2)^{-1/2} e^{-\left[\frac{(\tau-\mu_0)^2}{2\sigma_0^2}\right]} C_T! \prod_{j=1}^{K} \frac{(\hat{c}_j / C_T)^{c_j}}{c_j!}}{P'(\boldsymbol{E})} \tag{S5.6}$$

The logarithm of the posterior distribution can be written as:

$$\begin{aligned} \ln P(\boldsymbol{\beta} \mid \boldsymbol{E}) = \ln(2\pi\sigma_0^2)^{-1/2} - \frac{(\tau-\mu_0)^2}{2\sigma_0^2} + \ln C_T! + \sum_{j=1}^{K} c_j \ln \hat{c}_j \\ - \sum_{j=1}^{K} c_j \ln C_T - \sum_{j=1}^{K} \ln c_j! - \ln P'(\boldsymbol{E}) \end{aligned} \tag{S5.7}$$

Condensing all the terms that are independent of the parameters τ and b into γ_1, we obtain

$$\ln P(\boldsymbol{\beta} \mid \boldsymbol{E}) = \gamma_1 - \frac{(\tau-\mu_0)^2}{2\sigma_0^2} + \sum_{j=1}^{K} c_j \ln \hat{c}_j . \tag{S5.8}$$

Similarly, if we choose the exponential prior for the mean lifetime, then we have

$$\ln P(\boldsymbol{\beta} \mid \boldsymbol{E}) = \gamma_2 - \lambda_0 \tau + \sum_{j=1}^{K} c_j \ln \hat{c}_j \,, \tag{S5.9}$$

where γ_2 is another constant independent of the parameters τ and b.

5.9.3 Discussion of the results: identical prior for each data set

As mentioned in the text, it is possible to perform the Bayesian analysis by not updating the hyperparameters the prior from one decay trace to the other. Here, each of the fluorescence decay traces was analyzed using Gaussian (12) and exponential (13) priors with different initial values of the hyperparameters. The estimated lifetimes are shown in **Figure S5.1** for all 50 decay traces of each set of data with a total number of counts of 20, 200, and 20000, respectively. The initial values of μ_0 and σ_0 are given in each panel. The histograms of the lifetimes obtained by using Gaussian and exponential prior distributions with different sets of hyperparameters are given in **Figure S5.2.** The statistics of the histograms are summarized in **Table S5.1**.

In the case of a Gaussian prior, these results indicate that if its σ_0 is large (*e.g.*, 0.5 ns in the case of Rb), then the results approach the ML estimation, as observed previously[1,5]. In this case, the estimated lifetime is not very sensitive to the initial values of the prior mean, μ_0 (**Figure S5.2c**); and in all cases, we retrieved the correct lifetime with approximately 20%, 6%, and 1% standard deviation for data sets with 20, 200, and 20000 total counts, respectively. On the other hand, as seen from the central panel of **Figure S5.2a**, if the prior standard deviation is small and an appropriate prior mean is chosen, then we obtain a much narrower distribution (10% standard deviation) for the lifetime with the correct mean value (0.49 ns) even with 20 counts. (An "appropriate prior mean" is a value close to the correct answer. A rough estimation of the lifetime can be obtained using methods such as ML. It is necessary, however, to be careful when choosing such priors, since in the case of small standard deviations of the prior, the estimated lifetime depends on the initial prior mean.) For data with a higher total number of counts, this problem

does not appear since the larger number of evidence dominates over the choice of the prior. Therefore, the prior obtained from other experimental observations, where the experimental conditions are nearly identical, are the most useful to estimate the lifetime of the sample of interest in that particular experimental conditions, as we discuss in the next section.

In the case of an exponential prior, there is only one hyperparameter, the inverse mean lifetime, $\lambda_0 = 1/\mu_0$. As seen from, **Figure S5.2d**, the initial choice of the parameter λ_0 has very little influence on the estimated lifetime for the data set with a total number counts of 20. For the other two sets with a higher total number of counts, the choice of λ_0 has no effect on the results. This can be considered as an advantage over the Gaussian prior. On the other hand, the distribution of the estimated lifetime is wider than that of its Gaussian counterpart, where the narrow standard deviation of the prior can be defined. If, therefore, suitable parameters for the prior distribution are obtained, then the Gaussian prior seems to be preferable.

5.9.4 Supplementary tables and figures

Table S5.1

Fitting results for three sets of 50 decay traces employing a Bayesian analysis using identical prior distributions.

total number of counts	**mean lifetime ± one standard deviation (ns)***		
Gaussian prior	$\mu_0 = 0.2$ ns, $\sigma_0 = 0.1$ ns	$\mu_0 = 0.5$ ns, $\sigma_0 = 0.1$ ns	$\mu_0 = 1.0$ ns, $\sigma_0 = 0.1$ ns
20	0.35 ± 0.06	0.49 ± 0.05	0.93 ± 0.05
200	0.46 ± 0.03	0.49 ± 0.03	0.57 ± 0.04
20000	0.490 ± 0.004	0.490 ± 0.004	0.491 ± 0.004
Gaussian prior	$\mu_0 = 0.2$ ns, $\sigma_0 = 0.3$ ns	$\mu_0 = 0.5$ ns, $\sigma_0 = 0.3$ ns	$\mu_0 = 1.0$ ns, $\sigma_0 = 0.3$ ns
20	0.5 ± 0.1	0.5 ± 0.1	0.6 ± 0.1
200	0.49 ± 0.03	0.49 ± 0.03	0.50 ± 0.03
20000	0.490 ± 0.004	0.490 ± 0.004	0.490 ± 0.004
Gaussian prior	$\mu_0 = 0.2$ ns, $\sigma_0 = 0.5$ ns	$\mu_0 = 0.5$ ns, $\sigma_0 = 0.5$ ns	$\mu_0 = 1.0$ ns, $\sigma_0 = 0.5$ ns
20	0.5 ± 0.1	0.5 ± 0.1	0.5 ± 0.1
200	0.49 ± 0.03	0.49 ± 0.03	0.50 ± 0.03
20000	0.490 ± 0.004	0.490 ± 0.004	0.490 ± 0.004
Exponential prior	$\lambda_0 = 5.0$ ns^{-1}	$\lambda_0 = 2.0$ ns^{-1}	$\lambda_0 = 1.0$ ns^{-1}
20	0.4 ± 0.1	0.5 ± 0.1	0.5 ± 0.1
200	0.49 ± 0.03	0.49 ± 0.03	0.49 ± 0.03
20000	0.490 ± 0.004	0.490 ± 0.004	0.490 ± 0.004

* Mean lifetime ± one standard deviation (ns) of fifty decay traces calculated using a Bayesian analysis for three data sets with 20, 200, and 20000 total counts, respectively. The priors are identical for all fifty decay traces. The type of prior and the values of the hyperparameters are given in the shaded rows.

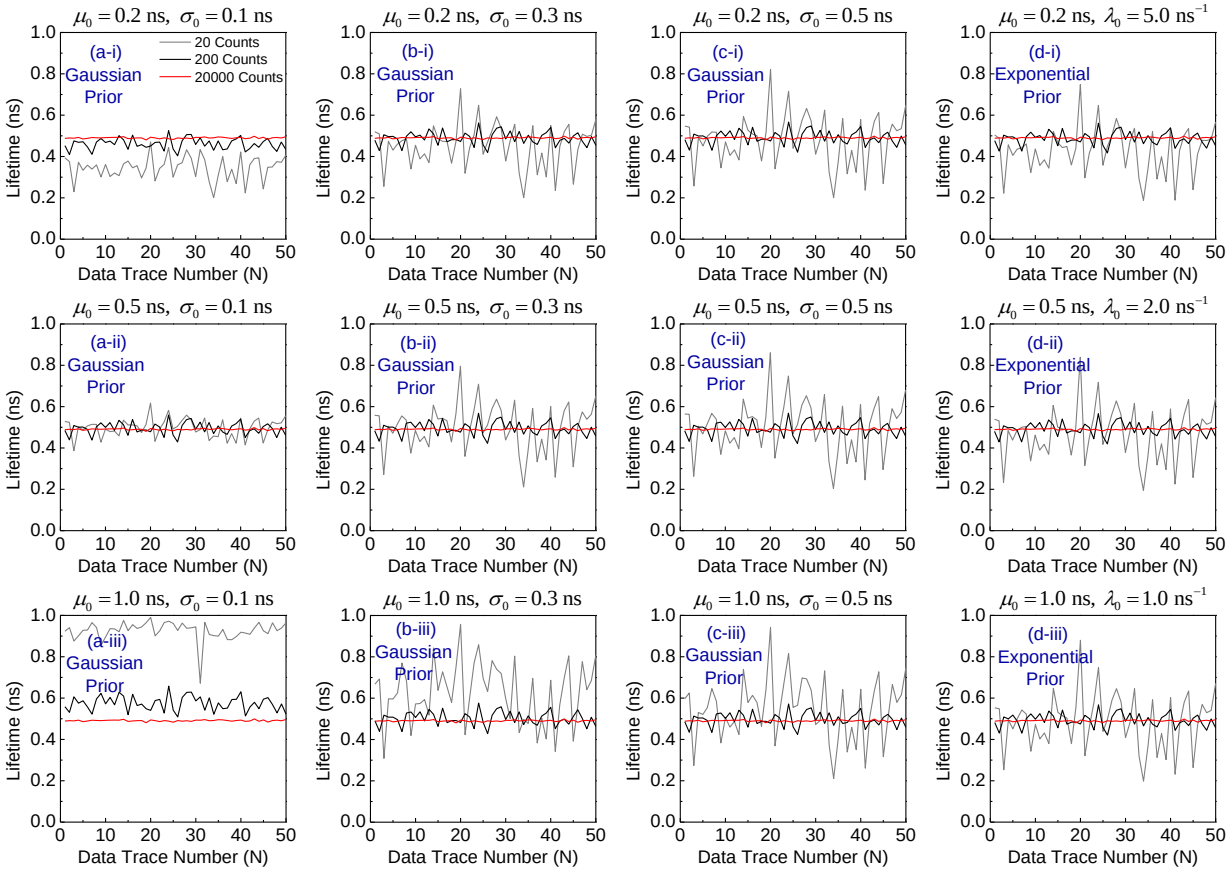

Figure S5.1. Estimated lifetimes of all decay traces obtained by the Bayesian analysis where identical priors are used. The results from the Gaussian prior are presented in (a)-(c); and the results from the exponential prior, in (d). Corresponding hyperparameters are given at the top of each panel. The data sets with 20, 200, and 20000 total counts are gray, black, and red, respectively.

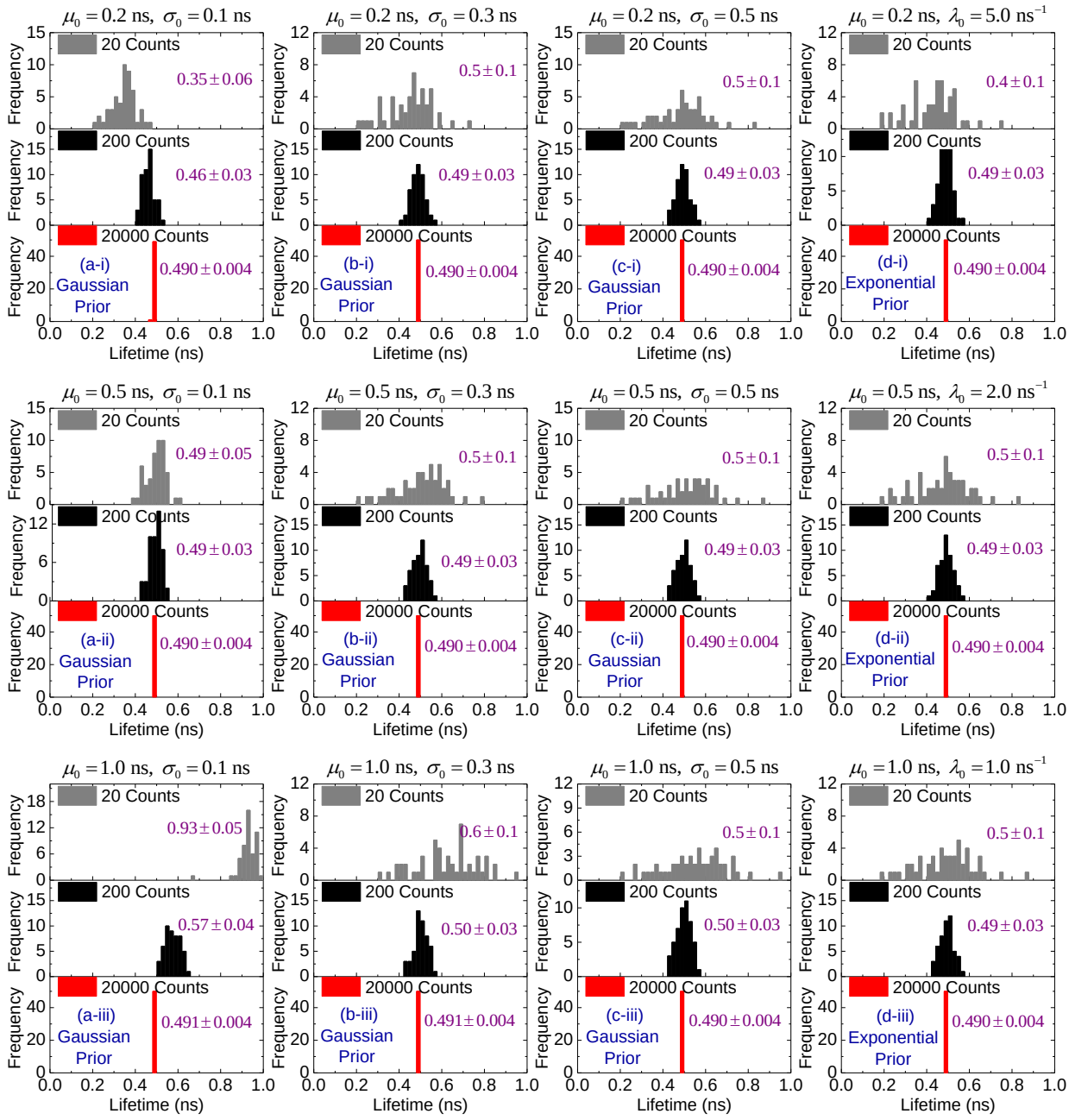

Figure S5.2. Histograms of the estimated lifetimes of all the decay traces obtained by the Bayesian analysis where identical priors are used. (a)-(c) represent the results using a Gaussian prior; and (d), the results using an exponential prior. Corresponding hyperparameters are given at the top of each panel. The mean and the standard deviations of the estimated lifetimes are given in each histogram.

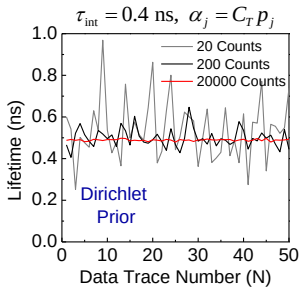

Figure S5.3. Estimated lifetimes of all fifty decay traces obtained by the Bayesian analysis using a Dirichlet prior distribution. The initial values of the lifetime τ_{int} and estimation of "pre-counts" are given at the top of the panel.

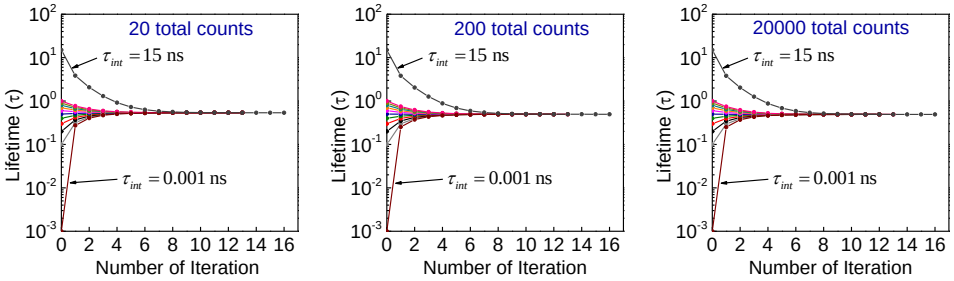

Figure S5.4. A representative trace from each data set is analyzed using a Dirichlet prior with various initial values (τ_{int}). The convergence curve for the lowest (0.001 ns) and the highest (15 ns) initial values that we considered are indicated by arrows. Regardless of the initial condition, all curves converge to the same value.

References for the supporting information

1. Santra, K.; Zhan, J.; Song, X.; Smith, E. A.; Vaswani, N.; Petrich, J. W. What Is the Best Method to Fit Time-Resolved Data? A Comparison of the Residual Minimization and the Maximum Likelihood Techniques as Applied to Experimental Time-Correlated, Single-Photon Counting Data. *J. Phys. Chem. B.* **2016**, *120* (9), 2484-2490.

2. Calligaris, F.; Ciuti, P.; Gabrielli, I.; Giamcomich, R.; Mosetti, R. Wavelength Dependence of Timing Properties of the Xp 2020 Photomultiplier. *Nucl. Instr. Meth.* **1978**, *157* (3), 611-613.

3. Fleming, G. R. *Chemical Application of Ultrafast Spectroscopy* Oxford University Press: New York, 1986.

4. Sipp, B.; Miehe, J.; Lopez-Delgado, R. Wavelength Dependence of the Time Resolution of High-Speed Photomultipliers Used in Single-Photon Timing Experiments. *Opt. Commun.* **1976**, *16* (1), 202-204.

5. Santra, K.; Smith, E. A.; Petrich, J. W.; Song, X. Photon Counting Data Analysis: Application of the Maximum Likelihood and Related Methods for the Determination of Lifetimes in Mixtures of Rose Bengal and Rhodamine B. *J. Phys. Chem. A.* **2016**, *121* (1), 122-132.

CHAPTER 6. EXPLOITING FLUORESCENCE SPECTROSCOPY TO IDENTIFY MAGNETIC IONIC LIQUIDS SUITABLE FOR THE ANALYTICAL SEPARATION OF OLIGONUCLEOTIDES

The modified content of this chapter to be submitted for publication

Kalyan Santra[1], Kevin D. Clark[1], Nishith Maity[1], Jacob W. Petrich*[,1], and Jared L. Anderson[1]

6.1 Abstract

Magnetic ionic liquids (MILs), which incorporate paramagnetic ions, promise to minimize manual user intervention, decrease extraction times, and facilitate rapid recovery of the analyte-enriched extraction solvent. If, however, fluorescence is employed in the downstream analysis of an analyte tagged with a fluorophore, the paramagnetic ion may quench fluorescence by introducing new nonradiative processes. Thus, it is necessary to employ a paramagnetic ion that offers a compromise between possessing a high magnetic moment and not introducing new nonradiative channels. Mn(II), Fe(III), Co(II), and Ni(II) are considered in combination with phosphonium cations and anionic ligands based upon halides or hexafluoroacetylacetonate. Among the possibilities examined, MILs containing Mn(II) provide the best alternative for a model system involving DNA.

---

*To whom correspondence should be addressed. Email: jwp@iastate.edu

[1]Department of Chemistry, Iowa State University, Ames, Iowa 50011, USA

6.2 Introduction

Nucleic acids play a myriad of roles in biological systems to govern the growth development of all living organisms. Modern DNA detection and sequencing technologies have made possible the extremely rapid acquisition of genetic information and are poised to drive the expansion of nucleic acid-based diagnostics,[1] personalized medicine,[2] and biomarker discovery.[3] As a result, the isolation and purification of DNA from biological samples has become a significant bottleneck in nucleic acid analysis. Conventional phenol-chloroform liquid-liquid extraction (LLE) or silica-based solid phase extraction (SPE) methods are limited by their ability to isolate a sufficient quantity of highly pure DNA that is suitable for sensitive downstream bioanalytical techniques such as polymerase chain reaction (PCR) amplification and fluorescence imaging.[4,5] Apart from variable DNA recoveries and purities,[6] the time-consuming and laborious sample handling procedures in LLE and SPE methods severely reduce sample throughput.[7]

Recently, DNA extraction methods involving ionic liquids (ILs) have shown great promise to improve the speed, efficiency, and specificity of DNA analysis.[8,9] ILs are a class of molten salts comprised of organic/inorganic cations and anions with melting temperatures at or below 100 °C. The unique ability to customize the structure of IL cations and anions through accessible synthetic methods is an attractive feature of these solvents that has led to their successful implementation as DNA extraction solvents,[10] PCR additives,[11] and nucleic acid preservation media.[12] Careful design of the IL structure has also generated a new class of solvents know as magnetic ionic liquids (MILs) that contain paramagnetic components in their chemical structure.[13,14,15] Unlike ferrofluids that are colloidal suspensions of magnetic particles in a carrier solvent, MILs are neat liquids that respond to applied magnetic fields.[16] The convergence of the liquid nature, magnetic susceptibility, and tunable structure of MILs represents a distinct advantage relative to conventional ILs by

providing a solvent that can be employed in magnet-based sample preparation workflows to minimize manual user intervention, decrease extraction times, and facilitate rapid recovery of the analyte-enriched extraction solvent.

The extraction of DNA using MIL solvents has recently been demonstrated as a rapid, magnet-based alternative to conventional DNA sample preparation methods. Several phosphonium and ammonium-based MILs with anionic components based on paramagnetic tetrahaloferrate(III) complexes were investigated to reveal that MILs with different chemical structures provided unique DNA solvation/extraction capabilities.[17] To capitalize on the rapid and selective extractions afforded by MIL solvents, a method coupling the extraction procedure with downstream PCR amplification and gel electrophoresis was developed to analyze directly the DNA enriched within the MIL.[18] Although it was possible to mitigate PCR inhibition caused by the Fe(III) component of the MIL by designing an appropriate PCR buffer system, the Fe(III)-based MILs precluded real-time fluorescence detection of the accumulation of PCR amplification products (*i.e.*, real-time quantitative PCR or qPCR), even under identical buffer conditions, because it strongly quenched the fluorescence of the tagged DNA.

Since fluorescence detection is central to quantification or imaging applications in DNA analysis, the identification of MIL extraction solvents that are compatible with fluorescence-based DNA assays is highly desirable. As the undesirable fluorescence quenching may arise from intersystem crossing promoted by spin-orbit coupling induced through the "heavy-atom" effect by the paramagnetic atom, excited-state electron transfer to or from the fluorescent label to any component of the MIL, or from Förster energy transfer from the label, such an identification requires assessing these quenching mechanisms as a function of various paramagnetic metals. Here, we examine the roles of the paramagnetic species Fe(III), Co(II), Mn(II), and Ni(II)

constituting part of a halide anion or a hexafluoroacetylacetonate (hfacac) anion. These anions differ structurally from each other considerably and hence vary the interactions between the paramagnetic ions and the fluorescent tag (cyanine5 carboxylic acid, Cy5). Quenching studies are employed to evaluate the interactions of MILs with the Cy5 to identify MILs that are appropriate for direct spectroscopic-based analysis of extracted DNA--and possibly other biological materials such as RNA or proteins.

6.3 Materials and Methods

The ILs, MILs, and fluorophores used for spectroscopic measurements are presented in **Figure 6.1**. (See the caption to the Figure for abbreviations.) Hydrophobic MILs containing metal halide anions were synthesized according to previously reported procedures.[14,19] Briefly, the corresponding metal halide salt was mixed with $[P_{66614}^+][Cl^-]$ at a 2:1 mole ratio (for Co and Mn-based MILs) or 1:1 mole ratio (for Fe(III)-based MILs) in methanol for 24 h. After solvent evaporation, the MIL was dried in a vacuum oven for 48 h. Syntheses of $[P_{66614}^+][Co(hfacac)_3^-]$, $[P_{66614}^+][Ni(hfacac)_3^-]$, and $[P_{66614}^+][Mn(hfacac)_3^-]$ were performed as reported.[20] For purification, the hfacac-based MILs were dissolved in diethyl ether and washed five times with 40 mL of deionized water, or until the addition of $AgNO_3$ to the water layer yielded no precipitation. All MILs were dried at 50 °C *in vacuo* for 48 h prior to spectroscopic measurements.

Cy5 and Coumarin 153 (C153) were obtained from Lumiprobe and Exciton, Inc., respectively. Cy5-tagged DNA (5´-Cy5-ACAGACTGATGTTGA-3´, subsequently referred as Cy5-DNA) was obtained from Integrated DNA Technologies (Coralville, IA). All chemicals and organic solvents (Fischer Scientific, HPLC or ACS grade) were used as received. Samples were prepared by dissolving the fluorophore or Cy5-DNA in a small volume (~10 µL) of methanol or

DMSO and added dropwise to the MILs. The samples were then dried at room temperature to constant mass using a Mettler Toledo NewClassic MF MS105 microbalance (Columbus, OH, USA) with 0.01-mg readability.

Steady-state absorption spectra were recorded using an Agilent 8453 UV-visible spectrometer (Agilent Technologies) with 1-nm resolution. Steady-state fluorescence spectra were obtained on a Fluoromax-4 spectrometer (Horiba Scientific) and corrected for lamp spectral intensity and detector response. A 3-mm path-length quartz cuvette was used for absorption and fluorescence measurements. Samples containing Cy5 and Cy5-DNA were excited at 600 nm; those containing C153, 400 nm.

Time-resolved data were collected using a home-made, time-correlated, single-photon counting (TCSPC) instrument using a SPC-630 TCSPC module (Becker & Hickl GmbH). A collimated Fianium pulsed laser (Fianium Ltd, Southampton, UK) at a 2-MHz repetition rate, was used to excite the sample at 550 nm. The excitation beam was vertically polarized. Emission was detected at the "magic angle" (54.7°) with respect to the excitation using a 590-nm, long-pass filter. The instrument response function (IRF) was measured by collecting scattered light at 550 nm (without the emission filter). The full-width at half-maximum of the instrument function was typically ~120 ps. TCSPC data were collected in 1024 channels (bins), providing a time resolution of 19.51 ps/channel, and a full-scale time window of 19.98 ns. The number of counts in the peak-channel was set to 65535 unless otherwise indicated. A 3-mm path-length quartz cuvette was used for the lifetime measurements.

6.4 Results and Discussion

6.4.1 The role of Förster resonant energy transfer

The rate of nonradiative energy transfer, k_{ET}, from a fluorescent donor to an acceptor was described by Förster[21-24]: $k_{ET} = \frac{1}{\tau_D}\left(\frac{R_0}{R}\right)^6$; where τ_D is the unquenched fluorescence lifetime of the donor, and, R is the distance between donor and acceptor; and R_0 is referred to as the "critical distance," defined by:

$$R_0^6 = \frac{9000\ln(10)\,\phi_D\,\kappa^2}{128\,\pi^5\,n^4 N_A}\int_0^\infty f_D(\bar{\nu})\epsilon_A(\bar{\nu})\bar{\nu}^{-4}d\bar{\nu} \qquad (6.1)$$

where $f_D(\bar{\nu}) = F(\bar{\nu})/\int_0^\infty F(\bar{\nu})d\bar{\nu}$, is the fluorescence intensity of the unquenched donor normalized to unit area on a wavenumber scale. The other parameters are: ϕ_D, the fluorescence quantum yield of the donor; κ^2, the orientation factor, assumed to be 2/3 for randomly oriented donors and acceptors; ϵ_A, the decadic molar extinction coefficient; n, the refractive index of the medium; and N_A, Avogadro's number. Quantifying the rate of nonradiative energy transfer thus reduces to evaluating R_0, which for random or nearly randomly-oriented samples is determined by the overlap of the emission spectrum of the donor and the absorption spectrum of the acceptor. **Figure 6.2** provides an example for Cy5 and Co(II). We have evaluated R_0 for Cy5 with Mn(II), Fe(III), Co(II), Ni(II), and hfacac and [P_{66614}^+], with or without the paramagnetic ions. Values of R_0 are compiled in **Table 6.1**. Co(II) is the only component of the MILs investigated here that has a significant R_0: for the isolated chloride salt of Co(II), $R_0 = 58.1$ Å, larger than nearly a factor of two or more than any other ligand. The ability, then, of Fe(III), for example, to quench Cy5 so efficiently[17,18] must lie in mechanisms other than nonradiative energy transfer. Distinguishing the two most likely, intersystem crossing and excited-state electron transfer, lies beyond the scope of

this investigation. But it is possible, however, to quantify the efficiency of quenching by the paramagnetic ions, which is done in the following sections.

6.4.2 Quantifying bimolecular quenching of fluorescence

Bimolecular quenching processes may occur, for example, by the collisions of the excited-state fluorophore with other molecules, which enhance nonradiative rates or introduce new ones. It may also occur through the formation of nonfluorescent ground-state complexes, which is referred to as static quenching. Both collisional and static quenching can be quantified by Stern-Volmer equations.[25-39] Collisional quenching (also referred to as dynamic quenching) can be quantified by a plot of fluorescence intensity or fluorescence lifetime as a function of quencher concentration:

$$\frac{F_0}{F} = \frac{\tau_0}{\tau} = 1 + K_D[Q], \tag{6.2}$$

where F and F_0 are the integrated fluorescence intensities of the corrected spectra when concentrations of the quencher are $[Q]$ and 0, respectively; τ and τ_0 are the fluorescence lifetimes of the fluorophore at the respective concentrations. K_D is the Stern-Volmer quenching constant or dynamic quenching constant.

In the case where the quencher forms a nonfluorescent ground-state complex with the fluorophore, the fluorescence intensity also decreases. The mechanism of the decrease is different, however, because in the simplest example of the process, the ground-state complex is nonfluorescent; and the uncomplexed fluorophores have the unquenched lifetime. (Another signature of this process is that the absorption spectrum changes with respect to that of the uncomplexed fluorophore.) This type of quenching is described by a static quenching model, whose form is identical to that of equation (6.2) if intensities are used:

$$\frac{F_0}{F} = 1 + K_S[Q] \quad \text{and} \quad \frac{\tau_0}{\tau} = 1 \tag{6.3}$$

where K_S is the association constant or the static quenching constant. Clearly, however, it is possible for quenching to occur by both collisions of the quencher with the excited-state fluorophore and its complexes with the ground-state fluorophore. In such cases the Stern-Volmer plot shows an upward curvature, which is nonlinear in the quencher concentration:

$$\frac{F_0}{F} = (1 + K_D[Q])(1 + K_S[Q]) \quad \text{and} \quad \frac{\tau_0}{\tau} = 1 + K_D[Q] \tag{6.4}$$

Equation (6.4) can be transformed into the following linear form:

$$\frac{F_0 / F}{\tau_0 / \tau} = (1 + K_S[Q]) \tag{6.5}$$

Alternatively, the first part of equation (6.4) can be modified so that it does not use the lifetime data

$$\frac{F_0}{F} = 1 + K_{\text{app}}[Q], \tag{6.6}$$

where, $K_{\text{app}} = (K_D + K_S) + K_D K_S[Q]$. The apparent quenching constant K_{app} is calculated using equation (6.6) and plotted against $[Q]$ to obtain the K_D and K_S from the slope and the intercept.

If the association of the fluorophore with the quencher is weak, then an apparent static quenching is observed along with the dynamic quenching. Then we have:

$$\frac{F_0}{F} = (1 + K_D[Q])\exp([Q]V) = \frac{\tau_0}{\tau}\exp([Q]V) \tag{6.7}$$

where V is the volume of the sphere of action, within which the quencher can quench the excited fluorophore. If, however, the interaction of the quencher with the fluorophore is very strong, V can be incorporated into equation (6.5):

$$\frac{F_0 / F}{\tau_0 / \tau} = (1 + K_S[Q]) \exp([Q]V) . \quad (6.8)$$

6.4.3 Fluorescence quenching of Cy5 by phosphonium metal-halide MILs

The steady-state and the time-resolved Stern-Volmer plots for fluorescence quenching of Cy5 in DMSO are presented in **Figures 6.3-6.4** and in **Figure S6.1** for the $[P_{66614}^+]_2[CoCl_4^{2-}]$, $[P_{66614}^+]_2[MnCl_4^{2-}]$, and $[P_{66614}^+][FeCl_4^-]$ MILs, respectively. The quenching parameters obtained from equations (6.2)-(6.8) are summarized in **Table 6.2**. Among these three MILs, $[P_{66614}^+]_2[CoCl_4^{2-}]$ is the most efficient quencher of Cy5 fluorescence. A plot (**Figure 6.3d**) of F_0/F against its concentration is highly nonlinear with an upward curvature, while a similar plot using τ_0/τ plot (**Figure 6.3e**) is linear with a nonzero slope. From this complex quenching of Cy5 by $[P_{66614}^+]_2[CoCl_4^{2-}]$, the dynamic quenching constant can be extracted: $K_D = 82 \pm 3$ M^{-1}. The plot (**Figure 6.3f**) of $(F_0/F)/(\tau_0/\tau)$ using equation (6.8) yields $K_S = 1200 \pm 100$ M^{-1} and $V = 520 \pm 30$ M^{-1} indicating a very large contribution from ground-state complex formation with the quencher. Also, as expected, the absorption spectrum at 600 nm (**Figure 6.3a)** is significantly altered in the presence of the quencher. Among the three MILs, the least efficient quencher of Cy5 in DMSO is $[P_{66614}^+]_2[MnCl_4^{2-}]$. The plot of τ_0/τ against its concentration (**Figure 6.4e**) is linear, providing a dynamic quenching constant, $K_D = 0.2 \pm 0.1$ M^{-1}, which is negligible compared to that obtained for $[P_{66614}^+]_2[CoCl_4^{2-}]$. The plot obtained from equation (6.5) provides the static quenching constant, $K_S = 1 \pm 1$ M^{-1}, indicating a negligible interaction of $[P_{66614}^+]_2[MnCl_4^{2-}]$ with Cy5. Finally, the time-resolved Stern-Volmer plot (**Figure S6.1e**) for $[P_{66614}^+][FeCl_4^-]$ yields $K_D = 6.0 \pm 0.2$ M^{-1}, while the linear plot (**Figure S6.1f**) using equation (6.5) yields $K_S = 30 \pm 2$ M^{-1}. Therefore, formation of the ground-state complex is the primary contributor to the overall quenching, which can also be noted from the considerable change of

absorption spectra near 600 nm. The overall quenching efficiency, however, is much less than that of $[P_{66614}^{+}]_2[CoCl_4^{2-}]$ and higher than that of $[P_{66614}^{+}]_2[MnCl_4^{2-}]$. The extent of quenching of Cy5 in neat $[P_{66614}^{+}][FeCl_4^{-}]$ is demonstrated in **Figure S6.4** and exhibits a thousand-fold decrease of the fluorescence intensity compared to Cy5 in methanol at the same concentration ($\sim 1\ \mu M$). The fluorescence lifetime of Cy5 measured in neat $[P_{66614}^{+}][FeCl_4^{-}]$ is ~150 ps compared to 810 ps in methanol. On the other hand, the fluorescence intensity of Cy5 in neat $[P_{66614}^{+}]_2[MnCl_4^{2-}]$ increases by a factor of two with respect to methanol and its fluorescence lifetime is 2.04 ns (**Figure S6.5)**. Not only does Mn(II) not quench the fluorescence of Cy5, but the phosphonium-Mn(II) chloride MIL increases the fluorescence intensity and lifetime of Cy5. These increases are most likely attributable to the high viscosity of the solvent, which reduces the flexibility[40] of Cy5. It is likely that a significant nonradiative pathway of Cy5 is torsion about its double bonds (**Figure 6.1**) similar to the situation for the well-studied molecule, stilbene.[22,41,42] For neat $[P_{66614}^{+}][FeCl_4^{-}]$, the viscosity[20] is 650 cP at 25 °C, whereas it is 75230 cP at 25 °C for $[P_{66614}^{+}]_2[MnCl_4^{2-}]$.

To elucidate the origin of the quenching mechanism of the phosphonium metal-halide MILs, we constructed Stern-Volmer plots of Cy5 dye using the nonmagnetic ionic liquid, $[P_{66614}^{+}][Cl^{-}]$, as a control (**Figure 6.6**). The Stern-Volmer plot, within experimental error, is flat, demonstrating that $[P_{66614}^{+}][Cl^{-}]$ does not quench Cy5: $K_D = -1 \pm 1\ M^{-1}$ (**Table 6.3**). This confirms that the metal ions in the three phosphonium MILs that we have considered are responsible for the quenching of the Cy5 fluorescence. This observation is further confirmed by performing quenching studies of Cy5 and C153 dye with chloride salts of manganese and iron (**Table S6.1** and **Figures S6.5-S6.9**). The quenching of C153 and Cy5 by $MnCl_2$ is purely dynamic; and the value of the quenching constants are $K_D = 2.1 \pm 0.1\ M^{-1}$ and $K_D = 0.1 \pm 0.3$

M^{-1} for C153 and Cy5, respectively. Therefore, the extent of quenching by $MnCl_2$ is negligibly small. On the other hand, $FeCl_3$ has a significant effect on the fluorescence of C153 ($K_D = 15 \pm 1$ M^{-1}, $K_S = 1700 \pm 60$ M^{-1}, and $V = 730 \pm 9$ M^{-1}). It also quenches the fluorescence of Cy5 considerably ($K_D = 3.0 \pm 0.2$ M^{-1} and $K_S = 11.9 \pm 0.6$ M^{-1}).

6.4.4 Fluorescence quenching of Cy5 by metal-hfacac MILs

Steady-state spectra and the Stern-Volmer plots for the quenching of Cy5 in methanol are presented in **Figures S2-S3** and in **Figure 5** for the $[P_{66614}^+][Co(hfacac)_3^-]$, $[P_{66614}^+][Ni(hfacac)_3^-]$, and $[P_{66614}^+][Mn(hfacac)_3^-]$ MILs, respectively. The quenching parameters obtained from equations (6.2)-(6.8) are summarized in **Table 6.3**. One of the most striking differences between the hfacac MILs with respect to the metal halide MILs is that hfacac solvents are all well described by dynamic quenching, equation (6.2), whereas it is necessary to describe the halide solvents by static quenching mechanisms as well. This suggests that hfacac is effective in preventing the formation of ground-state complexes. For example, the quenching by $[P_{66614}^+][Co(hfacac)_3^-]$ is quite different from that of $[P_{66614}^+]_2[CoCl_4^{2-}]$, the chloride analog. **Figure S6.2a** indicates that its absorption spectrum is not as significantly altered by the quencher, as in the case of the chloride analog. Unlike its chloride analog, the plot of F_0/F against the concentration of $[P_{66614}^+][Co(hfacac)_3^-]$ is linear within experimental error (**Figure S6.2c**), yielding the Stern-Volmer quenching constant, $K_D = 69 \pm 2$ M^{-1}. For $[P_{66614}^+][Ni(hfacac)_3^-]$, a plot of F_0/F against its concentration is best fit, within experimental error, to a line (**Figure S6.3c**), yielding $K_D = 73 \pm 4$ M^{-1}. It can thus be concluded that $[P_{66614}^+][Ni(hfacac)_3^-]$ quenches Cy5 to a similar degree as does $[P_{66614}^+][Co(hfacac)_3^-]$. The absorption spectra of Cy5 in the presence of $[P_{66614}^+][Mn(hfacac)_3^-]$ change the least for the three hfacac-based MILs. The plot of F_0/F against its concentration (**Figure 6.5c**) yields $K_D = 1.9 \pm 0.3$ M^{-1}, indicating a very small degree

of quenching, comparable to that of $[P_{66614}^+]_2[MnCl_4^{2-}]$. These results suggest that among the paramagnetic ions we investigated, Mn(II) is the optimum choice for fluorescence-based analytical techniques.

Finally, in order to illustrate the suitability of Mn(II)-MILs for fluorescence-based assays of DNA, we compared the labeled oligonucleotide, Cy5-DNA, in neat: $[P_{66614}^+][FeCl_4^-]$ and $[P_{66614}^+]_2[MnCl_4^{2-}]$. The absorption and the fluorescence emission of Cy5 are greatly modified and the fluorescence intensity was quenched significantly in $[P_{66614}^+][FeCl_4^-]$ as compared to $[P_{66614}^+]_2[MnCl_4^{2-}]$ (**Figure 6.7**). The fluorescence lifetime of Cy5-DNA in neat $[P_{66614}^+][FeCl_4^-]$ is < 100 ps; while in neat $[P_{66614}^+]_2[MnCl_4^{2-}]$, it is 1.56 ns and single exponential, demonstrating the effective homogeneity of the nonquenching environment to which the Cy5 is exposed. These data confirm the utility of Mn(II)-based MILs.

6.5 Conclusions

We have investigated MILs comprised of metal-based anions in the form of chloride or hfacac complexes with phosphonium ($[P_{66614}^+]$) cation counterparts using absorption and emission spectroscopy in order to identify MILs that render them compatible with downstream fluorescence assays for DNA biopolymers. This entailed the evaluation of the quenching efficiency, with respect to the commonly used fluorescent tag, Cy5, of the paramagnetic ions, Mn(II), Fe(III), Co(II), and Ni(II) both isolated and associated with various components of the MILs, and the MILs themselves.

Although MILs containing metal ions such as Fe(III) may be advantageous for magnet-based extraction applications due to their higher magnetic moments, Fe(III)-MILs strongly quench (probably by intersystem crossing or possibly by excited-state electron transfer) fluorescence that could potentially be used for emission-based techniques. Similarly, Co(II)-MILs are strong

quenchers that preclude the use of fluorescence. Mn(II)-MILs, however, balance a high magnetic moment with low fluorescence quenching.

A summary and assessment of the nature and the magnitude of the quenching processes follows. Co(II) is the only component of the MILs that can significantly quench by nonradiative Förster resonant energy transfer (**Table 6.1**). In contrast, Fe(III) is a quencher as can be determined from **Table 6.2**, but either functions *via* intersystem crossing or excited-state electron transfer as the overlap between the Cy5 emission spectrum with its absorption spectrum is small. Hfacac keeps the Co(II) farther away from the Cy5 than does the halide and thus changes the quenching interaction. Specifically, R_0 is smaller with hfacac than with the halide anion (**Table 6.1**). Furthermore, there seems to be little or no static quenching with hfacac. This is suggestive of the role hfacac may play with the other metals as well. The metal-hfacac anion is preferable to the metal-halide because it provides "cleaner" spectra by reduced ground-state complexation (and quenching) with the fluorescent tag, Cy5, as indicated by the relatively smaller or absent changes of the Cy5 absorption spectrum with hfacac concentration (**Table 6.3**). The Stern-Volmer quenching constants for Mn(II)-based MILs are one order of magnitude smaller than those of Co(II) or Ni(II)-based MILs. Mn(II) does not obfuscate the spectra of the fluorescent label, as do Fe(III) and Co(II). Finally, and most importantly, our results demonstrate that Mn(II)-based MIL extraction solvents such as $[P_{66614}^{+}]_2[MnCl_4^{2-}]$ and $[P_{66614}^{+}][Mn(hfacac)_3^{-}]$ are ideal for direct spectroscopic analysis of extracted DNA and possibly other biological materials, such as RNA or proteins.

6.6 Acknowledgments

JLA acknowledges support from the Chemical Measurement and Imaging Program of the National Science Foundation (CHE-1709372). We thank Mr. Matthew Klyman for technical assistance.

6.7 References

1. Goldberg, B.; Sichtig, H.; Geyer, C.; Ledeboer, N.; Weinstock, G. M. Making the Leap from Research Laboratory to Clinic: Challenges and Opportunities for Next-Generation Sequencing in Infectious Disease Diagnostics. *mBio*. **2015**, *6* (6),

2. Das, J.; Ivanov, I.; Sargent, E. H.; Kelley, S. O. DNA Clutch Probes for Circulating Tumor DNA Analysis. *J. Am. Chem. Soc.* **2016**, *138* (34), 11009-11016.

3. Schwarzenbach, H.; Hoon, D. S. B.; Pantel, K. Cell-Free Nucleic Acids as Biomarkers in Cancer Patients. *Nat. Rev: Cancer*. **2011**, *11* (6), 426-437.

4. Al-Soud, W. A.; Rådström, P. Purification and Characterization of PCR-Inhibitory Components in Blood Cells. *J. Clin. Microbiol.* **2001**, *39* (2), 485-493.

5. Kumar, C. V.; Turner, R. S.; Asuncion, E. H. Groove Binding of a Styrylcyanine Dye to the DNA Double Helix: The Salt Effect. *J. Photochem. Photobiol. A: Chem.* **1993**, *74* (2), 231-238.

6. Dauphin, L. A.; Stephens, K. W.; Eufinger, S. C.; Bowen, M. D. Comparison of Five Commercial DNA Extraction Kits for the Recovery of Yersinia Pestis DNA from Bacterial Suspensions and Spiked Environmental Samples. *J. Appl. Microbiol.* **2010**, *108* (1), 163-172.

7. Leslie, D. C.; Li, J.; Strachan, B. C.; Begley, M. R.; Finkler, D.; Bazydlo, L. A. L.; Barker, N. S.; Haverstick, D. M.; Utz, M.; Landers, J. P. New Detection Modality for Label-Free Quantification of DNA in Biological Samples Via Superparamagnetic Bead Aggregation. *J. Am. Chem. Soc.* **2012**, *134* (12), 5689-5696.

8. Wang, J.-H.; Cheng, D.-H.; Chen, X.-W.; Du, Z.; Fang, Z.-L. Direct Extraction of Double-Stranded DNA into Ionic Liquid 1-Butyl-3-Methylimidazolium Hexafluorophosphate and Its Quantification. *Anal. Chem.* **2007**, *79* (2), 620-625.

9. Clark, K. D.; Varona, M.; Anderson, J. L. Ion-Tagged Oligonucleotides Coupled with a Magnetic Liquid Support for the Sequence-Specific Capture of DNA. *Angew. Chem. Int. Ed.* **2017**, *56* 7630-7633.

10. Li, T.; Joshi, M. D.; Ronning, D. R.; Anderson, J. L. Ionic Liquids as Solvents for in Situ Dispersive Liquid–Liquid Microextraction of DNA. *J. Chromatogr. A.* **2013**, *1272* (0), 8-14.

11. Shi, Y.; Liu, Y.-L.; Lai, P.-Y.; Tseng, M.-C.; Tseng, M.-J.; Li, Y.; Chu, Y.-H. Ionic Liquids Promote PCR Amplification of DNA. *Chem. Commun. (Cambridge, U. K.)*. **2012**, *48* (43), 5325-5327.

12. Vijayaraghavan, R.; Izgorodin, A.; Ganesh, V.; Surianarayanan, M.; MacFarlane, D. R. Long-Term Structural and Chemical Stability of DNA in Hydrated Ionic Liquids. *Angew. Chem. Int. Ed.* **2010**, *49* (9), 1631-1633.

13. Hayashi, S.; Hamaguchi, H. O. Discovery of a Magnetic Ionic Liquid Bmim FeCl4. *Chem. Lett.* **2004**, *33* (12), 1590-1591.

14. Del Sesto, R. E.; McCleskey, T. M.; Burrell, A. K.; Baker, G. A.; Thompson, J. D.; Scott, B. L.; Wilkes, J. S.; Williams, P. Structure and Magnetic Behavior of Transition Metal Based Ionic Liquids. *Chem. Commun. (Cambridge, U. K.)*. **2008**, (4), 447-449.

15. Nacham, O.; Clark, K. D.; Yu, H.; Anderson, J. L. Synthetic Strategies for Tailoring the Physicochemical and Magnetic Properties of Hydrophobic Magnetic Ionic Liquids. *Chem. Mater.* **2015**, *27* (3), 923-931.

16. Mallick, B.; Balke, B.; Felser, C.; Mudring, A.-V. Dysprosium Room-Temperature Ionic Liquids with Strong Luminescence and Response to Magnetic Fields. *Angew. Chem. Int. Ed.* **2008**, *47* (40), 7635-7638.

17. Clark, K. D.; Nacham, O.; Yu, H.; Li, T.; Yamsek, M. M.; Ronning, D. R.; Anderson, J. L. Extraction of DNA by Magnetic Ionic Liquids: Tunable Solvents for Rapid and Selective DNA Analysis. *Anal. Chem.* **2015**, *87* (3), 1552-1559.

18. Clark, K. D.; Yamsek, M. M.; Nacham, O.; Anderson, J. L. Magnetic Ionic Liquids as PCR-Compatible Solvents for DNA Extraction from Biological Samples. *Chem. Commun. (Cambridge, U. K.)*. **2015**, *51* (94), 16771-16773.

19. Yu, H.; Merib, J.; Anderson, J. L. Faster Dispersive Liquid-Liquid Microextraction Methods Using Magnetic Ionic Liquids as Solvents. *J. Chromatogr. A*. **2016**, *1463* 11-19.

20. Pierson, S. A.; Nacham, O.; Clark, K. D.; Nan, H.; Mudryk, Y.; Anderson, J. L. Synthesis and Characterization of Low Viscosity Hexafluoroacetylacetonate-Based Hydrophobic Magnetic Ionic Liquids. *New J. Chem.* **2017**,

21. Főrster, T. 10th Spiers Memorial Lecture. Transfer Mechanisms of Electronic Excitation. *Discuss. Faraday. Soc.* **1959**, *27* 7-17.

22. Fleming, G. R. *Chemical Application of Ultrafast Spectroscopy* Oxford University Press: New York, 1986.

23. Birks, J. B. *Photophysics of Aromatic Molecules* Wiley-Interscience: London, New York, 1970.

24. Van Der Meer, B. W.; Coker, G.; Chen, S.-Y. S. *Resonance Energy Transfer:Theory and Data* VCH New York: 1994.

25. Medinger, T.; Wilkinson, F. Mechanism of Fluorescence Quenching in Solution. Part 1.—Quenching by Bromobenzene. *Trans. Farad. Soc.* **1965**, *61* 620-630.

26. Horrocks, A.; Kearvell, A.; Tickle, K.; Wilkinson, F. Mechanism of Fluorescence Quenching in Solution. Part 2.—Quenching by Xenon and Intersystem Crossing Efficiencies. *Trans. Farad. Soc.* **1966**, *62* 3393-3399.

27. Green, J. A.; Singer, L. A.; Parks, J. H. Fluorescence Quenching by the Stable Free Radical Di-T-Butylnitroxide. *J. Chem. Phys.* **1973**, *58* (7), 2690-2695.

28. Ware, W. R.; Watt, D.; Holmes, J. D. Exciple Photophysics. I.. Alpha.-Cyanonaphthalene-Olefin System. *J. Am. Chem. Soc.* **1974**, *96* (26), 7853-7860.

29. Eftink, M.; Ghiron, C. Fluorescence Quenching of Indole and Model Micelle Systems. *J. Phys. Chem.* **1976**, *80* (5), 486-493.

30. O'Connor, D. V.; Ware, W. R. Exciplex Photophysics. III. Kinetics of Fluorescence Quenching Of. Alpha.-Cyanonaphthalene by Dimethylcyclopentene-1, 2 in Hexane. *J. Am. Chem. Soc.* **1976**, *98* (16), 4706-4711.

31. Keizer, J. Nonlinear Fluorescence Quenching and the Origin of Positive Curvature in Stern-Volmer Plots. *J. Am. Chem. Soc.* **1983**, *105* (6), 1494-1498.

32. Peak, D.; Werner, T.; Dennin Jr, R. M.; Baird, J. K. Fluorescence Quenching at High Quencher Concentrations. *J. Chem. Phys.* **1983**, *79* (7), 3328-3335.

33. Blatt, E.; Chatelier, R.; Sawyer, W. Effects of Quenching Mechanism and Type of Quencher Association on Stern-Volmer Plots in Compartmentalized Systems. *Biophys. J.* **1986**, *50* (2), 349-356.

34. Gehlen, M. H.; De Schryver, F. C. Time-Resolved Fluorescence Quenching in Micellar Assemblies. *Chemical Reviews (Washington, DC, United States)*. **1993**, *93* (1), 199-221.

35. Zeng, H.; Durocher, G. Analysis of Fluorescence Quenching in Some Antioxidants from Non-Linear Stern—Volmer Plots. *J. Lumin.* **1995**, *63* (1-2), 75-84.

36. Castanho, M. A.; Prieto, M. J. Fluorescence Quenching Data Interpretation in Biological Systems: The Use of Microscopic Models for Data Analysis and Interpretation of Complex Systems. *Biochim. Biophys. Acta Biomembr.* **1998**, *1373* (1), 1-16.

37. Evale, B. G.; Hanagodimath, S. Static and Dynamic Quenching of Biologically Active Coumarin Derivative by Aniline in Benzene–Acetonitrile Mixtures. *J. Lumin.* **2010**, *130* (8), 1330-1337.

38. Kadadevarmath, J.; Malimath, G.; Melavanki, R.; Patil, N. Static and Dynamic Model Fluorescence Quenching of Laser Dye by Carbon Tetrachloride in Binary Mixtures. *Spectrochim. Acta, Part A.* **2014**, *117* 630-634.

39. Molina-Bolívar, J.; Ruiz, C. C.; Galisteo-González, F.; Medina-O, M.; Parra, A. Simultaneous Presence of Dynamic and Sphere Action Component in the Fluorescence Quenching of Human Serum Albumin by Diphthaloylmaslinic Acid. *J. Lumin.* **2016**, *178* 259-266.

40. Huang, Z.; Ji, D.; Wang, S.; Xia, A.; Koberling, F.; Patting, M.; Erdmann, R. Spectral Identification of Specific Photophysics of Cy5 by Means of Ensemble and Single Molecule Measurements. *J. Phys. Chem. A.* **2006**, *110* (1), 45-50.

41. Waldeck, D. H. Photoisomerization Dynamics of Stilbenes. *Chem. Rev.* **1991**, *91* (3), 415-436.

42. Haran, G.; Wynne, K.; Xie, A.; He, Q.; Chance, M.; Hochstrasser, R. M. Excited State Dynamics of Bacteriorhodopsin Revealed by Transient Stimulated Emission Spectra. *Chem. Phys. Lett.* **1996**, *261* (4-5), 389-395.

6.8 Tables and figures

Table 6.1

Förster Critical Distances

Quencher	R_0 (Å)
Mn(II) [a]	16.1
Fe(III) [a]	26.9
Co(II) [a]	58.1
Ni(II) [a]	33.6
hfacac	15.9
$[P_{66614}^+][Cl^-]$	10.2
$[P_{66614}^+][hfacac^-]$	17.0
$[P_{66614}^+][Mn(hfacac)_3^-]$	26.7
$[P_{66614}^+][Co(hfacac)_3^-]$	22.2
$[P_{66614}^+][Ni(hfacac)_3^-]$	33.8
$[P_{66614}^+]_2[CoCl_4^{2-}]$ in DMSO [b]	57.3
$[P_{66614}^+]_2[MnCl_4^{2-}]$	14.2
$[P_{66614}^+][FeCl_4^-]$	20.7

[a] A sufficient amount of Cl^- was used in the preparation of the solutions to ensure a tetrahedral arrangement of the halide about the metal cation.

[b] Methanol was the solvent for the measurement of Förster critical distances in all cases except for $[P_{66614}^+]_2[CoCl_4^{2-}]$, where DMSO was required. In methanol, the solution took on an uncharacteristic pink color; and $R_0 = 33.5$ Å. Note that R_0 for $[P_{66614}^+]_2[CoCl_4^{2-}]$ in DMSO is essentially equal to that for Co(II) in methanol.

Table 6.2

Parameters for the Quenching of Fluorescence of Cy5 by Metal Halide-Based MILs

Anion	Plot type[a]	K_D(M^{-1})	K_S(M^{-1})	V(M^{-1})
$[CoCl_4^{2-}]$[b]	τ_0/τ *vs.* $[Q]$	82 ± 3	--	--
	$(F_0/F)/(\tau_0/\tau)$ *vs.* $[Q]$[c]	--	1200 ± 100	520 ± 30
$[MnCl_4^{2-}]$	F_0/F *vs.* $[Q]$	--	1 ± 2	--
	τ_0/τ *vs.* $[Q]$	0.2 ± 0.1	--	--
	$(F_0/F)/(\tau_0/\tau)$ *vs.* $[Q]$[d]	--	1 ± 1	--
$[FeCl_4^-]$	F_0/F *vs.* $[Q]$	40 ± 2	--	--
	τ_0/τ *vs.* $[Q]$	6.0 ± 0.2	--	--
	$(F_0/F)/(\tau_0/\tau)$ *vs.* $[Q]$[d]	--	30 ± 2	--

[a] The relationships are given in equations (6.2) through (6.8). $[Q]$ is the quencher concentration.

[b] For $[P_{66614}^+]_2[CoCl_4^{2-}]$, the F_0/F *vs.* $[Q]$ plot shows a large deviation from linearity with an upward curvature.

[c] The plot of $(F_0/F)/(\tau_0/\tau)$ *vs.* $[Q]$ is nonlinear and fit to equation (6.8).

[d] The plot of $(F_0/F)/(\tau_0/\tau)$ *vs.* $[Q]$ is linear and fit to equation (6.5).

Table 6.3

Parameters for the Quenching of Fluorescence of Cy5 by [P_{66614}^+]-based MILs with hfacac ligands

Anion	K_D or K_S (M^{-1}) [a]
[$Co(hfacac)_3^-$]	69 ± 2
[$Ni(hfacac)_3^-$]	73 ± 4
[$Mn(hfacac)_3^-$]	1.9 ± 0.3
[Cl^-][b]	-1 ± 1

[a] The data are fit well to equations (6.2) and (6.3) are formally identical and which can only be distinguished by measuring fluorescence lifetimes, which was not possible for this series of samples. Because, however, there was no change in the absorption spectrum as a function of quencher concentration (**Figure 6.5a**), it is appropriate to conclude that the [$Mn(hfacac)_3^-$] solvent quenches by a dynamic process. There is evidence of some ground-state complexation for the [$Co(hfacac)_3^-$] and a considerable amount for [$Ni(hfacac)_3^-$] solvents (**Figures S6.2** and **S6.3**, respectively), but not to the extent as observed for the halides. In all instances, then, it appears that the hfacac ligand suppresses or substantially mitigates ground-state complexation.

[b] [P_{66614}^+][Cl^-] is a "conventional" ionic liquid with no magnetic moment and serves as a control.

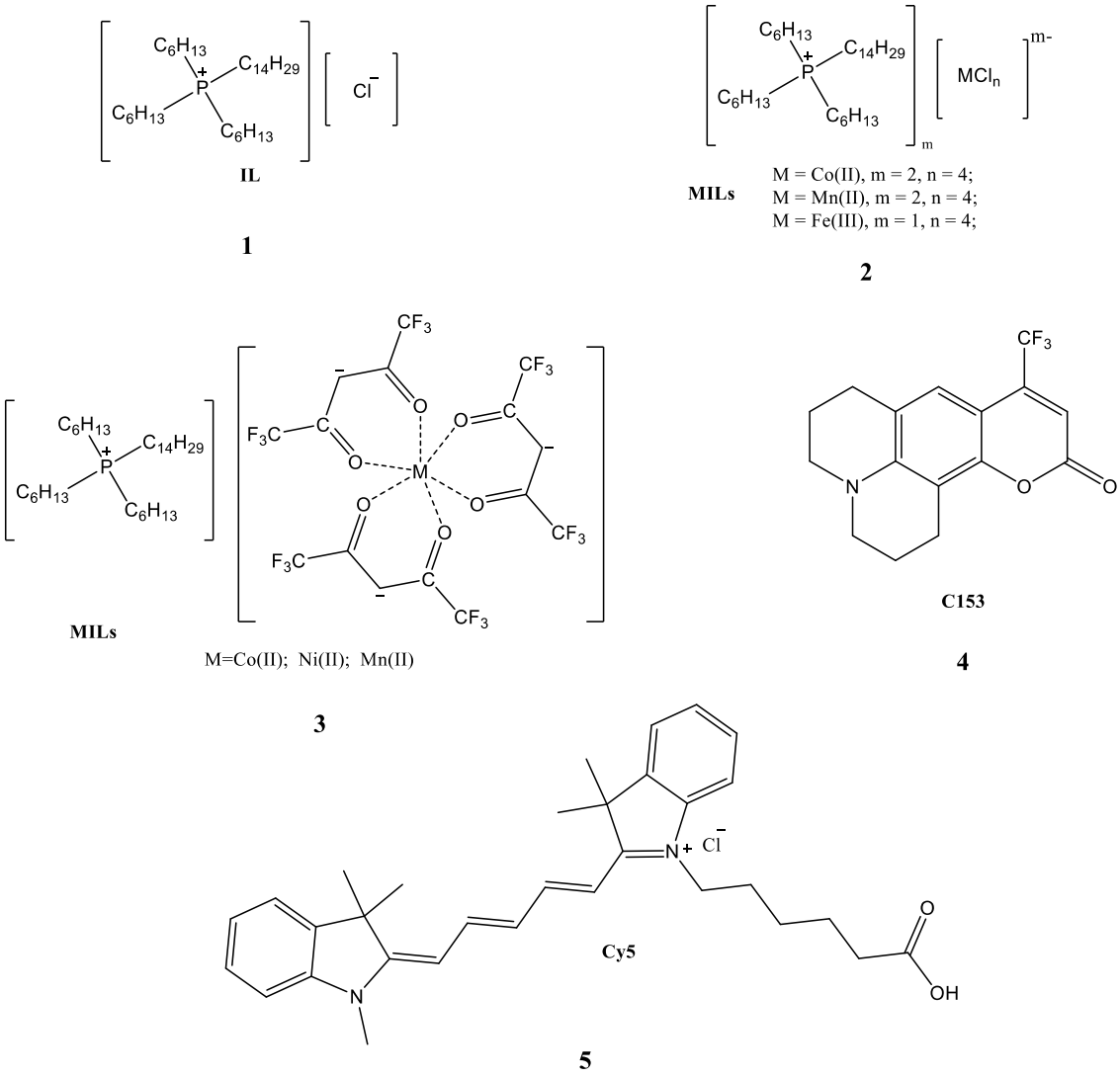

Figure 6.1. Structures of the IL, MILs, and fluorophores. (**1**) Phosphonium chloride, $[P_{66614}^{+}][Cl^{-}]$ (**2**) phosphonium cobalt(II) chloride, $[P_{66614}^{+}]_2[CoCl_4^{2-}]$; phosphonium manganese(II) chloride, $[P_{66614}^{+}]_2[MnCl_4^{2-}]$; and phosphonium iron(III) chloride, $[P_{66614}^{+}][FeCl_4^{2-}]$ (**3**) phosphonium cobalt(II) hexafluoroacetylacetonate, $[P_{66614}^{+}][Co(hfacac)_3^{-}]$; phosphonium nickel(II) hexafluoroacetylacetonate, $[P_{66614}^{+}][Ni(hfacac)_3^{-}]$; and phosphonium manganese(II) hexafluoroacetylacetonate, $[P_{66614}^{+}][Mn(hfacac)_3^{-}]$ (**4**) Coumarin 153, C153 (**5**) Cyanine5 carboxylic acid, Cy5. Experiments using C153 are discussed in the SI.

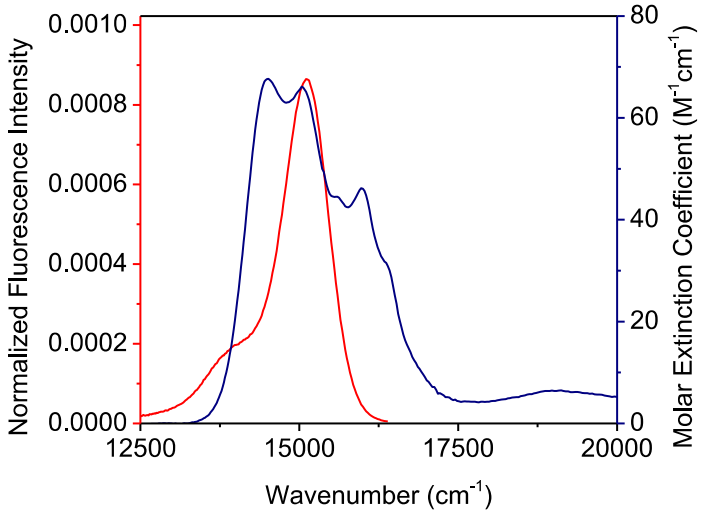

Figure 6.2. Fluorescence and absorption data required for the computation of the Förster overlap integral indicated in equation (6.1). The fluorescence spectrum of Cy5 (red) is plotted to have unit area on the wavenumber scale. The absorption of Co(II) is given in blue. A sufficient amount of Cl^- was used in the preparation of the solutions to ensure a tetrahedral arrangement of the halide about the metal cation.

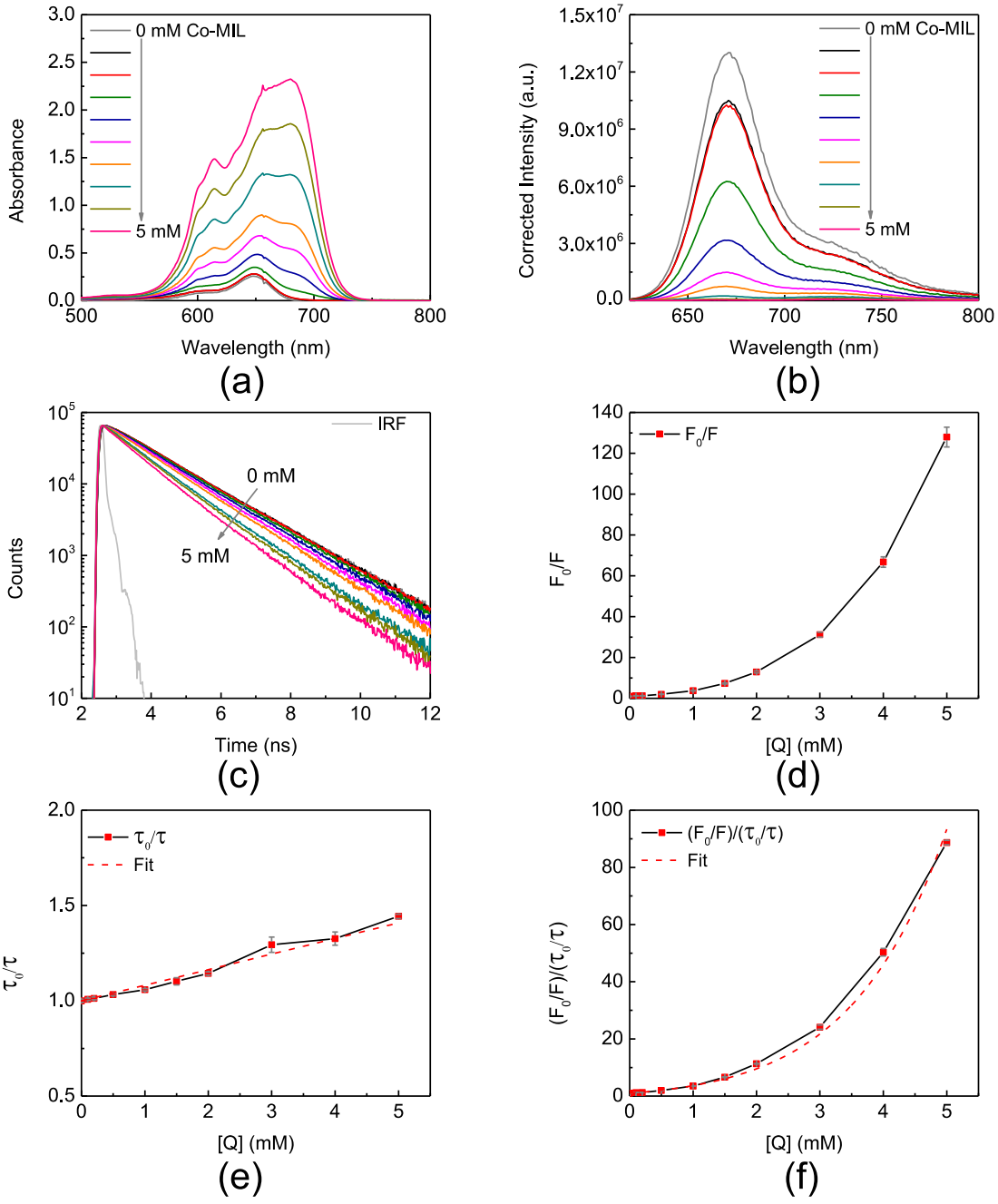

Figure 6.3. Fluorescence quenching of Cy5 in DMSO as a function of $[P_{66614}^{+}]_2[CoCl_4^{2-}]$ concentration. (a) Absorption spectra. (b) Fluorescence emission spectra, $\lambda_{ex} = 600$ nm. Intensities are corrected for the absorption at the wavelength of excitation. (c) Time-resolved fluorescence decay. The IRF is the instrument response function for the apparatus. (d) Stern-Volmer plot for the integrated fluorescence intensity ratio (F_0/F) as a function of the quencher concentration. (e) Stern-Volmer plot of (τ_0/τ) as a function of the quencher concentration. (f) Plot of $(F_0/F)/(\tau_0/\tau)$ as a function of the quencher concentration.

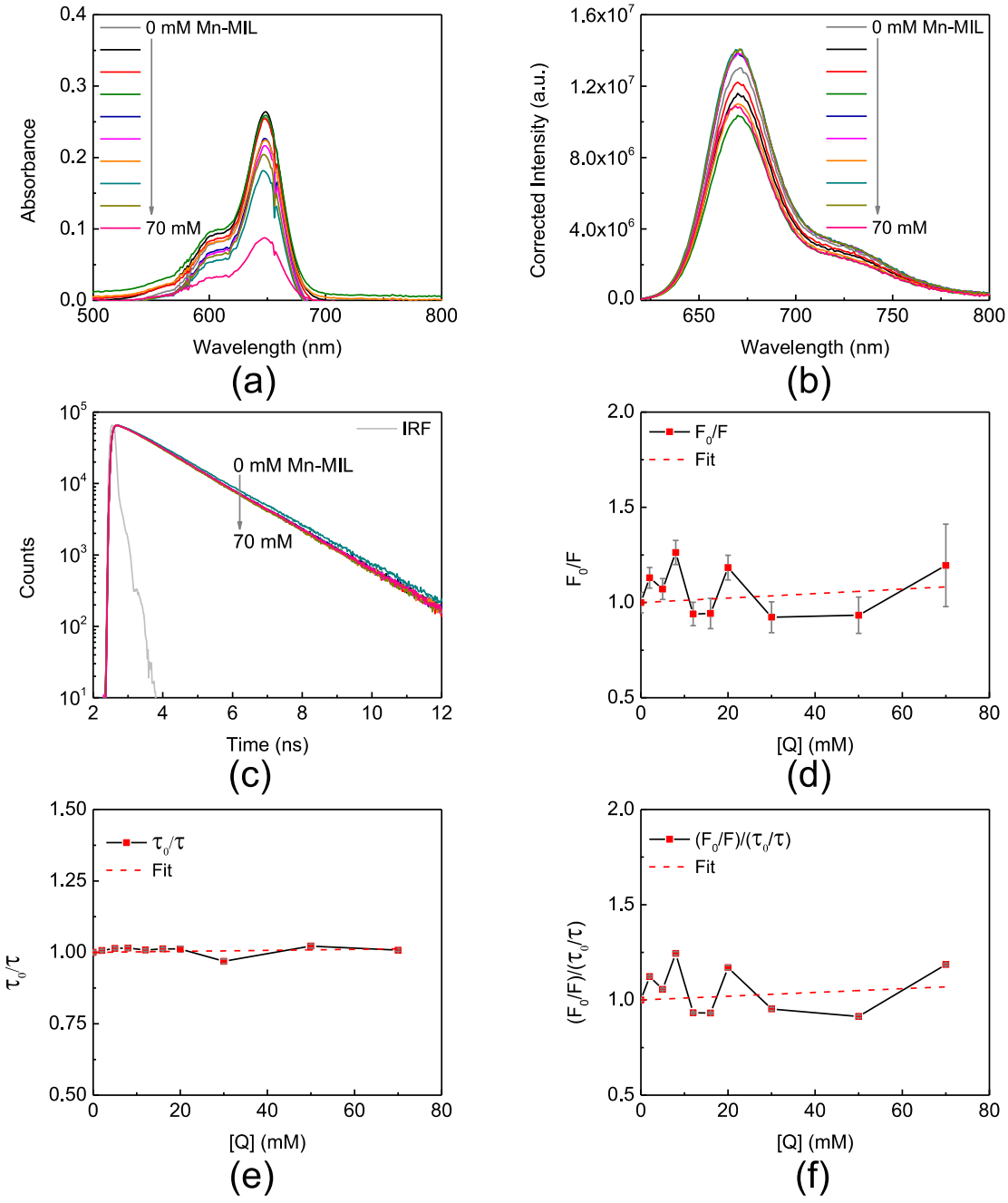

Figure 6.4. Fluorescence quenching of Cy5 in DMSO as a function of $[P_{66614}^{+}]_2[MnCl_4^{2-}]$ concentration. (a) Absorption spectra. (b) Fluorescence emission spectra at $\lambda_{ex} = 600$ nm. Intensities are corrected for the absorption at the wavelength of excitation (c) Time-resolved fluorescence decay (d) Stern-Volmer plot for the integrated fluorescence intensity ratio (F_0/F) as a function of the quencher concentration. (e) Stern-Volmer plot of (τ_0/τ) as a function of the quencher concentration. (f) Plot of $(F_0/F)/(\tau_0/\tau)$ as a function of the quencher concentration.

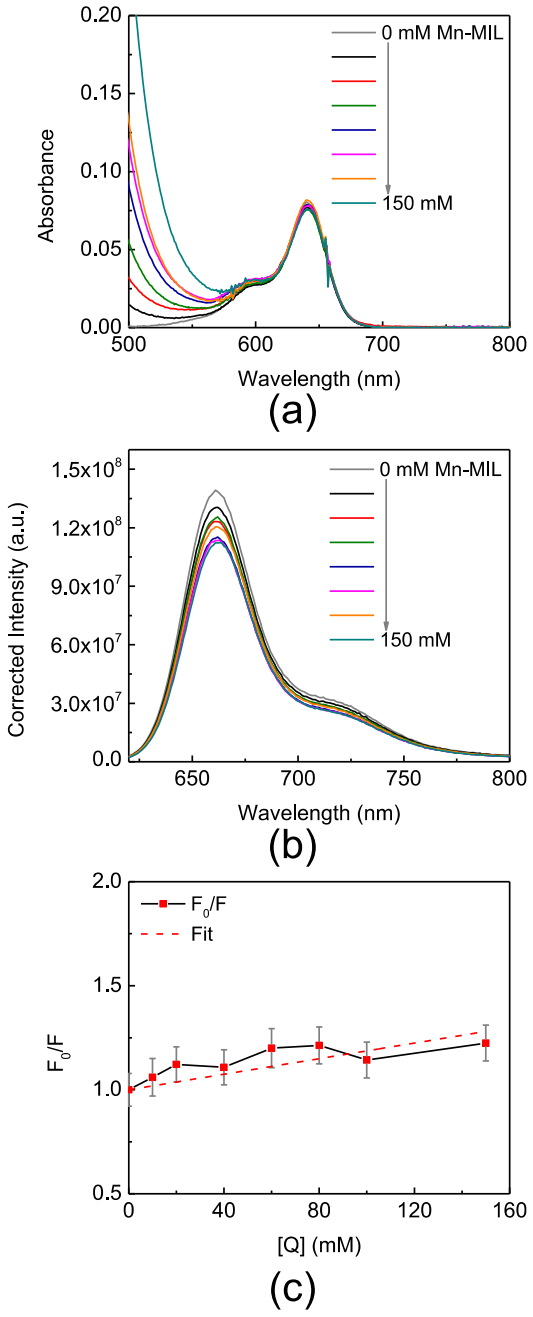

Figure 6.5. Fluorescence quenching of Cy5 in methanol as a function of $[P_{66614}^{+}][Mn(hfacac)_3^{-}]$ concentration. (a) Absorption spectra. (b) Fluorescence emission spectra at $\lambda_{ex} = 600$ nm. Intensities are corrected for the absorption at the wavelength of excitation (c) Stern-Volmer plot for the integrated fluorescence intensity ratio (F_0/F) as a function of the quencher concentration.

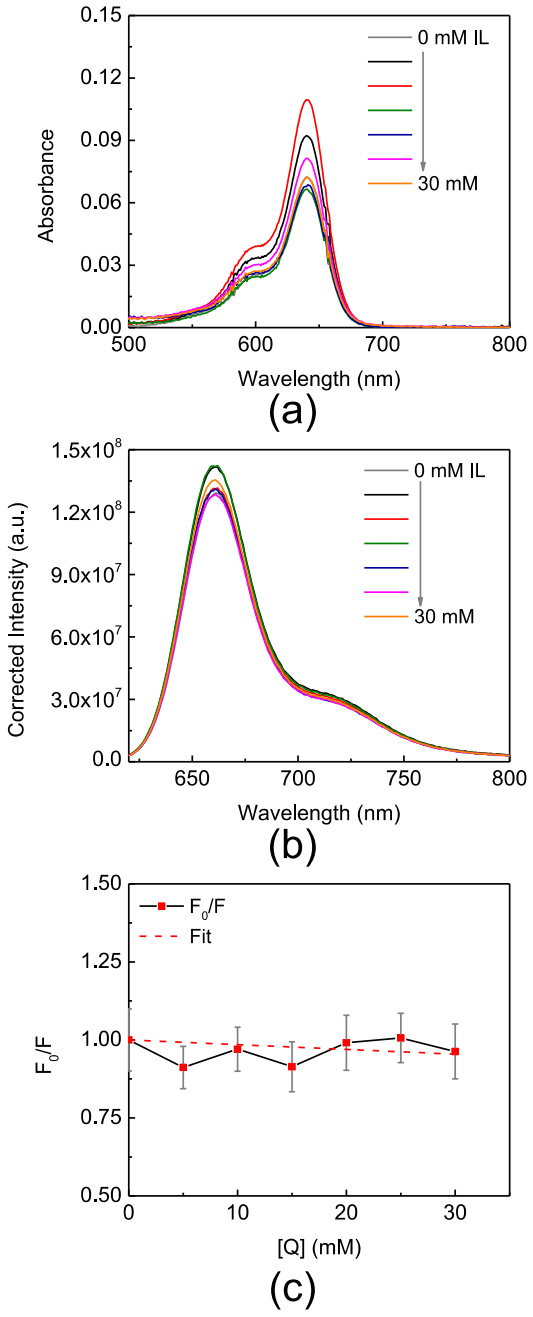

Figure 6.6. Fluorescence quenching of Cy5 in methanol as a function of $[P_{66614}^{+}][Cl^{-}]$ concentration. (a) Absorption spectra. (b) Fluorescence emission spectra at $\lambda_{ex} = 600$ nm. Intensities are corrected for the absorption at the wavelength of excitation. (c) Stern-Volmer plot for the integrated fluorescence intensity ratio (F_0/F) as a function of the IL concentration.

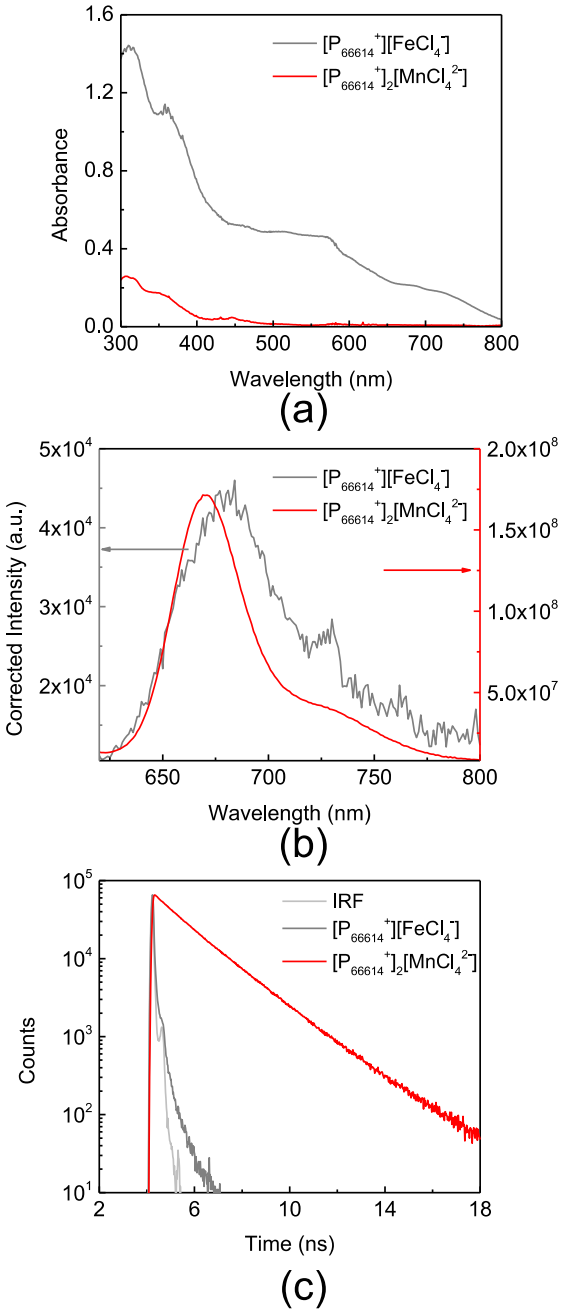

Figure 6.7. Absorption and emission of Cy5-DNA (~1 μM) in neat $[P_{66614}^{+}][FeCl_4^{-}]$ (gray) and in neat $[P_{66614}^{+}]_2[MnCl_4^{2-}]$ (red). (a) Absorption spectra. (b) Fluorescence emission spectra, $\lambda_{ex} =$ 600 nm. Note that the spectra are normalized to the same average peak intensity but that the intensity in the $[FeCl_4^{-}]$ solvent is roughly 200 times less than in the $[MnCl_4^{2-}]$ counterpart. (c) Time-resolved fluorescence decay traces confirming the results of panel (b). IRF is the instrument response function of the apparatus. The lifetimes of Cy5-DNA are < 100 ps in neat $[P_{66614}^{+}][FeCl_4^{-}]$ and 1.56 ns in neat $[P_{66614}^{+}]_2[MnCl_4^{2-}]$.

6.9 Supplementary Information

Table S6.1

Parameters for Fluorescence Quenching of C153 and Cy5 by Metal Chloride Salts

Dye	Salt	Plot type [a]	K_D(M^{-1})	K_S(M^{-1})	V(M^{-1})
C153	$FeCl_3$ [b]	τ_0/τ *vs.* $[Q]$	15 ± 1	--	--
		$(F_0/F)/(\tau_0/\tau)$ *vs.* $[Q]$[c]	--	1700 ± 60	730 ± 9
	$MnCl_2$	F_0/F *vs.* $[Q]$	2.2 ± 0.1	--	--
		τ_0/τ *vs.* $[Q]$	2.1 ± 0.1	--	--
Cy5	$FeCl_3$	F_0/F *vs.* $[Q]$	18.1 ± 0.4	--	--
		τ_0/τ *vs.* $[Q]$	3.0 ± 0.2	--	--
		$(F_0/F)/(\tau_0/\tau)$ *vs.* $[Q]$[d]	--	11.9 ± 0.6	--
	$MnCl_2$	F_0/F *vs.* $[Q]$	0.1 ± 0.2	--	--
		τ_0/τ *vs.* $[Q]$	0.1 ± 0.3	--	--

[a] The relationships are given in equations (6.2)-(6.8).

[b] For C153 and $FeCl_3$, the F_0/F *vs.* $[Q]$ plot shows a large deviation from linearity with an upward curvature.

[c] The plot of $(F_0/F)/(\tau_0/\tau)$ *vs.* $[Q]$ is nonlinear and fitted with equation (6.8).

[d] The plot of $(F_0/F)/(\tau_0/\tau)$ *vs.* $[Q]$ is linear and fitted with equation (6.5).

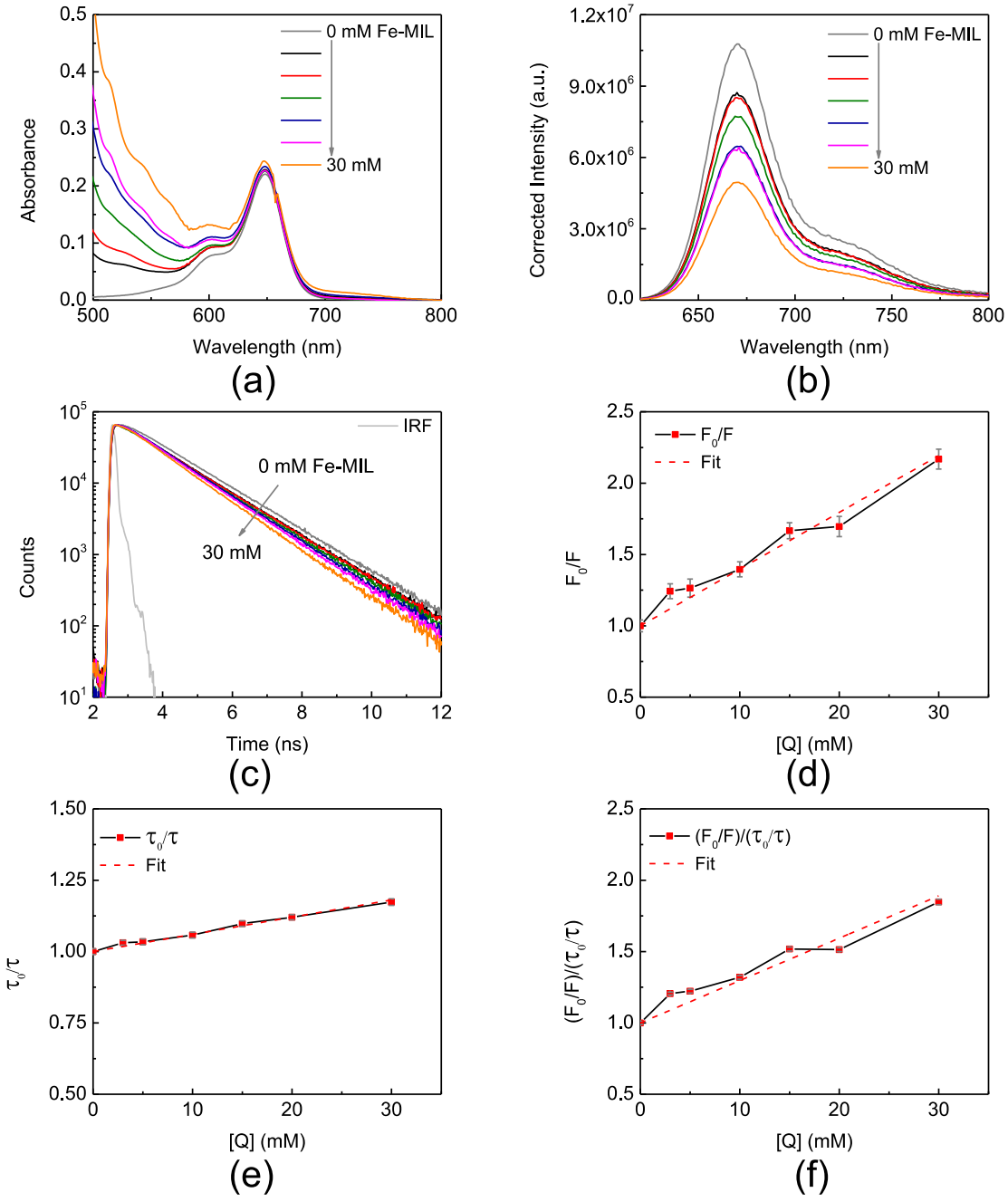

Figure S6.1. Fluorescence quenching of Cy5 in DMSO as a function of $[P_{66614}^{+}][FeCl_4^{-}]$ concentration. (a) Absorption spectra. (b) Fluorescence emission spectra at $\lambda_{ex} = 600$ nm. Intensities are corrected for the absorption at the wavelength of excitation. (c) Time-resolved fluorescence decay. (d) Stern-Volmer plot for the integrated fluorescence intensity ratio (F_0/F) as a function of the quencher concentration. (e) Stern-Volmer plot of (τ_0/τ) as a function of the quencher concentration. (f) Plot of $(F_0/F)/(\tau_0/\tau)$ as a function of the quencher concentration.

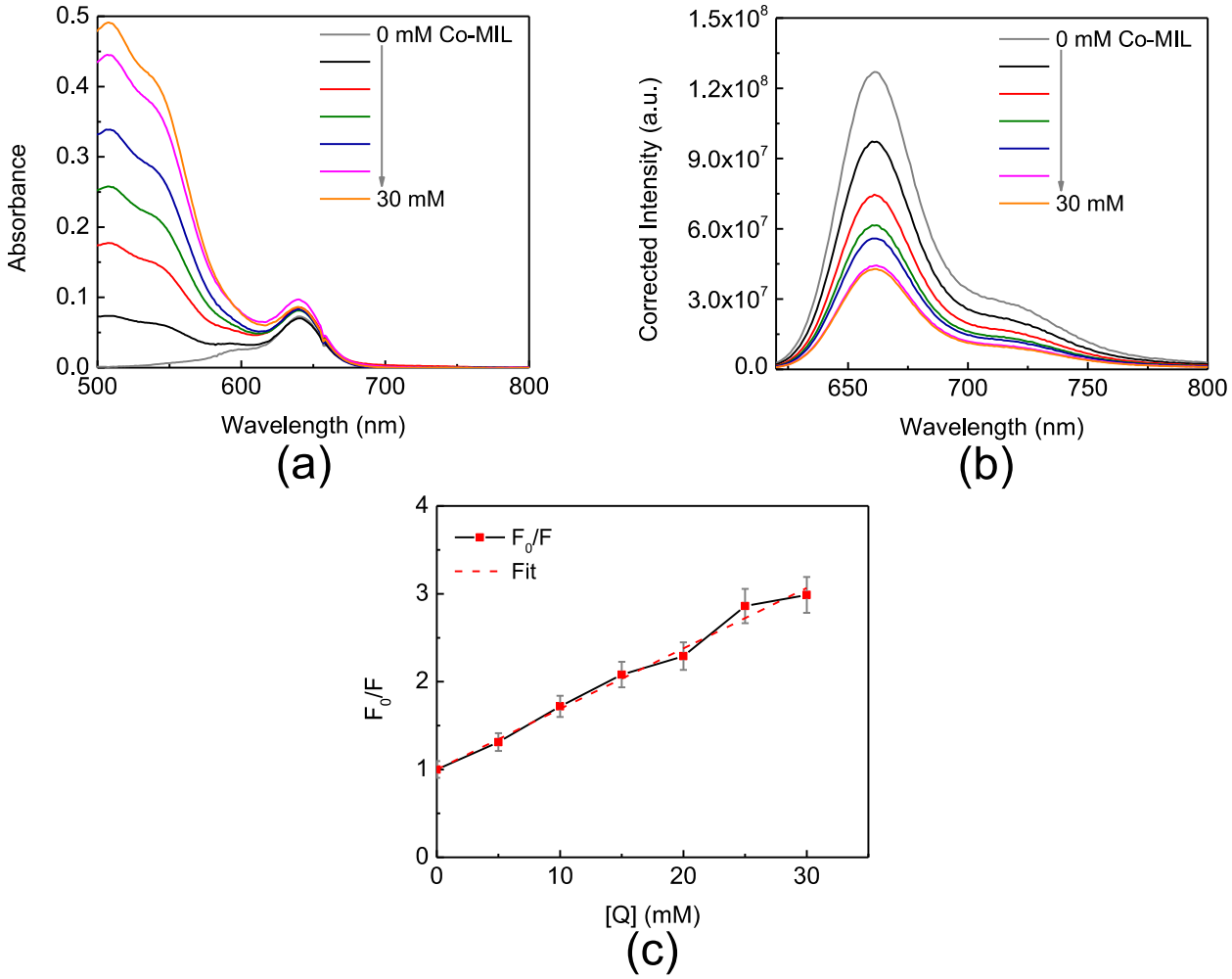

Figure S6.2. Fluorescence quenching of Cy5 in methanol as a function of $[P_{66614}^{+}][Co(hfacac)_3^{-}]$ concentration. (a) Absorption spectra. (b) Fluorescence emission spectra at $\lambda_{ex} = 600$ nm. Intensities are corrected for the absorption at the wavelength of excitation. (c) Stern-Volmer plot for the integrated fluorescence intensity ratio (F_0/F) as a function of the quencher concentration.

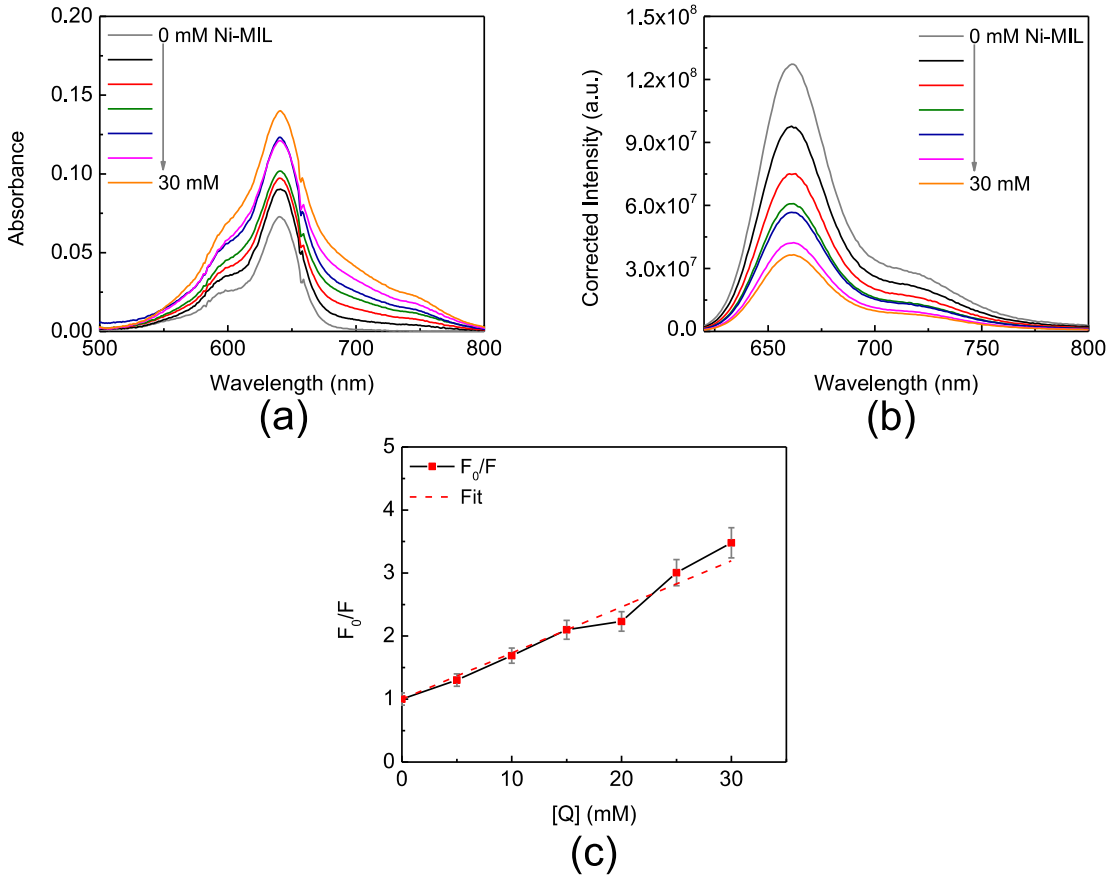

Figure S6.3. Fluorescence quenching of Cy5 in methanol as a function of $[P_{66614}^{+}][Ni(hfacac)_3^{-}]$ concentration. (a) Absorption spectra. (b) Fluorescence emission spectra at $\lambda_{ex} = 600$ nm. Intensities are corrected for the absorption at the wavelength of excitation. (c) Stern-Volmer plot for the integrated fluorescence intensity ratio (F_0/F) as a function of the quencher concentration.

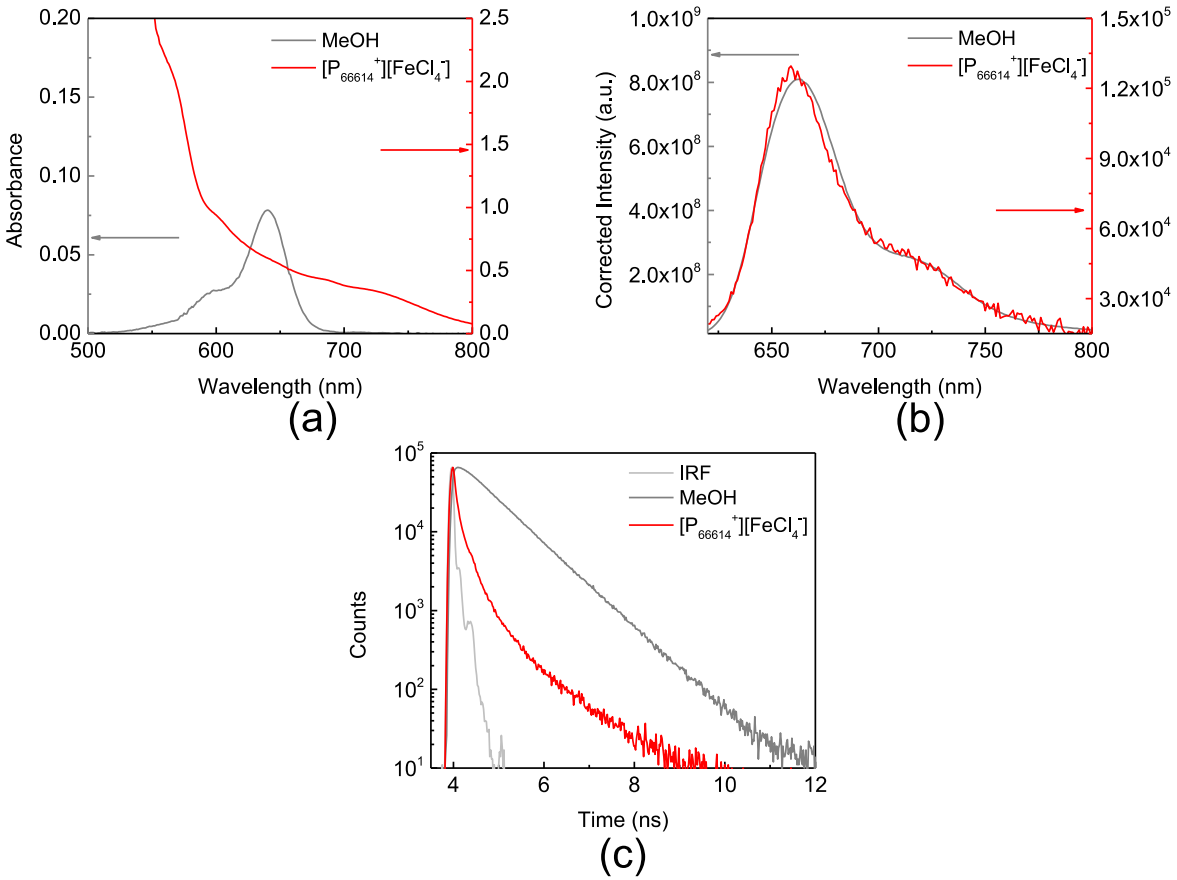

Figure S6.4. Fluorescence quenching of Cy5 (~1 μM) in neat $[P_{66614}^{+}][FeCl_4^{-}]$. (a) Absorption spectra of Cy5 in neat $[P_{66614}^{+}][FeCl_4^{-}]$ (red) and in methanol (gray). (b) Fluorescence emission spectra at $\lambda_{ex} = 600$ nm. Intensities are corrected for the absorption at the wavelength of excitation (c) Time-resolved fluorescence decay. The mean lifetime of Cy5 is 150 ps in neat $[P_{66614}^{+}][FeCl_4^{-}]$ whereas it is 810 ps in MeOH.

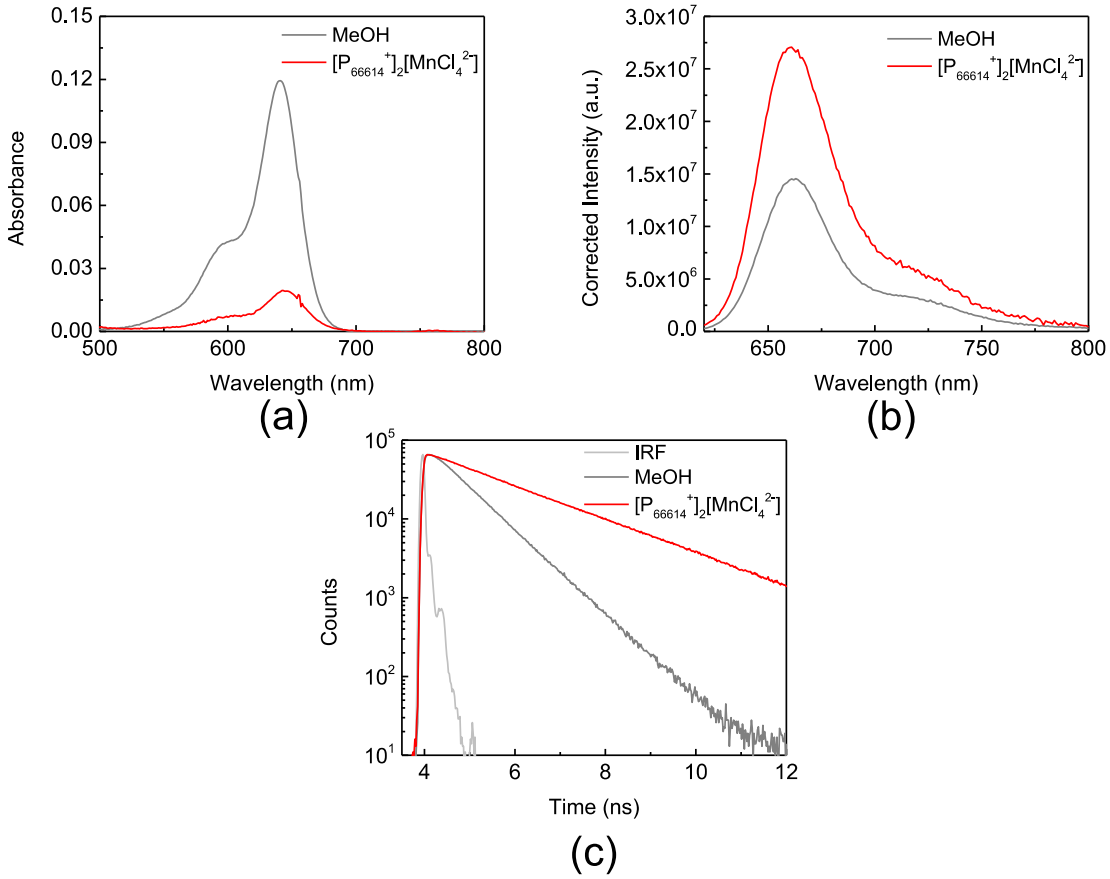

Figure S6.5. Fluorescence quenching of Cy5 (~1 μM) in neat $[P_{66614}^{+}]_2[MnCl_4^{2-}]$. (a) Absorption spectra of Cy5 in neat $[P_{66614}^{+}]_2[MnCl_4^{2-}]$ (red) and in methanol (gray). (b) Fluorescence emission spectra at $\lambda_{ex} = 600$ nm. Intensities are corrected for the absorption at the wavelength of excitation (c) Time-resolved fluorescence decay. The mean lifetime of Cy5 is 2.04 ns in neat $[P_{66614}^{+}]_2[MnCl_4^{2-}]$ whereas it is 810 ps in MeOH.

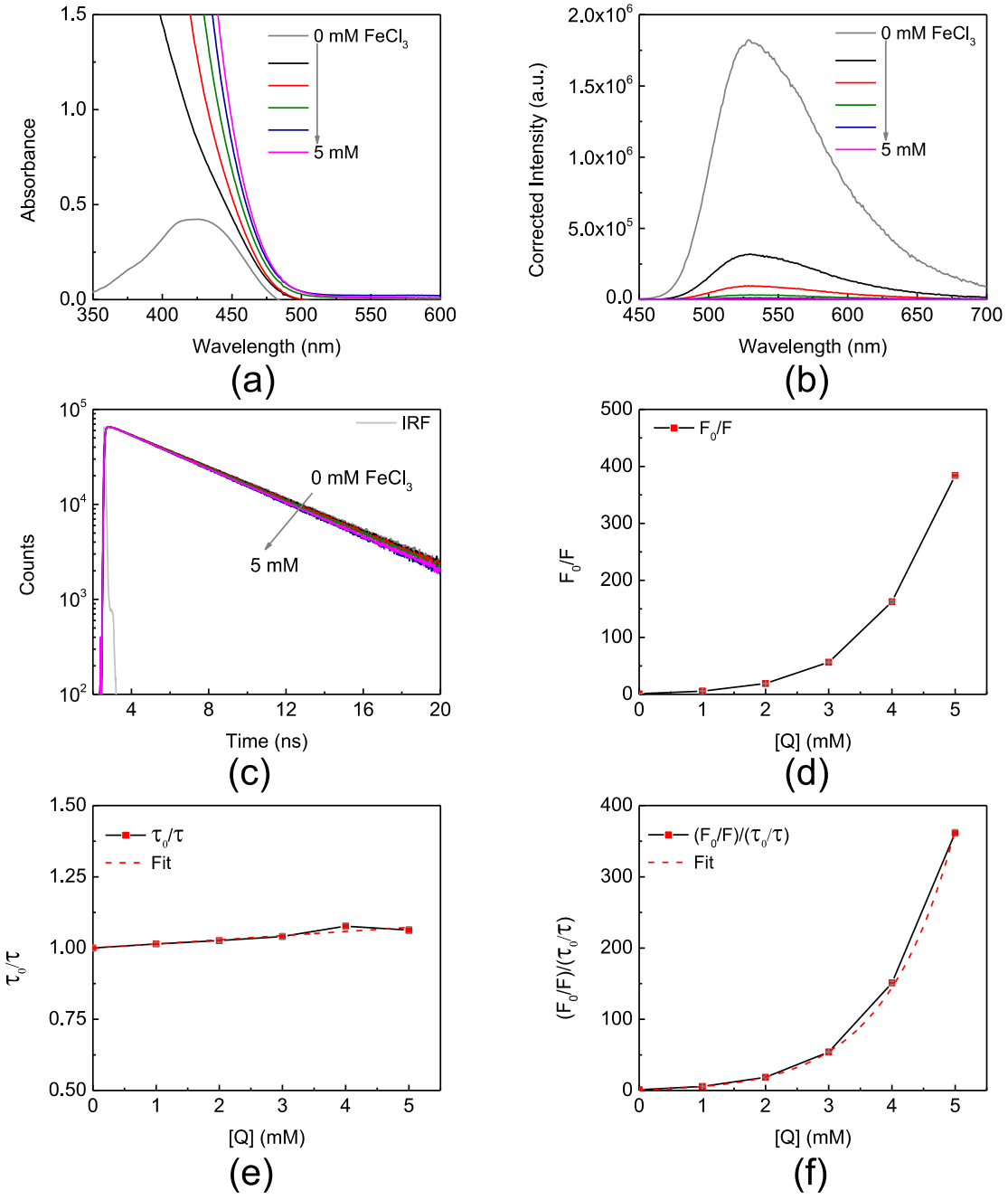

Figure S6.6. Fluorescence quenching of C153 in DMSO as a function of $FeCl_3$ concentration. (a) Absorption spectra. (b) Fluorescence emission spectra at $\lambda_{ex} = 600$ nm. Intensities are corrected for the absorption at the wavelength of excitation. (c) Time-resolved fluorescence decay. (d) Stern-Volmer plot for the integrated fluorescence intensity ratio (F_0/F) as a function of the quencher concentration. (e) Stern-Volmer plot of (τ_0/τ) as a function of the quencher concentration. (f) Plot of $(F_0/F)/(\tau_0/\tau)$ as a function of the quencher concentration.

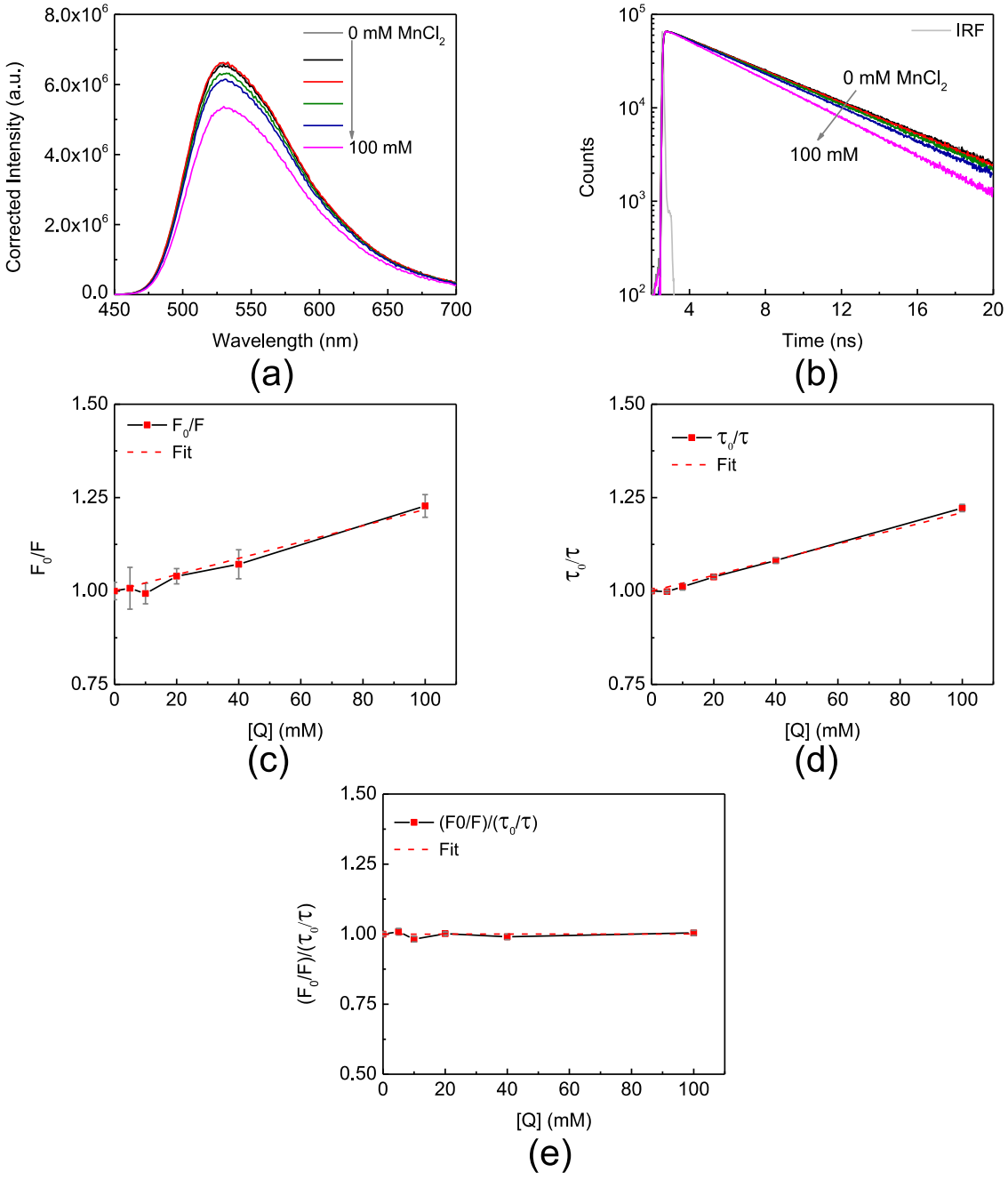

Figure S6.7. Fluorescence quenching of C153 in DMSO as a function of $MnCl_2$ concentration. (a) Fluorescence emission spectra at $\lambda_{ex} = 600$ nm. Intensities are corrected for the absorption at the wavelength of excitation. (b) Time-resolved fluorescence decay. (c) Stern-Volmer plot for the integrated fluorescence intensity ratio (F_0/F) as a function of the quencher concentration. (d) Stern-Volmer plot of (τ_0/τ) as a function of the quencher concentration. (e) Plot of $(F_0/F)/(\tau_0/\tau)$ as a function of the quencher concentration.

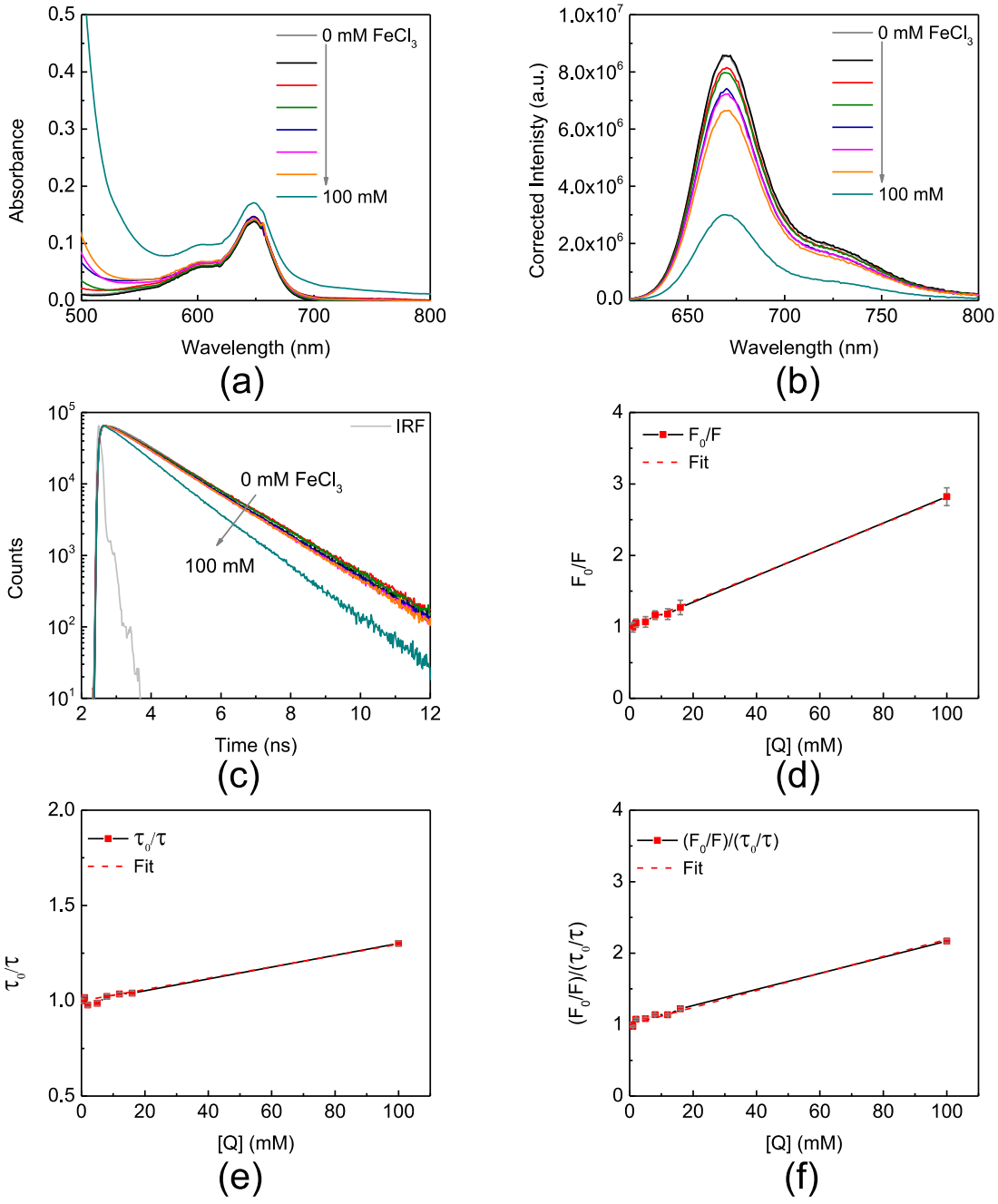

Figure S6.8. Fluorescence quenching of Cy5 in DMSO as a function of $FeCl_3$ concentration. (a) Absorption spectra. (b) Fluorescence emission spectra , $\lambda_{ex} = 600$ nm. Intensities are corrected for the absorption at the wavelength of excitation. (c) Time-resolved fluorescence decay. (d) Stern-Volmer plot for the integrated fluorescence intensity ratio (F_0/F) as a function of the quencher concentration. (e) Stern-Volmer plot of (τ_0/τ) as a function of the quencher concentration. (f) Plot of $(F_0/F)/(\tau_0/\tau)$ as a function of the quencher concentration.

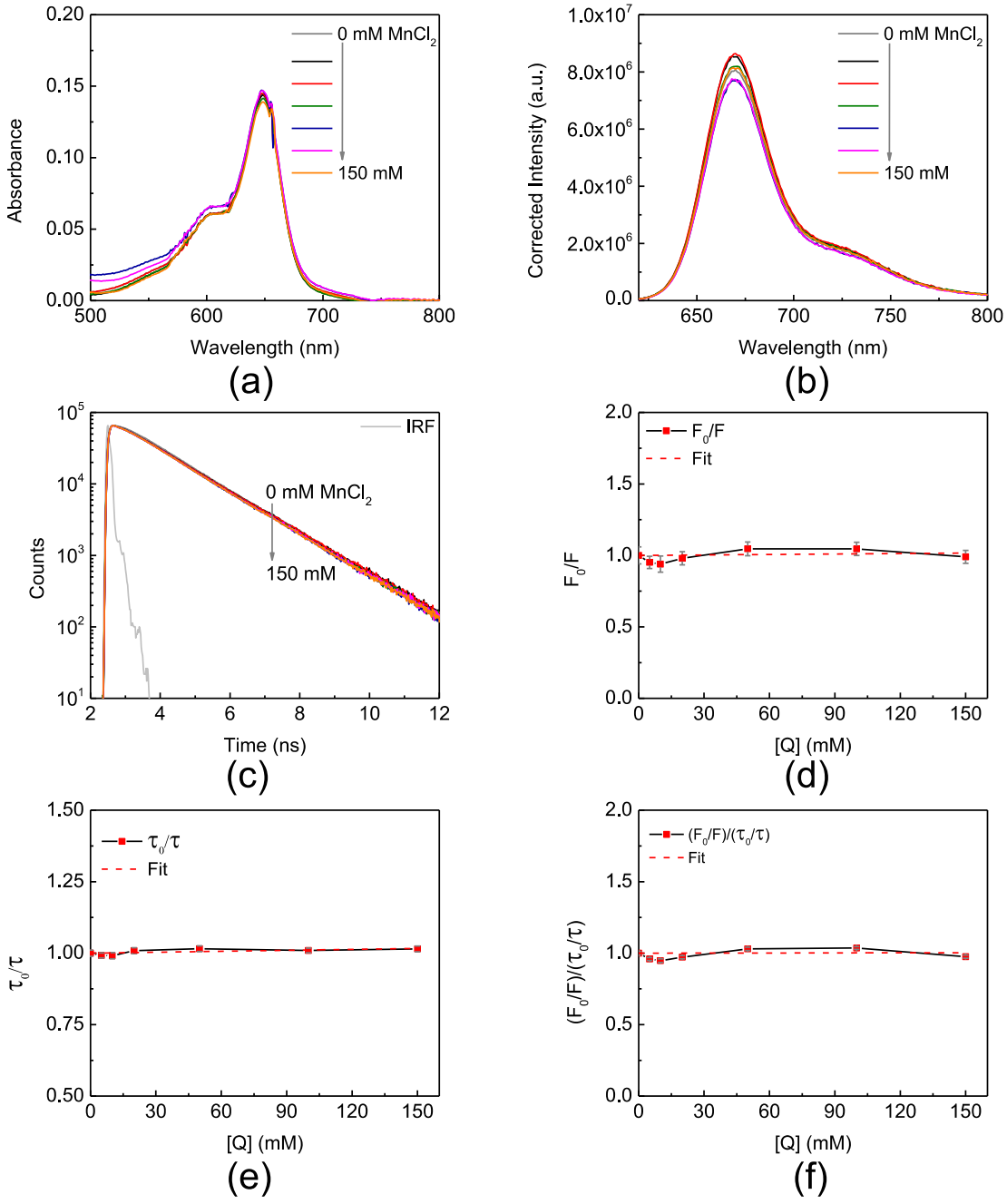

Figure S6.9. Fluorescence quenching of Cy5 in DMSO as a function of $MnCl_2$ concentration. (a) Absorption spectra. (b) Fluorescence emission spectra at $\lambda_{ex} = 600$ nm. Intensities are corrected for the absorption at the wavelength of excitation. (c) Time-resolved fluorescence decay. (d) Stern-Volmer plot for the integrated fluorescence intensity ratio (F_0/F) as a function of the quencher concentration. (e) Stern-Volmer plot of (τ_0/τ) as a function of the quencher concentration. (f) Plot of $(F_0/F)/(\tau_0/\tau)$ as a function of the quencher concentration.

CHAPTER 7. CHARACTERIZING ELECTRIC FIELD EXPOSED P3HT THIN FILMS USING POLARIZED-LIGHT SPECTROSCOPIES

A paper published in the *Macromolecular Chemistry and Physics*

Ujjal Bhattacharjee,[§,1,2] Moneim Elshobaki,[§,4] Kalyan Santra,[1,2] Jonathan M. Bobbitt[1,2], Sumit Chaudhary,[3] Emily A. Smith, and Jacob W. Petrich*

7.1 Abstract

P3HT (poly (3-hexylthiophene)) has been widely used as a donor in the active layer in organic photovoltaic devices. Although moderately high-power conversion efficiencies have been achieved with P3HT-based devices, structural details, such as the orientation of polymer units and the extent of H- and J-aggregation are not yet fully understood; and different measures have been taken to control the ordering in the material. One such measure, which we have exploited, is to apply an electric field from a Van de Graaff generator. We used fluorescence (to measure *anisotropy* instead of *polarization*, which is more commonly measured) and Raman spectroscopy

---

Reprinted with permission from *Macromolecular Chemistry and Physics* **2016**, 217: 1801–1809. doi:10.1002/macp. 201600113 Copyright (2016) John Wiley and Sons.

*To whom correspondence should be addressed. Email: jwp@iastate.edu

§ Contributed equally to this work.

[1]Department of Chemistry, Iowa State University, Ames, Iowa 50011, USA

[2]U. S. Department of Energy, Ames Laboratory, Ames, Iowa 50011, USA

[3]Materials Science & Engineering Department, Iowa State University, Ames, IA, USA.

[4]Physics Department, Mansoura University, Mansoura, Egypt

to characterize the order of P3HT molecules in thin films resulting from the field. We determine preferential orientations of the units in a thin film, consistent with observed hole mobility in thin-film-transistors, and observe that the apparent H-coupling strength changes when the films are exposed to oriented electrical fields during drying.

7.2 Introduction

Π-conjugated polymers (π-CP) have been of considerable interest and applicability since their discovery.[1,2] The combination of the properties of metals and semiconductors, mechanical properties such as tensile strength, ductility, *etc.*, and the ease of processing gives these materials a very important role in the development of organic photovoltaic (OPV) devices. Among the polymers used for solar cells, P3HT (poly (3-hexylthiophene)), is the most extensively studied. The efficiency of P3HT-based solar cells typically lies in the range of 4-6 %;[3-7] and in similar polymers, such as poly[[4,8-bis[(2-ethylhexyl)oxy] benzo [1,2- b:4,5-b′]dithiophene-2,6-diyl] [3-fluoro-2- [(2-ethylhexyl) carbonyl] thieno [3,4-b] thiophenediyl]] (PTB7), an efficiency as high as ~10% has been achieved.[8]

The two main challenges that P3HT-based solar cells face are: (1) poor overlap between the absorption spectrum of P3HT and the solar spectrum; and (2) structural defects. The first can be somewhat alleviated by making the film thicker, ensuring sufficient absorption of solar light. On the other hand, owing to the small exciton-diffusion length and the large charge-transfer radius (4.8 to 9 nm), excitons reach interfaces by swift delocalization in P3HT domains instead of by diffusion.[9] Disorder in the polymer matrix, however, limits the carrier mobility.[10] Studies directed towards reducing structural disorder and, thus, increasing carrier mobility are fundamental to enhancing the efficiency of these materials. Thermal annealing,[11-13] solvent annealing,[14,15] slow growth,[16] epitaxy,[17] and the use of shear forces,[18,19] high boiling solvents[20,21] and solvent

additives[22,23] have been explored as a means to attenuate the problem. Electric fields have previously been used to align[24] or to generate a particular morphology of nanomaterials.[25] There are also a few reports in the literature concerning the orienting of P3HT "nanofibers" in microchannels by the field between two electrodes.[26,27] Attraction of the P3HT solution towards the cathode is believed to be a result of the generation of positive charge in the nanofibers owing to solvent-P3HT interaction preceding their alignment.[26,28]

There is not, however, any report concerning the orientation of P3HT polymer units using a unipolar electric field while the polymer solution is spin coated on an ITO substrate. To date, studies have only been performed on P3HT nanofibers (*i.e.*, crystalline phases). As there is a possibility of forming amorphous phases in addition to crystalline phases while the film is drying, there is the possibility of orienting the polymer units in the both phases and producing a concomitant change in charge mobility.[29] In other words, it is possible that the orientation of the P3HT polymers in the amorphous phases can also play a role irrespective of crystallinity itself, which has previously been studied in a microchannel.[26,27] While crystallinity can, of course, provide strong orientational effects, it is important to note that the carrier diffusion length in P3HT is very small (less than 2 nm[9,30,31]) and that amorphous character may be helpful in connecting nanocrystalline domains. Thus, understanding the molecular ordering of P3HT is critical when using these thin films as active layers in various electronic devices.

Here we investigate the use of steady-state and time-resolved fluorescence anisotropy along with polarized Raman spectroscopy to characterize the orientation of the polymer units. (Although several reports have appeared in the literature using polarization to investigate ordering of P3HT nanofibers,[26,27,32] our study is the first to measure the anisotropy, a quantitative measure of orientation, as rigorously defined below in equation (7.1).) Consistent with our anisotropy

measurements, we observed an enhancement of in-plane charge mobility in the films exposed to an electric field.[29]

Barnes and coworkers have studied P3HT nanofibers with polarized time- and wavelength-resolved fluorescence microscopy.[33] They showed that the dominant inter-chain exciton coupling (H-aggregation) in low-molecular-weight nanofibers changes to predominantly intra-chain coupling (J-aggregation) for high molecular-weight nanofibers.[33] In thin films, P3HT remains a weakly coupled H-aggregate,[34,35] although varying amounts of inter- and intra-chain coupling can be observed depending on the molecular weight, processing conditions, and other parameters.[36] We show that an applied electric field can change the effective coupling strength in the polymer and that these orientational changes can be effectively probed by spectroscopic techniques using polarized light.

7.3 Materials and Methods

7.3.1 Solution preparation

Neat P3HT (92% regio-regular) with molecular weight 70 kDa (1-Materials, Inc., Dorval, Québec, Canada) was dissolved in 1, 2-dichlorobenzene (DCB) with a dilution of 20 mg/ml. The solutions were stirred at 850 rpm on a hot plate at 50°C and then filtered.

7.3.2 Substrate preparation under an E-field

Indium tin oxide (ITO)-coated glass slides (25-mm × 25-mm) (Delta Technologies, Loveland, CO) were cleaned following the method described by Chaudhary et al.[37] The solution-processed π-CP based films were subjected to an electric field immediately after they were formed by spin coating at 500 rpm for 40 s while they were still wet. This was accomplished by placing the coated substrates around a Van de Graaff dome in three different orientations: 0°, 45°, and 90°

relative to the normal of the surface of the dome (**Figure 1**). The field strength was approximately 5.88 kV/m at the surface of the generator's dome, and the films were kept at a distance of approximately 1 cm from the surface of the dome. Furthermore, the degree of crystallinity in our P3HT films has been calculated following the procedure described by Hashimoto and co-workers[38]: a value of 39% is obtained (**Figure S7.1,** available online doi:10.1002/macp. 201600113).

7.3.3 Steady-state fluorescence measurements: Excitation anisotropy

These were performed with a Spex Fluoromax-4 with a 4- or 5-nm excitation and emission bandpass and corrected for lamp spectral intensity and detector response. The steady-state spectra were collected using a front-faced orientation. Glan-Thompson polarizers were appropriately placed before and after the sample. A 550-nm long-pass filter was used to eliminate scattered light. Excitation spectra were collected with a 720 ± 5-nm interference filter. To obtain the excitation anisotropy spectra, the films were excited with vertically polarized light, and emission polarized both parallel and perpendicular to the excitation polarization was collected. The anisotropy (r) was computed as[39,40]:

$$r = \frac{I_{||} - I_{\perp}}{I_{||} + 2I_{\perp}} \tag{7.1}$$

Note that the anisotropy, as defined in equation (7.1), differs from a frequently used quantity, the polarization, by the presence of the 2 in the denominator. The factor of two normalizes the difference in $I_{||}$ and $I_{\perp}$ to the excited-state lifetime of the fluorophores, since the denominator in equation (7.1) is proportional to the excited-state lifetime.[39,40] More importantly, the anisotropy is rigorously defined to have values such that $-0.2 \leq r \leq 0.4$.[39] These limits on the value of r provide an invaluable means for gauging the precision of the experimental measurement: *e.g.*, the quality of the polarizers employed and whether they are properly aligned parallel or

perpendicular to each other; the optical quality of the sample (scattering can provide spurious results); and the wavelength dependence of the grating and optics of the spectrometer

Because the grating and optics of a monochromator may be sensitive to polarization, a correction factor must also be determined. Such a factor, g, is obtained by taking the ratio of two spectra of a dye in solution. (Here we used ATTO 655 in water, as its absorption and emission spectra overlapped those of P3HT). Insofar as the dye can be considered to be freely rotating on the time scale of the measurement, $I_{||}$ and $I_{\perp}$ should be identical, regardless of the excitation polarization. Any differences in $I_{||}$ and $I_{\perp}$ must thus be attributed to the monochromator and detection optics. As discussed in our previous work and that of other groups,[41-44] the steady-state anisotropy, corrected for instrumental polarization dependence, is thus given by:

$$r = \frac{I_{V,V} - g\, I_{V,H}}{I_{V,V} + 2\, g\, I_{V,H}} \qquad (2)$$

where the notation $I_{V,V}$ indicates fluorescence obtained using excitation light polarized vertically to the plane of the table and collected vertically to the plane of the table. $I_{V,H}$, similarly, indicates vertical excitation and horizontal collection. The correction factor is given as: $g = \frac{I_{H,V}}{I_{H,H}} = \frac{I_{V,V}}{I_{V,H}}$. Measurements were repeated at least three times. The optical system was optimized by comparing results with those obtained from the excitation anisotropy of hypericin, which emits in the same region and which we had reported previously.[41]

7.3.4 Time-resolved fluorescence measurements

These were obtained with the time-correlated, single-photon counting (TCSPC) technique. The apparatus for time-correlated, single-photon counting is described elsewhere.[45] Our system provides an instrument response function whose full-width at half-maximum (FWHM) is ~40-50 ps. Experiments were performed in a front-faced orientation. Crossed polarizers provided an

extinction of 10^5. An interference filter at 720 ± 5 nm was used to collect photons, to be consistent with the steady-state measurements. Fluorescence lifetimes were measured with a polarizer oriented at "the magic angle," 54.7˚ to the vertical in order to prevent depolarizing events from skewing the measured fluorescence lifetime.[46] For each sample, fluorescence lifetime and anisotropy decays were measured at three random locations on the sample. Fluorescence decays were best fit to two decaying exponentials, after deconvolution with the instrument response function. The time-dependent anisotropy, $r(t)$, was constructed using the equation (7.1) and was well described by a single-exponential decay. The parallel and the perpendicular traces were collected for equal amounts of time, during which the incident excitation power remained constant. This resulted in the overlap of the "tails" of the parallel and perpendicular traces at sufficiently long times, thus obviating the need for "tail matching."[40,44]

7.3.5 Raman measurements

All Raman spectra were collected using a lab-built microscope system (Leica, Wetzlar, Germany) with a 532-nm laser excitation (Sapphire SF 532-nm 150 mW, Coherent, Santa Clara, CA) after the fluorescence measurements were completed. The laser beam was expanded with a 10× beam expander in order to backfill a 10× Leica microscope objective with a 0.25 numerical aperture. The laser spot size after the objective was 1.6 $\pm$ 0.2 μm. The objective was used for focusing and collecting the Raman scattering from the epi-direction and then directed to a side port on the microscope where it was focused onto an f/1.8i HoloSpec spectrograph (Kaiser Optical Systems, Ann Arbor, MI). A Newton 940 (2048 × 512 pixels) charged-coupled device (CCD) was used to detect the Raman signal (Andor Technology, Belfast, UK).

Raman spectra were collected at 5 different locations from the center of each P3HT film under ambient laboratory conditions. An XY translation-stage (ProScan, Prior Scientific,

Rockland, MA) controlled by a lab-developed LabVIEW program (2010 version, National Instruments, Austin, TX) was used to move 1 mm to each new location. The spectra were collected for 10 s with 2 accumulations and illuminated with 1.09×10^4 W/cm^2, which is a low enough power density to avoid film degradation.[47] Two accumulations were used in order to remove cosmic rays.

Polarized Raman spectra were also collected on the P3HT films from the center of the film. The excitation polarization was controlled by a half-wave plate, and was set to s-polarization. A linear polarizer was placed at the side port of the microscope to collect either s- or p-polarized Raman scattering. A second linear polarizer set 45° to the collection polarizer was placed before the spectrometer to correct the spectrometer response function.[48] The ratio of the scattered light intensity with the detection polarizer set to p (I_p) to the intensity with the detection polarizer set to s (I_s) was calculated. Benzene was used to test the instrument setup (I_p/I_s 0.035 ± 0.009 at 991 cm^{-1}, 0.77 ± 0.02 at 1171 cm^{-1} and 0.783 ± 0.009 at 1588 cm^{-1}), and similar ratios were obtained to those found in literature.[48,49] The polarized spectra were collected for 30 s with 2 accumulations at a power density of 1.32×10^4 W/cm^2.

Igor Pro 6.36 (Wavemetrics, Lake Oswego, OR) was used to correct for background and to analyze the Raman spectra. The spectra were fit with a linear baseline and to a Gaussian function from 1250 to 1550 cm^{-1} with Igor Pro's batch fitting macro. The full-width at half-maximum (FWHM) and peak amplitudes were extracted from the fits.

7.4 Results and Discussion

7.4.1 Steady-state fluorescence measurements

Spano, Barnes, and coworkers have shown that two vibronic transitions in the steady-state fluorescence spectra of P3HT are exquisitely sensitive to the state of aggregation of the polymer chains: the 0-0 transition at ~650 nm and the 0-1 transition at ~720 nm.[50] In particular, the ratio

between the intensities of these bands ($S_r = I_{0-0}/I_{0-1}$) is indicative of the resultant H- coupling strength in the polymer chain.[51] In H-aggregation, the columbic interaction arising from the side-by-side stacking of the chromophores between the chains of the crystalline films is suggested to suppress the 0-0 transition, yielding $S_r < 1$.[51] In contrast, in J-aggregation, the head-to-tail conformation of chromophores is suggested to enhance a one-dimensional intrachain interaction, increasing the intensity of the 0-0 band, yielding $S_r > 1$.[51,52] In addition, emission spectra exhibit red shifts for H-aggregation; blue shifts, for reduction of effective H-aggregation strength.

Polarized emission spectra of neat P3HT films are presented in **Figure 7.2**. The results are summarized in **Table 7.1**. For emission collected parallel to the excitation polarization (**Figure 7.2a**), the 0-0 peak of the normalized steady-state spectra decreased with increasing angle of the applied E-field, and was always less than 1. Such low values of S_r, coupled with the spectral red-shift with increasing E-field angle, suggest H-aggregation. In contrast, for emission collected perpendicular to the excitation polarization, S_r was consistently higher than for the parallel case. This suggests an decrease of apparent H-coupling strength, which is consistent with the attendant spectral blue shift with E-field angle (**Figure 7.2b**).[53] Thus, the polarized emission spectra are sensitive to the extent of H- and J- aggregation of the film, induced by the applied electric field. The values of excitonic coupling (J_0) in the different films are also given in **Table 7.1**.[53,54]

Several optical methods have been used for studying the orientation of units in polymers, for example: polarized UV-Vis absorption,[17,26] polarized electroluminescence,[32] and polarized emission.[55] We note, however, that while these orientational measurements often are discussed in terms of the "anisotropy" of the sample, the anisotropy is not measured in the sense of equation (7.1). Because simple polarization measurements are not subject to theoretical upper and lower bounds, this renders comparisons between different experiments difficult. A good example of this

difficulty is an attempt to compare our results with those of Lobov et al.[26] Although there are differences in the methods of sample preparation (we subject P3HT films to an electric field while they are drying; they place a P3HT nanofiber solution between two electrodes), nevertheless, we only use an electric field of 5.88 kV/m while they use a field of 600 kV/m. One would expect the higher field strength to yield a greater degree of orientation, but they report very small orientational effects. It is difficult to determine the origin of this discrepancy because of the arbitrariness which simple polarization measurements are subjected to.

Also, while polarized absorption provides some information that is comparable to our fluorescence anisotropy measurements, absorption is much more subject to artifacts arising from scattering in solid samples. Scattering can become even more problematic in very heterogeneous samples. Polarized electroluminescence is limited to semiconductor materials, and it does not address the possibility of losing anisotropy in other processes, such as molecular rotation and coupling between chromophores. Also, a nonuniform electric field, an anisotropic distribution of trap states, and molecular reorientation will directly alter the electroluminescence intensity. Finally, while emission anisotropy is a powerful tool (especially if time-resolved data are acquired and if care is taken to quantify rigorously the anisotropy) it is most useful when coupled with the excitation anisotropy.

Figure 7.3 (right ordinate) presents the fluorescence excitation spectrum (with parallel orientation of excitation and emission polarizers) of a P3HT film in the absence of an applied electric field. The maximum of the 0-0 transition is ~615 nm. The fluorescence excitation anisotropy spectra, constructed as described above, of P3HT films prepared at angles of 0°, 45°, and 90° with respect to the E-field, are presented in **Figure 7.3 (left ordinate).** In all cases, the anisotropy decreases from 0.35-0.40 (0.40 being the theoretical maximum[39]) at the reddest edge

of the excitation spectrum (~690 nm), to 0.10-0.17 at the bluest part of the excitation spectrum that we excited (400 nm). Our ability to attain an anisotropy near the theoretical upper limit confirms the proper alignment of our apparatus and good extinction of the excitation and analyzer polarizers. Most importantly, however, there is a clear and reproducible decrease in the anisotropy of the entire spectrum in going from an angle of the applied electric field of 0˚ to 90˚. The lowest values of the anisotropy occur when there is no applied electric field. Thus, the 0˚-film exhibits the maximum anisotropy, that is, preferential orientation of the polymeric units in the plane parallel to the substrate. This is consistent with measured hole mobility in P3HT-based transistors, which showed an enhancement: 12.1×10^{-3} cm^2 V^{-1} s^{-1} for the 0˚-film, as opposed to 7.13×10^{-3} cm^2 V^{-1} s^{-1} for the film that was not exposed to electric field.[29]

7.4.2 Time-resolved fluorescence measurements: Fluorescence lifetime and anisotropy decays

Time-resolved polarized emission of P3HT films is presented in **Figure 7.4**. The parameters for the decay of the fluorescence lifetime and anisotropy of the P3HT films are summarized in **Table 7.2**. The average fluorescence lifetimes are 0.30, 0.25, 0.32, and 0.28 ns for the films made with E-field at 0°, 45°, 90°, and with no E-field, respectively. Time-resolved anisotropies of the films yield *r(0)* values, that is, the anisotropies at $t = 0$, similar to those obtained from the steady-state measurements (**Table 7.2**), as expected. This result provides another check on the accuracy of the steady-state anisotropy measurements presented in **Figure 7.3**. The fluorescence depolarization times, *i.e.*, the decay of the anisotropy, are on the order of a nanosecond. This is not attributed to rotational motion of the polymer film but rather to electronic coupling between the chromophores in the polymer, for which there is precedent for organic molecules.[44,56]

7.4.3 Raman measurements

Raman spectroscopy can be used to characterize polymer-based organic photovoltaic device morphology by measuring changes in the full-width at half-maximum (FWHM) and the resulting polarization of the scattered light.[47,48,57-60] Extensive work on P3HT aggregation has been reported by Grey et al.[61,62] They classify P3HT films with a ratio of the peak intensities for aggregated and unaggregated chains ($I_{1450\ cm^{-1}}/I_{1470\ cm^{-1}}$) greater than 1.5 as highly aggregated chains with correlated planarity and an average intrastack chain-to-chain spacing of approximately 3.8 Å. **Table 7.3** presents measured parameters for the P3HT carbon-carbon double bond peak at 1450 cm^{-1} for films prepared in the absence of an external electric field, or with an electric field oriented in the noted directions. These parameters were also measured for a P3HT crystal. Representative spectra are presented in **Figure 7.5**. All films have statistically similar peak maxima and FWHM values. The films have $I_{1450\ cm^{-1}}/I_{1470\ cm^{-1}}$ values for both s and p polarized light ranging from 1.73 $\pm$ 0.01 to 1.923 $\pm$ 0.007. Based on the classification of Gray et al.,[61,62] these are highly aggregated chains with intra- and inter-chain order and long conjugation lengths.

The ratio of the polarized Raman scattered light is statistically lower for the 0°, 45°, and 90° films (**Table 7.3**). Based on the work of Kleinhenz et al. and the polarized Raman data, there is an increasing order of the axis of the polymer backbone toward the orientation of the polarization of the excitation light for the 0°, 45°, and 90° films. The film prepared in the absence of an electric field (E = 0) has a statistically similar ratio of the polarized Raman scattered light as the P3HT crystal. Both fluorescence anisotropy and polarized Raman measurements show altered polymer orientation for the samples prepared in the electric field. The polarized Raman measurements, however, show no distinction between the 0°, 45°, and 90° films, indicating the fluorescence anisotropy measurement is a more sensitive technique in these cases.

7.5 Conclusions

We have shown that the P3HT polymer units can be oriented when the films are subjected to a unipolar electric field of ~5.88 kV/m generated by Van de Graaff dome as they dry and that this orientation can be probed effectively by steady-state and time-resolved fluorescence anisotropy measurements. It is important to note that the degree of orientation is weak, which is likely a consequence of the relatively poor regio-regularity (92%) and the MW (which is well above the MW threshold for polymer self-folding).[17,33] Though electric fields have been used previously to align nanofibers, they were performed under a very controlled experimental conditions and in a microchannel between two electrodes. Ours, however, is an easy and efficient method to use in conjunction with thin films prepared directly from P3HT solution *where amorphous domains are present* (degree of crystallinity is 39%), though the study by Srinivasarao and co-workers strongly suggest that this ordering is mediated by a liquid crystalline phase. [63] The highest degree of ordering, as quantified by the limiting anisotropy (r_0 for the steady-state measurement; *r(0)*, for the time-resolved measurement), is attained when the electric filed is parallel to the film, as depicted in **Figure 7.1**. In agreement with the anisotropy measurements, hole mobility in P3HT-based transistors increases when the films are exposed to electric field. The 0˚-film shows a 1.7-fold enhancement over control film (E = 0). The polarized emission spectra are also sensitive to the orientation of the electric field (**Figure 7.2** and **Table 7.1**) as quantified by the ratio of the first two vibronic transitions, which are in turn related to the extent of H- or J-aggregation. Finally, polarized Raman experiments suggest differences between the samples in the presence and absence of electric field. Taken as a whole, these results suggest that the polymeric units of P3HT can be ordered with an electric field, that this ordering can be probed and quantified by spectroscopies using polarized light, and that applying an electric field in excess of

5.88 kV/m to drying films of P3HT could be beneficial in improving the performance of organic solar cells—or in systems where in-plane mobility is important.

7.6 Acknowledgements

This research is supported by the U.S. Department of Energy, Office of Basic Energy Sciences, Division of Chemical Sciences, Geosciences, and Biosciences through the Ames Laboratory. The Ames Laboratory is operated for the U.S. Department of Energy by Iowa State University under Contract No. DE-AC02-07CH11358. The work related to P3HT thin-film processing was supported by NSF (ECCS – 1055930). Moneim Elshobaki thanks the fellowship support from the Egyptian government, under the contract No. GM915.

7.7 References

1. Shirakawa, H.; Louis, E. J.; MacDiarmid, A. G.; Chiang, C. K. H. A. J. Synthesis of Electrically Conducting Organic Polymers: Halogen Derivatives of Polyacetylene, (Ch). *Chem. Comm.* **1977**, 578-580.

2. Chiang, C. K. Electrical Conductivity in Doped Polyacetylene. *Phys. Rev. Lett.* **1977**, *39* 1098-1101.

3. Schilinsky, P.; Waldauf, C.; Brabec, C. J. Recombination and Loss Analysis in Polythiophene Based Bulk Heterojunction Photodetectors. *Appl. Phys. Lett.* **2002**, *81* (20), 3885-3887.

4. Padinger, F.; Rittberger, R. S.; Sariciftci, N. S. Effects of Postproduction Treatment on Plastic Solar Cells. *Adv. Funct. Mater.* **2003**, *13* (1), 85-88.

5. Ma, W.; Yang, C.; Gong, X.; Lee, K.; Heeger, A. J. *Adv. Funct. Mater.* **2005**, *15* 1617-1622.

6. Reyes, M. R.-.; Kim, K.; Dewald, J.; Sandoval, R. L.-.; Avadhanula, A.; Curran, S.; Carrol, D. L. Meso-Structure Formation for Enhanced Organic Photovoltaic Cells. *Org. Lett.* **2005**, *7* (26), 5749-5752.

7. Zhao, G.; He, Y.; Li, Y. 6.5% Efficiency of Polymer Solar Cells Based on Poly(3-Hexylthiophene) and Indene-C60 Bisadduct by Device Optimization. *Adv. Mater.* **2010**, *22* 4355–4358.

8. He, Z.; Zhong, C.; Su, S.; Xu, M.; Wu, H.; Cao, Y. *Nat. Photonics*. **2012**, *6* 591-595.

9. Wang, H.; Wang, H.-Y.; Gao, B.-R.; Wang, L.; Yang, Z.-Y.; Du, X.-B.; Chen, Q.-D.; Song, J.-F.; Sun, H.-B. Exciton Diffusion and Charge Transfer Dynamics in Nano Phase-Separated P3HT/PCBM Blend Films. *Nanoscale*. **2011**, *3* (5), 2280-2285.

10. Noriega, R. A General Relationship between Disorder, Aggregation and Charge Transport in Conjugated Polymers. *Nat. Mater.* **2013**, *12* 1038-1044.

11. Liu, Y. X.; Summers, M. A.; Edder, C.; Frechet, J. M. J.; McGehee, M. D. Using Resonance Energy Transfer to Improve Exciton Harvesting in Organic-Inorganic Hybrid Photovoltaic Cells. *Adv. Mater.* **2005**, *17* (24), 2960-+.

12. Ma, W. L.; Yang, C. Y.; Gong, X.; Lee, K.; Heeger, A. J. Thermally Stable, Efficient Polymer Solar Cells with Nanoscale Control of the Interpenetrating Network Morphology. *Adv. Funct. Mater.* **2005**, *15* (10), 1617-1622.

13. Oklobia, O.; Shafai, T. S. Correlation between Charge Carriers Mobility and Nanomorphology in a Blend of P3HT/PCBM Bulk Heterojunction Solar Cell: Impact on Recombination Mechanisms. *Sol. Energ. Mat. Sol. Cells*. **2014**, *122* (0), 158-163.

14. Miller, S.; Fanchini, G.; Lin, Y.-Y.; Li, C.; Chen, C.-W.; Su, W.-F.; Chhowalla, M. Investigation of Nanoscale Morphological Changes in Organic Photovoltaics During Solvent Vapor Annealing. *J. Mater. Chem.* **2008**, *18* (3), 306-312.

15. Li, G.; Yao, Y.; Yang, H.; Shrotriya, V.; Yang, G.; Yang, Y. "Solvent Annealing" Effect in Polymer Solar Cells Based on Poly(3-Hexylthiophene) and Methanofullerenes. *Adv. Funct. Mater.* **2007**, *17* (10), 1636-1644.

16. Mihailetchi, V. D.; Xie, H.; de Boer, B.; Popescu, L. M.; Hummelen, J. C.; Blom, P. W. M.; Koster, L. J. A. Origin of the Enhanced Performance in Poly(3-Hexylthiophene): [6,6]-Phenyl

C61-Butyric Acid Methyl Ester Solar Cells Upon Slow Drying of the Active Layer. *Appl. Phys. Lett.* **2006**, *89* (1), 12107.

17. Brinkmann , M.; Hartmann, L.; Biniek, L.; Tremel, K.; Kayunkid, N. Orienting Semi-Conducting Π -Conjugated Polymers. *Macromol. Rapid Commun.* **2014**, *35* 9-26.

18. Toney, M. F.; Russell, T. P.; Logan, J. A.; Kikuchi, H.; Sands, J. M.; Kumar, S. K. Nature. *Nature*. **1995**, *374* 709.

19. Wittmann, J.-C.; Smith, P. *Nature*. **1991**, *352* 414.

20. Ma, W.; Yang, C.; Gong, X.; Lee, K.; Heeger, A. J. Thermally Stable, Efficient Polymer Solar Cells with Nanoscale Control of the Interpenetrating Network Morphology. *Adv. Funct. Mater.* **2005**, *15* (10), 1617-1622.

21. Bao, Z.; Dodabalapur, A.; Lovinger, A. J. Soluble and Processable Regioregular Poly(3-Hexylthiophene) for Thin Film Field-Effect Transistor Applications with High Mobility. *Appl. Phys. Lett.* **1996**, *69* (26), 4108-4110.

22. Chen, F.-C.; Tseng, H.-C.; Ko, C.-J. Solvent Mixtures for Improving Device Efficiency of Polymer Photovoltaic Devices. *Appl. Phys. Lett.* **2008**, *92* (10), -.

23. Moon, J. S.; Takacs, C. J.; Cho, S.; Coffin, R. C.; Kim, H.; Bazan, G. C.; Heeger, A. J. Effect of Processing Additive on the Nanomorphology of a Bulk Heterojunction Material†. *Nano Lett.* **2010**, *10* (10), 4005-4008.

24. He, H.; Cai, W.; Lin, Y.; Chen, B. Surface Decoration of Zno Nanorod Arrays by Electrophoresis in the Au Colloidal Solution Prepared by Laser Ablation in Water. *Langmuir*. **2010**, *26* (11), 8925-8932.

25. Petchsang, N.; McDonald, M. P.; Sinks, L. E.; Kuno, M. Light Induced Nanowire Assembly: The Electrostatic Alignment of Semiconductor Nanowires into Functional Macroscopic Yarns. *Adv. Mater.* **2013**, *25* (4), 601-605.

26. Lobov, G. S.; Zhao, Y.; Marinins, A.; Yan, M.; Li, J.; Toprak, M. S.; Sugunan, A.; Thylen, L.; Wosinski, L.; Östling, M.; Popov, S. Electric Field Induced Optical Anisotropy of P3HT Nanofibers in a Liquid Solution. *Opt. Mater. Express*. **2015**, *5* 2642-2647.

27. Fischer, F. S. U.; Tremel, K.; Sommer, M.; Crosslandbd, E. J. C.; Ludwigs, S. Directed Crystallization of Poly(3-Hexylthiophene) in Micrometre Channels under Confinement and in Electric Fields. *Nanoscale*. **2012**, *4* 2138-2144.

28. Tremel, K.; Ludwigs, S. Morphology of P3HT in Thin Films in Relation to Optical and Electrical Properties. *Adv. Polym. Sci.* **2014**, *265* 39–82.

29. Ismail, M. R. *Tailoring Device-Scale Properties in Organic Electronics: Morphological, Optical and Electrode-Interface Related Approaches* Iowa State University: Ames, IA, 2015.

30. Marsh, R. A.; Hodgkiss, J. M.; Albert-Seifried, S.; Friend, R. H. *Nano Lett.* **2010**, *10* 923–930.

31. Guo, J. M.; Ohkita, H.; Benten, H.; Ito, S. *J. Am. Chem. Soc.* **2010**, *132* 6154–6164.

32. Grell, M.; Bradley, D. D. C. Polarized Luminescence

from Oriented Molecular Materials. *Adv. Mater.* **1999**, *11* 895-905.

33. Baghgar, M.; Labastide, J. A.; Bokel, F.; Hayward, R. C.; Barnes, M. D. Effect of Polymer Chain Folding on the Transition from H- to J-Aggregate Behavior in P3HT Nanofibers. *J. Phys. Chem. C*. **2014**, *118* 2229-2235.

34. Clark, J.; Silva, C.; Friend, R. H.; F.C, S. Role of Intermolecular Coupling in the Photophysics of Disordered Organic Semiconductors: Aggregate Emission in Regioregular Polythiophene. *Phys. Rev. Lett.* **2007**, *98* 206406.

35. Paquin, F.; Latini, G.; Sakowicz, M.; Karsenti, P.-L.; Wang, L.; Beljonne, D.; Stingelin, N.; Silva, C. Charge Separation in Semicrystalline Polymeric Semiconductors by Photoexcitation: Is the Mechanism Intrinsic or Extrinsic? *Phys. Rev. Lett.* **2011**, *106* 197401.

36. Sirringhaus, H.; Brown, P. J.; Friend, R. H.; Nielsen, M. M.; Bechgaard, K.; Langeveld-Voss, B. M. W.; Spiering, A. J. H.; Janssen, R. A. J.; Meijer, E. W.; Herwig, P.; De Leeuw, D. M. Two-Dimensional Charge Transport in Self-Organized, High-Mobility Conjugated Polymers. *Nature*. **1999**, *401* (7), 685-688.

37. Elshobaki, M.; Anderegg, J.; Chaudhary, S. Efficient Polymer Solar Cells Fabricated on Poly(3,4-Ethylenedioxythiophene):Poly(Styrenesulfonate)-Etched Old Indium Tin Oxide Substrates. *ACS Appl. Mater. Interfaces*. **2014**, *6* 12196-12202.

38. Yamamoto, S.; Yasuda, H.; Ohkita, H.; Benten, H.; Ito, S.; Miyanishi, S.; Tajima, K.; Hashimoto, K. Charge Generation and Recombination in Fullerene-Attached Poly(3-Hexylthiophene)-Based Diblock Copolymer Films. *J. Phys. Chem. C*. **2014**, *118* 10584−10589.

39. Fleming, G. R.; Morris, J. M.; Robinson, G. W. Direct Observation of Rotational Diffusion by Picosecond Spectroscopy. *J. Chem. Phys.* **1976**, *17* 91-100.

40. Cross, A. J.; Fleming, G. R. Analysis of Time-Resolved Fluorescence Anisotropy Decays *Biophys. J.* **1984**, *46* 45-56.

41. Das, K.; Dertz, E.; Paterson, J.; Zhang, W.; Kraus, G. A.; Petrich, J. W. Hypericin, Hypocrellin, and Model Compounds: Steady-State and Time-Resolved Fluorescence Anisotropies. *J. Phys. Chem. B.* **1998**, *102* 1479-1484.

42. Valeur, B.; Weber, G. Resolution of the Fluorescence Excitation Spectrum of Indole into the 1la and 1lb Excitation Bands. *Photochem. Photobiol.* **1977**, *25* 441-444.

43. Eftink, M. R.; Selvidge, L. A.; Callis, P. R.; Rehms, A. A. *J. Phys. chem.* **1990**, *94* 3469.

44. Rich, R. L.; Chen, Y.; Neven, D.; Negrerie, M.; Gai, F.; Petrich, J. W. Steady-State and Time-Resolved Fluorescence Anisotropy of 7-Azaindole and Its Derivatives. *J. Phys. chem.* **1993**, *97* 1781-1788.

45. Bhattacharjee, U.; Beck, C.; Winter, A.; Wells, C.; Petrich, J. W. Tryptophan and Atto 590: Mutual Fluorescence Quenching and Exciplex Formation. *J. Phys. Chem. B.* **2014**, *118* (29), 8471-8477.

46. Fleming, G. R. *Chemical Applications of Ultrafast Spectroscopy* University Press: Oxford,London, 1986.

47. Lesoine, M. D.; Bobbitt, J. M.; Carr, J. A.; Elshobaki, M.; Chaudhary, S.; Smith, E. A. Quantitative Comparison of Organic Photovoltaic Bulk Heterojunction Photostability under Laser Illumination. *J. Phys. Chem. C*. **2014**, *118* (51), 30229-30237.

48. Zhao, J.; McCreery, R. L. Polarized Raman Spectroscopy of Metallophthalocyanine Monolayers on Carbon Surfaces. *Langmuir*. **1995**, *11* (10), 4036-4040.

49. McCreery, R. L. *Raman Spectroscopy for Chemical Analysis* John Wiley & Sons: 2005.

50. Clark, J.; Silva, C.; Friend, R. H.; Spano, F. C. Role of Intermolecular Coupling in the Photophysics of Disordered Organic Semiconductors: Aggregate Emission in Regioregular Polythiophene. *Phys. Rev. Lett.* **2007**, *98* (20), 206406.

51. Spano, F. C.; Jenny, C.; Silva, C.; Friend, R. H. Determining Exciton Coherence from the Photoluminescence Spectral Line Shape in Poly(3-Hexylthiophene) Thin Films. *J. Chem. Phys.* **2009**, *130* 074904.

52. Niles, E. T.; Roehling, J. D.; Yamagata, H.; Wise, A. J.; Spano, F. C.; Moulé, A. J.; Grey, J. K. J-Aggregate Behavior in Poly-3-Hexylthiophene Nanofibers. *J. Phys. Chem. Lett.* **2012**, *3* 259-263.

53. Spano, F. C.; Silva, C. H- and J-Aggregate Behavior in Polymeric Semiconductors. *Annu. Rev. Phys. Chem.* **2014**, *65* 477-500.

54. Spano, F. C. The Spectral Signatures of Frenkel Polarons in H- and J-Aggregates. *Acc. Chem. Res.* **2010**, *43* 429-439.

55. Pagliara, S.; Vitiello, M. S.; Camposeo, A.; Polini, A.; Cingolani, R.; Scamarcio, G.; Pisignano, D. Optical Anisotropy in Single Light-Emitting Polymer Nanofibers. *J. Phys. Chem. C*. **2011**, *115* 20399–20405.

56. Ruggiero, A. J.; Todd, D. C.; Fleming, G. R. Subpicosecond Fluorescence Anisotropy Studies of Tryptophan in Water *J. Am. Chem. Soc.* **1990**, *112* 1003-1014.

57. Gao, Y.; Martin, T. P.; Niles, E. T.; Wise, A. J.; Thomas, A. K.; Grey, J. K. Understanding Morphology-Dependent Polymer Aggregation Properties and Photocurrent Generation in Polythiophene/Fullerene Solar Cells of Variable Compositions. *J. Phys. Chem. C*. **2010**, *114* (35), 15121-15128.

58. Tsoi, W. C.; James, D. T.; Kim, J. S.; Nicholson, P. G.; Murphy, C. E.; Bradley, D. D.; Nelson, J.; Kim, J. S. The Nature of in-Plane Skeleton Raman Modes of P3HT and Their Correlation to the Degree of Molecular Order in P3HT:PCBM Blend Thin Films. *J. Am. Chem. Soc.* **2011**, *133* (25), 9834-9843.

59. Veerender, P.; Saxena, V.; Chauhan, A. K.; Koiry, S. P.; Jha, P.; Gusain, A.; Choudhury, S.; Aswal, D. K.; Gupta, S. K. Probing the Annealing Induced Molecular Ordering in Bulk Heterojunction Polymer Solar Cells Using in-Situ Raman Spectroscopy. *Sol. Energ. Mat. Sol. Cells*. **2014**, *120* 526-535.

60. Kleinhenz, N.; Rosu, C.; Chatterjee, S.; Chang, M.; Nayani, K.; Xue, Z.; Kim, E.; Middlebrooks, J.; Russo, P. S.; Park, J. O.; Srinivasarao, M.; Reichmanis, E. Liquid Crystalline Poly(3-Hexylthiophene) Solutions Revisited: Role of Time-Dependent Self-Assembly. *Chem. Mater.* **2015**, *27* (7), 2687-2694.

61. Gao, Y.; Grey, J. K. *J. Am. Chem. Soc.* **2009**, *131* 9654-9662.

62. Gao, Y.; Martin, T. P.; Thomas, A. K.; Grey, J. K. *J. Phys. Chem. Lett.* **2009**, *1* 178-182.

63. Park, M. S.; Aiyar, A.; Park, J. O.; Reichmanis, E.; Srinivasarao, M. Solvent Evaporation Induced Liquid Crystalline Phase in Poly(3-Hexylthiophene). *J. Am. Chem. Soc.* **2011**, *133* 7244–7247.

64. Piris, J.; Dykstra, T. E.; Bakulin, A. A.; Loosdrecht, P. H. M. V.; Knulst, W.; Trinh, M. T.; Schins, J. M.; Siebbeles, L. D. A. Photogeneration and Ultrafast Dynamics of Excitons and Charges in P3HT/PCBM Blends. *J. Phys. Chem. C.* **2009**, *113* 14500–14506.

7.8 Tables and Figures

Table 7.1

Ratio of the Intensity of the Emission of the 0-0 to 0-1 Vibronic Bands of P3HT, S_r, as a Function of Electric Field Orientation for Emission Collected Parallel and Perpendicular to the Excitation Polarization[a]

S_r, parallel	S_r, perpendicular	J_0 (cm^{-1})[b]	Electric field angle [c]
0.89 ± 0.02	0.71 ± 0.01	68	No field ($E = 0$)
0.81 ± 0.01	0.98 ± 0.02	107	0˚
0.77 ± 0.01	0.88 ± 0.02	126	45˚
0.73 ± 0.01	0.85 ± 0.02	160	90˚

[a] Data summarized from the polarized fluorescence spectra presented in **Figure 7.2**.

[b] The excitonic coupling, J_0 is calculated using the equation, $J_0 = J_{k=0}/2$, where the excitonic shift of the $k = 0$ exciton ($J_{k=0}$) is given by: $\frac{I_{0-0}}{I_{0-1}} = \frac{\left(1-0.48\frac{J_{k=0}}{\omega_0}\right)^2}{\left(1+0.146\frac{J_{k=0}}{\omega_0}\right)^2}$.[54] ω_0 is the energy difference (in cm^{-1}) between the 0-0 and 0-1 transitions in the *absorption spectrum*, given by the *I* in the equation above. $\omega_0 = 1198$, 1401, 1293, and 1289 cm^{-1} for $E = 0$ (no applied field), and for $E = 0˚, 45˚, 90˚$ field angles, respectively.

[c] Angles are defined for the applied electric field ($E \neq 0$) as described in **Figure 7.1**.

Table 7.2

Fluorescence Anisotropy Parameters for Oriented P3HT Films
($\lambda_{ex} = 425$ nm and $\lambda_{em} = 720$ nm)

E-field direction [a]	r_0 [b]	$r(0)$ [c]	τ_D (ns) [c]	τ_F (ns) [d]
0˚	0.17 ± 0.01	0.18 ± 0.02	1.6 ± 0.4	0.30 ± 0.05
45˚	0.15 ± 0.01	0.16 ± 0.01	1.3 ± 0.4	0.25 ± 0.03
90˚	0.13 ± 0.01	0.12 ± 0.01	0.5 ± 0.3	0.32 ± 0.03
Reference (*i.e.*, $E = 0$)	0.11 ± 0.02	0.09 ± 0.02	0.7 ± 0.3	0.28 ± 0.05

[a] See **Figure 7.1** for the definitions of the angles specifying the E-field orientations.

[b] r_0 is the steady-state anisotropy: $-0.2 \leq r_0 \leq 0.4$

[c] Fluorescence anisotropy decays are constructed from equation (7.1) and fit to a single exponential of the form: $r(t) = r(0)\exp(-t/\tau_D)$. $r(0)$ is the anisotropy at time zero (*i.e.*, the limiting anisotropy): $-0.2 \leq r(0) \leq 0.4$.[39] At the same excitation wavelength, r_0 should equal $r(0)$. τ_D is the fluorescence depolarization time, *i.e.*, the $1/e$ time at which the parallel and perpendicular curves coalesce. Factors that contribute to depolarization are molecular motion (such as rotational diffusion) or nonradiative events such as interactions between electronic states of different polarization.

[d] τ_F, the average fluorescence lifetime, *i.e.*, $\langle\tau_F\rangle = A_1\tau_1 + A_2\tau_2$, where the A_i and the τ_i are the amplitudes and lifetimes of the two components in the double-exponential fit used to fit the fluorescence decay. The τ_1 and τ_2 are ~ 0.20 ns and ~ 0.62 ns, respectively in the reference film, which is consistent with the reported values in the literature.[64] The values of the two lifetime components are similar in the films exposed to electric field.

Table 7.3

Average Peak Maximum, FWHM and Ratio of the p- to s-Polarized Scattered Light Intensity (I_p/I_s) for the 1450 cm^{-1} Band of P3HT

P3HT	Peak Max (cm^{-1})[a]	FWHM (cm^{-1})[a]	I_p/I_s
film, 0°	1450.1 ± 0.1	31.6 ± 0.3	0.490 ± 0.010
film, 45°	1449.8 ± 0.2	31.9 ± 0.4	0.490 ± 0.009
film, 90°	1449.9 ± 0.1	31.5 ± 0.2	0.499 ± 0.008
film, E = 0	1449.7 ± 0.2	32.1 ± 0.4	0.521 ± 0.007
crystal, E = 0	1453.5 ± 0.1	31.3 ± 0.3	0.512 ± 0.009

[a] The p- and s-polarized excitation spectra were averaged, as there was no statistically significant difference measured between the spectra collected with different polarizations.

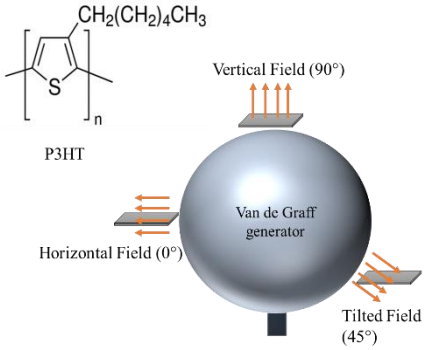

Figure 7.1. Diagram of the Van de Graaff electric-field generator, showing the sample placement and directions of the electric field relative to the sample. Also included is the structure of P3HT.

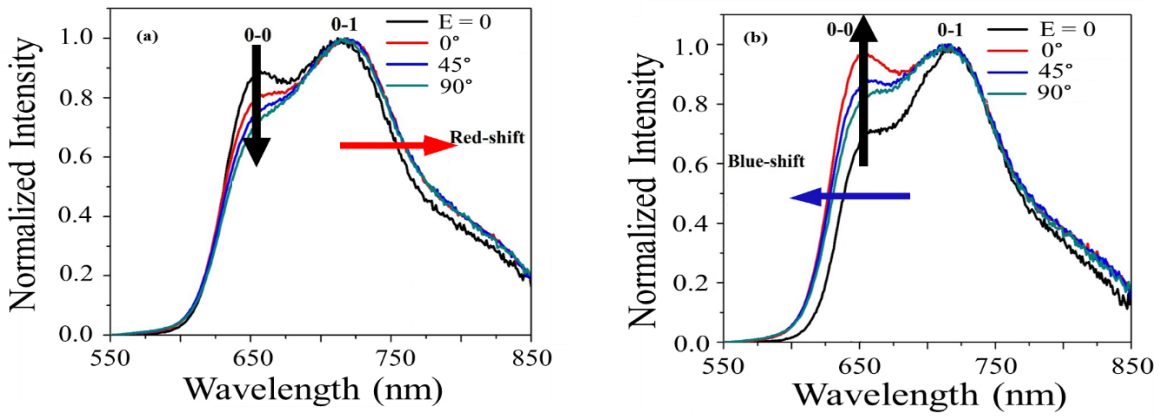

(a) (b)

Figure 7.2. Polarized fluorescence emission spectra of P3HT thin films: (a) emission parallel, and (b) perpendicular to the polarization of the 520 nm excitation beam. The spectra are normalized at the 0-1 vibronic transition. $S_r = I_{0\text{-}0}/I_{0\text{-}1}$. For (a) S_r = 0.81, 0.77, 0.76 and 0.89 for angles of 0°, 45°, and 90° and for the control (E = 0), respectively. Changing the electric field orientation from 0˚ to 90˚ decreases $I_{0\text{-}0}$, and hence S_r, as indicated by the direction of the black arrow. This change in electric field also induces a red shift in the spectra, as indicated by the direction of the red arrow. For (b) S_r = 0.98, 0.88, 0.85, and 0.71, for angles of 0°, 45°, and 90° and for the control (E = 0), respectively. From reference (E = 0) film to the films exposed to E-field, $I_{0\text{-}0}$ increases, and hence S_r, as indicated by the direction of the black arrow. This change in electric field also induces a blue shift in the spectra, as indicated by the direction of the blue arrow. (The orientation of the polarizers with respect to the electric field is given in **Figure S7.2** for further clarification).

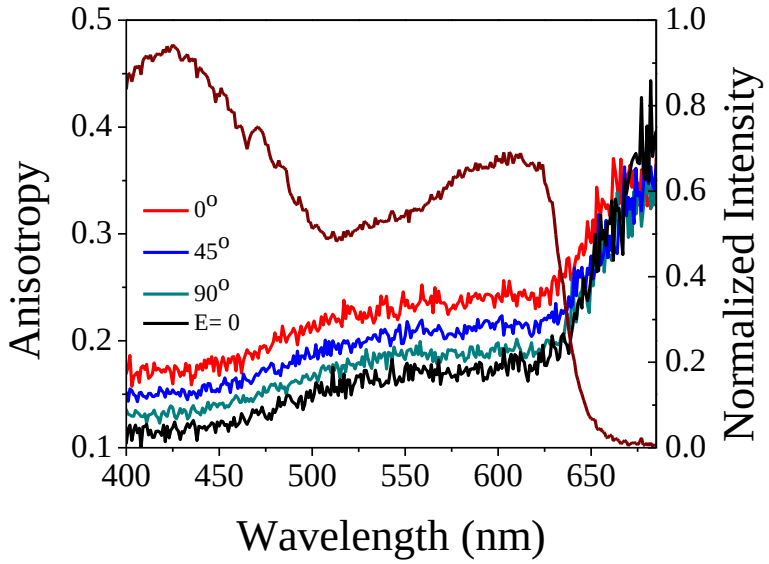

Figure 7.3. Fluorescence excitation spectrum of a P3HT film collected with parallel orientation of excitation and emission polarizers) (brown curve, right ordinate). Fluorescence excitation anisotropy of P3HT films prepared under different orientations of the applied electric field (left ordinate). λ_{em} = 720 nm.

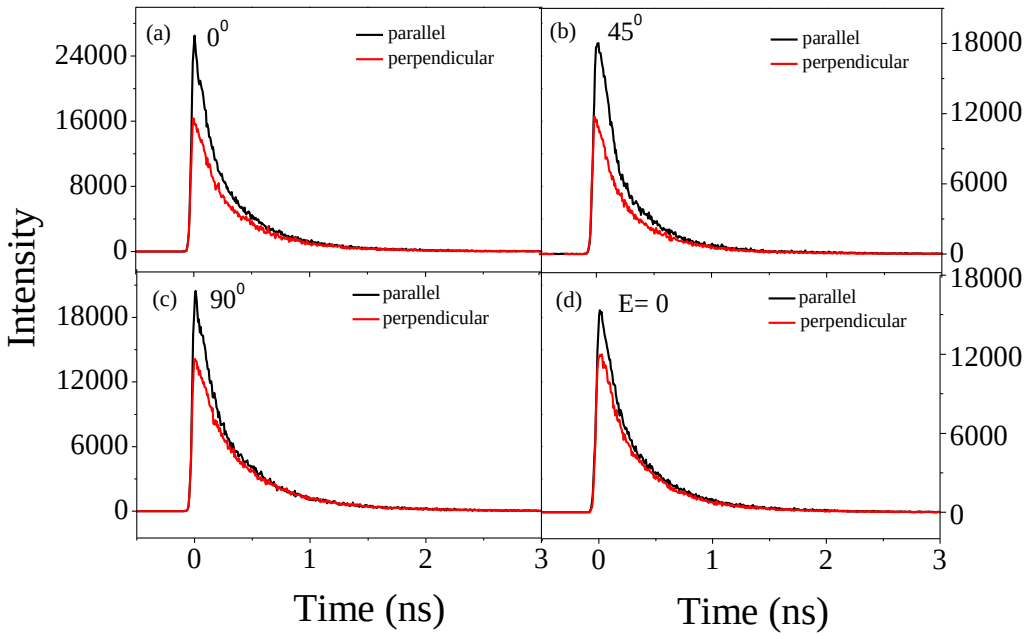

Figure 7.4. Time-resolved polarized emission of P3HT films prepared under (a) 0°, (b) 45°, (c) 90°, (d) and E = 0 with the emission polarizer parallel to the excitation polarizer (black), and the emission polarizer perpendicular to the excitation polarizer (red). λ_{ex} = 425 ± 10 nm, and λ_{em} = 720 ± 5 nm.

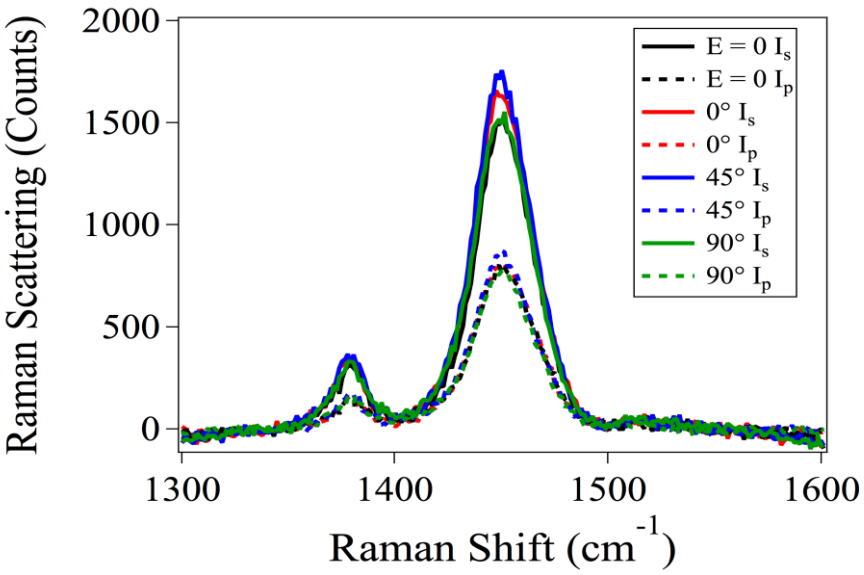

Figure 7.5. Example polarized Raman spectra for P3HT films oriented under an electric field. Peak location and FWHM values do not change. The relative intensities of I_p/I_s, however, do change for the samples prepared in an external electric field as reported in **Table 7.3**.